AD-A253 682

RL-TR-92-42, Vol II (of two)
In-House Report
February 1992

PROCEEDINGS OF THE 1991 ANTENNA APPLICATIONS SYMPOSIUM

Paul Mayes, et al

APPROVED FOR PUBLIC RELEASE; DISTRIBUTION UNLIMITED.

Rome Laboratory
Air Force Systems Command
Griffiss Air Force Base, NY 13441-5700

92-13757

92 5 22 076

This report has been reviewed by the Rome Laboratory Public Affairs Office (PA) and is releasable to the National Technical Information Service (NTIS). At NTIS it will be releasable to the general public, including foreign nations.

RL-TR-92-42, Vol II (of two) has been reviewed and is approved for publication.

APPROVED:

DANIEL J. JACAVANCO, Acting Chief
Antenna and Components Division

APPROVED:

JOHN K. SCHINDLER, Director
Electromagnetics and Reliability Directorate

REPORT DOCUMENTATION PAGE

Public reporting burden for this collection of information is estimated to average 1 hour per response, including the time for reviewing instructions, searching existing data sources, gathering and maintaining the data needed, and completing and reviewing the collection of information. Send comments regarding this burden estimate or any other aspect of this collection of information, including suggestions for reducing this burden, to Washington Headquarters Services, Directorate for Information Operations and Reports, 1215 Jefferson Davis Highway, Suite 1204, Arlington, VA 22202-4302, and to the Office of Management and Budget, Paperwork Reduction Project (0704-0188), Washington, DC 20503

1. AGENCY USE ONLY (Leave blank)	2. REPORT DATE February 1992	3. REPORT TYPE AND DATES COVERED Final Report

4. TITLE AND SUBTITLE Proceedings of the 1991 Antenna Applications Symposium	5. FUNDING NUMBERS PE 62702F PR 4600 TA 14 WU PF
6. AUTHOR(S) Paul Mayes et al	Contract F30602-88-D-0028

7. PERFORMING ORGANIZATION NAME(S) AND ADDRESS(ES) University of Illinois Champaign–Urbana, Illinois 61801	8. PERFORMING ORGANIZATION REPORT NUMBER

9. SPONSORING/MONITORING AGENCY NAME(S) AND ADDRESS(ES) Rome Laboratory/ERAS Hanscom AFB, MA 01731-5000 Contract Manager: John Antonucci	10. SPONSORING/MONITORING AGENCY REPORT NUMBER RL-TR-92-42 (Volume II)

11. SUPPLEMENTARY NOTES
Volume I consists of pages 1 – 252; Volume II consists of pages 253-473

12a. DISTRIBUTION/AVAILABILITY STATEMENT Approved for public release; distribution unlimited	12b. DISTRIBUTION CODE

13. ABSTRACT (Maximum 200 words)

The Proceedings of the 1991 Antenna Applications Symposium is a collection of state-of-the-art papers relating to phased array antennas, multibeam antennas, satellite antennas, microstrip antennas, reflector antennas, HF, VHF, UHF and various other antennas.

14. SUBJECT TERMS Antennas	Microstrip UHF	15. NUMBER OF PAGES 228
Satellite antennas Broadband antennas	Reflector Multibeam antennas HF Array antennas VHF	16. PRICE CODE

17. SECURITY CLASSIFICATION OF REPORT Unclassified	18. SECURITY CLASSIFICATION OF THIS PAGE Unclassified	19. SECURITY CLASSIFICATION OF ABSTRACT Unclassified	20. LIMITATION OF ABSTRACT SAR

CONTENTS

WEDNESDAY, SEPTEMBER 25, 1991

PHASED ARRAY SIGNAL PROCESSING

ARRAYS

*   NOT INCLUDED IN THIS VOLUME

iii

By		
Distribution/		
Availability Codes		
Dist	Avail and/or Special	
A-1		

Contents

THURSDAY, SEPTEMBER 26, 1991

REFLECTORS AND LENSES

* NOT INCLUDED IN THIS VOLUME

MICROWAVE AND MM WAVE

FRIDAY, SEPTEMBER 27, 1991

BROADBAND AND OTHERS

* NOT INCLUDED IN THIS VOLUME

The Continuous Transverse Stub (CTS) Array: Basic Theory, Experiment, and Application

W. W. Milroy
Hughes Aircraft Company
Radar Systems Group

Abstract

A new microwave coupling/radiating element, the Continuous Transverse Stub (CTS) is introduced. The basic theory and application of this element in antenna arrays, filters, and couplers are described. Performance, producibility, and packaging advantages relative to competing technologies are enumerated. Prototype antenna array designs, hardware, and measurements at Ku- and V-band are described.

1.0 Introduction

A continuous transverse stub (CTS) residing in one or both conductive plates of a parallel plate waveguide may be utilized as a reactive or radiating element in microwave, millimeter-wave, and quasi-optical filter and antenna applications. Purely reactive elements are realized through conductively terminating or narrowing the end of the stub. Radiating elements are formed when stubs of moderate height are opened to freespace. Precise control of element coupling or amplitude and phase excitation via coupling of the parallel plate waveguide modes is accomplished through variation of longitudinal stub length, stub height, parallel plate separation, and the constituent properties of the parallel plate and stub dielectric medium(s).

The CTS element can be arrayed to form a planar aperture or structure of arbitrary area, comprised of a linear array of continuous transverse elements fed by an arbitrary line source. Conventional methods of coupler, filter, or antenna array synthesis and analysis can be used in either the frequency or spatial domains.

2.0 Basic Theory

Figure 1 illustrates the basic CTS element. Incident waveguide modes, launched via a primary line feed of arbitrary configuration, have associated with them longitudinal electric current components which are interrupted by the presence of a continuous or quasi-continuous transverse stub, thereby exciting a longitudinal, z-directed displacement current across the stub/parallel plate interface. This induced displacement current in turn excites equivalent x-traveling waveguide modes in the stub which travel to its terminus and either radiate into freespace, are coupled to a second parallel plate region, or are totally reflected.

253
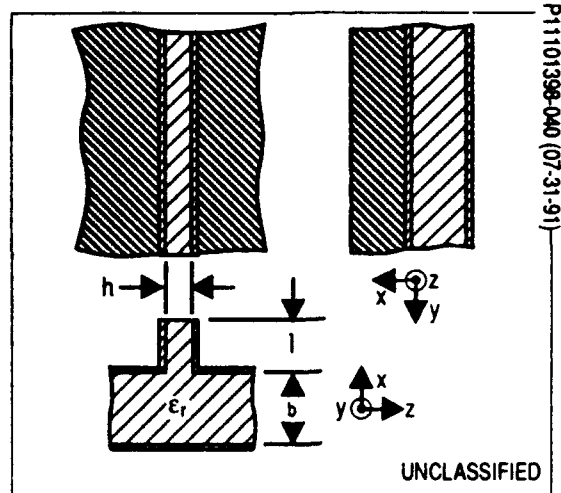
(U) Figure 1. Radiating CTS Element

a. Reactive CTS Element (Short)   b. Reactive CTS Element (Open)   c. Coupling CTS Element
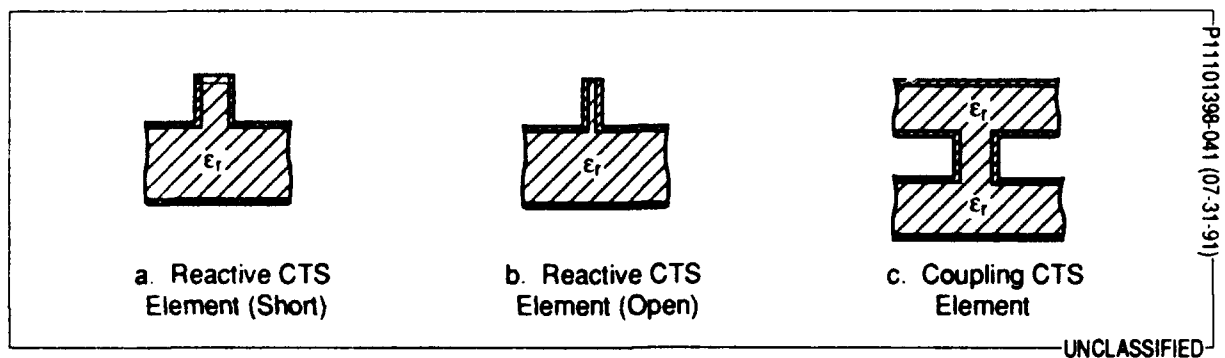
(U) Figure 2. CTS Element Configurations

254

For the radiator case, the electric field vector is linearly oriented transverse to the CTS element. Radiating, coupling, or reactive CTS elements can be combined in a common parallel plate structure to form a variety of microwave, millimeter-wave, and quasi-optical components including integrated filters, couplers, and antenna arrays. Figure 2 shows the basic CTS element in its short-circuit, open-circuit, and coupler configurations.

Backscattered energy from both the parallel plate/stub and stub/freespace or stub/secondary guide interfaces coherently interact with incident energy in the conventional transmission line sense as shown in Figure 3. These basic interactions are adequately modeled and exploited using standard transmission line theory. Fringing effects at both interfaces are adequately modeled using conventional mode matching techniques and/or two-dimensional finite element analysis. The variable length (1) and height (h) of the coupling stub controls its electrical line length (B_1l) and characteristic admittance (Y_1) and allows for controlled transformation of its terminal admittance (dependent primarily on h, e_r, and external mutual coupling effects) back to the main parallel plate transmission line, whose characteristic admittance is governed by its height, b, thus allowing for a wide range of discrete coupling values, $|K|^2$ from -3 dB to less than -35 dB. Variations in coupling stub length also allow for straightforward phase modulation of the coupled energy, as required in shaped beam antenna and multistage filter applications.

Figure 4 shows the derived scattering parameters ($S_{11},S_{22},S_{12},S_{21}$) and coupling coefficient, $|K|^2$, for the CTS element based on simple transmission line theory (neglecting fringing effects.) Note that coupling values are chiefly dependent on the mechanical ratio of stub height (h) relative to the height (b) of the parallel plate waveguide region, consistent with a simple voltage divider relationship. Because this mechanical ratio is independent of the operating frequency and dielectric constant of the structure, the CTS element is inherently broadband and forgiving of small variations in mechanical and constituent material specifications. Y_s may be set to infinity, zero, or Y_2 configurations without loss of generality. Note that the two-dimensional, semi-infinite, non-resonant nature of the CTS structure lends itself well to relatively simple finite-element and mode-matching analyses.

Based on the simple transmission-line model and assuming an isolated element, parameterized coupling curves for radiating element coupling versus stub height (h) may be computed for the purpose of sensitivity analysis. Figure 5 illustrates a nominal coupling curve (solid) for an element intended for operation at 60 GHz. Note the benign effect of frequency, dielectric constant, stub height, and parallel-plate separation variation on predicted coupling values (dash).

As an overmoded structure, the parallel plate transmission line within which the CTS elements reside will support a number of waveguide modes which simultaneously meet the boundary conditions imposed by the two conducting plates of the structure. The number and relative intensity of these propagating modes depends

255

$$\Gamma_s = \frac{Y_1 \cdot Y_s}{Y_1 + Y_s}$$
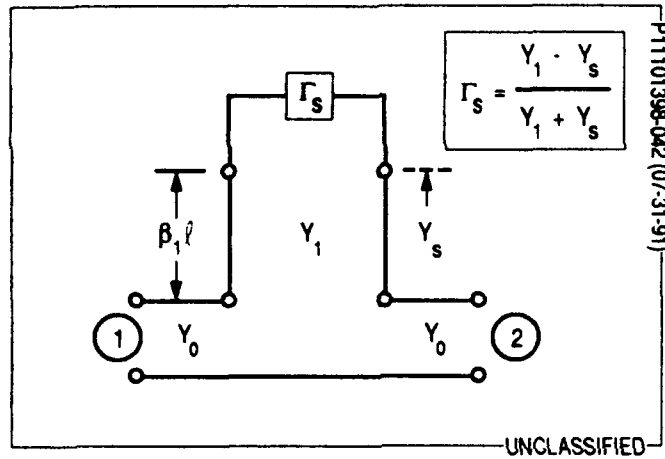
UNCLASSIFIED

(U) Figure 3. Simplified Equivalent Circuit

$$\hat{S}_{11} = \hat{S}_{22} = \frac{\alpha}{(1+\alpha)} \qquad \hat{S}_{12} = \hat{S}_{21} = \frac{1}{(1+\alpha)}$$
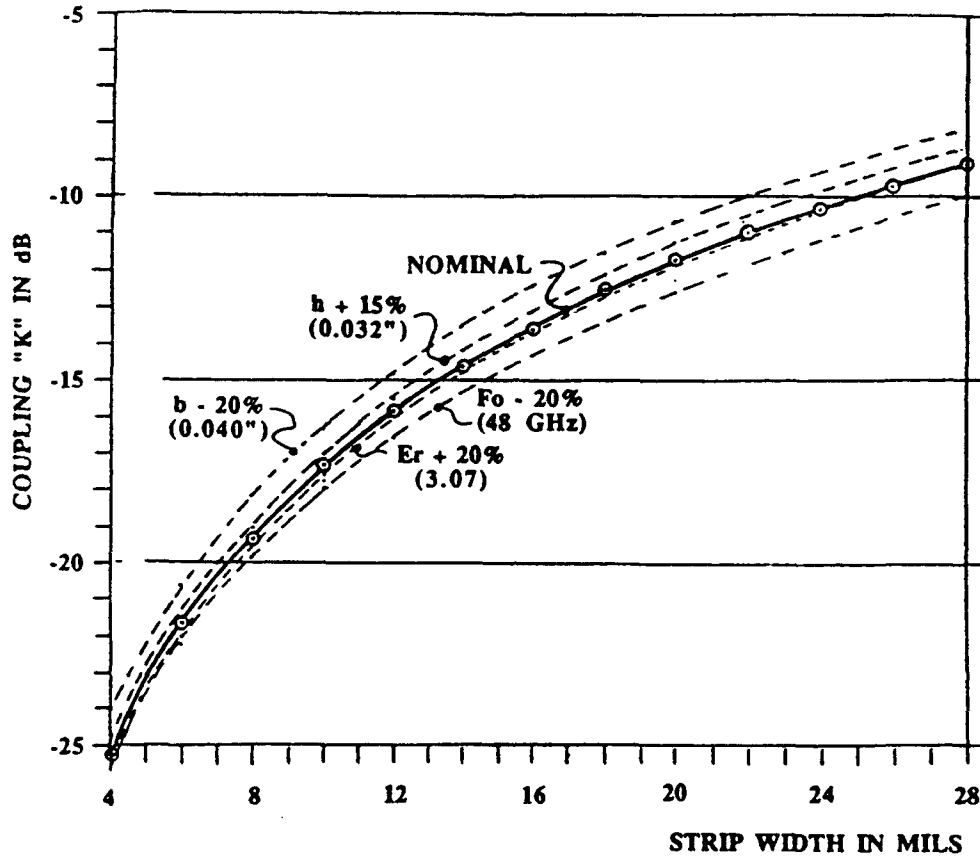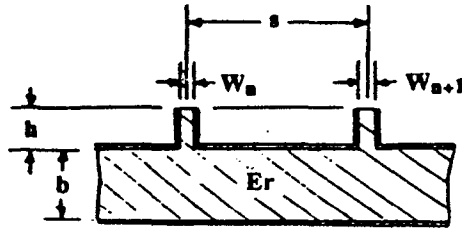
$$|K|^2 = 1 - \frac{1+|\alpha|^2}{|1+\alpha|^2}$$

WHERE:
$$\alpha = \left(\frac{h}{2b}\right)\left[\frac{1 + \Gamma_{se}^{-j2\beta_1 l}}{1 - \Gamma_{se}^{-j2\beta_1 l}}\right]$$

UNCLASSIFIED

(U) Figure 4. Equivalent Circuit Design Equations

(U) Figure 5. Sensitivity Analysis of CTS Coupling Factor Versus Key Design Parameters

exclusively upon the transverse excitation function imposed by the finite line source. Once excited, these mode coefficients are unmodified by the presence of the CTS element because of its continuous nature in the transverse plane.

In theory, each mode has associated with it a unique propagation velocity which, given enough distance, will cause undesirable dispersive variation of the line source imposed excitation function in the longitudinal direction of propagation. However, for typical excitation functions, these mode velocities differ from that of the dominant TEM mode by much less than one percent and the transverse plane excitation imposed by the line source is therefore essentially translated, without modification, over the entire finite longitudinal extent of the CTS array structure.

Figure 6 illustrates the theoretical constant amplitude contours for the x-directed electric field within an air filled 6 by 15 inch parallel plate region fed by a discrete linear array located at y=0 and radiating at a frequency of 60 GHz. A cosine-squared amplitude excitation was chosen so as to excite a multitude of odd modes within the parallel plate region. Note the consistency of the imposed transverse excitation over the entire longitudinal extent of the cavity.

The relative importance of edge effects in the CTS array depends primarily on the imposed line source excitation function, but they are generally small because of the strict longitudinal d.rection of propagaticn in the structure. In many cases, especially those employing steep excitation tapers, short circuits may be introduced at the edge boundaries with little effect on internal field distributions. In those applications where edge effects are not negligible, load materials may be applied as required at the array edges.

3.0 Relative Advantages

For antenna applications, a CTS array realized as a conductively plated dielectric has many performance, producibility, and application advantages over conventional slotted waveguide array, printed patch array, and reflector/lens antenna approaches. Some distinct advantages in filter and coupler applications may be realized as well.

The CTS technology is applicable to all planar array applications at microwave, millimeter-wave, and quasi-optical frequencies. Shaped beams, multiple beams, dual-polariza+ion, dual-bands, and monopulse functions can be accommodated. In addition, the planar CTS array is a prime candidate to replace reflector and lens antennas in applications for which planar arrays have proved inappropriate because of traditional bandwidth or cost limitations.

Field Amplitude
(E_z) Over
Parallel-Plate
Region

Cylindrical Outgoing
Waves (Hankel)
Assumed for Each
Discrete Element

λ_g for
TE_{mo}/TM_{mo}
Modes

m	λ_g
0	0.1967200"
1	0.1967242"
3	0.1975581"
5	0.1968252"
7	0.1969276"
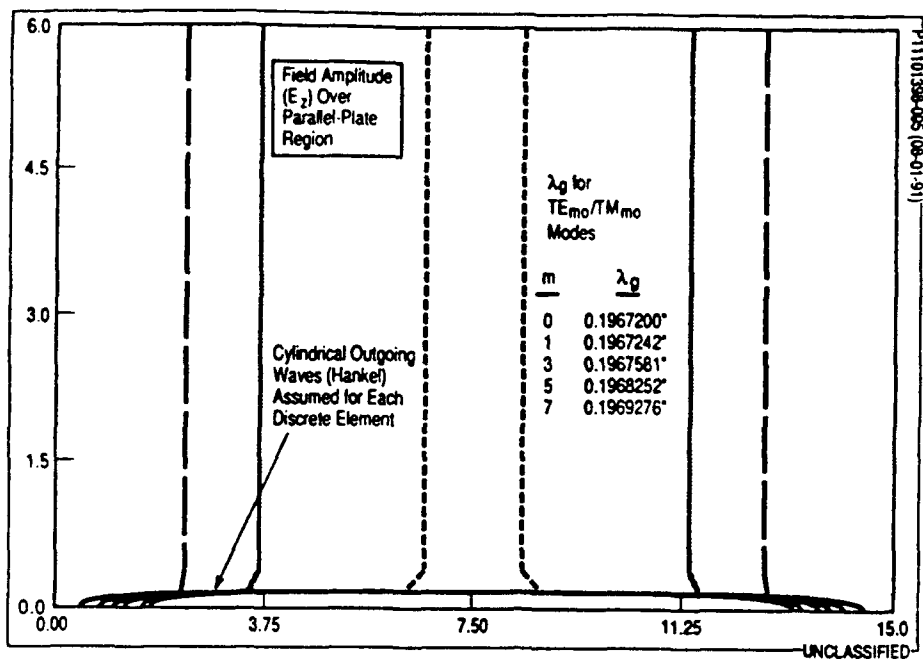
(U) Figure 6. Constant Amplitude Contours in CTS Parallel Plate Region
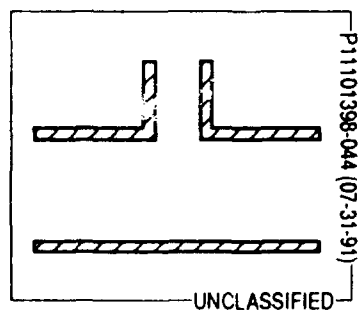
(U) Figure 7. Air-Filled CTS Element

(U) a. Artificial Dielectric CTS Element

(U) b. Laminated Dielectric CTS Element
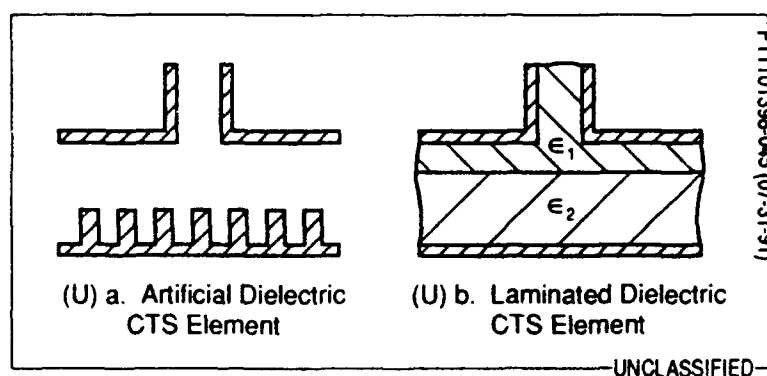
(U) Figure 8. Inhomogeneous Structures

Additional advantages in millimeter-wave and quasi-optical filter and coupler markets can be realized due to the enhanced producibility and relative low loss of the CTS element over stripline, microstrip, and even waveguide elements. Filter and coupler capabilities can be fully integrated with radiator functions in a common structure.

Performance advantages include:

- Superior aperture efficiency/enhanced filter "Q", approximately one-half the loss of dielectrically-filled waveguide.

- Superior frequency bandwidth of up to one octave per axis, with no resonant components or structures.

- Superior broadband polarization purity, typically -50 dB cross-pol.

- Superior broadband element excitation range and control, coupling values from -3 dB to -35 dB per element are realizable.

- Superior broadband shaped-beam capability. Nonuniform excitation phase is implemented through modulation of stub length and/or position.

- Superior E-plane element factor. Recessed groundplane allows for wide scanning capability, even to endfire.

- Superior power handling capability.

Producibility advantages include:

- Superior insensitivity to dimensional and material variations, <0.50 dB coupling variation for 20 percent change in dielectric constant, no resonant structures.

- Totally externalized construction.

- Simplified fabrication procedures and processes. Units can be thermoformed/extruded/injected in a single molding process, and no additional joining or assembly is required.

- Reduced design NRE costs and cycle time through modular/scalable design, simple and reliable RF theory/analysis, and two-dimensional complexity which is reduced to one dimension.

<u>Application advantages include:</u>

¨ Very thin profile.

¨ Lightweight.

¨ Conformal array can be curved without affecting internal coupling mechanisms.

¨ Superior durability with no internal cavities.

¨ Dual-polarization/dual-band/dual beam capable.

¨ Frequency-scannable.

¨ Electronically scannable.

¨ Reduced radar cross section (RCS).

¨ Applicable at millimeter-wave and quasi-optical frequencies.

¨ Integrated filter/coupler/radiator functions in common structure.

4.0 <u>CTS Element Variants and Applications</u>

There are several variations on the basic CTS element that may prove useful in particular applications. They are:

4.1 <u>Nondielectrically Loaded</u>

A low density foam can be used as the transmission line medium for the CTS element as shown in Figure 7 to realize an efficient element for an endfire array. The CTS radiator is particularly well-suited in such applications due to its broad pseudo-uniform E-plane element pattern, even at endfire.

4.2 <u>Slow-Wave/Inhomogeneous Structures</u>

Figure 8 shows that an artificial dielectric or multiple dielectric can be used in the parallel plate region in applications for which minimal weight, complex frequency dependence, or precise phase velocity control is required.

4.3 Oblique Incidence

As shown in Figure 9, an oblique incidence of propagating waveguide modes can be achieved through mechanical or electrical variation of the incoming phase front relative to the CTS radiator element axis for scanning the beam in the transverse H-plane. This variation would normally be imposed through mechanical or electrical variation of the primary line feed exciting the parallel plate region. The precise scan angle of this scanned beam will be related to the angle of incidence of the waveguide mode phase front via Snell's Law. That is, refraction will occur at the stub/freespace interface in such a way as to magnify any scan angle imposed by the mechanical or electrical variation of the line feed. This phenomenon can be exploited to allow for relatively large antenna scan angles with only small variations in line feed orientation/phasing. Coupling values can be expected to be pseudo-constant (cosine-dependent) for small angles of incidence.

4.4 Longitudinal Incidence

A narrow CTS element will not couple dominant waveguide modes having phase fronts parallel to the stub axis. This characteristic, shown in Figure 10, can be exploited through implementation of orthogonal CTS radiator elements in a common parallel plate region. In this way, two isolated, orthogonally polarized antenna modes can be simultaneously supported in a shared aperture for the purpose of realizing dual-polarization, dual-band, or dual-beam capabilities.

4.5 Parameter Variation in the Transverse Dimension

Slow variation of stub dimensions in the transverse dimension can be used to realize tapered coupling in the transverse plane, as shown in Figure 11. This capability proves useful in antenna array applications in which nonseparable aperture distributions are desirable or for nonrectangular array shapes. The modified element is called a quasi-continuous transverse stub (QCTS.) Analysis results based on the continuous transverse slot model can be expected to remain locally valid for the case of transverse variation, assuming that variation profiles are smooth and gradual.

262

$$\sqrt{\varepsilon_r}\, \sin\theta_i = \sin\theta_r$$
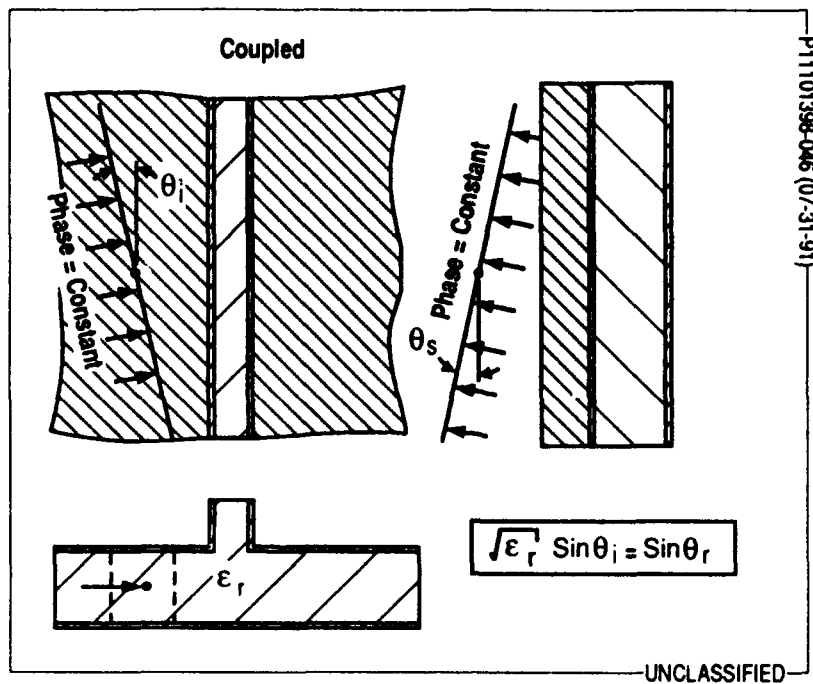
(U) Figure 9. H-Plane Scanning Utilizing a Canted Phase-Front
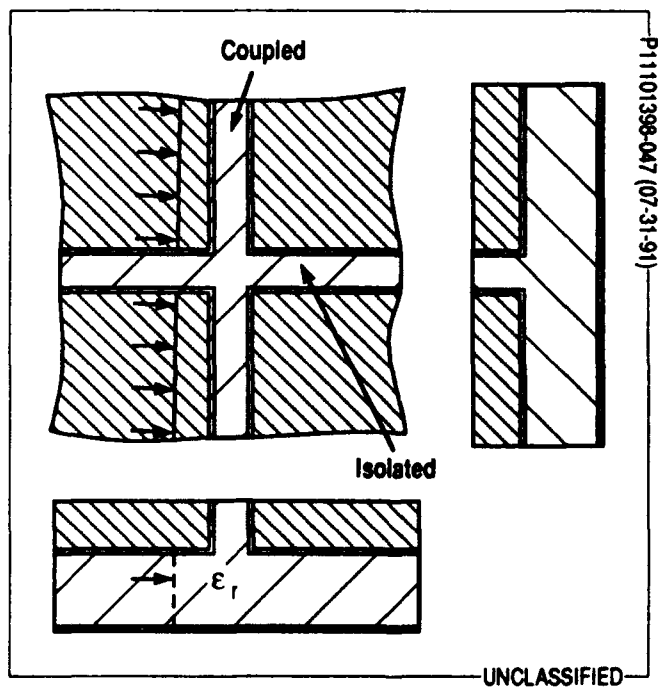
(U) Figure 10. Dual-Aperture Realization Utilizing CTS
Elements
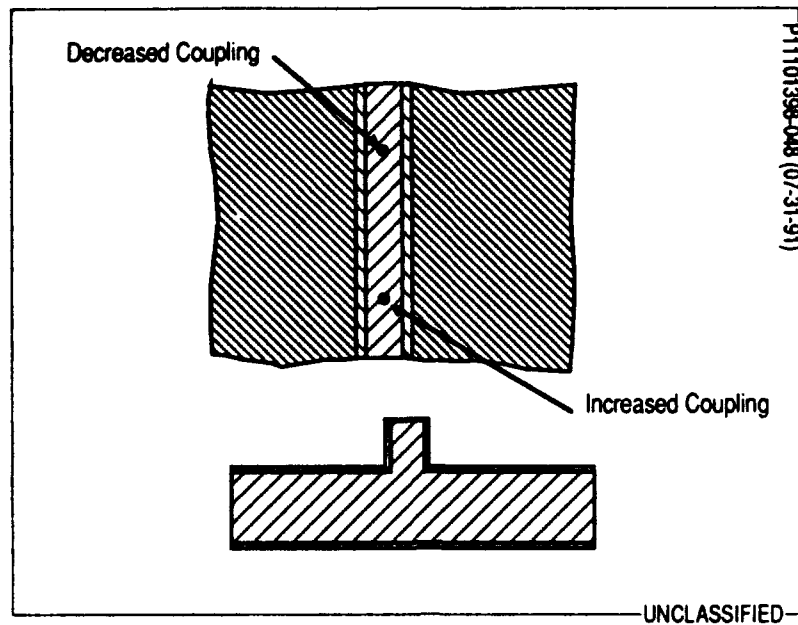
(U) Figure 11. Quasi-Continuous Transverse Stub (QCTS)
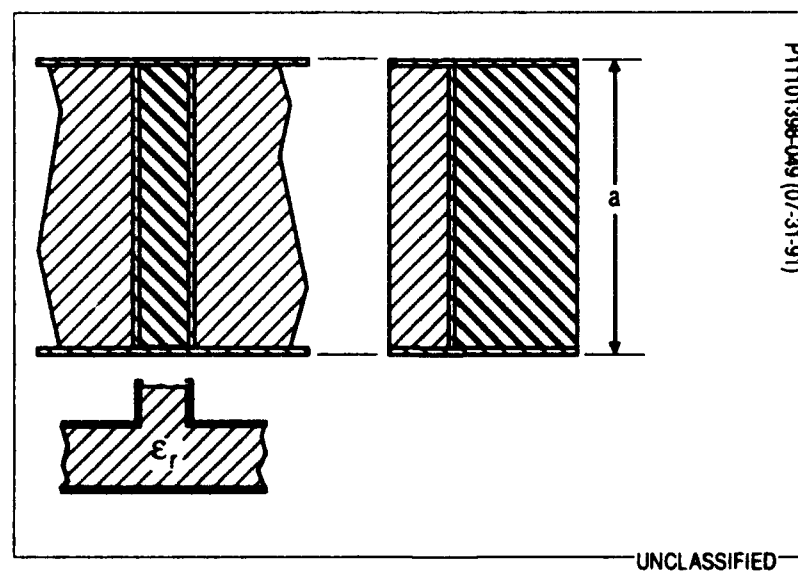
(U) Figure 12. Truncated CTS Element

4.6 Finite Width Element

Although conventionally very wide in the transverse extent, the CTS element can be utilized in reduced width configurations down to and including simple rectangular waveguide. The sidewalls of such a truncated CTS element, shown in Figure 12, may be terminated in short circuits, open circuits, or loads as dictated by the particular application.

4.7 Multistage Stub/Transmission Sections

Figure 13 shows that multiple stages can be employed in the stub or parallel plate regions to modify coupling or broaden frequency bandwidth characteristics of the structure as dictated by specific electrical and mechanical constraints.

4.8 Paired Elements (Matched Couplet)

Figure 14 shows how pairs of closely spaced similar CTS radiator elements can be used to customize composite antenna element factors or to minimize composite element VSWR through destructive interference of individual reflection contributions. Bandpass filter implementations can also be realized in a similar fashion when purely reactive CTS elements are used.

4.9 Radiating/Nonradiating Stub Pairs (Matched Couplet)

Figure 15 shows how a nonradiating purely reactive CTS element can be paired with a CTS radiator element to suppress coupler/radiator reflections through destructive interference of individual reflection contributions, resulting in a matched CTS couplet element. Such couplet elements may prove particularly useful in CTS array antennas when scanning the beam at or through broadside is required.

4.10 Double Sided Radiator/Filter

Figure 16 shows how radiator, coupler, and/or reactive stubs can be realized on both sides of the parallel plate structure to economize space or for antenna applications in which radiation from both sides of the parallel plate is desirable.

4.11 Radial Applications

The CTS element can be utilized in applications in which cylindrical waveguide modes are used in place of plane waveguide modes. As shown in Figure 17, the CTS element forms closed concentric rings in this

265

13. Multistage CTS Elements

14. Radiating Couplet

15. Reactive-Radiating Couplet

16. Two Side CTS Element
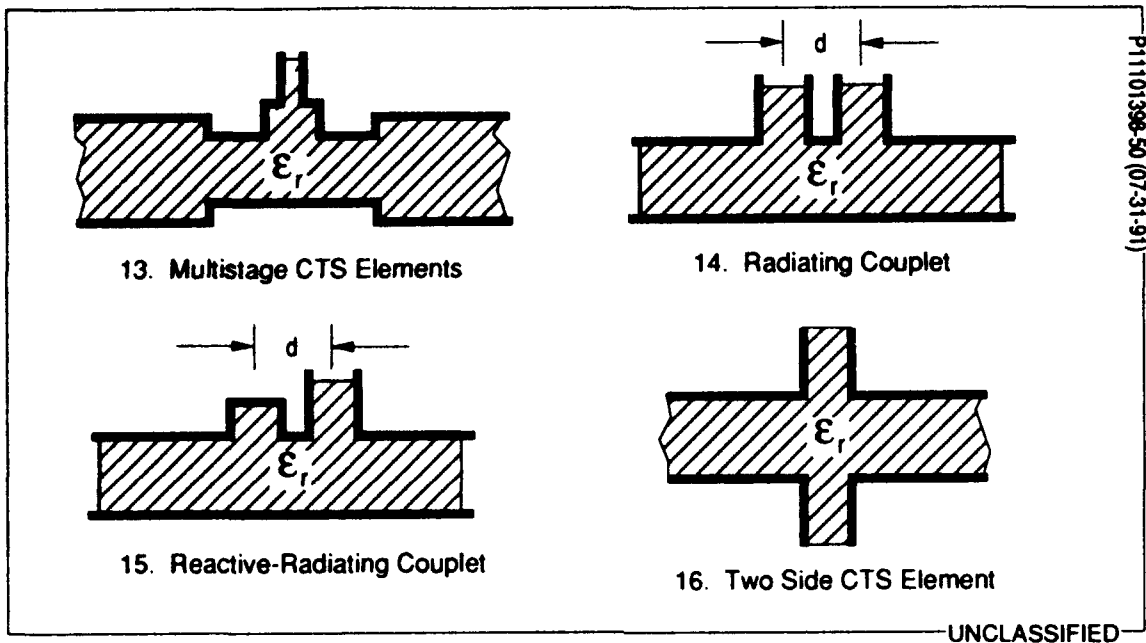
(U) Figure 13-16. Multistage Stub/Transmission Sections
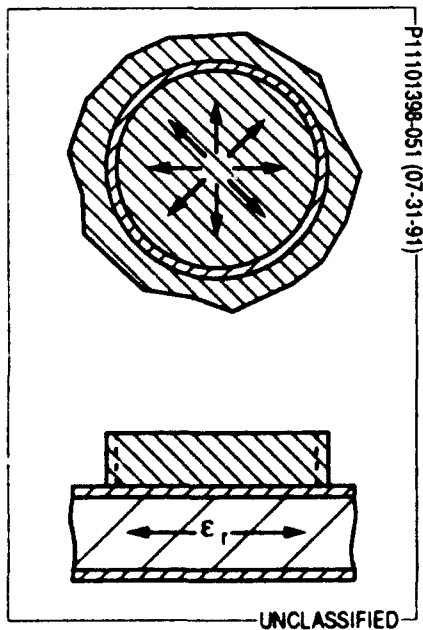
(U) Figure 17. Annular Ring
CTS Element
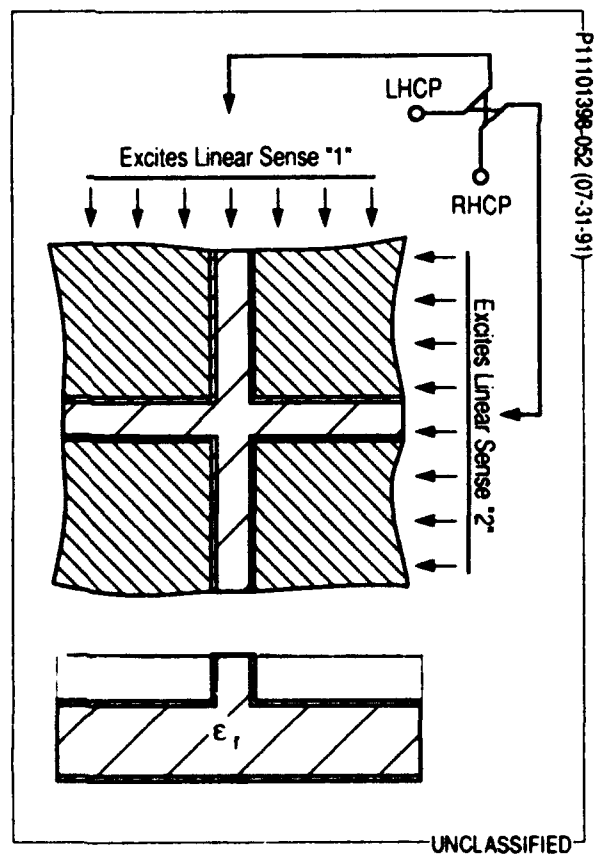
(U) Figure 18. Circular Polarization Utilizing CTS
Elements

266

radial configuration with coupling mechanisms and characteristics similar to those for the plane wave case. Single or multiple point sources serve as a primary feed. Both radiating and nonradiating versions of the CTS element can be realized for the cylindrical case. Such arrays may be particularly useful for antennas requiring high gain 360 degree coverage oriented along the radial direction and in one-port filter applications.

4.12 Circular Polarization

Although the CTS radiator element is exclusively a linearly polarized antenna element, Figure 18 shows how circular polarization can be realized in a straightforward fashion either through a standard quarter-wave plate polarizer or through quadrature coupling of orthogonally oriented CTS radiator elements or arrays.

5.0 Array Variants and Applications

The CTS element can be combined or arrayed to form a planar structure fed by an arbitrary line source. This line source may be either a discrete linear array, such as a slotted waveguide, or a continuous linear source, such as a pill-box or sectoral horn. Two line sources are used in filter and coupler applications to form a two-port device. In the case of antenna applications, a single line feed is utilized to impose the desired aperture distribution in the transverse plane while the parameters of individual CTS radiator elements are varied to control the aperture distribution in the longitudinal plane.

In filter and coupler applications, a second line feed can be introduced to form a two-port device comprised of CTS coupler or reactive elements. For antenna applications, either a short circuit, open circuit, or load can be placed at end of the CTS array opposite the line source to form a conventional standing wave or traveling wave feed.

Standard array, coupler, and filter synthesis and analysis techniques can be used in the selection of interelement spacings and electrical parameters for individual CTS elements in CTS array specifications. Normalized design curves relating the physical attributes of the CTS element to electrical parameters are derived either analytically or empirically to realize the desired CTS array characteristics.

The simple modular design of the CTS array greatly reduces the design NRE costs and cycle time associated with conventional planar arrays. Typical planar array developments require the individual specification and fabrication of each discrete radiating element along with associated feed components such as angle slots, input slots, and corporate feed. In contrast, the CTS planar array requires the specification of only two

267

linear feeds, one comprised of the array of CTS elements, the other of the requisite line feed. These feeds can be designed and modified separately and concurrently and are fully specified by a minimum number of unique parameters. Drawing counts and drawing complexities are thus reduced. Design modifications or iterations are easily and quickly implemented.

5.1 Pencil Beam Array

A standard pencil beam antenna array as shown in Figure 19 can be constructed using the CTS array concept with principle plane excitations implemented through appropriate selection of line source and CTS element parameters. Element spacings are conventionally chosen to be approximately equal to an integral number of wavelengths within the parallel plate region. Monopulse functions can be realized through appropriate modularization and feeding of the CTS array aperture.

5.2 Shaped Beam Array

The variable length of the stub portion of the CTS radiator allows for convenient and precise control of individual element phases in CTS antenna array applications. This control, in conjunction with the CTS element's conventional capability for discrete amplitude variation, allows for precise specification and realization of complex shaped beam antenna patterns, as shown in Figure 20. Examples include cosecant-squared and nonsymmetric sidelobe applications.

5.3 Multi-Aperture Array

The continuous stubs of a CTS array typically occupy no more than 10 to 20 percent of the total planar antenna aperture or filter area. The radiating apertures of these stubs are at their termination and are therefore raised above the groundplane formed by the main parallel plate transmission line structure. Relatively wide, continuous, transverse, conductive troughs are therefore formed between individual CTS elements as shown in Figure 21. These troughs can be exploited to introduce secondary array structures.

Possible exploitations include closing the trough to form a slotted waveguide cavity as shown in Figure 22; interdigitation of a printed patch array; slotting of the trough region to couple alternative modes from the parallel plate transmission line; or introduction of active elements as adjuncts to the CTS array structure.
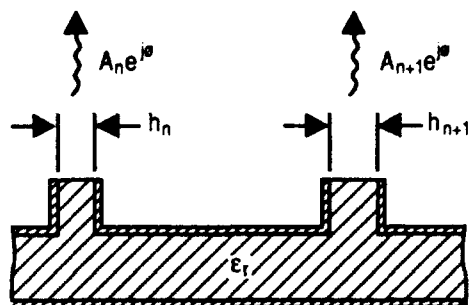
(U) 19. Pencil Beam Antenna Array
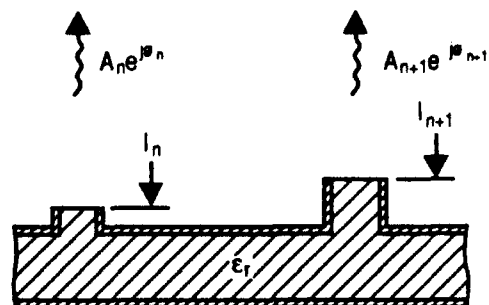
(U) 20. Shaped Beam Array
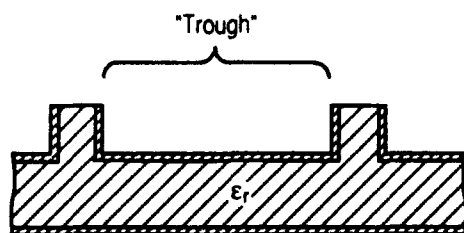
(U) 21. CTS Element Trough

(U) 22. Slotted Waveguide Cavity

(U) Figure 19-22. CTS Array Applications

5.4 Dual Polarization Array

An identical pair of orthogonally oriented CTS arrays can be utilized as shown in Figure 23 to realize a dual-polarization planar array sharing a common aperture area. Circular or elliptical polarizations can be realized through appropriate combination of the two orthogonal signals via a fixed or variable quadrature coupler or with the introduction of a conventional linear-to-circular polarizer. The pure linear polarization of individual CTS radiating elements and the natural orthogonality of the parallel plate waveguide modes provides this approach with superior broadband polarization isolation.

5.5 Dual-Beam Array

In a manner similar to the dual polarization approach, two dissimilar orthogonally oriented CTS arrays can be employed to provide a simultaneous dual antenna beam capability. For example, one CTS array might provide a vertically polarized pencil beam for air-to-air radar modes while another provides a horizontally polarized cosecant-squared beam for ground mapping. Dual squinted pencil beams for microwave relay represents a second application of this dual beam capability.

5.6 Dual-Band Array

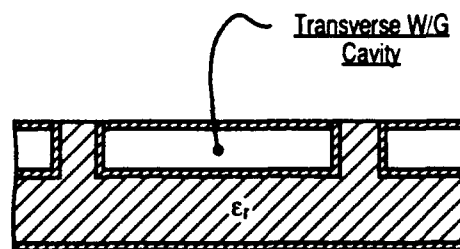Again utilizing a pair of orthogonally oriented CTS arrays, a dual-band planar array can be constructed through appropriate selection of interelement spacings and CTS element parameters for each array. The two selected frequency bands can be widely separated due to the dispersionless nature of the parallel plate transmission line structure and the frequency independent orthogonality of the waveguide modes.

5.7 Dual Guided Mode Array

Periodically spaced slots can be introduced in the trough regions between individual CTS array elements to couple alternative mode sets from the parallel plate transmission line structure. For example, a TE mode whose electric field vector is oriented parallel to the conducting plates of the parallel plate transmission line may be selectively coupled through the introduction of thick or thin inclined slots in the interelement trough regions, as shown in Figure 24. These slots may protrude slightly from the conductive plate groundplane to aid in fabrication. Such a mode is not coupled by the CTS elements due to the transverse orientation of its induced wall currents and the cut-off conditions of the CTS stubs. Likewise, the waveguide modes of the parallel plate waveguide structure, with its electric field vector oriented perpendicular to the conducting plates of the parallel plate transmission line, are not coupled to the inclined slots due to the disparity in operating and slot resonant frequencies, particularly for thick slots. In this way a dual-band planar array is formed with frequency band offsets regulated by the

270
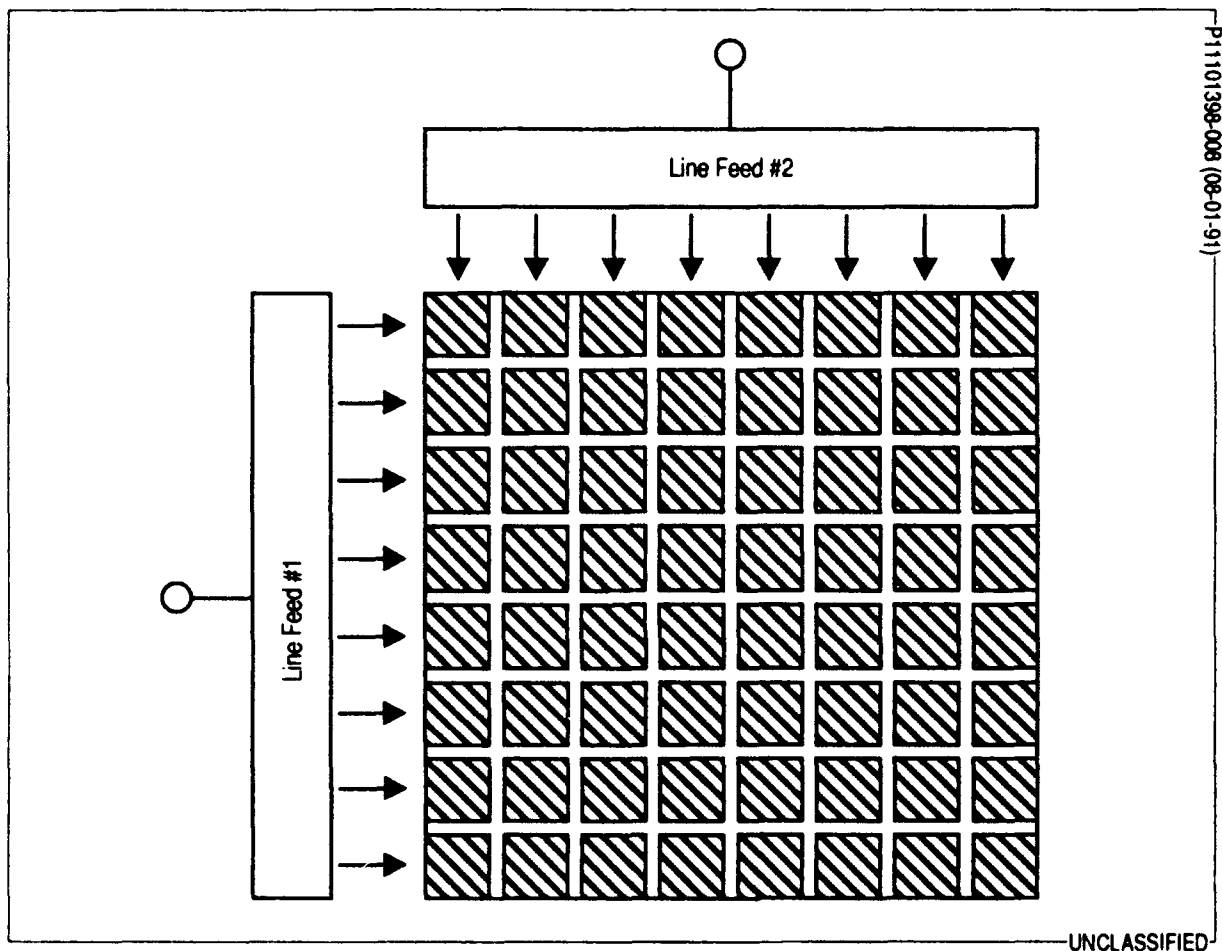
(U) Figure 23. Dual Polarization Array
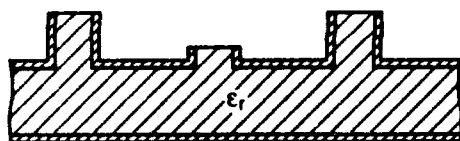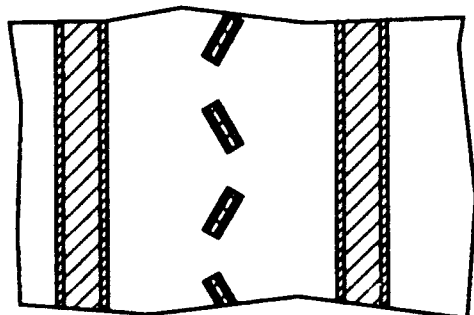
(U) 24. Interelement Trough Regions   (U) 25. Electric Field Components

UNCLASSIFIED

(U) Figure 24-25. Multimode Capabilities

interelement spacing of the CTS and inclined slot elements and the parallel plate spacing of the parallel plate transmission line.

Figure 25 shows the electric field components for TEM and TE_{01} modes. Dual-beam and dual-polarization apertures may also be realized using intentional multimode operation.

5.8 Fixed or Variable H-Plane Beam-Squint Array

As shown in Figure 26, an intentional fixed or variable beam squint (in one or both planes) can be realized with a CTS array through appropriate selection of CTS array element spacing, constituent material dielectric constant, or requisite line feed characteristics. Such a squinted array may be desirable for applications in which mounting constraints require deviation between the mechanical and electrical boresights of the antenna.
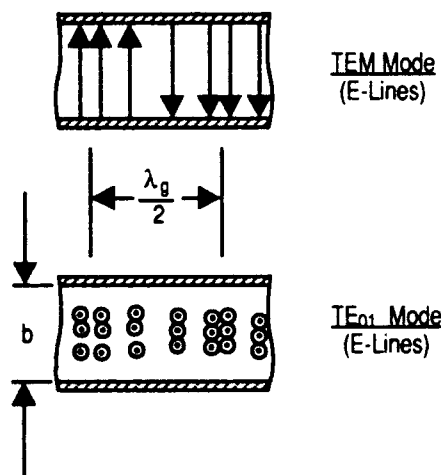
5.9 H-Plane Scanning by Mechanical Dithering of Line-Feed

The requisite line feed for a CTS antenna array can be mechanically dithered to vary the angle of incidence, or phase slope, of the propagating parallel plate waveguide modes relative to the CTS element axis. In doing so, a refraction enhanced beam squint of the antenna beam is realized in the transverse H-plane of the array, as shown in Figure 27.

5.10 H-Plane Scanning by Electrical Variation of Line-Feed Propagation Constant

Figure 28 shows an alternate method of varying of the angle of incidence of the propagating parallel plate waveguide modes relative to the CTS element axis. Such variation causes squinting of the phase front emanating from the line source while maintaining a fixed, parallel, mechanical orientation relative to the CTS element axis.

5.11 E-Plane Scanning by Variation of Planar Propagation Constant

Variation of the phase velocity within the parallel plate transmission line structure will scan the beam in the longitudinal E-plane. Such a variation may be induced through appropriate electrical or mechanical modulation of the constituent properties of the dielectric material contained within the parallel plate region. This scanning technique can be combined with scanning techniques in the transverse plane to achieve simultaneous beam scanning in two dimensions. This is the basic Hughes approach for exploiting voltage-controlled dielectric materials.

273
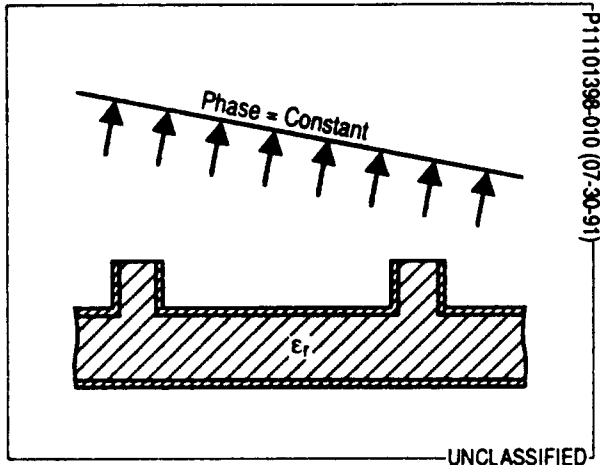
(U) Figure 26. Squint Beam Array
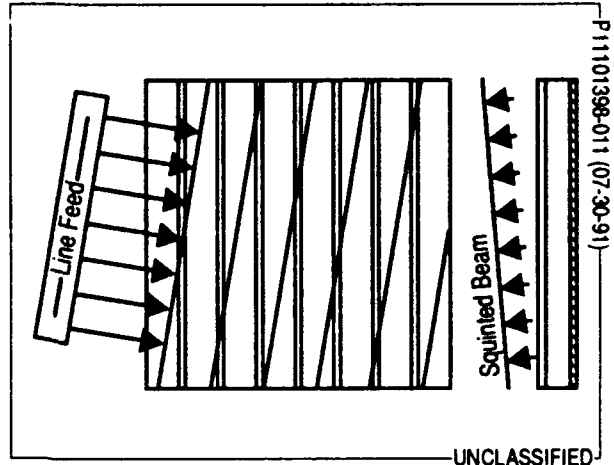
(U) Figure 27. Mechanical Line Feed Scanning
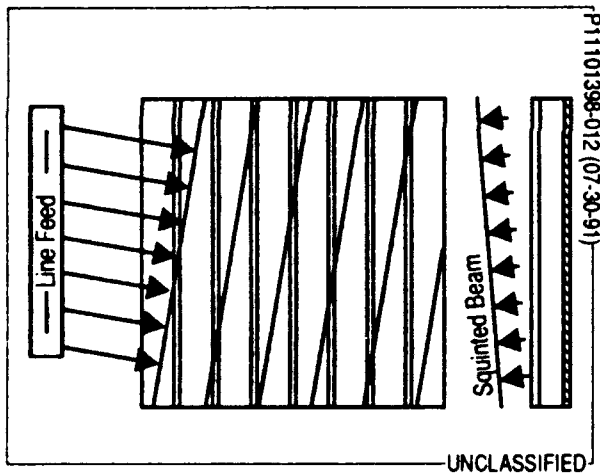
(U) Figure 28. Line Feed Phase Velocity
Variation Scanning
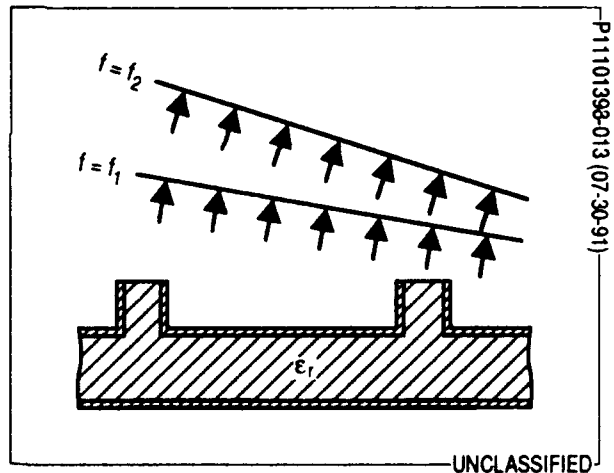
(U) Figure 29. Frequency Scanning

This modulation in phase velocity within the parallel plate transmission line structure can also be used in CTS array filter and coupler structures to frequency tune their respective passbands or stopband responses.

5.12 E-Plane Frequency Scanning

As shown in Figure 29, when used as a traveling wave antenna array structure, the position of the antenna mainbeam will vary with frequency. In applications where this phenomenon is desirable, interelement spacings and material dielectric constant values can be chosen to enhance this frequency dependent effect. For example, a CTS array fabricated from a high dielectric material ($e_r=12$) will exhibit approximately a two degree beam scan for a one percent variation in operating frequency.

5.13 Conformal Array

The absence of internal details within the CTS structure allows for convenient deformation of its shape to conform to curved mounting surfaces, e.g., wing leading edges, missile/aircraft fuselages and automobile bodywork. As shown in Figure 30, the overmoded nature of the CTS structure allows such deformation to large radii of curvature without perturbation of its planar coupling characteristics.

The interelement trough regions in the CTS array structure can provide a means for suppression of undesirable surface wave phenomena normally associated with conformal arrays. Deformation of the radiated phase front emanating from such a curved CTS array may be corrected to planar through appropriate selection of line feed and individual CTS element radiator phase values.

5.14 End-fire Array

The CTS array can be optimized for endfire operation, as shown in Figure 31, through appropriate selection of interelement spacings and constituent material characteristics. The elevated location relative to the interstub groundplane of the individual CTS radiator element surfaces affords a broad element factor and yields a distinct advantage to the CTS element in endfire applications.

5.15 Non-Rectangular Apertures

As shown in Figure 32, variation of CTS element parameters in the transverse plane yields a quasi-continuous transverse stub (QCTS) element that can be used in QCTS arrays for which nonseparable aperture distributions or nonrectangular aperture shapes (circular or elliptical) are desired. For continuous, smoothly varying modulation of QCTS element parameters, the excitation, propagation, and
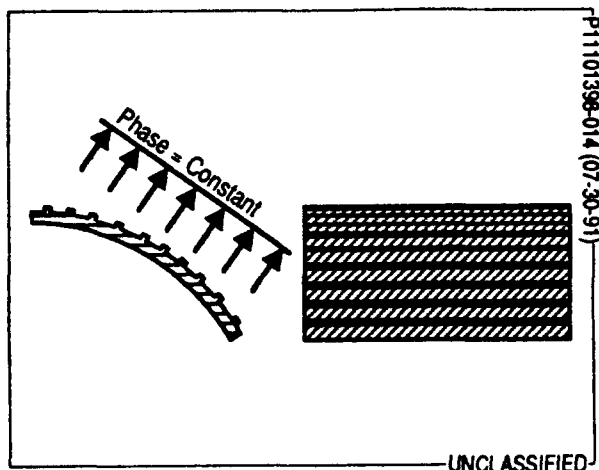
(U) Figure 30. Conformal Array
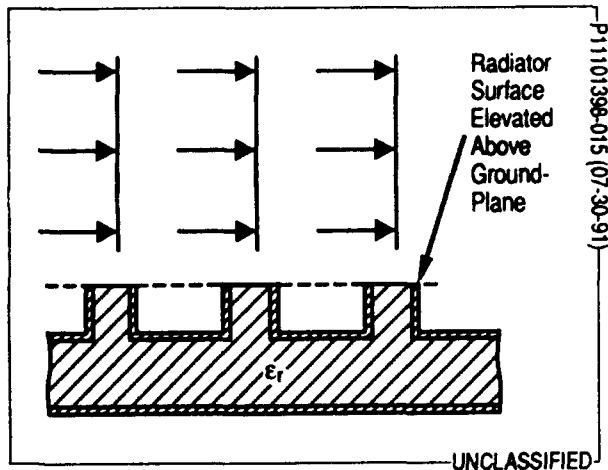
(U) Figure 31. Endfire Array
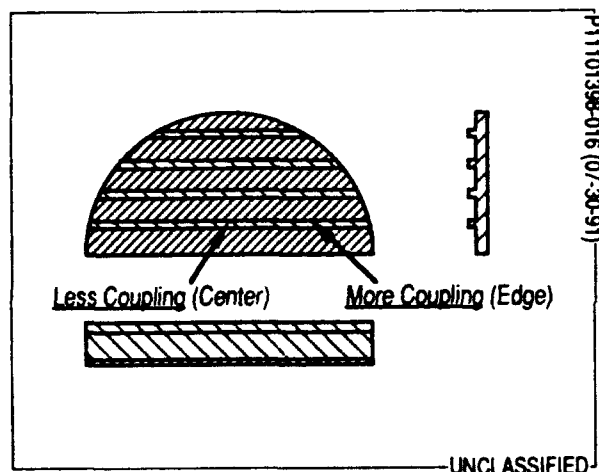
(U) Figure 32. Nonseparable Shaped Array
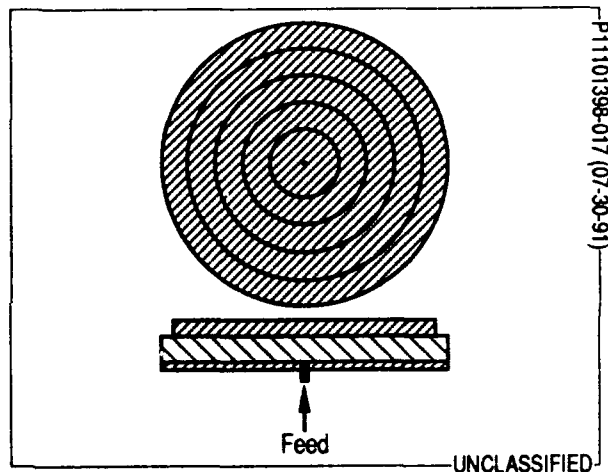
(U) Figure 33. Radial Array

(U) a. 2-Port Filter

(U) b. Equivalent Circuit
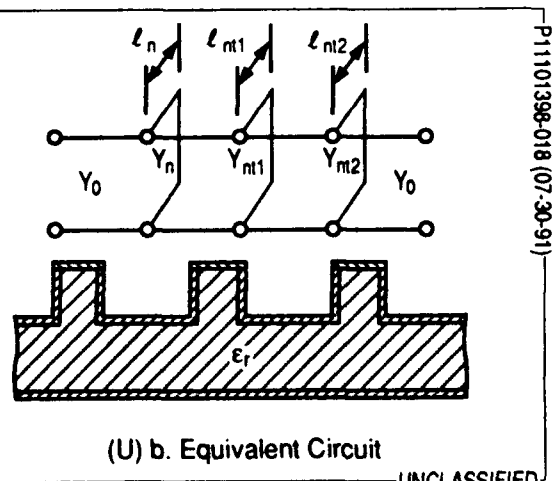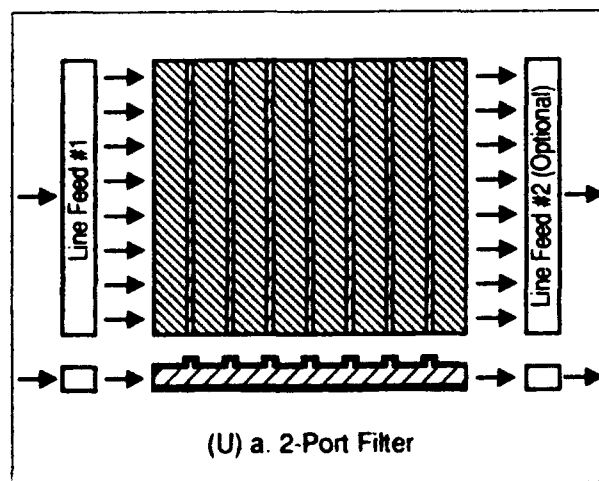
(U) Figure 34. CTS Filters

coupling of higher order modes within the QCTS array structure can be assumed to be locally similar to that of the standard CTS array and hence the CTS array design equations can be applied locally across the transverse plane in QCTS applications.

5.16 RCS Characteristics

The absence of variation in the transverse plane for CTS arrays eliminates scattering contributions (Bragg lobes) which would otherwise be present in traditional two-dimensional arrays comprised of discrete radiating elements. In addition, the dielectric loading in the CTS array allows for tighter interelement spacing in the longitudinal plane and therefore provides a means for suppression or manipulation of Bragg lobes in this plane. The capability to intentionally squint the mainbeam in CTS array applications also affords it an additional design advantage in RCS performance.

5.17 Radial CTS Arrays

As shown in Figure 33, the CTS array can also be realized in radial form, in which case the continuous transverse stubs form continuous concentric rings. A single or a multimode point source replaces the traditional line source in such applications. Radial waveguide modes are used in a similar manner to plane waveguide modes to derive design equations for the radial CTS array.

Dual-polarization, dual-band, and dual-beam capabilities can be realized with the radial CTS array through appropriate selection of feeds, CTS element, and auxiliary element characteristics in a manner directly parallel to that for the planar CTS array. Similar performance, application, and producibility advantages apply. Both endfire and broadside mainbeam patterns can be realized with the radial CTS array.

5.18 Filters

As shown in Figure 34, nonradiating reactive CTS elements terminated in an open or short circuit can be arrayed to conveniently form filter structures. Such structures can function independently as filters or be combined with radiating elements to form an integrated filter/multiplexer/antenna structure. Conventional methods of filter analysis and synthesis may be employed with the CTS array filter without loss of generality.

The CTS array enjoys advantages over conventional filter realizations, particularly at millimeter-wave and quasi-optical frequencies where its diminished dissipative losses and reduced mechanical tolerance sensitivities allow for the efficient fabrication of high precision, high "Q" devices. Note that the

277

theoretical dissipative losses for the CTS array parallel plate transmission line structure are approximately one-half of those associated with a standard rectangular waveguide operating at the identical frequency and comprised of identical dielectric and conductive materials.

5.19 Couplers

As well as for filters, as shown in Figure 35, precision couplers may also be realized and integrated using the CTS array structure with individual CTS elements functioning as branch guide surrogates. Again, conventional methods of coupler analysis and synthesis can be used without loss of generality.

6.0 Fabrication Methods

Fabrication of the dielectrically loaded CTS element can be efficiently accomplished through machining or molding of the dielectric structure, followed by uniform conductive plating to form the parallel plate transmission line, and finally, in the case of antenna applications, machining or grinding of the stub terminus to expose the stub radiator.

Mature fabrication technologies such as extrusion, injection molding, and thermomolding are ideally suited to the fabrication of CTS arrays. In many cases the entire CTS array, including all feed details, can be formed in a single exterior molding operation.

A typical three step fabrication cycle includes structure formation by continuous extrusion or closed single step molding; uniform exterior metalization by plating, painting, lamination, or deposition; and planar grinding to expose input, output, and radiating surfaces. Due to the absence of interior details, the CTS array requires metalization on exterior surfaces only with no stringent requirement for metalization thickness, uniformity, or masking.

Figure 36 shows a typical continuous extrusion process whereby the stubs of the CTS array structure are formed, metalized, and trimmed in a continuous sequential operation. Such an operation results in long CTS array sheets which may subsequently be diced to form individual CTS array structures. Figure 37 depicts a similar discrete process by which individual CTS array structures are molded or formed, metalized, and trimmed in a sequence of discrete operations.

The relative insensitivity of the nonresonant CTS element to dimensional and material variations greatly enhances its producibility over competing resonant approaches. This, in conjunction with the relative simplicity of the design and fabrication of the CTS array, makes it an ideal candidate for low cost high production rate applications.   278

(U) Figure 35. CTS Couplers

36. Extrusion Fabrication Example
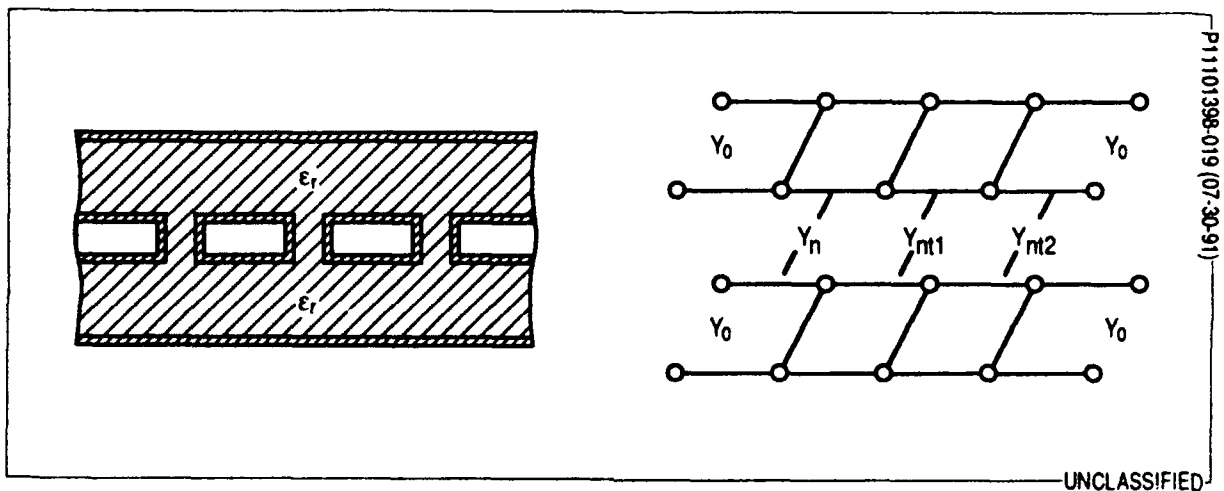
37. Pressing Fabrication Example
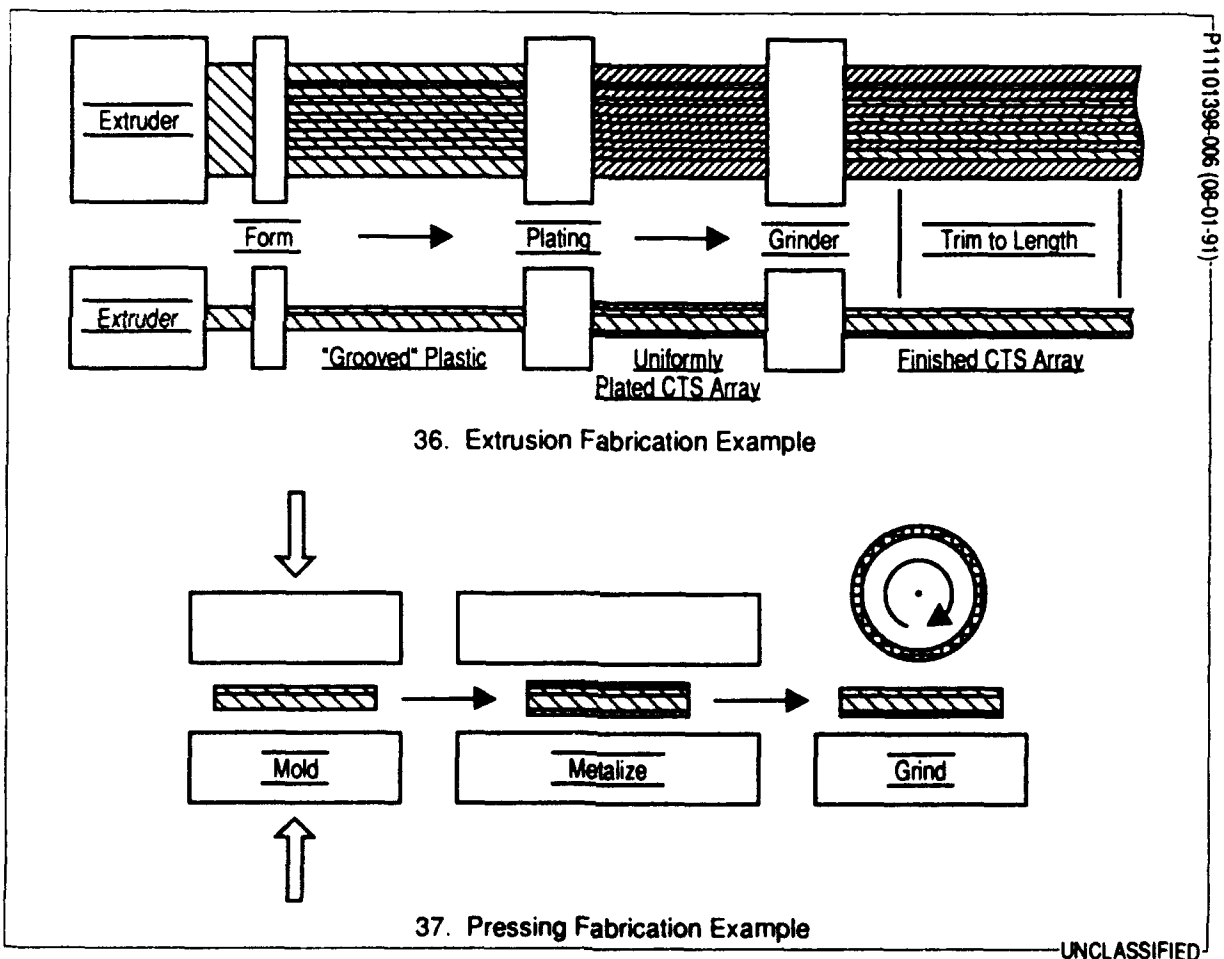
(U) Figure 36-37. CTS Fabrication Options

279

7.0 Specific Application Examples

As an initial effort, a small CTS antenna array was fabricated to demonstrate the CTS element and array concepts for antenna applications. Coarse approximations for coupling and radiating characteristics were used in lieu of precise analytical models and empirical design data. This test piece was thus a feasibility demonstration and not an optimized design.

A 6.0 by 10.5-inch CTS antenna array was fabricated from rexolite (e_r=2.35, ltan=0.0003). This array was comprised of 20 CTS radiator elements and designed for operation in the 12.5 to 18 GHz frequency band. A moderate amplitude excitation taper was imposed in the longitudinal plane through appropriate variation of CTS stub widths having constant individual heights. Interelement spacing was 0.500 inch and parallel plate spacing was 0.150 inch. A silver based paint provided a uniform conductive coating over all exposed areas of the CTS array. Input and stub radiator surfaces were exposed after plating using a mild abrasive.

An H-plane sectoral horn, 0.15 by 6 inches, was designed and fabricated as a simple low cost Ku-band line source, providing a cosinusoidal amplitude and a 90 degree peak-to-peak parabolic phase distribution at the input of the CTS array. A quarter-wave transformer was built into the CTS array to match the interface between it and the sectoral horn line source.

E-plane antenna patterns were measured for the CTS antenna array over the frequency band of 13 to 17.5 GHz, exhibiting a well-formed mainbeam with <-13.5 dB sidelobe level over the entire frequency range. Cross polarization levels were measured and found to be better than -50 dB. H-plane antenna patterns exhibited characteristics identical to that of the sectoral horn itself, consistent with the separable nature of the aperture distribution used for this configuration. Figure 38 shows a measured E-plane pattern for this CTS array measured at 17.5 GHz.

A second design, fabrication, and test of a planar CTS array was performed at 60 GHz. A 6 by 6 inch aperture was fabricated from rexolite, copper-sputtered, and measured. A folded half-pillbox antenna was used as a line source. Figure 39 shows the completed array. Figure 40 shows the measured E-plane pattern for the array, demonstrating a 1.75 degrees beamwidth. An aperture efficiency of 71 percent was measured, compared with approximately 10 percent for printed antennas of similar size and gain.

280
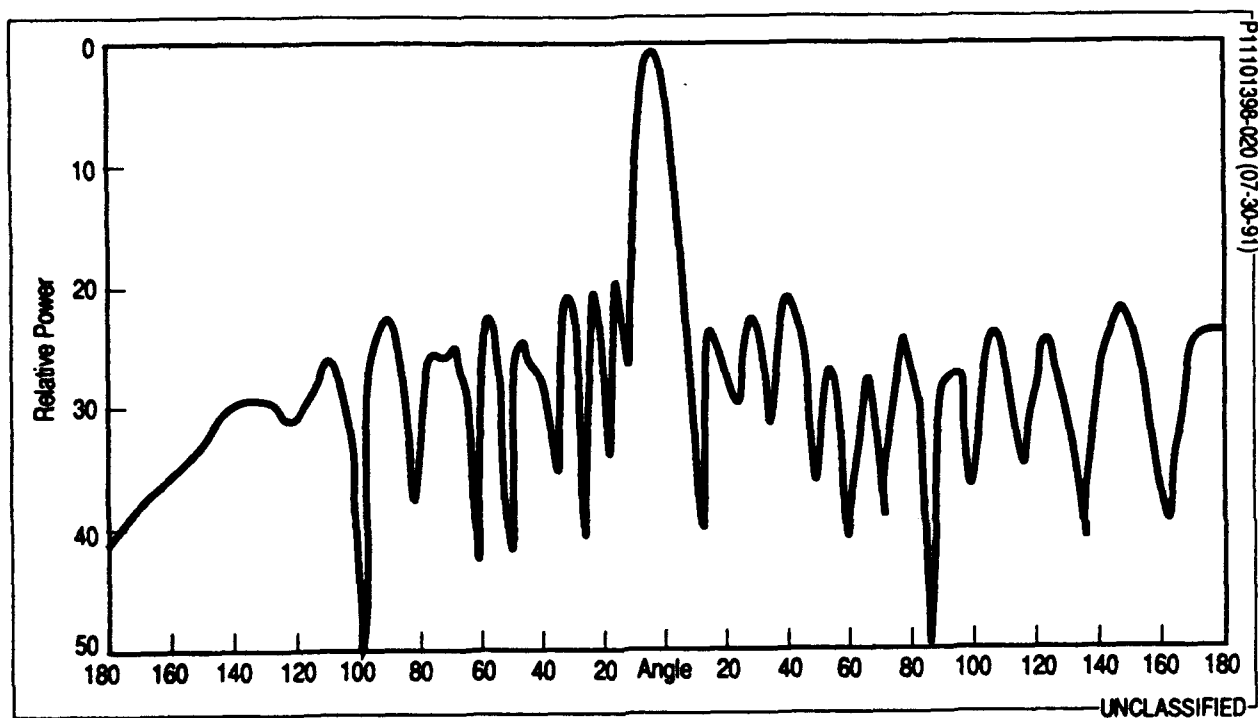
Figure 38. Measured Performance of Breadboard CTS Array at 17.5 GHz
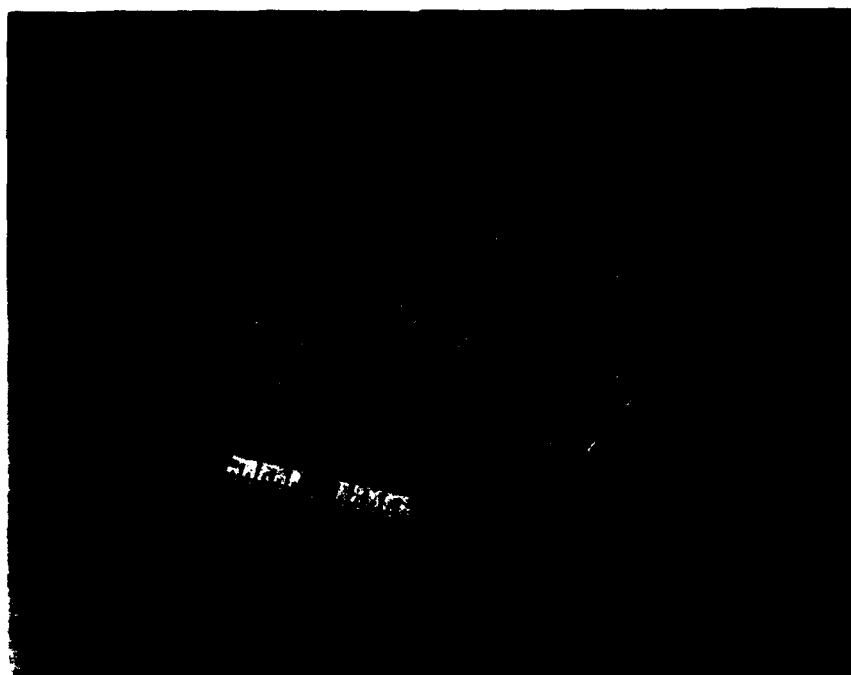
(U) Figure 39. Array Used in Second Test Series

281

Relative Power

BW₋₃ = 1.75°

180 160 140 120 100 80 60 40 20 Angle 20 40 60 80 100 120 140 160 180
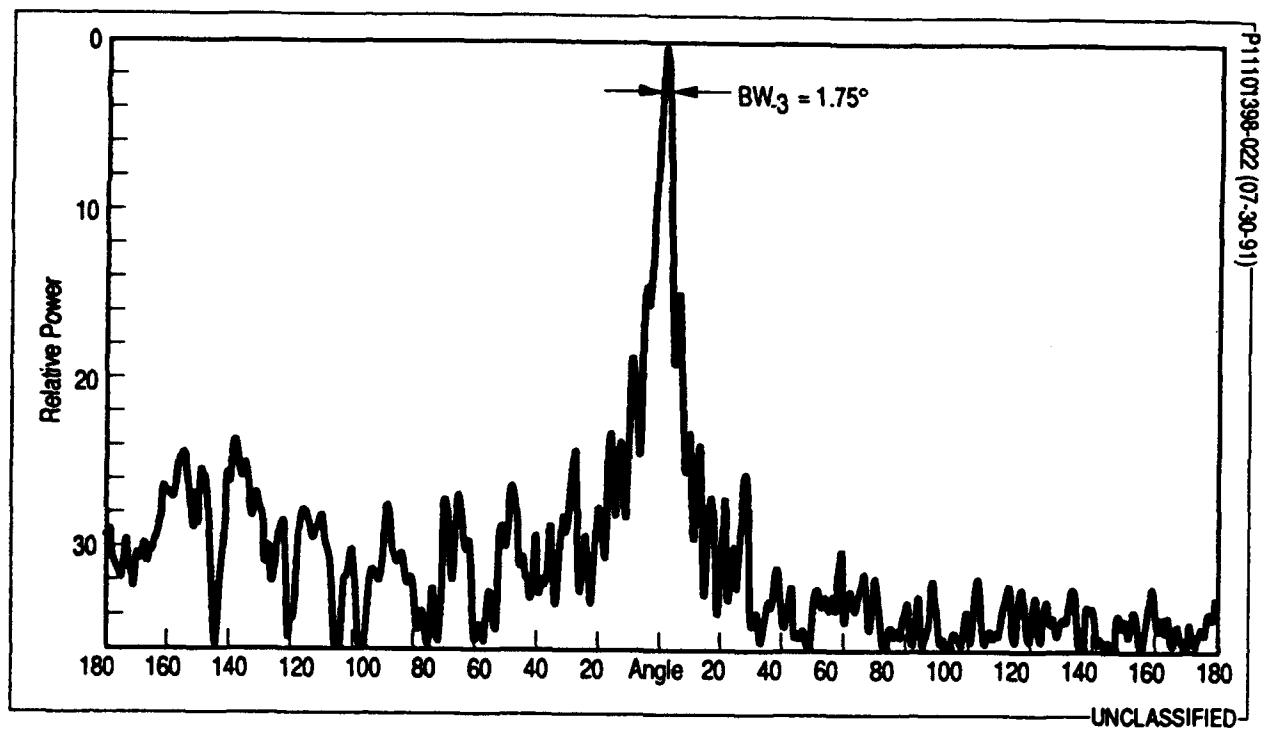
(U) Figure 40. Measured Performance of Millimeter-Wave CTS Array at 60 GHz
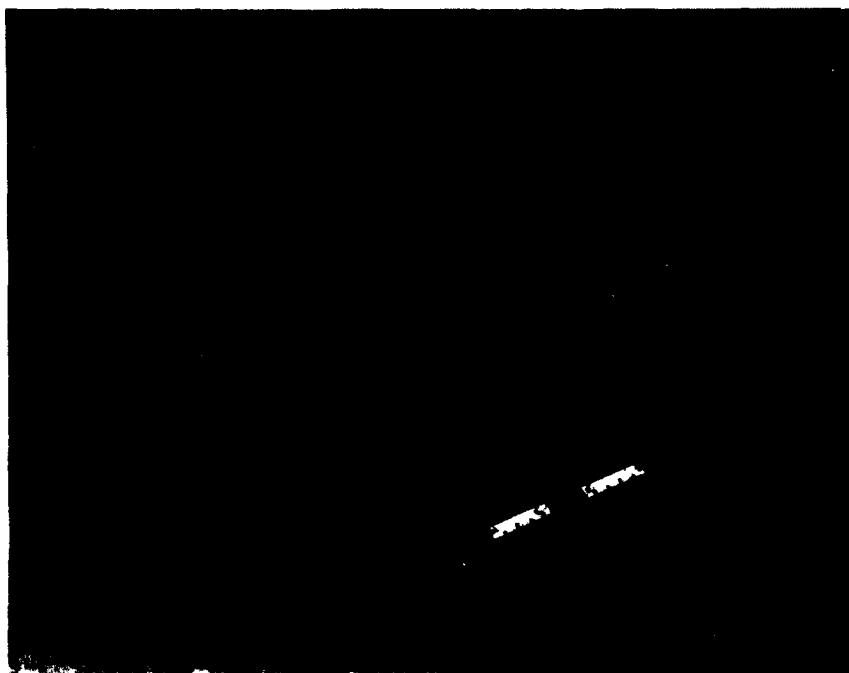
Figure 41. Dual-Polarization CTS Array (Ku-Band)

8.0 Continuing and Future Development

Current ongoing developments of the CTS antenna array include fixed and one-dimensional scanning applications at 12, 33-50, 35, and 94 GHz. These applications include both single and dual polarization realizations for the military, automotive, commerical avionics, and consumer marketplaces. As an example, Figure 41 depicts a prototype dual-polarization Ku-band CTS array currently under development as a low-cost planar antenna for the Direct Broadcast Satellite (DBS) consumer market. Applications of dual-band, two-dimensional scanning, and conformal capabilities have been formally proposed.

Analytical developments underway include improved equivalent circuit, mode-matching and finite-element models in order to more rigorously account for mutual-coupling, fringing, and dissipative loss effects. Analysis of inhomogeneous, time-varying, and anisotropic dielectric materials and CTS geometries have been proposed.

A CENTER-FED PLANAR ANTENNA

USING A SURFACE/LEAKY WAVE

by: S. Carrillo and J. Ladds

GTE

SECURE COMMUNICATIONS SYSTEMS DIVISION
GTE GOVERNMENT SYSTEMS CORPORATION
NEEDHAM HEIGHTS, MASSACHUSETTS 02194

A CENTER-FED PLANAR ANTENNA

USING A SURFACE/LEAKY WAVE

By: S. Carrillo and J. Ladds

SECURE COMMUNICATIONS SYSTEMS DIVISION

GTE GOVERNMENT SYSTEMS CORPORATION

NEEDHAM HEIGHTS, MASSACHUSETTS 02194

ABSTRACT

A new type of leaky-wave planar antenna for millimeter-wave applications is described. This low cost antenna is an alternative to microstrip arrays for which the transmission line losses seriously limit gain.

The circularly polarized antenna uses a surface wave to feed perturbations over a planar dielectric aperture and thus, is not subject to transmission line losses. Also, conventional leaky-wave antennas are side or end fed, which inherently leads to beam scanning as the frequency is varied. This is due to an asymmetrical phase distribution and is undesirable for communication antennas. By center-feeding, the phase is symmetrical and the aperture radiates a broadside beam, the direction of which is independent of frequency.

A description of the antenna is presented and the principles of operation discussed. The various design parameters, such as perturbation size and dielectric thickness, are examined. Finally, the measured performance of the prototype antenna is presented and discussed.

INTRODUCTION

In applications requiring low cost planar millimeter-wave antennas, the principal choices are microstrip and surface wave antennas. Microstrip arrays suffer from increasing losses as frequency is increased in the millimeter range. Loss in microstrip consists of the loss in the dielectric and the resistive losses in the ground plane and the feed line on the dielectric surface. Because the current is concentrated in this line, this gives the largest part of the loss. One author[1] has pointed out that these losses in microstrip place a limit on the maximum achievable gain of microstrip-fed array antennas.

For a surface wave supported by a layer of dielectric over a conducting ground plane, there are just 2 loss elements - the loss in the dielectric and the loss in the ground plane, both of which can be kept low. A surface wave antenna should therefore achieve a higher gain.

We define a surface wave as a wave which propagates across a surface without loss by radiation. If periodic disturbances are distributed across the surface, radiation is

obtained and we now have a leaky wave. It is this combination of surface wave and leaky wave that we utilize to construct a planar antenna.

There have been many recent developments in dielectric leaky wave antennas. In most cases, the surface wave structure employed is a long dielectric slab waveguide with either corrugations[2] or thin metallic strips[3] providing radiation. These antennas are end-fed, usually via rectangular waveguide.

To achieve a two dimensional aperture, several such slab antennas may be placed side-by-side[4] and a feed waveguide couples, via slots, to the slabs. Radiating elements consisting of metallic slots are spaced one guide wavelength apart across the slab. As a consequence of this spacing and the spacing of the feed slots, all the radiating elements are in phase and the resultant beam is broadside to the array. This will only be true for only one frequency, however, and as frequency is changed, the beam will scan in both planes as the phase relationship changes between radiating elements. This is an inherent characteristic of such leaky wave antennas. For many applications, this is a useful feature, but for a communications antenna, it is desirable to have a beam that is fixed in direction as the frequency changes.

To solve the frequency scanning problem, a circularly polarized center-fed leaky wave antenna was designed and developed, and is described below. This antenna is fabricated using standard photolighographic processes and printed circuit board ma rials leading to a very low cost design.

3

ANTENNA DESCRIPTION

The antenna is illustrated in Figure 1. It is constructed from a copper clad dielectric adhered to an aluminum back plate. The antenna is fed via circular waveguide through a hole in the back plate. A spiral was etched from the copp r-clad material to provide the required leakage.

In operation, a waveguide adapter converts the TE_{10} mode in rectangular waveguide to the TM_{01} mode in circular waveguide. The TM_{01} mode propagates to the dielectric, where it is converted to the TM_0 surface wave mode. The top cap helps to efficiently launch the surface wave.

The TM_0 mode is the logical mode to use since it has no cut-off frequency, regardless of the thickness of the dielectric layer. But the thickness may be chosen so that the next higher order mode, the TE_1 mode, cannot propagate. Hence, with proper choice of thickness, higher-order mode problems may be completely avoided.

We now consider how to radiate the TM_0 mode. As its designation implies, the magnetic field is entirely transverse to the direction of propagation and is parallel to the metal base plate. The electric field is orthogonal to the magnetic field, but has a longitudinal as well as a transverse component. Figure 2 shows the configuration of the electric field (solid lines) outside the dielectric where both components of the

field fall off exponentially with distance from the surface. Radiation can be produced by placing flat metallic elements on the dielectric surface.

The TM_0 mode has a component of electric field at the surface of the dielectric in the direction of propagation. A metallic patch or strip will be polarized by the field and radiate. The radiating strip is a spiral with a radius that increases by one surface wavelength for every 360 degrees of rotation.

The spiral is shown in Figure 3. The following discussion explains how circular polarization is achieved.

Any two diametrically opposite points, equidistant from center, are 180° out of phase. This is due to the nature of the TM_{01} waveguide mode used to feed the TM_0 mode. Hence, if we used concentric copper rings instead of a spiral, a null would be produced on boresight. But, as explained previously, the spiral radius can be made to increase one surface wavelength per rotation, that is, one half wavelength per half turn. Thus, the radiated field at A and B is in phase.

Similarly, the spiral radius increases by a quarter wavelength per quarter turn. Therefore, the field produced by C and D in the figure is 90° out of phase with that produced by A and B. The result is a circularly polarized beam.

Furthermore, by feeding the antenna in its center, frequency scanning is eliminated. The phase relationship described above is true only for the design frequency for

5

which the strip-to-strip spacing is one surface wavelength. As the frequency is varied, a phase error occurs. This is a symmetrical phase error, however, and hence, does not cause a beam displacement, as opposed to end-fed or side-fed antennas.

DESIGN CONSIDERATIONS

To determine the proper spiral, the surface wavelength λ_{sw}, for the TM_0 mode is determined. For a dielectric slab antenna, of infinite width, λ_{sw} is given by:

$$\lambda_{sw} = 2 \pi / (\varepsilon \ k_o^2 - k_d^2)^{1/2} \tag{1}$$

where ε is the dielectric constant, k_o is the free-space propagation constant and k_d is the cutoff wavenumber in the dielectric. For the TM modes, kd may be determined by:

$$\varepsilon \ ht = (kdt) \ tan \ (kdt) \tag{2}$$

and

$$(kdt)^2 + (ht)^2 = (\varepsilon - 1) (k_o t)^2 \tag{3}$$

where jh is the cutoff wavenumber in the air region and t is the thickness of the dielectric layer. Equations (2) and (3) cannot be solved explicitly, but may be solved with a zero-finding algorithm, or, graphically[5], as in Figure 4 where the two equations are plotted by computer for varying t. For a given t, the points of

intersection between the two curves determine the value of k_d, which is then substituted into (1).

The graphical solution also determines what higher order modes, if any, may be propagated. As Figure 4 illustrates, the $t = 0.05''$ curve does not intersect the TE_1 ht curve (obtained by replacing the tan function in (2) with |cot|) and, hence, the TE_1 mode cannot propagate. The $t = 0.06''$ and $0.07''$ curves do intersect the TE_1 curve, and therefore, these thicknesses support this mode for the given frequency and dielectric constant.

Another parameter to consider is the spiral line width W. Trinh, et. al.[6], derived an empirical formula for the line width of the n th strip.

$$W_n/\lambda sw = 0.15 + 0.015 (n - 1) \qquad n \leq 18$$

$$(4)$$

$$W_n/\lambda sw = 0.4 \qquad n > 18$$

where Wn is the width on the nth strip.

Equation (4) puts W in the range 0.15 λsw to 0.4 λsw. Using this as a guide, a constant line width of .25 λsw was chosen for the first prototype and the results are discussed in the next section.

RESULTS

Two 10 inch antennas were built and tested at 47 GHz. The thickness of the
dielectric chosen was partly dictated by available circuit board materials. A Teflon-
glass fiber material of .060 inches backed by 1/4 inch aluminum plate was obtained.
The dielectric constant of this material is 2.17. (The plot of Figure 4 shows that
this material will support the TE_1 mode.)

The first prototype antenna had a measured gain of 30.5 dBi, compared to a 42 dBi
maximum possible gain. An aperture probe revealed that the antenna was radiating
only over the central 6 inches, a result of too large a line thickness. Reducing the
width by 1/2 in the second prototype resulted in a 5.2 dB increase in gain. Further
improvements in gain are expected with line width optimization.

A 0.8 dB on-axis axial ratio was measured, indicating that proper line spacing was
achieved. The E and H plane patterns are shown in Figure 5. Although the H
plane pattern is fairly symmetrical, the E plane pattern exhibits pattern distortion
near the peak of the beam. This indicates a strong interaction between the launcher
cap and the radiating spiral, which occurs in the E plane. Another possibility is that
the TE_1 mode is somehow contributing to this distortion. Further prototypes are
planned to investigate the cause of this.

ACKNOWLEDGEMENT

REFERENCES

1. J. R. Forrest, "Assessing Antennas for Small SATCOM Terminals," Microwave Systems News, October, 1981, pp. 77 - 101.

2. F. Schwering and S. T. Peng, "Design of Periodically Corrugated Dielectric Antennas for Millimeter-Wave Applications", Antenna Applications Symposium, Rome Air Development Center and Department of Electrical Engineering - University of Illinois, Urbana, IL, 1982. RADC-TR-82-339, ADA129356

3. F. Schwering and A. A. Oliner, "Millimeter-Wave Antennas", Chapter 17 in Antenna Handbook, Y. T. Lo and S. W. Lee (Editors), Van Nostrand, New York, 1988.

4. K. Solbach, "Hybrid Design proves Effective for Flat Millimeter-Wave Antennas", Microwave Systems News, June, 1985, pp. 123 - 138.

5. R. E. Collin, (1960). "Field Theory of Guided Waves", McGraw-Hill, New York, pp. 470 - 477.

6. T. N. Trinh, R. Mittra and R. J. Paleta, Jr., "Horn Image Guide Leaky-Wave Antenna", IEEE-MTT Conference Proceedings, 1981, pp. 20 - 22.

Aluminum Base Plate

Circular Waveguide
TM or Stotch

1 1/2 "

12"
Diameter

1/2"

(b) Side View

Etched Copper Spiral

Top Cap
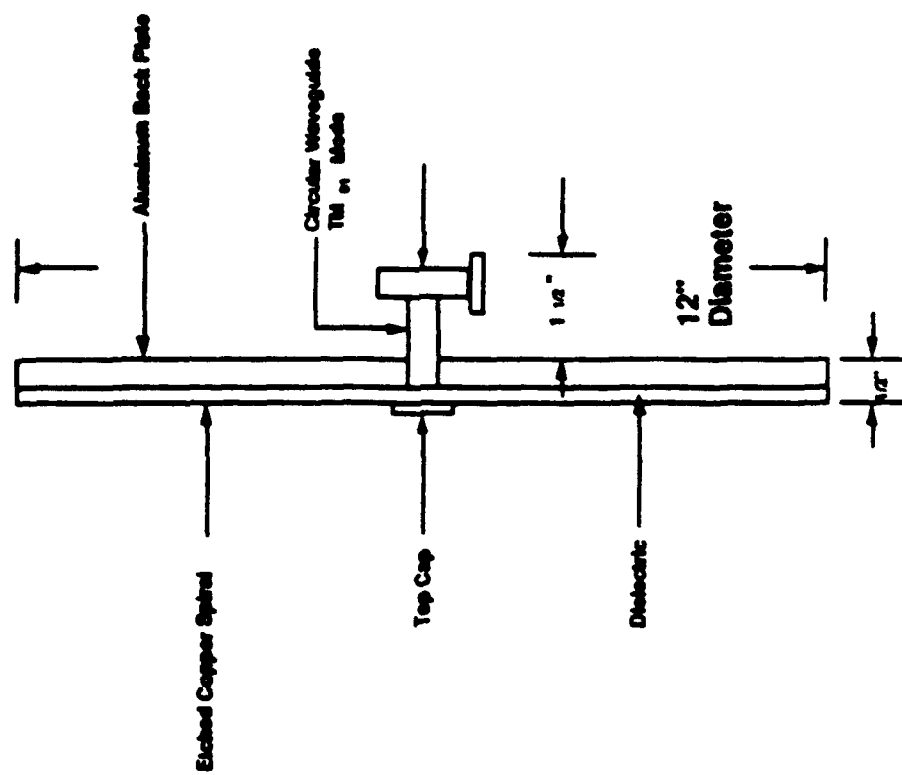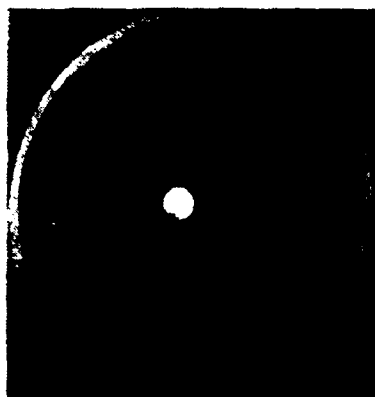
Dielectric

(a) Front View

FIGURE 1

LEAKY WAVE ANTENNA

Dielectric Layer Over Conducting Ground Plane

(a)

TM₀ Mode Field Pattern (E-Field Lines Solid)
(Z is direction of propagation)

(b)
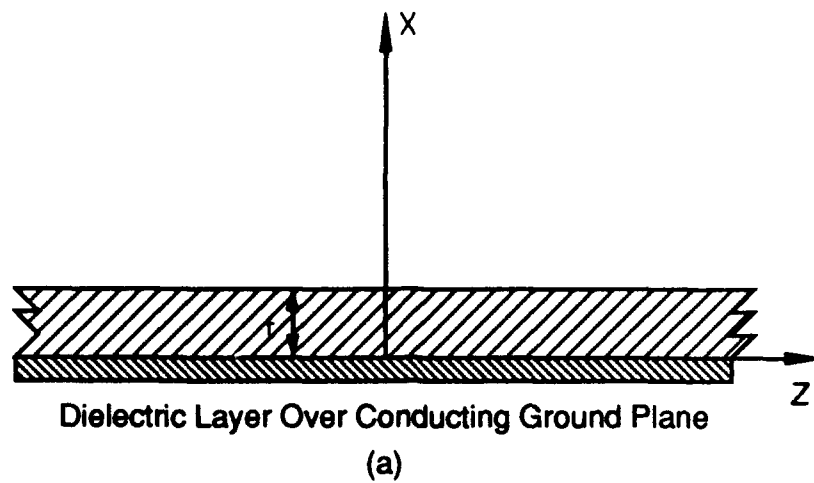
Figure 2

12
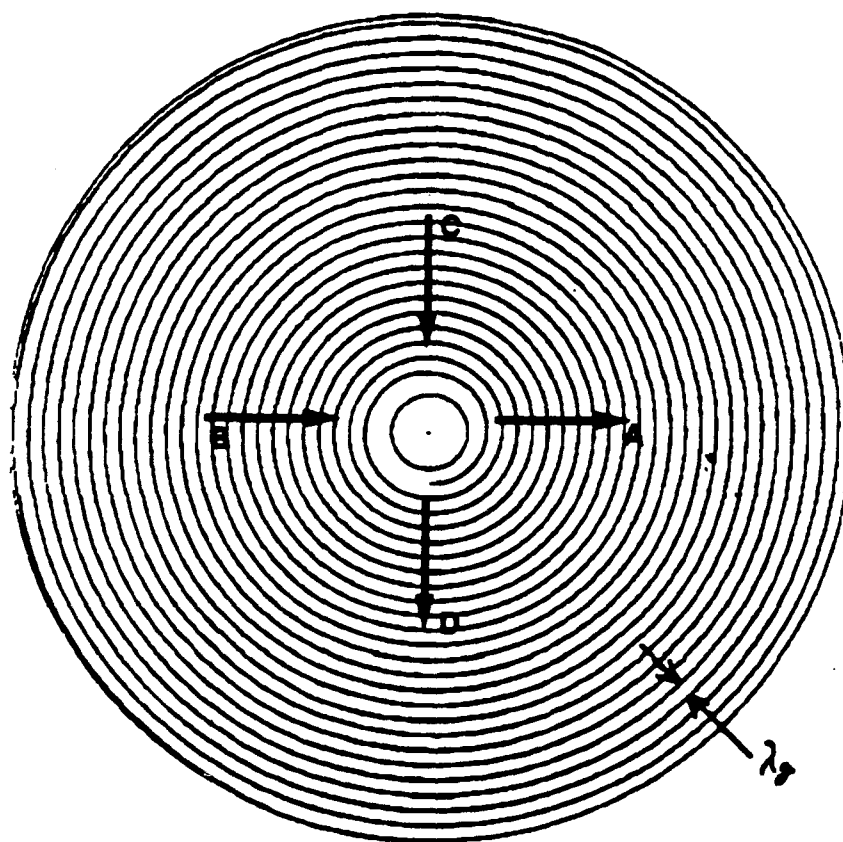
Figure 3   Etched Spiral Geometry

13
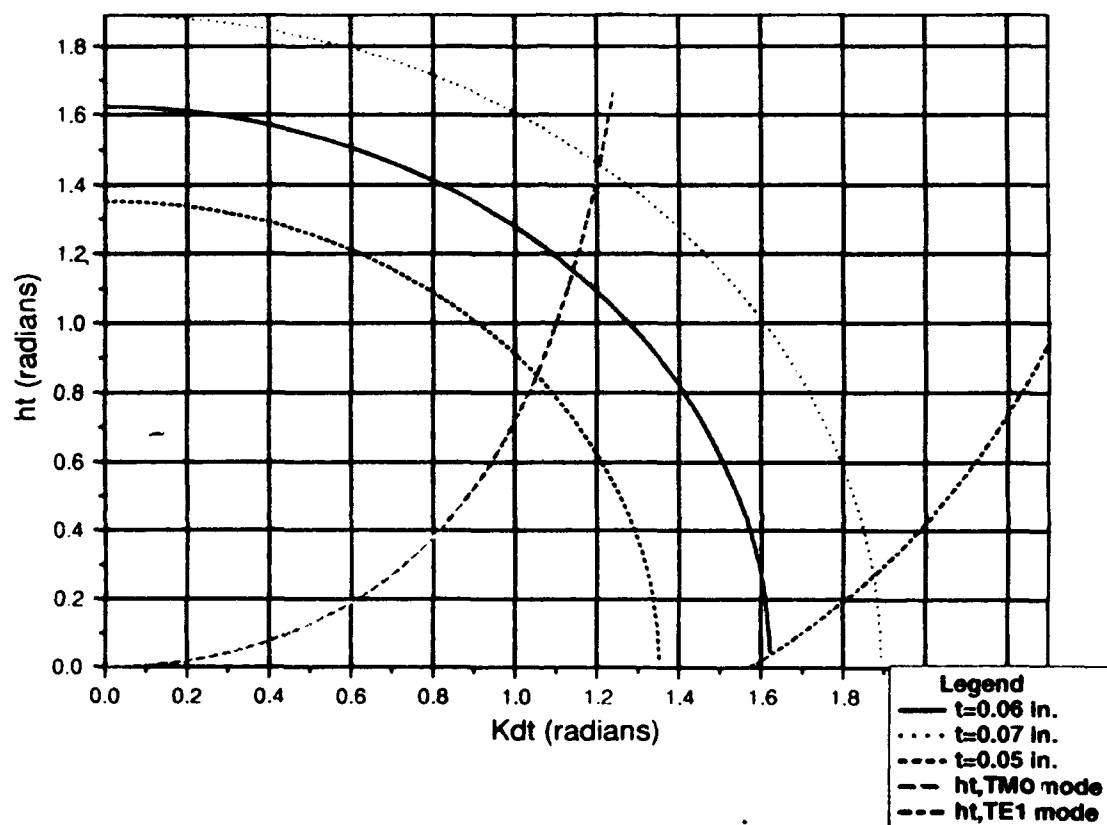
Figure 4 TM$_0$ and TE$_1$ Modes For Varying Dielectric Thickness, t
(f= 47.0 GHz, Rel. Permittivity=2.17)

14
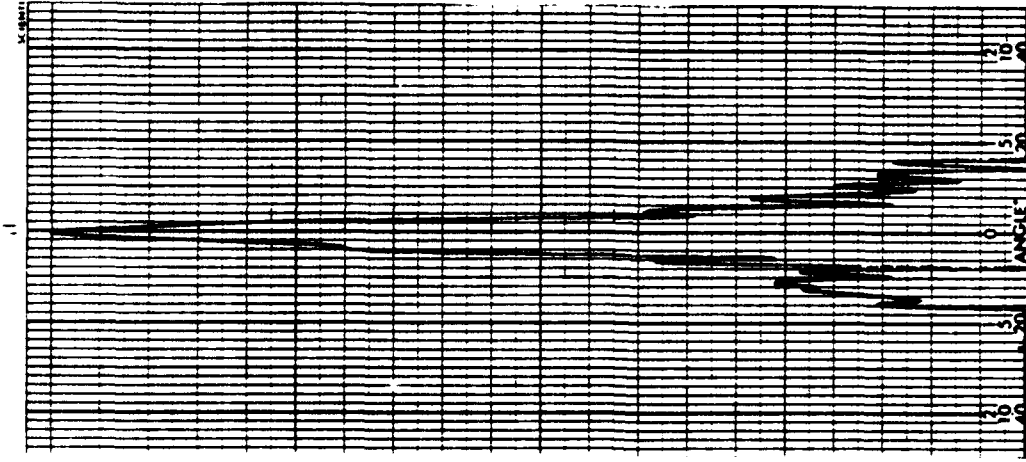
(b) H-Plane

(a) E-Plane

Scale: 2 dB per major division
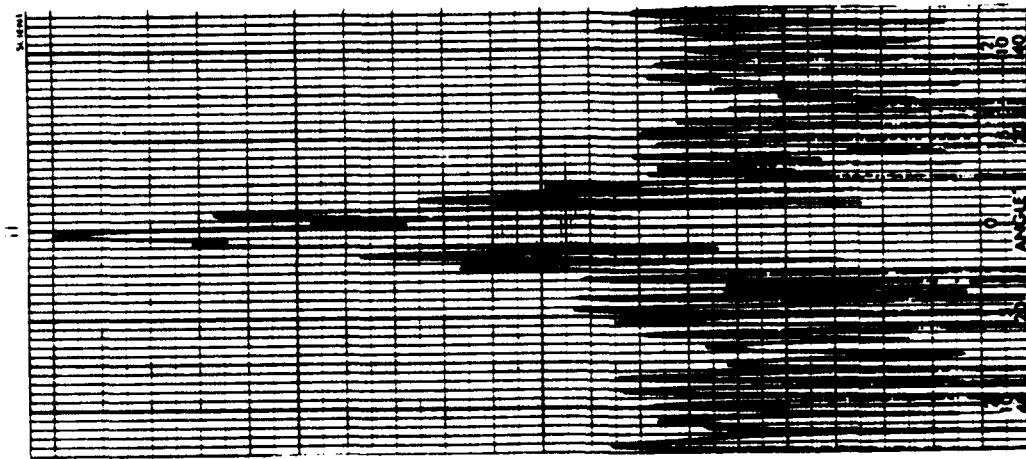
Figure 5   Radiation Patterns

15

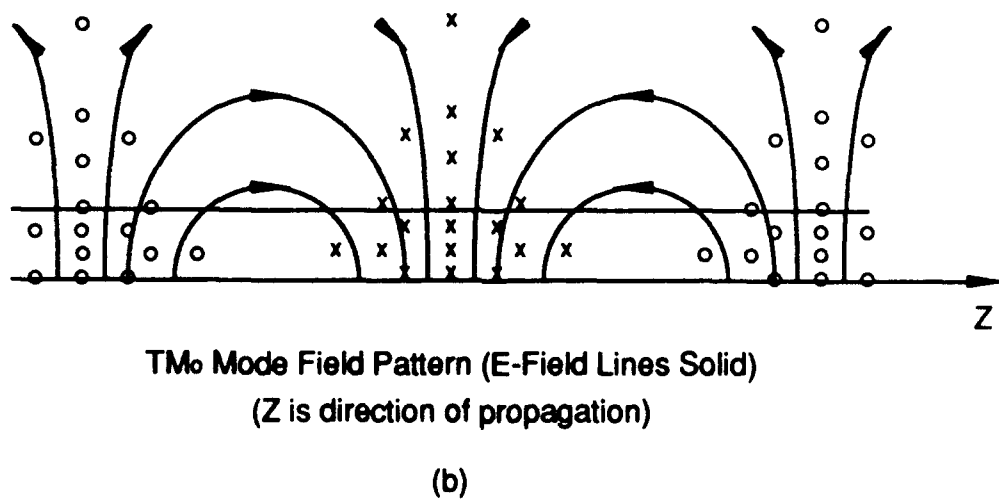# OFFSET CASSEGRAIN WITH TRIPLE POLARIZATION GAUSSIAN OPTICS LENS ANTENNA FEED SYSTEM FOR HIGH POWER Ka-BAND WEATHER RADAR

E. L. Moore
Millitech Corporation
South Deerfield, MA 01373

ABSTRACT

The design and test results of a 122 cm diameter offset Cassegrain antenna with a Gaussian optics lens antenna feed assembly are presented. A blend of geometrical optics and Gaussian optics is used in the design and analysis of this antenna.

1. INTRODUCTION

To satisfy the many requirements of the weather radar research program for which this subsystem was developed, a compact medium gain lens antenna was designed to illuminate an offset Cassegrain. This antenna operates at 34.5 ± 0.5 GHz in 3 polarizations: RHCP, LHCP, and LHP. Quasioptical polarization components are used in the Gaussian optics lens antenna (GOLA), which is sealed and pressurized to 3 atmospheres to accommodate a peak pulse of 150 kW with a 0.0005 duty cycle. The antenna was designed to maintain a pointing accuracy of $0.1°$ in windspeeds up to 80 mph over a temperature range of $-30°$ to $110°F$.

Most of the design is based on Gaussian optics principles, in which a beam originates from a source of finite radius and has a Gaussian radial field distribution. The behavior of Gaussian beams is well known and use of this theory simplifies the analysis of beam waveguide systems. Scalar feed horns launch a beam which is approximately Gaussian and are usually the type of horn chosen in these systems. After a beam is launched its radius grows as it propagates away from the source and it must be periodically refocused. This beam growth in free space makes the technique ideal for high power applications. As the beam grows in diameter, the power density incident on components is reduced and the problems of heating and arcing can be eliminated. For this reason, the components in the feed system are all quasioptical. The growth of a Gaussian beam is given by

$$w(z) = w_0 \left[1 + \left(\frac{\lambda z}{\pi w_0^2} \right)^2 \right]^{1/2} , \qquad (1)$$

where w_0 is the beam waist radius, z is the longitudinal distance from w_0, and w is the beam radius at z. Both w_0 and w are the radii at which the electric field is e^{-1} of the peak value.

The GOLA is composed of two orthogonally polarized scalar feeds separated by a wire grid polarizer, a motorized quarterwave plate, a biconvex lens, and a quartz window, all in 1 cylindrical container 30 cm

from the secondary focus. The Cassegrain antenna consists of 4 modular pieces, each painted white for thermal stability. The waveplate switches between RHCP and LHCP at a 0.3 second rate during precipitation studies, or it can be used to transmit/receive LHP during observations of chaff. Other requirements were a 0.5° half power beamwidth, -25 dB sidelobes, a 1.2:1 VSWR, and most importantly, polarization isolation of at least 30 dB.

Measurements were made on Millitech's large compact range having a 6' diameter x 6' long quiet zone. Final test results show a HPBW of 0.5°, a linear cross polarization maximum of -34 dB below the copolar peak, an axial ratio of 0.45 to 1.25 dB, and a return loss from -16.7 to -26 dB at center frequency. The antenna is shown in Figure 1.

2.   OFFSET CASSEGRAIN ANTENNA DESIGN

The offset Cassegrain antenna has the following design parameters, which were chosen to satisfy the cross polarization requirement.

Main reflector diameter	122 cm
Primary focal length	170 cm
Secondary focal length	124.4 cm
Subreflector diameter	21.076 cm
Magnification	3.33
Edge illumination	-14 dB

Our design program uses geometrical optics to define the reflectors and to calculate the cross polarization at one point - the tip of the main reflector on the symmetrical axis. The program predicted a cross polarization level of -33 dB for this design, within 1 dB of the measured value of -34 dB.

The antenna is illuminated by a 3.0 cm Gaussian beam waist at the secondary focus, 97 cm from the subreflector. The beam radius w(z) required to give an edge taper TE at the subreflector radius a is shown by Goldsmith[1] to be

$$w(z) = \frac{a}{0.339\sqrt{TE}} \quad . \tag{2}$$

Near field effects from the proximity of the 15.24 cm diameter GOLA to the subreflector include defocusing and cross polarization. Focusing problems can be predicted and corrected by techniques described by McEwan and Goldsmith[2]. A Gaussian beam has a phase front with a radius of curvature R given by

$$R(z) = z \left[1 + (\frac{\pi w_0^2}{\lambda z})^2 \right] \tag{3}$$

At the beam waist, $z=0$ and $R = \infty$. In the near field of a feed or beamwaist, defocusing can occur because of a phase mismatch between the beam and the subreflector, which in many cases can be improved by repositioning the feed. However, when the relationship between the subreflector diameter D,

4

the separation f, and λ, given by $D^2/f\lambda$, drops below a threshold value, the problem is uncorrectable.

The depolarization stems from the fact that the E and H fields in the near field of a beam waist or feed are not purely transverse. McEwan[3] uses Gaussian optics aperture field functions to calculate the far field cross polarization. The copolar, bilobe cross polar, and quadrupole cross polar functions are given by e^{-r^2/w^2}, $\left(\dfrac{x}{x_o}\right) e^{-r^2/w^2}$, and $\left(\dfrac{xy}{x_o y_o}\right) e^{-r^2/w^2}$, respectively. The maximum theoretical cross polarization stems from the bilobe term, at -44 dB, well below the level generated by the Cassegrain geometry.

3. GAUSSIAN OPTICS LENS ANTENNA

The GOLA is shown in Figure 2. It has three requirements, which are: (1) illuminate, in focus, the subreflector with a -14 dB edge taper (2) transmit/receive LH and RHC/LHC polarization, and switch between LHC and RHC, and (3) withstand a pulse peak of 150 kW.

The orthogonally polarized scalar feeds have a beam waist of 1.0 cm which is transformed by the biconvex lens to a 3.0 cm waist about 30 cm beyond the quartz window. Input and output waist radii w_{o1} and w_{o2} are related by the focal length f, and the distance d_1, from w_{o1} to the lens by

5

$$\left(\frac{w_{02}}{w_{01}}\right)^2 = \frac{1}{\left[\left(\frac{d_1}{f}\right) - 1\right]^2 + \left[\frac{\pi w_{01}^2}{\lambda f}\right]^2} \quad . \tag{4}$$

shown in Goldsmith[1]. For this lens d_1 is about 15 cm and f is 12.95 cm. The lens geometry is hyperbolic, the material is Rexolite™, and there are quarter wavelength deep antireflection grooves parallel to the linear polarization. The wire grid transmits electric field perpendicular to the wires and reflects the parallel field component. The wires are 0.001" diameter gold plated tungsten, 320 wires/inch. The rear feed transmits LH polarization.

A slotted Rexolite™ quarterwave plate (QWP) was installed between the lens and the GOLA aperture to provide both circular and linear polarization. The design is based on theory by Kirschbaum and Chen[4], who report that slots in dielectric material produce a sample with two different indices of refraction n, depending on whether the electric field is parallel or perpendicular to the slots. When the electric field is oriented 45° to the slots, the field component parallel to the higher dielectric constant is delayed with respect to the perpendicular electric field component. The total amount of relative delay ϕ is determined by the slot thickness and should be 90° for a QWP. The dielectric constants ε_x and ε_y are given by

$$\varepsilon_x = \frac{2\varepsilon_d}{\varepsilon_d + 1} \quad \text{and} \quad \varepsilon_y = \frac{\varepsilon_d + 1}{2} \quad , \tag{5}$$

where $\varepsilon_d = 2.56$ (for Rexolite™) and the slots are air. The total slot thickness d is determined by the phase shift ϕ, where $\phi = 2\pi\lambda^{-1}d |n_x - n_y|$.

4. LOSS AND FIELD STRENGTH IN THE DIELECTRICS AND GRID

A comparison between the electric field strength inside the dielectric materials and the dielectric strength of the materials in the GOLA predicts no arcing problems. The dielectric strength must always be greater than the electric field which is

$$S = \left[\frac{150 \text{ kW}}{\text{area}} \times \frac{377\Omega}{\sqrt{\varepsilon}} \right]^{1/2} \frac{V}{m} . \qquad (6)$$

At the GOLA aperture the area is assumed to be defined by the -1 dB contour of the beam at a distance of 15.24 cm from the input waist. The radius r of the beam at any power level can be calculated by the expression

$$\frac{P(r)}{P_{max}} = \exp\left[-2 \left[\frac{r}{w(z)} \right]^2 \right] . \qquad (7)$$

The area used for all the dielectrics is 10^{-3} m^2. At the output beam waist the -1 dB contour has an area of 5.10^{-4} m^2 at a distance ~30 cm from the GOLA aperture. The field strength calculation at the output beam waist does not include real operating conditions such as rain, snow, and dust. The ohmic loss is calculated by $P(z) = P_0e^{-az}$, where $a = 2\pi\lambda^{-1} \sqrt{\varepsilon}$ tanδ and z = material

thickness. Values of dielectric strength, ε, z, and tanδ for each component are given by Schwartz and Goodman[5], Goldsmith[1], and Reference Data for Radio Engineers[6]. The thickness is always assumed to be the maximum value, such as the center of the lens, so it is a conservative estimate. The maximum ohmic and mismatch losses are predicted to be about 0.7 dB or 13 W, and the dielectric strength of the rexolite and quartz components is greater than the electric field strength by about a factor of 100.

5. MEASUREMENT TECHNIQUES AND DATA

For all measurements the GOLA feeds were used to transmit and the compact range scalar feed was used to detect. The compact range feed was oriented to detect LV or LH polarization, and it has a maximum cross polarization level of about -36 dB. E and H plane patterns were measured in $\pm$ 0.075° increments over a $\pm$ 3° scan. To measure linear cross polarization we measured the copolar and cross polar response in 2-D contour maps and compared peak copolar to peak cross polar power. Axial ratio was measured on boresight by slowly rotating the compact range feed through 360°. For the gain measurement, the transmitter was at the compact range. Gain was measured by comparing the output power of the Cassegrain in linear polarization to that of a WR-28 standard gain horn. Test results are summarized in Table 1.

TABLE 1

<u>Data Summary</u>

FREQ., GHz	PLANE	PORT	POL.	FWHM, DEGREE	GAIN, dBi	SIDELOBE, dB	RETURN LOSS, dB	CROSS POLAR., dB	AXIAL RATIO, dB
34.5	E	Rear	LH	0.5	50 ± 0.5	-23	-26	-34.2	--
	H	Rear	LV	0.5	--	-23	--	--	--
34.5	E	Side	LV	0.5	50 ± 0.5	-22	-13	-37.5	--
	H	Side	LV	0.5	--	-26	--	--	--
34.5	--	Rear	RHC	--	--	--	-19	--	0.7
	--	Rear	LHC	--	--	--	-19	--	0.45
34.5	--	Side	RHC	--	--	--	-16.7	--	--
	--		LHC	--	--	--	-16.7	--	--
34.6	--	Rear	RHC	--	--	--	-18	--	0.75
	--		LHC	--	--	--	-18	--	0.45
34.7	--	Rear	RHC	--	--	--	-17	--	0.8
	--		LHC	--	--	--	-17	--	0.65

9

NOTE:
ALL DIMENSIONS ARE IN INCHES

BEAM AXIS

SUBREFLECTOR

83.9 REF

49.7 DIA REF

1.1 REF

GOLA

ELEVATION AXIS

45.4 REF

3" DIA ACCESS HOLE
FOR CABLES OR WAVEGUIDE
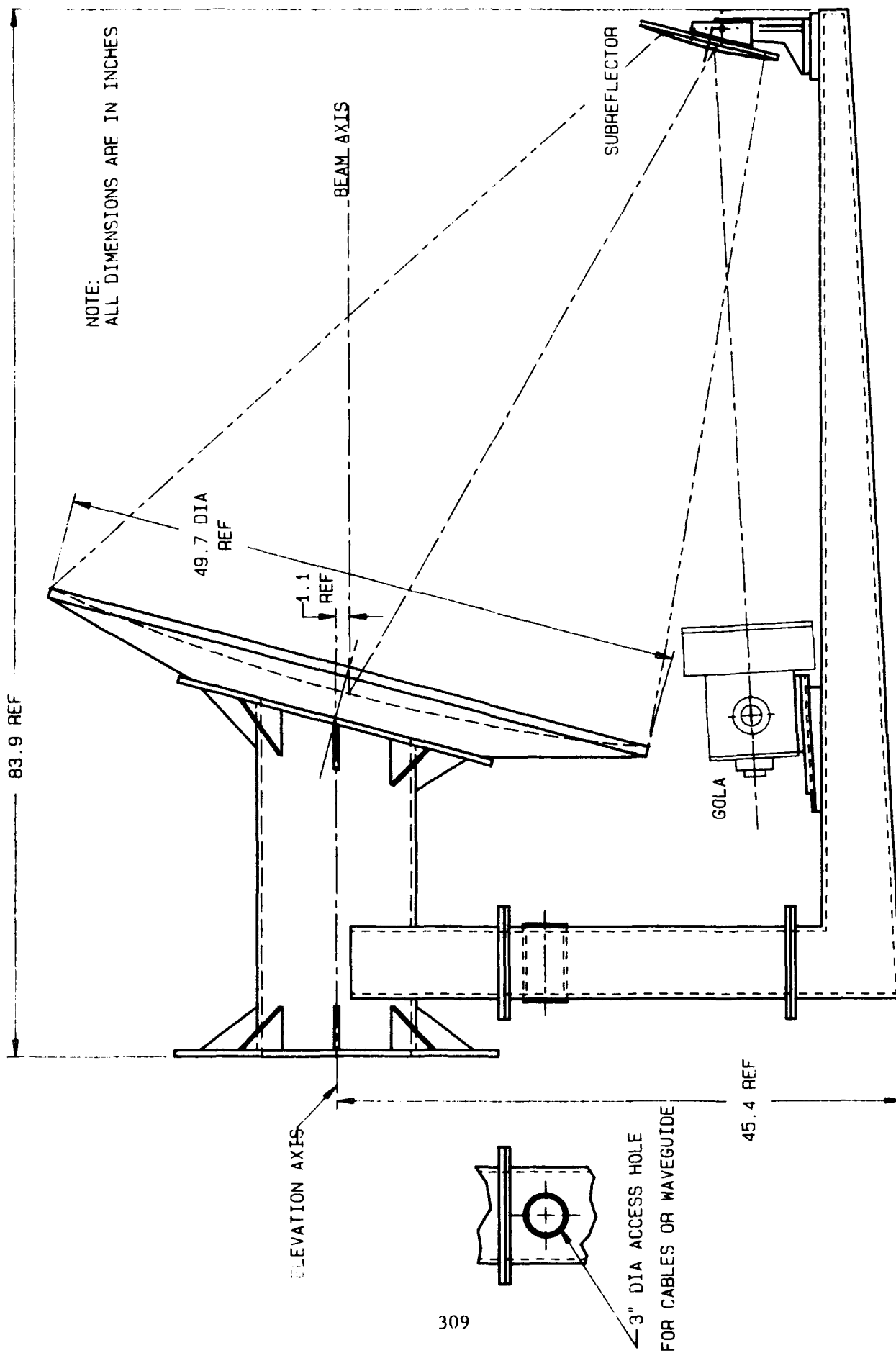
FIGURE 1
OUTLINE OF OFFSET CASSEGRAIN ANTENNA
WITH GAUSSIAN LENS ANTENNA FEED SYSTEM.

309

MOTOR

CONNECTOR

REAR FEEDHORN

SIDE FEEDHORN

WIRE GRID

QUARTZ WINDOW

WAVE PLATE
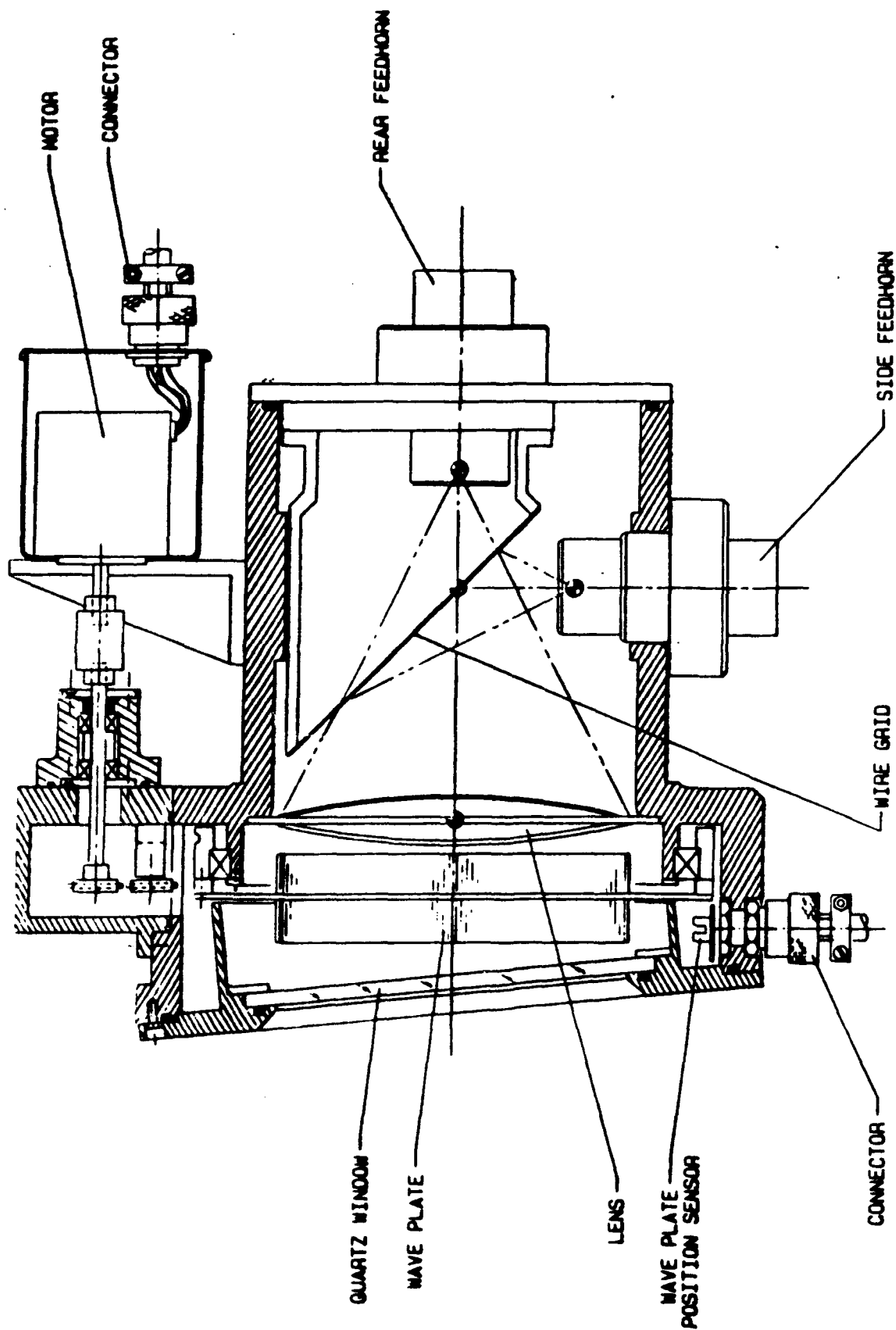
LENS

WAVE PLATE
POSITION SENSOR

CONNECTOR

FIGURE 2
GAUSSIAN OPTICS LENS ANTENNA FEED SYSTEM

CONCLUSIONS

A medium gain antenna which performs many different functions can be used to illuminate an offset Cassegrain antenna. Gaussian optics techniques are used to optimize the focusing and edge illumination, and for the component design.

ACKNOWLEDGMENTS

REFERENCES

1. Goldsmith, P. F., "Quasioptical Techniques at Millimeter and Submillimeter Wavelengths", in Infrared and Millimeter Waves, vol. 6, K. J. Button, ed., Academic Press, NY, pp. 272-343, 1982.

2. McEwan, N. J., Goldsmith, P. F., "Gaussian Beam Techniques for Illuminating Reflector Antennas", IEEE Trans. Antennas Propagat., vol. AP-37, pp. 297-304, 1989.

3. McEwan, N. J., "Theoretical Cross Polarization Estimate for Offset Cassegrain Antenna", in Appendix C of Final Report for Department of Commerce Contract No. 50-DKNA-8-00167, 1991.

4. Kirschbaum, M. S., Chen, S., "A Method of Producing Broad Band Circular Polarization Employing an Anisotropic Dielectric", IRE Trans. MTT, pp. 199-203, July 1957.

5. Schwartz, S. S., Goodman, S. H., Plastics, Materials, and Processes, Van Nostrand Reinhold Co., Inc., NY, 1982.

6. Westman, H. P., ed., Reference Data for Radio Engineers, Fourth Ed., American Book - Stratford Press Inc., NY, pp. 64-65, 1956.

PERFORMANCE OF THE TDRSS SPACE DEPLOYABLE ANTENNA

MICHAEL J. LYNCH

HARRIS CORPORATION
GOVERNMENT AEROSPACE SYSTEMS DIVISION
P.O. BOX 94000
MELBOURNE, FLORIDA

ABSTRACT

Satellite communication applications are continuously searching for ways to either reduce earth terminal antenna size or increase the data rate of the communication link. The Tracking and Data Relay Satellite System (TDRSS) space deployable mesh antennas provide an alternative for increased satellite antenna gain. The TDRSS space-to-space link uses a 4.8 meter diameter deployable mesh antenna. Harris Corporation delivered two deployable antennas for each of the six TDRSS satellites built during the 1980's. As of July 1991 six of these antennas are on orbit. Harris Corporation has nearly completed two more antennas for the seventh TDRSS satellite, designated F7. F7 provides an opportunity for the presentation of current measured data for a deployable mesh antenna. This paper presents the technical performance of this multifrequency (S-band and Ku-band) tracking antenna. Measured data from the F7 units are presented, including S-band and Ku-band secondary antenna patterns, and

mesh reflection data. An antenna pattern measured for one of the previous units while on orbit is also included with theoretical analysis. Additional development testing is ongoing at Harris, including Passive Intermodulation (PIM) testing on the Harris mesh to predict the system PIM performance for multiple carrier communication applications. Results of this, and related developments are included.

1.0 INTRODUCTION

The success of the deployable mesh antennas on the TRW built Tracking and Data Relay Satellite System (TDRSS) satellites has demonstrated their feasibility for spaceborne communication antennas. The unique capability to provide high gain, small launch volume, and low mass make deployable mesh antennas particularly attractive to the communication system designer. Harris delivered the first of the TDRSS 4.8 meter diameter Single Access (SA) antennas in 1980. The first TDRSS satellite was launched in April 1983. Antennas were delivered for the first six TDRSS satellites during the 1980's. These antennas continue to provide on-orbit service with no sign of performance degradation. In August of 1991 the fifth TDRSS satellite is scheduled for launch on the shuttle Atlantis, and the two antennas for the seventh TDRSS satellite (F7) are currently nearing completion at Harris. Each TDRSS satellite utilizes two identical SA antennas, shown deployed in Figure 1. The SA antennas provide space-to-space communications between the geostationary orbit TDRSS satellite and low earth orbit user satellites. The antennas have dual polarization transmit and receive capability in both S-band and Ku-band and tracking is provided in Ku-band. A shaped cassegrain geometry employing thermally stable components and a unique

multifrequency feed were required to meet the antenna requirements. This paper describes some of the background that went into the TDRSS deployable antenna development and presents results of some recent RF tests performed on the F7 SA antennas. Results of additional testing performed by Harris, not associated with the TDRSS program, to fully characterize the deployable mesh antennas for commercial communication applications are also included.

2.0 DEPLOYABLE ANTENNA DESIGN

The TDRSS SA antenna conserves satellite mass by operating a single reflector antenna in multiple frequency bands. One dualband SA antenna weighs 53 pounds. The shaped cassegrain reflector system consists of a deployable mesh main reflector with a diameter of 188.8 inches, a focal length of 56 inches, and a 21.8 inch diameter subreflector The TDRSS spaceborne feed, shown in Figure 2, is a du   quency cassegrain feed operating in both S-band and Ku-band. The TDRSS SA antenna was designed for 2.025 GHz to 2.3 GHz S-band operation and 11.7 GHz to 15.121 GHz Ku-band operation with tracking at both 14.4 GHz and 15.121 GHz.

The TDRSS SA antenna design maximizes gain in both frequency bands while providing tracking capabilities at Ku-band. The configuration is based on a five horn Ku-band feed surrounded by an array of S-band cavity backed crossed dipoles. The diameter of the multifrequency feed is minimized to limit blockage and therefore improve sidelobe performance. The subreflector is supported by a low loss quartz epoxy radome attached to the top of the feed tower. The wide frequency-spacing between operational bands, 7.5:1 ratio, creates a particularly difficult challenge for a shaped antenna system. The subreflector is 3.7

wavelengths in diameter at the lowest operating frequency. The shaping function is a compromise to improve gain in both sum channels, with the benefit in S-band being limited by the electrically small subreflector at S-band.

The TDRSS 30 percent bandwidth corrugated feedhorn is designed for Ku-band communication channel operation with high primary pattern gain. The sum channel feedhorn aperture diameter forces the four tracking horns to a relatively wide spacing with the difference crossover on the first sidelobe. Four rectangular waveguides, with the narrow dimension in the tracking plane, are used for the error horns. This design takes advantage of the broader illumination in this plane to generate high sidelobes in the difference pattern.[1] The S-band primary pattern gain is produced by using an array of four elements for the feed. Each element is a cavity backed dipole with two element directors used on each dipole to further increase feed gain.

The gain budget for the TDRSS SA antenna, Table 1, combines analyzed and measured contributors to arrive at the predicted gain for the system. Defocus, surface roughness and pointing contributions result from worst case on-orbit analysis. Measured data is analyzed to determine mesh reflectivity and illumination efficiencies. Radome losses include measured ambient performance and analysis to account for the on-orbit contributions. Blockage accounts for the central feed, tower, and subreflector assembly. Feed losses account for all components behind the radiating aperture, and are referenced to the antenna interface at the base of the feed tower. Aperture efficiency, which includes spillover, taper, phase and cross-polarization losses, is calculated by integrating the appropriate measured primary and scatter patterns.

Table 1. *TDRSS Efficiency (Gain) Budget*

Frequency GHz	0.0	2.3	13.7	15.1
Defocus dB	0.01	0.01	0.09	0.10
Surface dB	0.01	0.01	0.31	0.38
Mesh Reflection dB	0.03	0.03	0.50	0.75
Scallop dB	0.15	0.15	0.10	0.10
Radome dB	0.03	0.03	0.43	0.50
Blockage dB	0.30	0.30	0.30	0.30
Feed Loss dB	1.08	1.08	0.43	0.41
Aperture Efficiency dB	2.25	2.05	1.20	1.40
Total Loss dB	3.86	3.66	3.36	3.94
Efficiency	0.411	0.430	0.461	0.404
Gain, 100% dBi	40.1	41.3	56.8	57.6
Net Gain dBi	36.3	37.6	53.4	53.7

The main reflector is a mesh surface with 10 openings per inch tricot knit pattern made of 0.001 inch (1 mil) diameter gold plated molybdenum monofilament wire. The choice of knit pattern is a trade between RF performance, reflectivity, system mass, and stiffness. Figure 3 is an enlarged view of the mesh. The support structure for the main reflector is 18 graphite epoxy ribs. Accurate surface control is maintained through the use of a secondary surface control technique. This technique allows the ribs to be designed to a constant radius of curvature rather than a parabolic shape and it also relaxes the dimensional tolerances on the graphite rib fabrication. The reflective mesh surface is attached to the ribs with a system of gore edge strips and adjustable standoffs.

Surface control is achieved with a network of parallel quartz front and back cords connected by adjustable ties, Figure 4.

The surface contour is measured in the face-up and the face-down configurations and averaged to remove gravity induced distortions. The antenna

ribs are counterbalanced to remove gravity effects during the setting operation. The procedure is performed with the four theodolite system shown in Figure 5. The measured zero-gravity surface contour is then compared to the undistorted shaped surface. Through the use of specialized interactive software, developed by Harris, the appropriate surface adjustments are determined. Adjustments are then made in the face-up position to achieve the required manufacturing surface tolerance consistent with the total, on-orbit surface tolerance budget. The surface setting is an iterative process where the number of iterations is driven by the surface accuracy required to meet the antenna gain budget.[2] The reflector distortion budget is shown in Table 2. The maximum on-orbit surface error for the TDRSS SA antenna is less than 0.023 inches RMS. This value is used to determine the loss due to surface roughness in the efficiency budget. The use of quartz surface control cords, graphite ribs, and low stiffness mesh ensures dimensional stability over the entire range of on-orbit thermal conditions.

The TDRSS SA antennas are deployed in a slow controlled manner to avoid the transfer of stored energy to the spacecraft, and unpredictable surface distortions. The mechanical deployment system (MDS), shown in Figure 6, employs a ball screw and a carrier with independent linkages to each rib pivot arm and an over-center type toggle action. Rotation of the ballscrew results in translation of the carrier which pushes the ribs to their deployed position. The over-center toggle ensures that once deployed the ribs maintain their deployed position with adequate preload. The MDS drive unit has two motors attached to a common shaft for redundancy and increased reliability.

Table 2. TDRSS On-Orbit Reflector Surface Distortions
(Source: CDR PKG PG 2-92)

Contributor	RMS (inches)
Subreflector	0.005
Pillow Effects	0.011
Surface Set	0.018
On-orbit Thermal	0.004
Total (RSS)	0.023

3.0 MEASURED PERFORMANCE

Reflection measurements have been made on the TDRSS SA antenna mesh. Average loss for TDRSS F7 mesh reflection tests was 0.6 dB. These measurements were performed at the highest TDRSS operating frequency, 15.121 GHz. These results are better than the worst case mesh reflection term, 0.75 dB, used in the efficiency budget.

Additional mesh tests have been performed on mesh samples which were exposed to a high temperature and humidity environment to simulate long term storage. Figure 7 is a plot of reflection loss, in dB, as a function of time exposed to the accelerated aging conditions. Three samples were exposed to 70 °C and 70 percent relative humidity to simulate long term storage at 25 °C and 60 percent relative humidity. Samples were tested for reflection performance prior to exposure and at regular intervals which corresponded to 2.5 years of storage. This data shows no reflection degradation after the equivalent of more than 12 years of storage.

Secondary antenna patterns are measured on the TDRSS program with the flight feed assembly, including subreflector and radome, in a solid reflector which is built to the same shaped contour as the TDRSS mesh reflectors. A three

meter diameter antenna, calibrated at the National Institute of Standards and Technology (NIST), is used as the gain standard for TDRSS acceptance testing. A 1.7 dBi range is available at Harris for these antenna tests. The antenna pattern range shown in Figure 8 is used to measure Ku-band antenna patterns. Figure 9 is a representative sum channel antenna pattern measured from one of the TDRSS F7 SA antennas. Measured Ku-band, 13.775 GHz, antenna gain is 54.2 dBi versus a specification of 52.2 dBi and a net gain of 53.4 dBi from the efficiency budget. Figure 10 is an overlay of a Ku-band sum and difference channel antenna pattern. The calculated modulation slope for the pattern is 1.0 volt/volt/degree, which exceeds the specification of 0.35 volts/volt/degree minimum.

S-band antenna patterns are measured using a different far field source tower. Because of the lower gain at S-band additional rejection is required to reduce multipath effects on the antenna measurements. A network analyzer is used to provide time domain gating to increase the signal-to-interference level attributable to multipath. The antenna pattern range shown in Figure 11 is used to measure S-band antenna patterns. Figure 12 is a measured S-band antenna pattern from one of the TDRSS F7 SA antennas. Measured S-band, 2.025 GHz, antenna gain is 37.1 dBi versus a specification of 35.9 dBi and a net gain of 36.3 dBi from the efficiency budget.

Within one year of launch, on-orbit Ku-band antenna patterns were measured for the SA antennas on the first TDRSS spacecraft. Figure 13 is an overlay of a measured on-orbit antenna pattern with the computed pattern for the predicted on-orbit reflector surface. The excellent agreement verifies the

on-orbit antenna performance predictions. During 1988, after five years on orbit, calibrations were performed on the first TDRSS satellite (F1). During these tests no degradation in performance was noted for the deployable mesh antennas.

4.0 RELATED WORK

Work is constantly underway at Harris to improve our products and processes. A few examples of this continuous improvement process for mesh deployable antennas are briefly described below.

Recently L-band PIM tests were performed at Spar Aerospace, (Montreal, Canada) in conjunction with David Florida Laboratories on samples of Harris mesh. Transmit power flux densities incident on the mesh were 52 mW/cm2. Seventh order intermodulation products were measured for the tests. The noise floor for the measurement system was -160 dBm when video bandwidth averaging was used on the spectrum analyzer. Figure 14 is a plot of measured PIM power level for a mesh sample. The measured PIM power level for Harris mesh was below the -160 dBm noise floor of the measurement system.

Another development is the direct measurement of mesh tension as a function of temperature. The procedure allows biaxial tension to be measured as the sample is thermally cycled from ambient temperature to more than 450 °F, Figure 15. Harris mesh exhibits linear highly repeatable tension performance over on-orbit temperature extremes.

Harris has also developed a nondeployable fixed-mesh antenna which applies the advantages of low weight and dimensional stability over large temperature variations, associated with deployable mesh antennas, to smaller

spaceborne antennas. Figure 16 is a graphical comparison of mass for conventional solid reflectors and fixed-mesh reflectors.

5.0 SUMMARY

Deployable mesh antennas have several benefits which could be employed for future commercial satellite communication networks. The TDRSS space-borne deployable mesh antennas described in this paper have been on orbit since 1983. As of July 1991 three TDRSS satellites with six SA antennas are operational. On-orbit measured performance has been measured and excellent agreement with predicted performance has been demonstrated.

REFERENCES

1. Bartlett, H.E., Space Deployable Antennas, IEEE Antennas and Propagation Society Newsletter, April 1980.

2. Tankersley, B.C. and Bartlett, H. E., Tracking and Data Relay Satellite Single Access Deployable Antenna, NTC Conference Record, 1977.
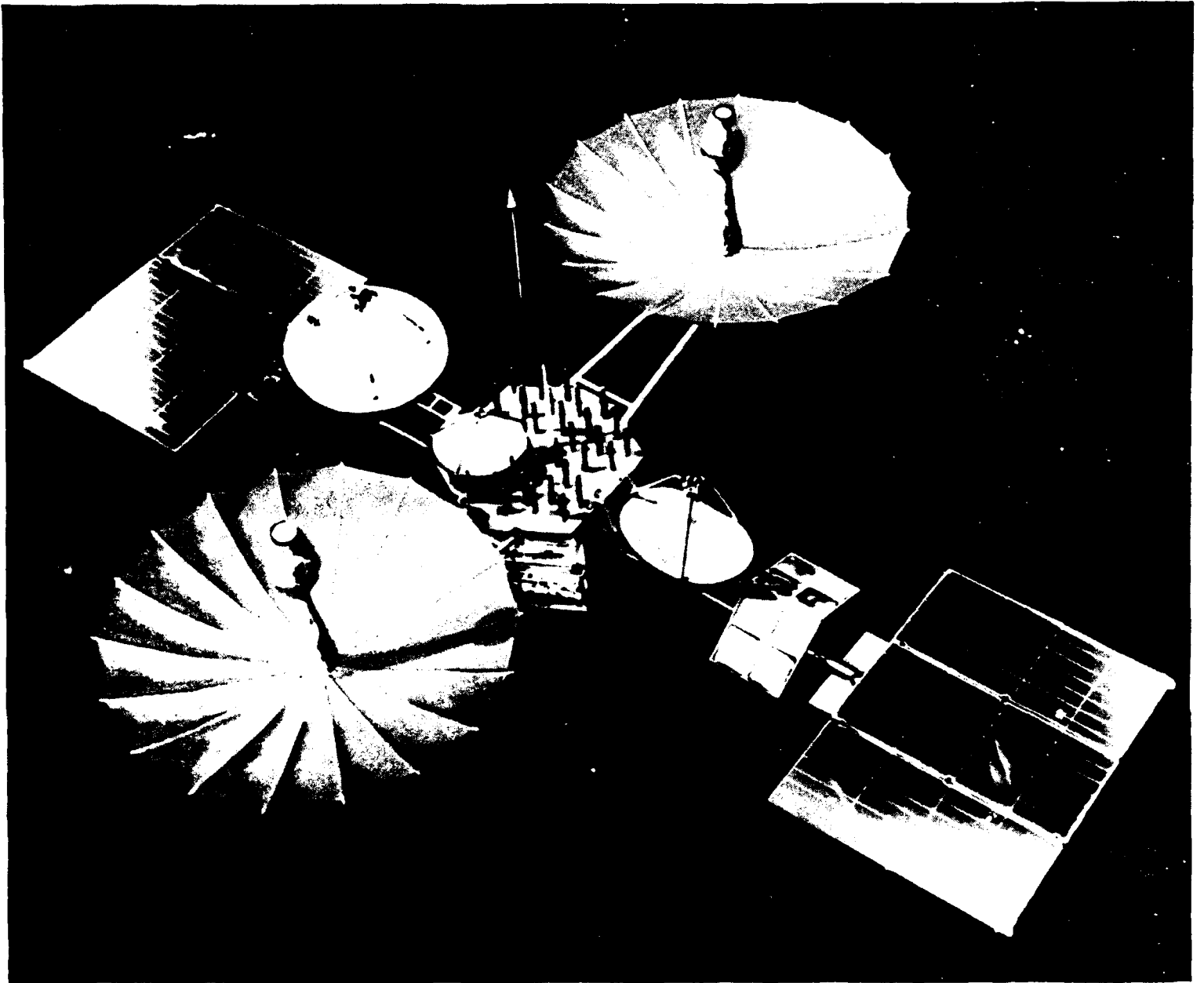
Figure 1. TDRSS Satellite
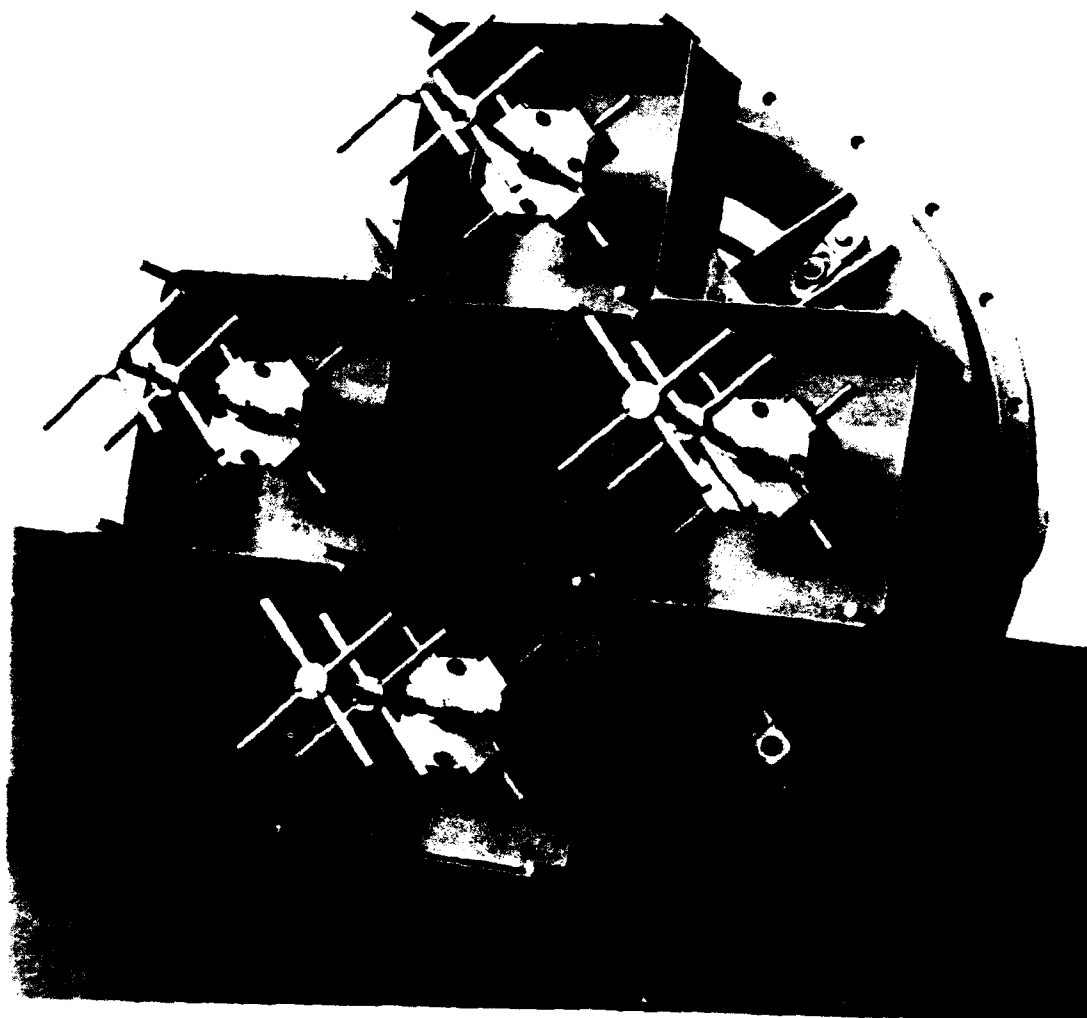
*Figure 2. Multifrequency, S-band and Ku-band, TDRSS Feed Provides Data
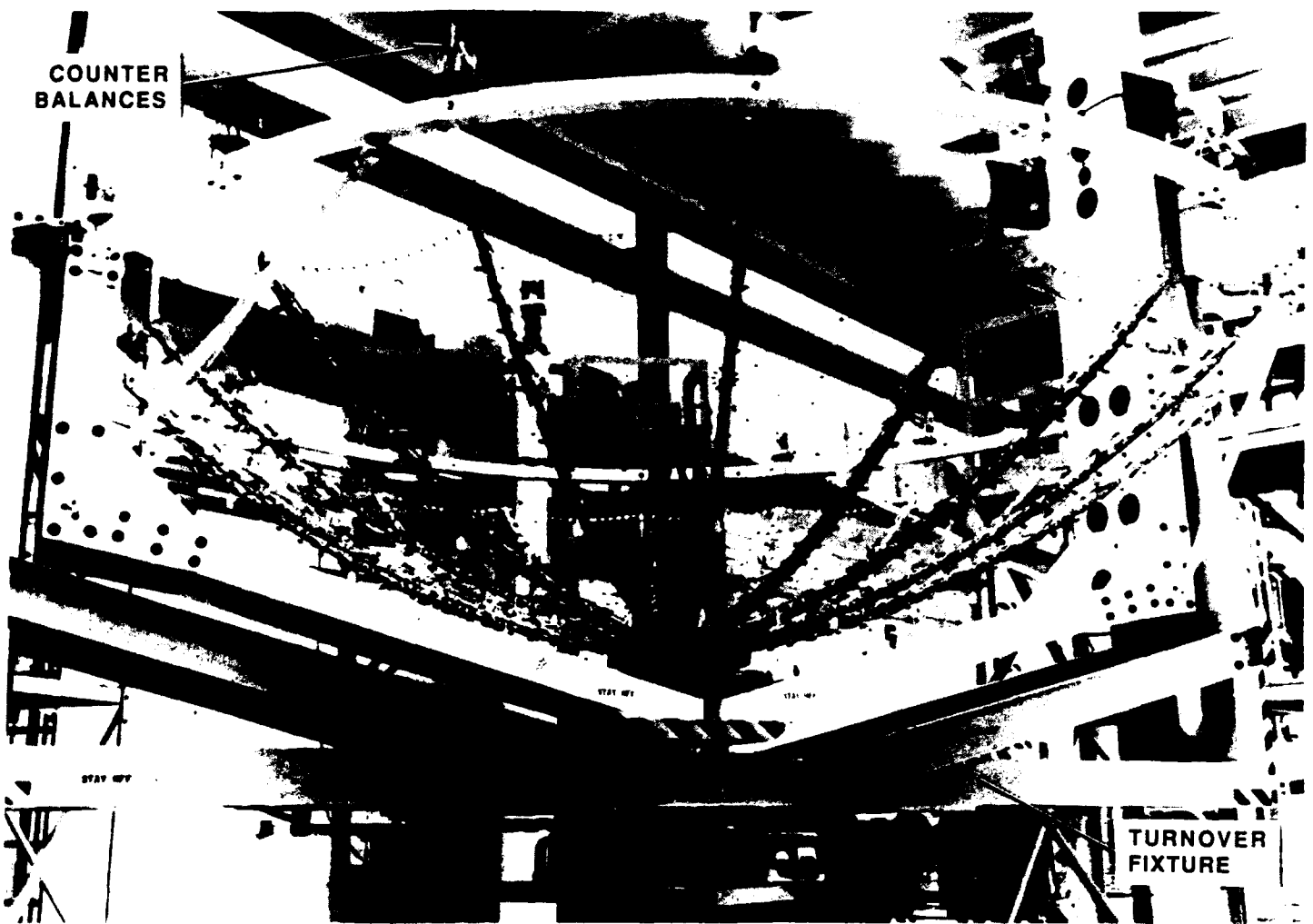Channels in Both Bands and Tracking Channel in Ku-band*
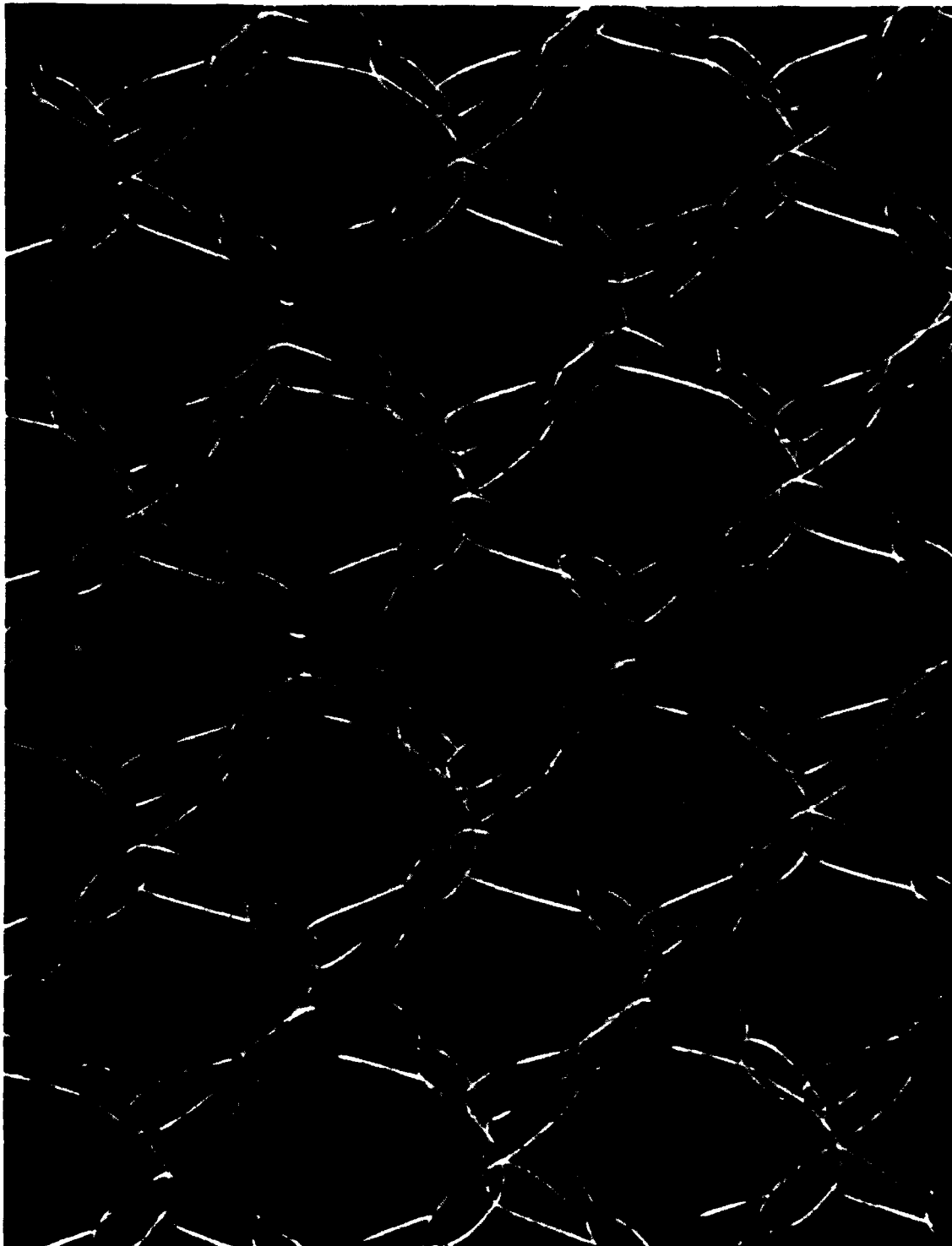
Figure 3.   Harris Molybdenum Wire Mesh
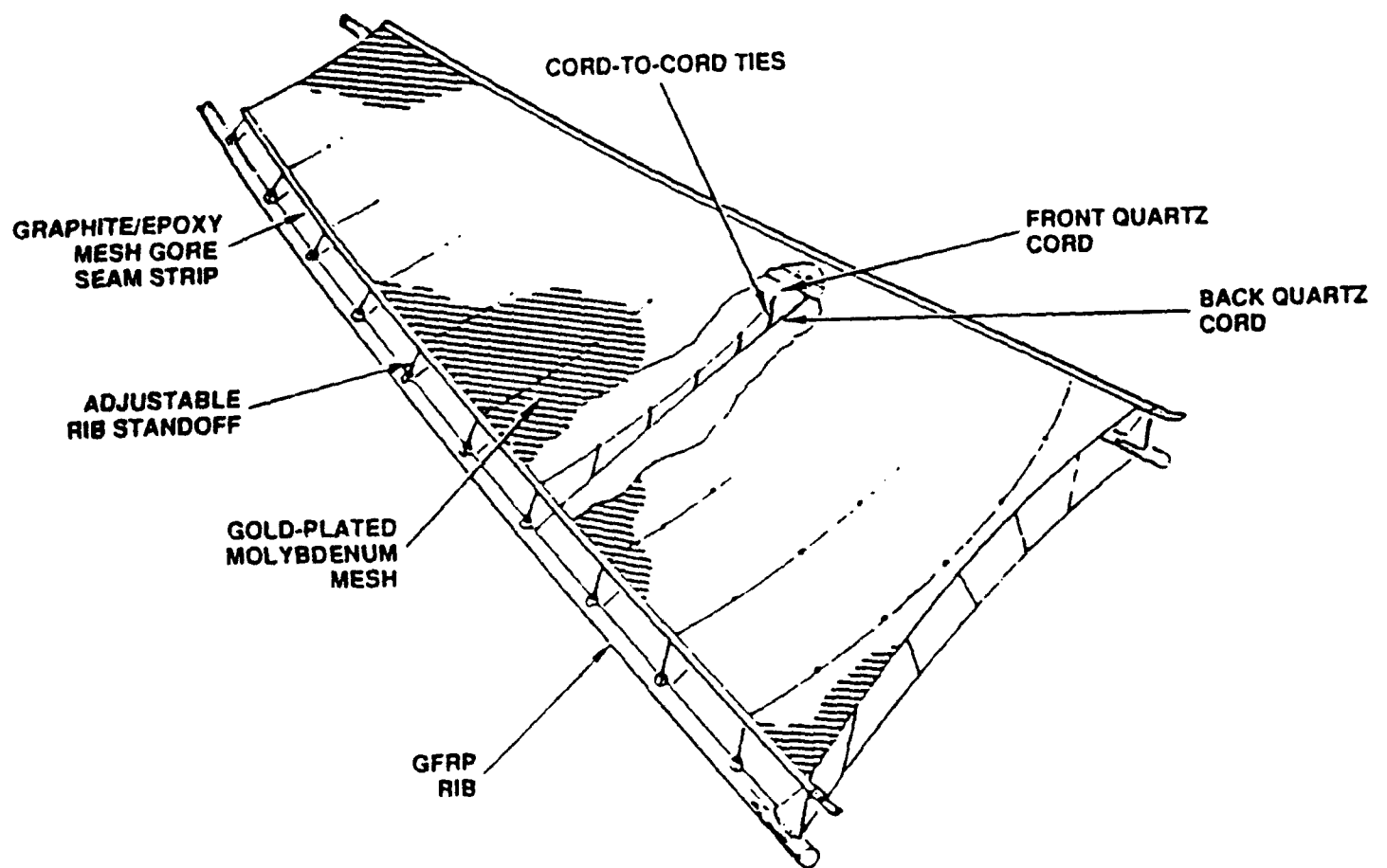
Figure 4.   TDRSS Dual Surface Design

COUNTER
BALANCES

TURNOVER
FIXTURE

Figure 5. TDRSS Surface Contour Measurement Technique
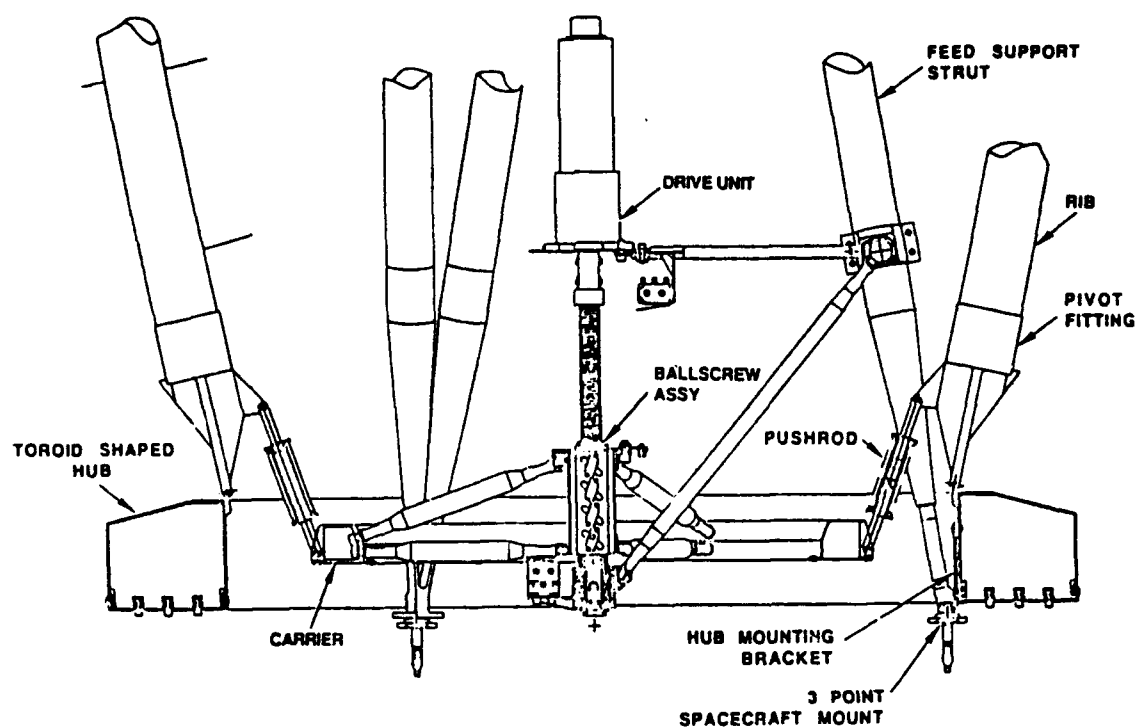
Figure 6. *Mechanical Deployment System*

SIMULATED YEARS OF STORAGE
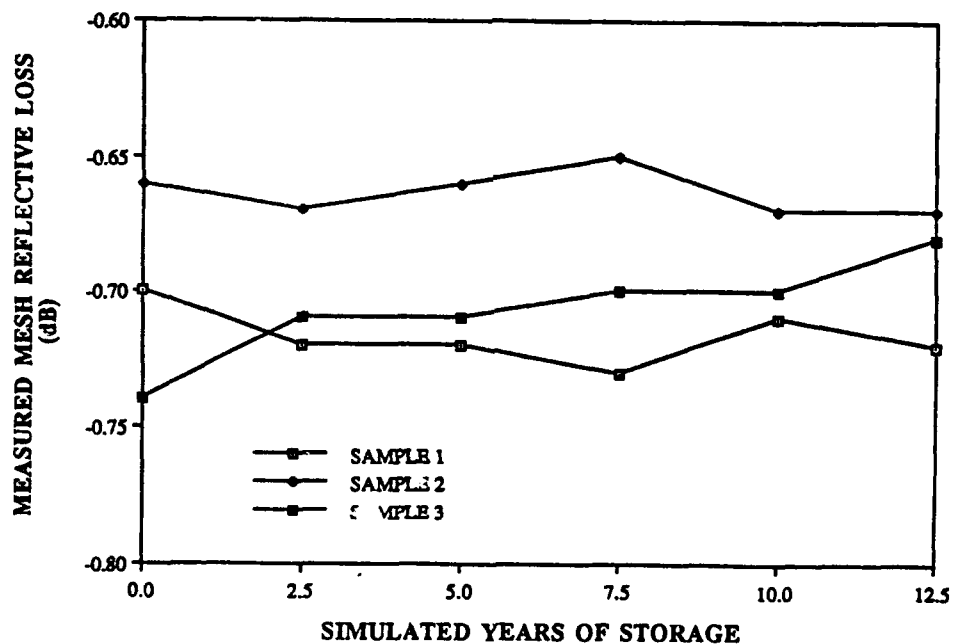
Figure 7. *Simulated Long-Term Storage Has No Effect*
On Mesh Reflection Loss
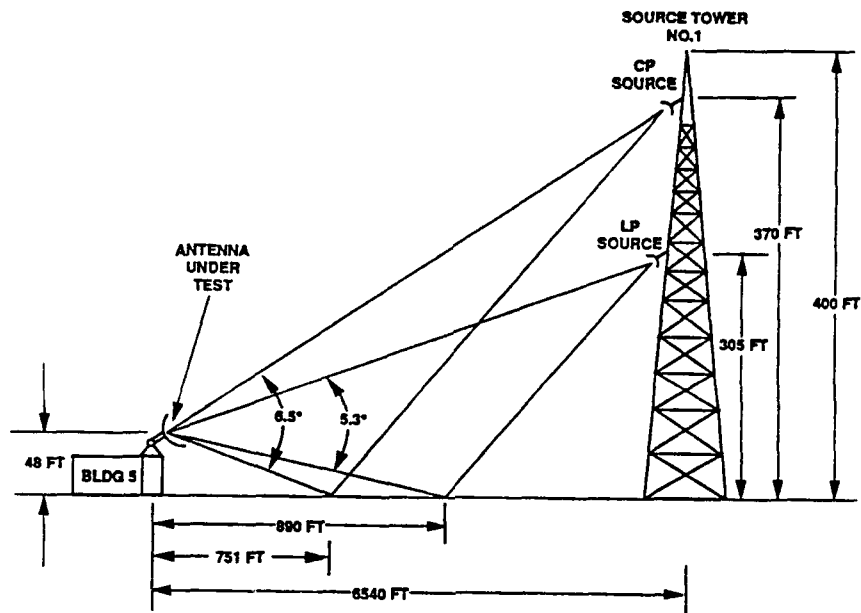
Figure 8.   Ku-band Antenna Pattern Range
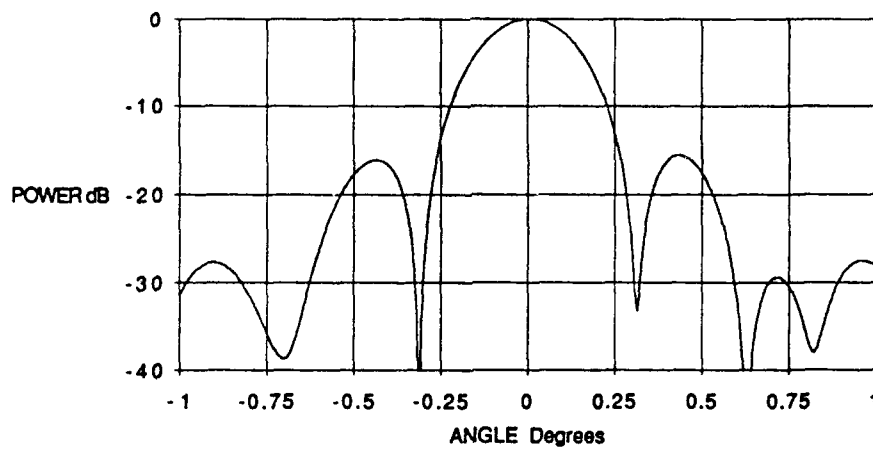
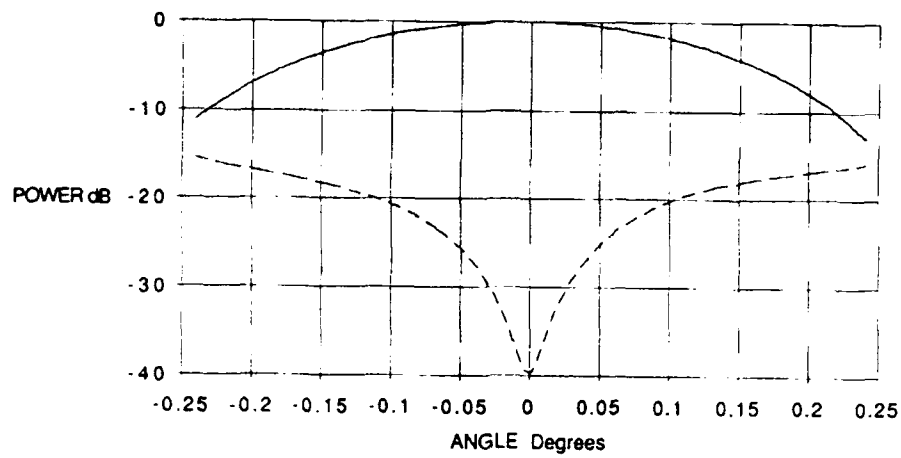*Figure 9.   Measured TDRSS Ku-band Antenna Pattern*

Figure 10. Measured Ku-band Sum and Difference Antenna Patterns Over Tracking Region
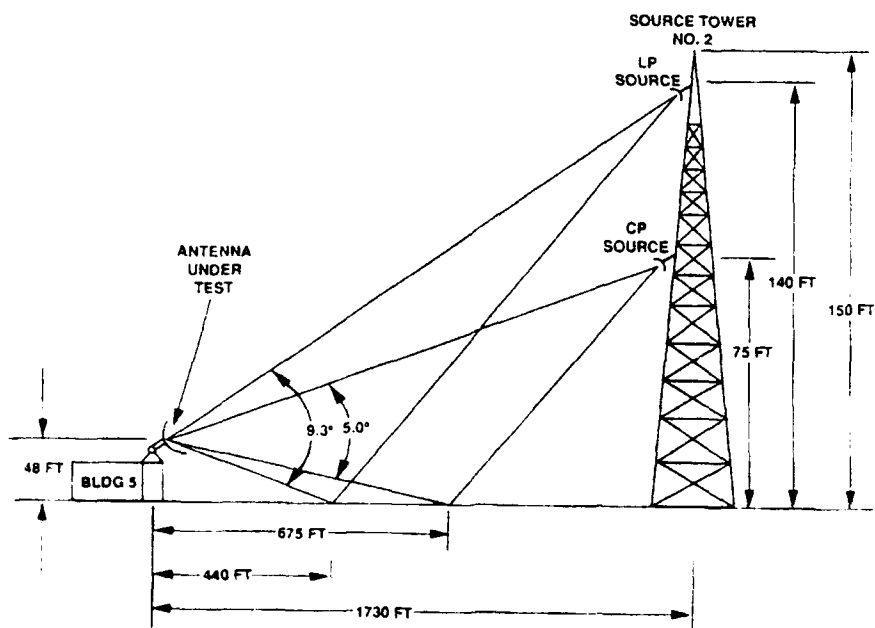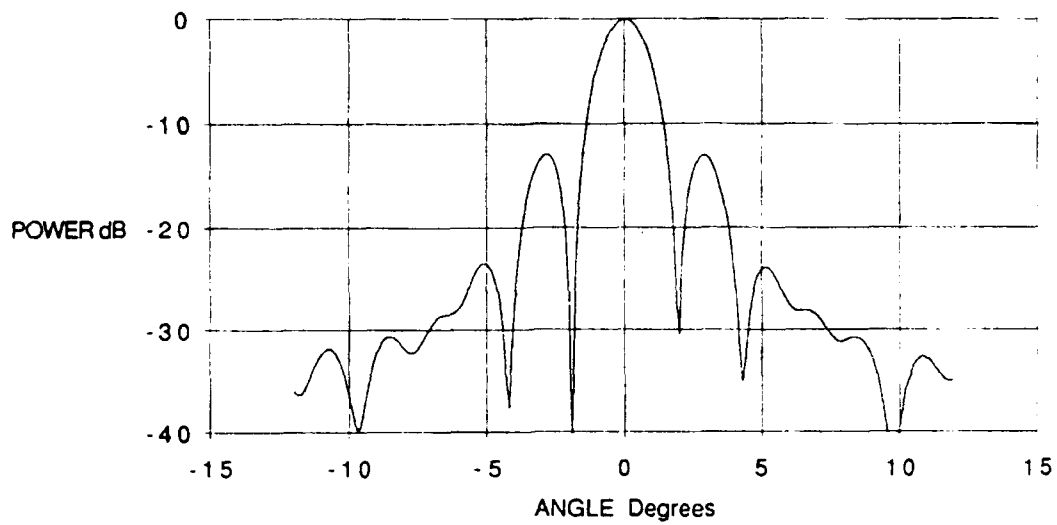

Figure 11. S-band Antenna Pattern Range
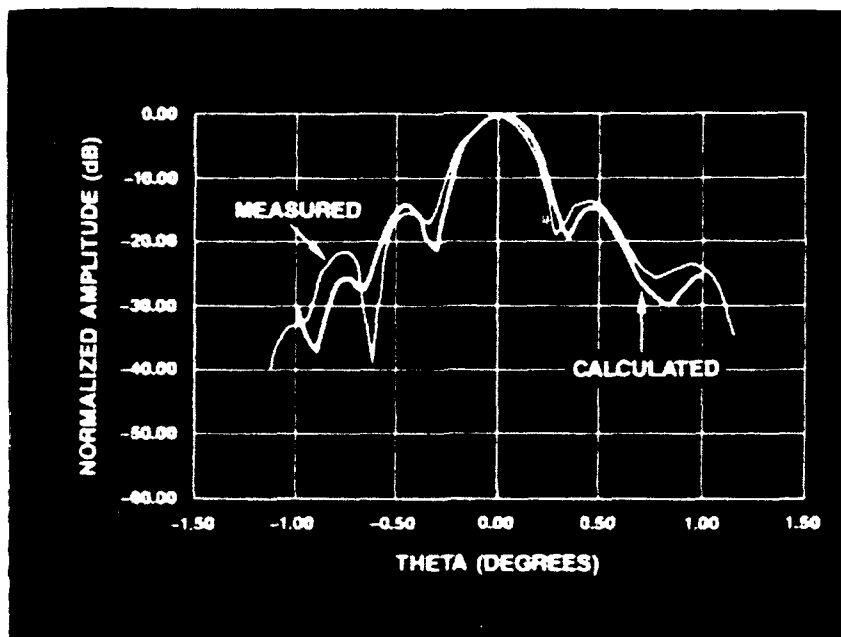
Figure 12.   Measured TDRSS S-band Antenna Pattern

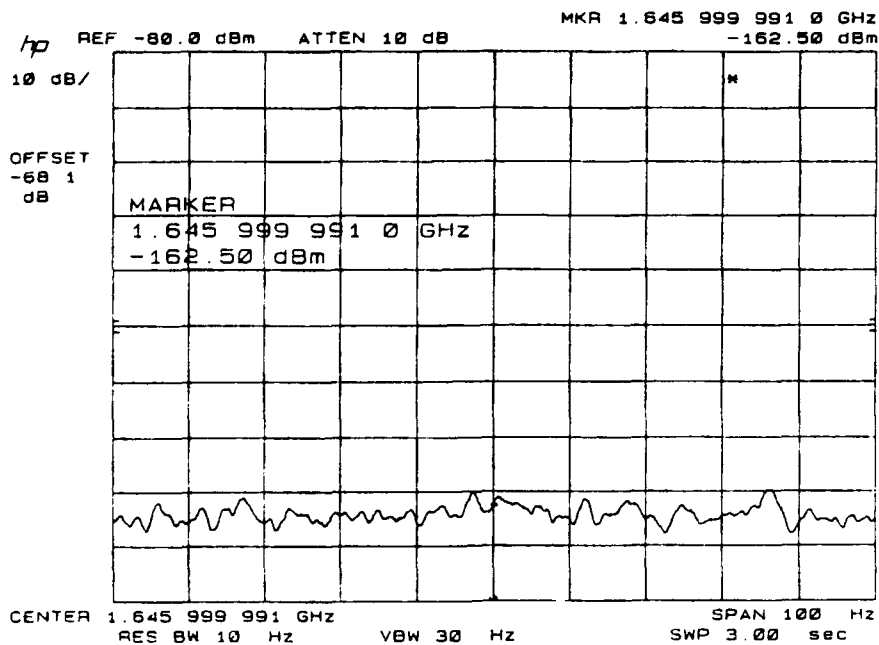*Figure 13.   Measured and Predicted Ku-band
On-Orbit TDRSS Antenna Patterns*

0122Z

19

Figure 14. *Measured PIM Power Level for Harris Mesh Below the Test Setup Noise Floor of –160 dBm*

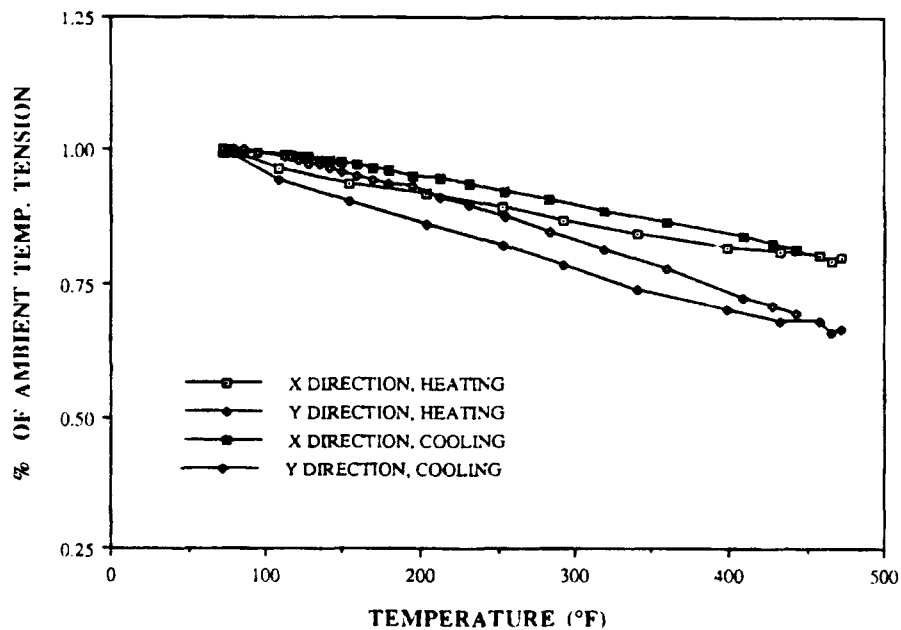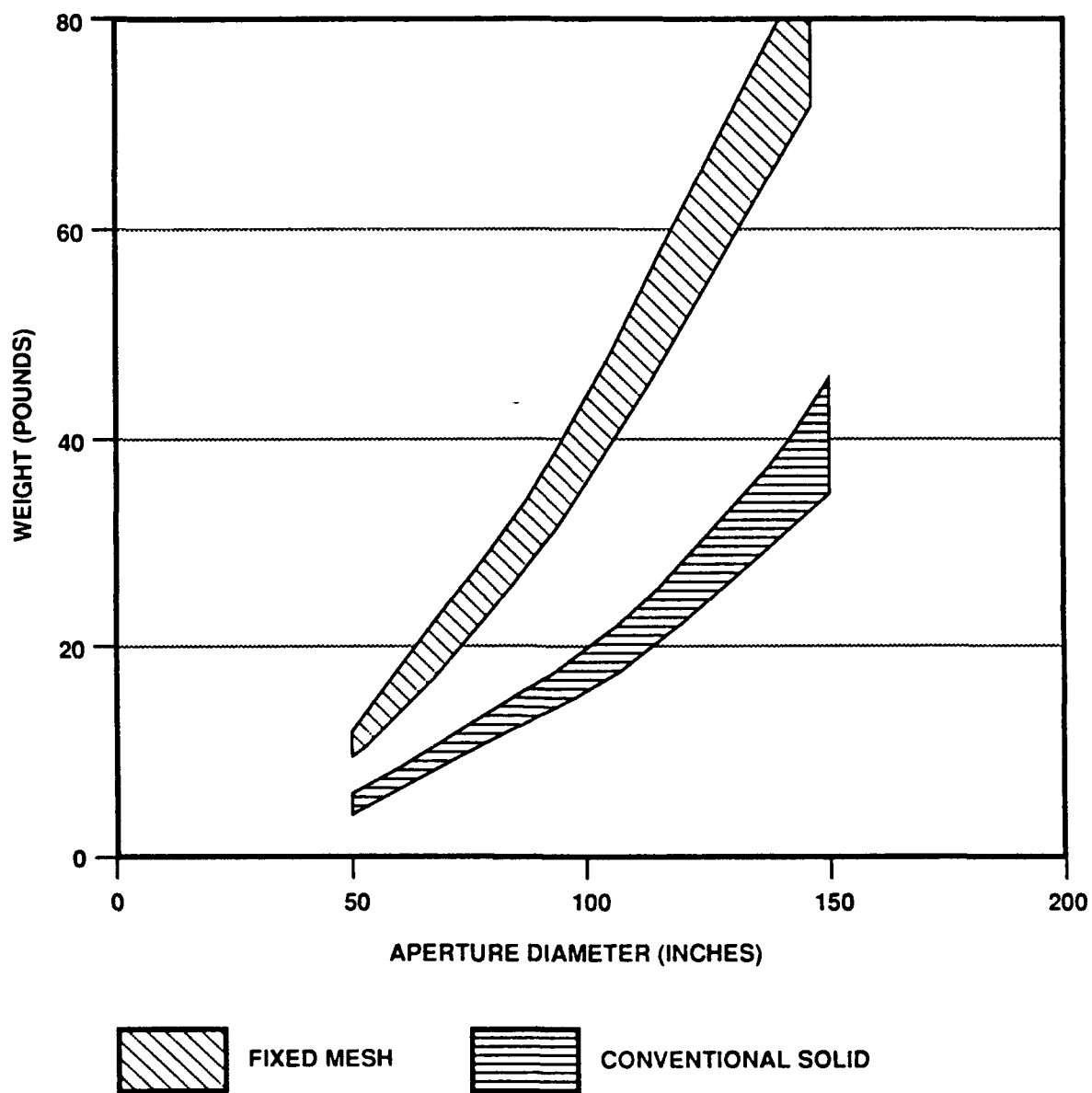**Figure 15.** *Mesh Tension Over On-Orbit Temperature Extremes*

Figure 16. Fixed, Nondeployable Mesh Reflector

TOPEX SPACECRAFT

DUAL-FREQUENCY RADAR ALTIMETER ANTENNA

Allan R. Jablon

The Johns Hopkins University

Applied Physics Laboratory

Laurel, MD 20723

Abstract - The design of the TOPEX Radar Altimeter antenna is described. The TOPEX/POSEIDON satellite is a joint U.S.-France (NASA-CNES) spacecraft scheduled for launch in 1992. The spacecraft will carry the TOPEX and POSEIDON radar altimeters, which will map the circulation of the global oceans. The TOPEX radar altimeter (NASA) is a dual-frequency altimeter operating at Ku- and C-bands. The POSEIDON radar altimeter (CNES) operates at Ku-band. A common antenna is used for the two altimeters. The antenna is a focal-fed 1.5 meter diameter parabolic reflector antenna. The feed includes a waveguide circuit to combine the three signals from the two altimeters. The radiating portion of the feed is a conical dual-depth corrugated scalar horn. The C-band signal is launched by a coaxial probe into the C-band circular waveguide feeding the horn. The two Ku-band signals are launched with orthogonal polarizations by an orthomode transducer. To achieve coupling (at Ku-band) to the horn through the large waveguide, a step discontinuity is used to generate TE_{11} and TM_{11} modes in the large waveguide.

1. INTRODUCTION

This paper describes the design of the TOPEX Radar Altimeter antenna. The TOPEX/POSEIDON satellite is a joint U.S.-France (NASA-CNES) spacecraft scheduled for launch in 1992. The spacecraft will carry the TOPEX and POSEIDON radar altimeters, which will map the circulation of the global oceans. The TOPEX radar altimeter (NASA) is a dual-frequency radar altimeter operating at Ku- and C-bands (13.44-13.76 GHz, and 5.14-5.46 GHz). The use of two frequency bands allows for correction of ionospheric effects. The POSEIDON radar altimeter (CNES) operates at Ku-band (13.485-13.815 GHz).

A common antenna is used for the two altimeters. The antenna is a focal-fed 1.5 meter (4.92 ft.) diameter parabolic reflector with a 2 ft. focal length. The feed for this antenna consists of a conical dual-depth corrugated scalar horn and a combining network to couple the three altimeter signals to the horn (Figs. 1 and 2).

2. HORN DESIGN

To radiate the three signals at the two widely-spaced frequency bands, a conical dual-depth corrugated scalar horn was developed. For maximum isolation between the TOPEX and POSEIDON altimeters, the Ku-band signals are launched with orthogonal linear polarizations. The
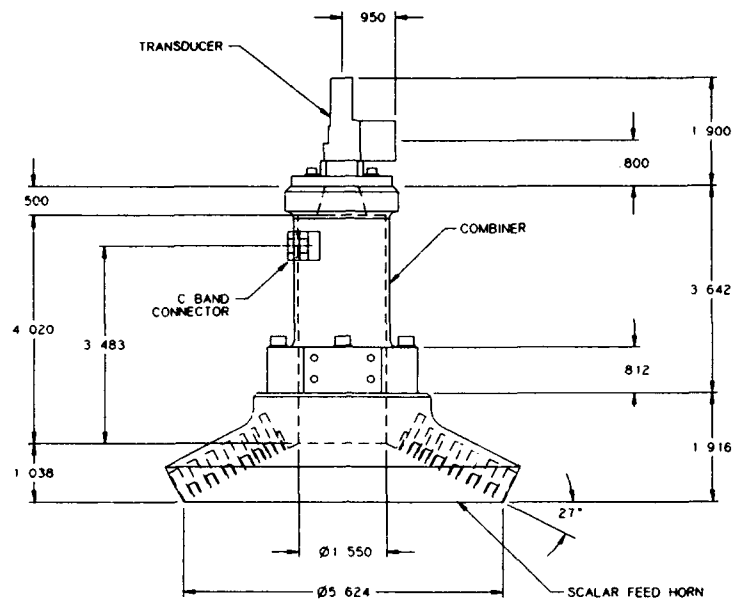
Fig. 1   TOPEX Radar Altimeter Antenna Feed
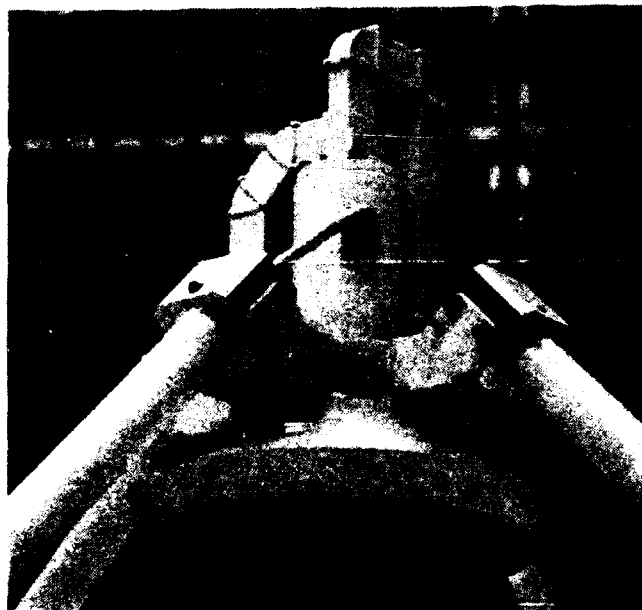
Fig. 2   Horn and Combiner

conical horn geometry allows the radiation of these orthogonal signals. The scalar (wide-flare, corrugated) horn[1] provides for frequency independent operation, as well as pattern symmetry. Dual-depth corrugations[2] provide for dual-frequency operation.

The design method and curves of Thomas[3] were used to determine the horn dimensions. To produce low secondary pattern sidelobes, the feed illumination taper was chosen to be -20 dB. The horn phase error, aperture size, and flare semiangle are related by the following expression:

$$\Delta = \frac{R}{\lambda_o} \sin(\theta_o) \tan(\theta_o/2) \qquad (1)$$

where Δ = phase error, R = horn radius, λ_o = free-space wavelength, θ_o = horn flare semiangle. To minimize the horn aperture size for minimum blockage, the horn phase error (Δ) was chosen to be 0.75 at C-band, giving a phase error of 1.92 at Ku-band. The horn flare semiangle was then determined to be 63 deg., based on a -20 dB edge illumination.

The slots were designed to produce minimum VSWR, as well as pattern symmetry at Ku- and C- bands. Dual-

3

frequency operation is achieved by using pairs of slots. Six slot pairs are used. Each slot pair includes one Ku-band slot and one C-band slot. The approximate surface reactance of a corrugated surface is given by[4]

$$X = 377 \; \frac{w}{w + t} \; \tan\left[\frac{2\pi d}{\lambda_o}\right] \tag{2}$$

where w = slot width, t = ridge width, d = slot depth, λ_o = free-space wavelength. The surface reactance due to a slot is dependent on the slot width and depth, as well as the ridge width. Surface reactance is also dependent on horn radius at the slot.

The surface reactance due to a slot pair is the sum of the two slot reactances. To produce pattern symmetry, the surface reactance across each slot should be infinite (capacitive). To achieve infinite surface reactance, the slots should be slightly greater than one-quarter wavelength in depth. However, for good VSWR, the surface reactance on the horn wall must change gradually from the zero reactance of the input waveguide to the required infinite reactance in the horn. To achieve this transition, the slot depths are gradually tapered from

4

approximately one-half wavelength near the horn throat to approximately one-quarter wavelength closer to the horn aperture. Slot width should be no more than one-half wavelength to prevent the generation of higher order modes.[3]

For the TOPEX feed horn, the ridge widths were held constant, and the slot depths and widths were varied to achieve the required reactances. The impedance transition was achieved using three of the six slot pairs. The combined width of each corrugation pair was limited to one-half wavelength at Ku-band to prevent higher order mode generation. Since it is impossible to achieve infinite surface reactance at both Ku- and C-bands simultaneously, compromises were necessary in the design of the slot dimensions. The final slot geometry is shown in Fig. 3 (dimensions in inches).

3. COMBINER

C-band circular waveguide (1.55 in. diameter) was chosen as the waveguide input for the feed horn. To accommodate the Ku-band signals, the waveguide diameter was chosen to be as small as possible. To couple the C-band signal into this waveguide, a coaxial probe to circular waveguide transition was developed.

5

Fig. 3   Dual-Depth Corrugation Geometry

Fig. 4   TOPEX Radar Altimeter Antenna
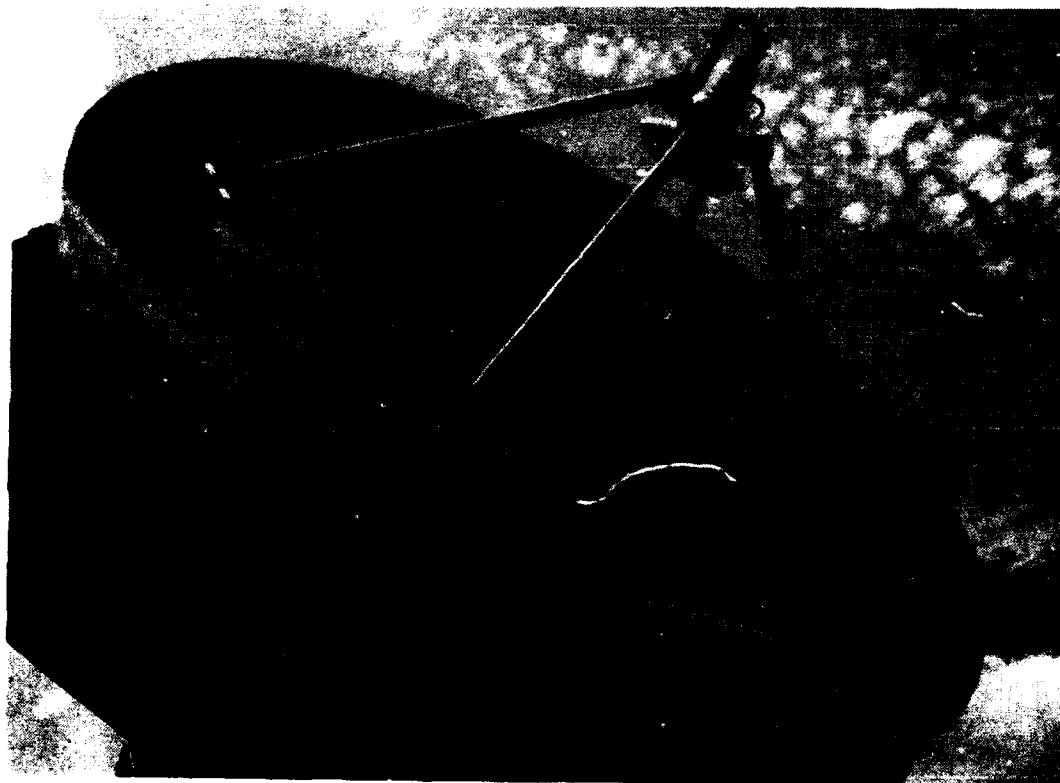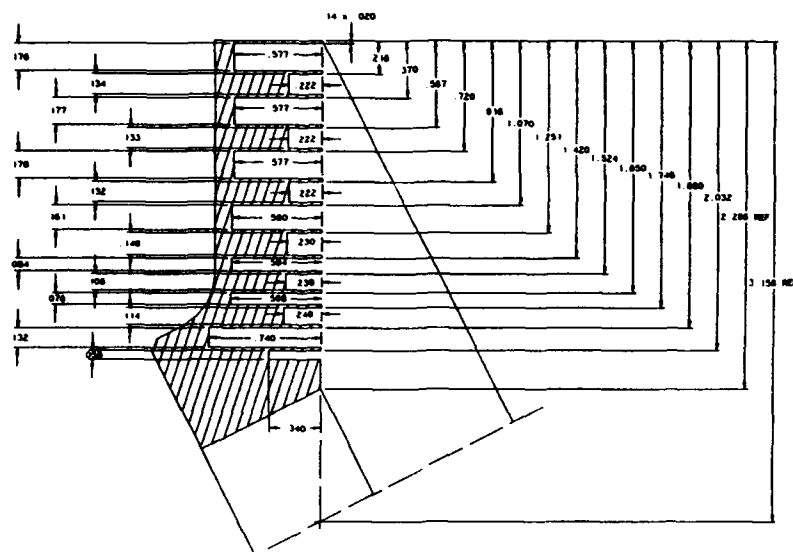
Isolation between the two Ku-band signals is achieved by an orthomode transducer (OMT), which launches the two signals with orthogonal linear polarizations. To couple the Ku-band signals to the scalar horn through the C-band waveguide, a step discontinuity[5] is used to introduce the TE_{11} and TM_{11} modes in the waveguide. The waveguide length between the step discontinuity and the horn throat is chosen so the two modes will be in phase at the horn throat. Since the horn produces the HE_{11} mode (which consists of degenerate TE_{11} and TM_{11} modes), the waveguide modes are matched to the horn mode. The diameters of the waveguides at the step discontinuity are .875 in. and 1.55 in.

For the C-band probe transition, the Ku-band step discontinuity acts as a short circuit. To reduce coupling of the Ku-band signals into the C-band probe, the probe is situated at 45 deg. to the E-fields of the two Ku-band signals. This gives an isolation between the C-band and Ku-band ports of 17 dB at Ku-band. Further isolation is achieved using a low-pass filter near the front end of the C-band receiver.

7

4. ASSEMBLED ANTENNA

Two lengths of Ku-band WR62 waveguide (with circular exterior wall) serve as two of the four support struts for the feed. To decrease aperture blockage and to save weight, the C-band signal is transmitted to the feed using a flexible coaxial cable, which runs inside one of the two non-waveguide struts.

To hold the feed in place during the stresses of launch, the struts are relatively large (0.875 , in. diameter). At Ku-band, the struts are slightly larger than one wavelength in diameter. The Ku-band sidelobes are adversely affected by the large size of these struts. The gain is also decreased by the strut blockage.

To reduce the VSWR at C-band, a vertex matching plate[6] was designed for the reflector. The vertex matching plate reduced the C-band VSWR from 1.6:1 to better than 1.25:1.

To reduce the weight of the antenna, the reflector consists of a honeycomb support structure sandwiched by two thin parabolic surfaces. The antenna support deck is also a honeycomb structure.

To reduce on-orbit thermally induced distortion of the reflector and struts, the antenna is painted white.

8

5. MEASURED RESULTS

E-plane and H-plane feed radiation patterns for C- and Ku-bands (measured at the center frequencies) are shown in Figs. 5-8. The reflector edge is 63 deg. from boresight.

The results given below are for secondary pattern measurements and apply over the operating bandwidths of the antenna.

The measured VSWRs for the antenna are better than 1.3:1 for the C-band and two Ku-band ports.

At Ku-band, the minimum power gain is 43.5 dBi. At C-band, the minimum power gain is 35.2 dBi. These power gain measurements include waveguide run and coaxial line losses.

Measured 3 dB beamwidths are 1.1 deg. at Ku-band and 2.9 deg. at C-band.

The maximum cross-polarization levels (within the 9 dB beamwidths) are -20 dB at Ku-band and -24 dB at C-band.

At C-band, the maximum sidelobe level is -21 dB. At Ku-band, the sidelobe level is -17 dB in the 45 and 135 deg. planes. The sidelobes are higher (-14 dB max.) in the E- and H-planes due to the fact that the feed support
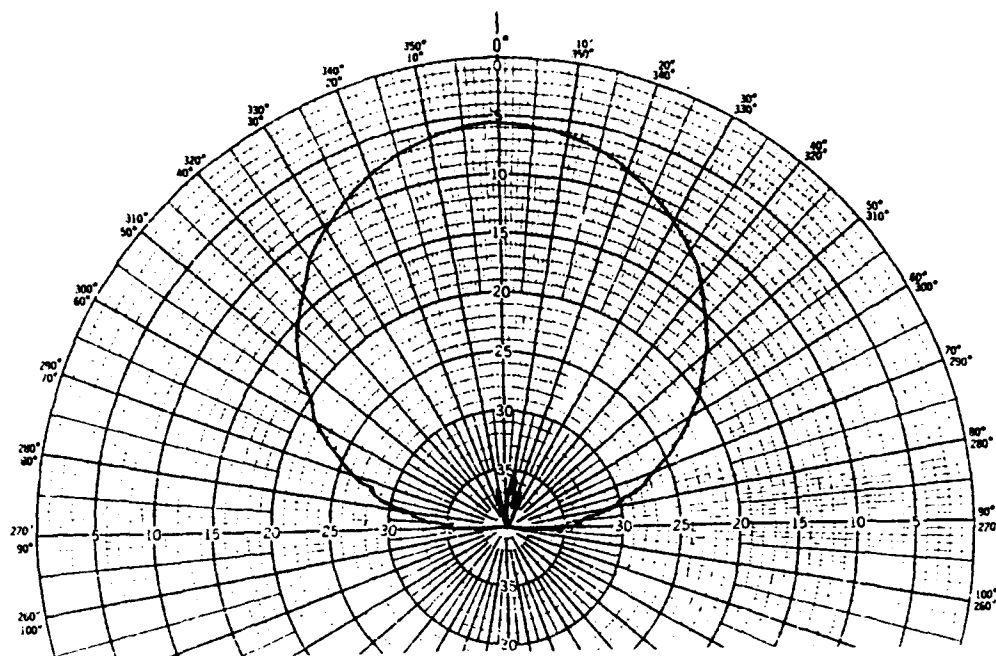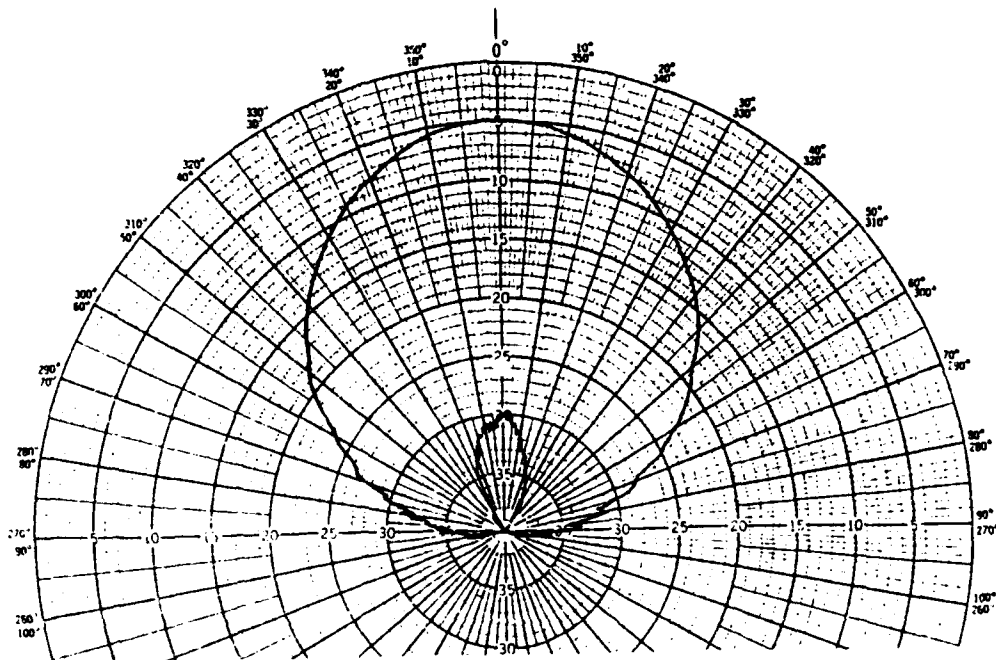
9

Fig. 5 Feed Pattern - C-band, E-Plane

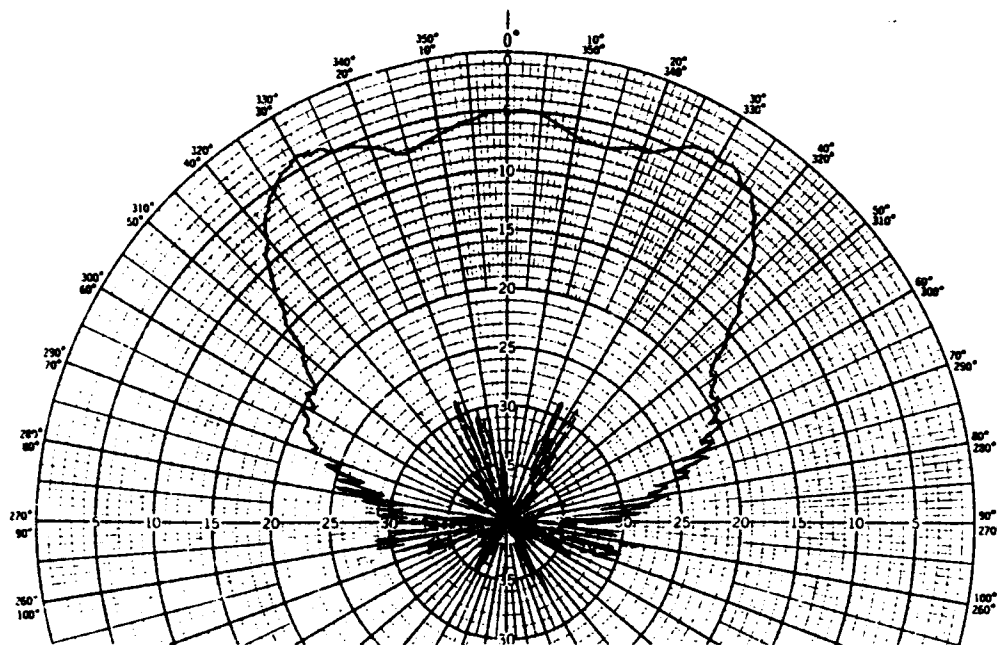Fig. 6 Feed Pattern - C-band, H-Plane
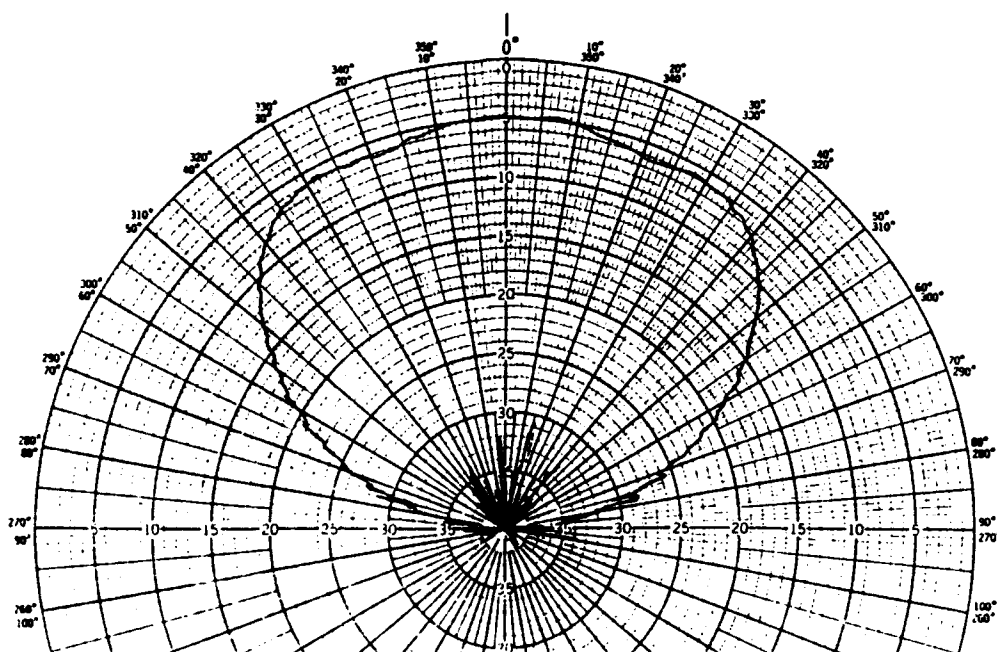
10

Fig. 7   Feed Pattern - Ku-band, E-Plane

Fig. 8 Feed Pattern - Ku-band, H-Plane

11

struts are in these planes. The Ku-band sidelobe levels include a 3 dB increase due to the vertex matching plate.

The measured isolation between the two Ku-Band ports is 37 dB.

ACKNOWLEDGEMENT

The author gratefully acknowledges the work of J. T. Will, for his contributions to the design and testing of the antenna, and R. K. Stilwell for technical guidance during the antenna development.

12

REFERENCES

1. Kay, A. F. (1964) <u>The Scalar Feed</u>, US Air Force
    Cambridge Labs Report 62-347, AD60169.

2. Ghosh, S. (1980) A Corrugated Wave Guide Feed for
    Discrete Multi-Band Applications Having Dual Depth
    Corrugations. Paper presented at the IEEE Int.
    Symp. on Antennas and Propagation, Quebec, Canada.

3. Thomas, B. M. (1978) Design of Corrugated Conical
    Horns, <u>IEEE Transactions on Antennas and
    Propagation</u>, vol. AP-26: 367-372.

4. Lawrie, R. E., Peters, L. (1966) Modifications of
    Horn Antennas for Low Sidelobe Levels, <u>IEEE
    Transactions on Antennas and Propagation</u>, vol.
    AP-14: 605-610.

5. Potter, P. D. (1963) A New Horn Antenna with
    Suppressed Sidelobes and Equal Beamwidths, <u>Microwave
    Journal</u>, vol. 6: 71-78.

6. Silver, S. (1949) <u>Microwave Antenna Theory and
    Design</u>. McGraw-Hill, New York.

13

SHORT BACKFIRE ANTENNA MODELING
WITH DIPOLE OR WAVEGUIDE EXCITATION

G.P. Otto, C. Lu, and W.C. Chew
Electromagnetics Laboratory
Department of Electrical and Computer Engineering
University of Illinois
1406 W. Green Street
Urbana, IL 61801

ABSTRACT- A three-dimensional short backfire antenna structure with circular symmetry is modeled using the mode matching method and the vector Hankel transform. The excitations considered are thin wire dipole antennas and flush waveguide feeds. The efficiency of computation can be increased by ignoring the higher order harmonics in the model. Then this model is used to design a structure with a larger directivity than previously reported. Theoretical predictions of the radiation pattern yield good agreement with measurements performed on a prototype. In addition, this model could be modified to approximate rectangular waveguide excitations or corrugated cavities.

1. INTRODUCTION

The backfire antenna principle was conceived by Ehrenspeck[1-2] in 1960 and uses a pair of plane reflectors to increase the directivity of an antenna. A short backfire antenna (SBA) is the shortest conceivable type of backfire structure as the subreflector is separated from the main reflector by one-half wavelength. Several excitations for this type of structure have been suggested including dipole antennas[2], waveguide feeds[3] (flush and inserted versions), surface-wave structures[4], linear slot arrays[3], and sectoral horn feeds[3]. The applications of the short backfire antenna lie in situations in which parabolic dishes are not competitive and have been summarized previously[3].

With the exception of Chen et al.[5] and Leong et al.[6], most of the work on the SBA has been experimental[3,7-10]. Chen et al.assume the dipole excites a

cosinusiodal field over an effective aperture in both the horizontal and vertical planes. Obviously, this first-order approximation in the far-field predicts an identical pattern for both the E-plane and H-plane fields. In contrast, experiments consistently show a narrower beam and the presence of sidelobes in the H-plane. On the other hand, Leong *et al.* use the method of moments (MOM) and the cosine transform to solve for the unknown aperture fields of a two-dimensional SBA. Although this model is applicable to a rectangular SBA[4], it has no apparent advantage over the cylindrical SBA with a circular symmetry.

This paper presents a rigorous theoretical analysis for the 3-D circular SBA for the purpose of design optimization. It will be shown that this model can be used to design a structure with a larger directivity than previously reported. This structure is slightly different from those previously described, in that *the rim extends from the backplate to the plane of the subreflector* and has an infinite ground plane, as shown in Fig. 1. Also, we describe excitation via a thin wire dipole antenna or a flush waveguide feed. We will use the mode matching method and the vector Hankel transform to find the unknown fields in the coaxial aperture.

2. MODE MATCHING MODEL

2.1 INTRODUCTION

A model of a short backfire antenna with an infinite flange is shown in Fig. 1. The radius and length of the cavity is denoted by w and d, respectively, and the radius of the subreflector is h. Notice that the cavity has an infinite flange in the plane containing the subreflector , while those described by other authors[2-5] have a short rim with no flange.

In order to facilitate understanding of the physics involved, we describe a

four step solution:

(1) Solve a canonical problem of cylindrical waves impinging on a subreflector.

(2) Find the excited fields in the circular waveguide.

(3) Compose the complete solution of the resonant fields in the cavity.

(4) Find the far-field radiation pattern.

2.2 CANONICAL PROBLEM

The first step in modeling the SBA is to solve a canonical problem with circular symmetry shown in Fig. 2. This simpler problem models waves in a circular waveguide impinging on a flanged end with a subreflector, and hence radiating power into space. The inclusion of the infinite flange at the discontinuity eliminates a third region in this problem. Effectively, this is a two region problem with the unknowns being the fields in the coaxial aperture. The total transverse electric field can be represented in *vector notation*[11] (assuming $e^{-i\omega t}$ time dependence) as

$$
\mathbf{E}_s(\rho, \phi, z) = \sum_{n=1}^{\infty} e^{in\phi} \begin{cases} \vec{\mathbf{f}}_n^t(\rho) \cdot \left(e^{i\overline{\mathbf{K}}_{1n}z} + e^{-i\overline{\mathbf{K}}_{1n}z} \cdot \overline{\mathbf{R}}_{12n} \right) \cdot \mathbf{e}_n, & z < 0, \\ \vec{\phi}_n^t(\rho) \cdot \mathbf{a}_n, & z = 0, \\ \int_0^{\infty} k_\rho \, dk_\rho \, \overline{\mathbf{J}}_n(k_\rho\rho) \cdot \mathbf{c}_n(k_\rho) \, e^{ik_{2z}z}, & z > 0. \end{cases}
$$

$$(1)$$

The complex matrix $\vec{\mathbf{f}}_n^t(\rho) = [\cdots, \overline{\mathbf{J}}_{nm}(\rho), \cdots]$, where $\overline{\mathbf{J}}_{nm}$ is a 2×2 matrix, contains the radial dependence of the TM and TE modes for each harmonic n in the circular waveguide. In the aperture, $\vec{\phi}_n^t(\rho)$ is a similar matrix for the coaxial basis functions. These radial functions are orthonormal in each waveguide[12]. Here, $\overline{\mathbf{K}}_{1n}$ is a complex diagonal matrix with elements corresponding to the z-components of alternating TM and TE cylindrical wavenumbers. Also, the matrix $\overline{\mathbf{R}}_{12n}$ is defined to be the generalized reflection operator for the electric field. While the mode amplitudes in the circular

waveguide, denoted $\mathbf{e}_n$, are arbitrary, $\mathbf{a}_n$ and $\mathbf{c}_n(k_\rho)$ are determined by the boundary conditions. Notice that the lack of a waveguide for $z > 0$ implies a continuous spectrum of modes in the k_ρ-space, represented as a vector Hankel transform[11,13] (VHT) of the field in the coaxial aperture. Similarly, the tangential magnetic field has the same form as Eqn. (1) with the inclusion of diagonal matrices[11], $\overline{\mathbf{g}}_n$ and $\overline{\mathbf{G}}_n(k_\rho)$, containing the complex TM and TE wave admittances in the waveguides and the unbounded region, respectively.

For this problem, there are four unknowns and four continuity conditions at the aperture plane. Fortunately, due to the orthogonality between harmonic modes $e^{\pm in\phi}$, the modes decouple and the unknowns can be solved separately for each n. First, it is apparent that the radiated field spectrum is the vector Hankel transform of the aperture field given by

$$\mathbf{c}_n(k_\rho) = \overset{\sim}{\overline{\boldsymbol{\phi}}}_n^t(k_\rho) \cdot \mathbf{a}_n, \tag{2}$$

where $\overset{\sim}{\overline{\boldsymbol{\phi}}}_n^t(k_\rho)$ is the vector Hankel transform of $\overline{\boldsymbol{\phi}}_n^t(\rho)$ and can be found in closed form[15]. After testing the tangential magnetic field continuity equation by the aperture basis functions and integrating over the aperture, the cylindrical-coaxial mode cross-coupling matrix, called $\overline{\mathbf{C}}_n$, is defined as

$$\overline{\mathbf{C}}_n = \int_0^\infty k_\rho \, dk_\rho \, \overset{\sim}{\overline{\boldsymbol{\phi}}}_n^*(k_\rho) \cdot \overline{\mathbf{G}}_n(k_\rho) \cdot \overset{\sim}{\overline{\boldsymbol{\phi}}}_n^t(k_\rho). \tag{3}$$

One can then identify the aperture basis function amplitudes as

$$\mathbf{a}_n = 2 \left(\overline{\mathbf{C}}_n + \overline{\mathbf{L}}_{1an}^\dagger \cdot \overline{\mathbf{g}}_n \cdot \overline{\mathbf{L}}_{1an} \right)^{-1} \cdot \overline{\mathbf{L}}_{1an}^\dagger \cdot \overline{\mathbf{g}}_n \cdot \mathbf{e}_n, \tag{4}$$

where $\overline{\mathbf{L}}_{1an} = \langle \overline{\mathbf{f}}_n^*(\rho), \overline{\boldsymbol{\phi}}_n^t(\rho) \rangle$ is a matrix for the projection coefficients. Then, the generalized reflection operator is[16]

$$\overline{\mathbf{R}}_{12n} = 2 \, \overline{\mathbf{L}}_{1an} \cdot \left(\overline{\mathbf{C}}_n + \overline{\mathbf{L}}_{1an}^\dagger \cdot \overline{\mathbf{g}}_n \cdot \overline{\mathbf{L}}_{1an} \right)^{-1} \cdot \overline{\mathbf{L}}_{1an}^\dagger \cdot \overline{\mathbf{g}}_n - \overline{\mathbf{I}}. \tag{5}$$

4

For example, the magnitude of the generalized reflection operator for a typical SBA is shown in Fig. 3 with $n=1$. The matrix is very complicated for the smaller-order modes, but becomes increasingly diagonal for the higher-order modes. However, the higher-order modes are highly evanescent.

2.3.1 WIRE DIPOLE EXCITATION

Next, we find the excited fields in the circular waveguide. We can expand the excited fields in terms of cylindrical modes with amplitudes e'_n. The first case uses a thin wire dipole as the excitation source. Here, a wire dipole source at a distance d_o from the backplate excites the waveguide with mode amplitudes

$$e'_n = \frac{1}{2\pi} (1 - (-1)^n) \left(e^{i\overline{\mathbf{K}}_{zn}(d-d_o)} - e^{i\overline{\mathbf{K}}_{zn}(d+d_o)} \right) \cdot \overline{\mathbf{g}}_n^{-1} \cdot$$
$$\int_0^L \rho d\rho \, \overline{\mathbf{f}}_n^*(\rho) \cdot \begin{bmatrix} I(\rho) \\ 0 \end{bmatrix}, \qquad \forall \, n \geq 1, \tag{6}$$

referenced at $z=0$, where the backplate reflection operator is $-\overline{\mathbf{I}}$ and $I(\rho)$ is the assumed current along the dipole of length $2L$. A good approximation for a half-wavelength dipole is the cosine function. (In the complete solution of the SBA, the subreflector and the backplate are in the near-field of the dipole, as well as the rim. This will affect the currents on the dipole and hence the exact solution must be solved simultaneously, including the near-field scatterers. Nevertheless, this paper assumes that these scatterers are distant enough from the dipole that their effects can be neglected.)

Later, the input impedance of the antenna can be approximated by the reaction formula

$$Z_{in} = -\frac{\langle \mathbf{E}_T, \mathbf{J} \rangle}{I^2}. \tag{7}$$

where $\mathbf{E}_T$ is the total electric field generated by dipole current density $\mathbf{J}$.

5

2.3.2 WAVEGUIDE EXCITATION

Similarly, a waveguide feed flush with the backplate, denoted region 0, with incident modal amplitudes e'_{0n} excite the circular waveguide with amplitudes

$$e'_n{}^{WG} = e^{i\overline{K}_{zn}d} \cdot \overline{T}_{01n} \cdot e'_{0n}, \qquad \forall\, n \geq 1, \tag{8}$$

where $\overline{T}_{01n}$ is the transmission operator from region 0 to region 1. For example, $\overline{T}_{01n}$ can be found in closed form for circular waveguide excitations using two region mode matching analysis for each orthogonal harmonic n. This could be extended to approximate flush rectangular feeds in a similar manner.

2.4 COMPLETE SOLUTION

Now, we can compose the complete solution of the SBA from the canonical problem already described and the excited modes in the circular waveguide. The complete solution must take into account the multiple reflections between the subreflector and the backplate. The constraint condition relates the total mode amplitudes due to multiple reflections, e_n, to the excited mode amplitudes, e'_n, and is satisfied by

$$e_n = e'_n + e^{i\overline{K}_{zn}d} \cdot \overline{R}_{10n} \cdot e^{i\overline{K}_{zn}d} \cdot \overline{R}_{12n} \cdot e_n, \tag{9}$$

where $\overline{R}_{10n}$ is the reflection operator from the backplate. For dipole excitations, the backplate is planar and $\overline{R}_{10n} = -\overline{I}$ (the identity matrix). On the other hand, for waveguide excitations there will be an aperture in the backplate. Now, Eqn. (9) can be solved for e_n resulting in

$$e_n = \left(\overline{I} - e^{i\overline{K}_{zn}d} \cdot \overline{R}_{10n} \cdot e^{i\overline{K}_{zn}d} \cdot \overline{R}_{12n}\right)^{-1} \cdot e'_n. \tag{10}$$

Eqn. (10) relates the total mode amplitudes to the excited mode amplitudes. The aperture mode amplitudes are given by Eqn. (4) and now the total fields can be found in each region.

2.5 FAR-FIELD RADIATION PATTERN

Now that the complete solution for the SBA has been determined, the radiation fields can be found. In the far-field, the waves are spherical and the slowly varying parts of the z-component fields can be approximated using the stationary phase point method[14,17]. Then the time-averaged power flow is given by

$$\langle S_r(r, \theta, \phi) \rangle = \frac{k_2^2 \cos\theta}{2\, r^2} \sum_{n=1}^{\infty} \mathbf{c}_n^\dagger(k_2 \sin\theta) \cdot \overline{\mathbf{P}}_n^\dagger(\phi) \cdot \overline{\mathbf{G}}_n(k_2 \sin\theta)$$
$$\cdot \overline{\mathbf{P}}_n(\phi) \cdot \mathbf{c}_n(k_2 \sin\theta), \tag{11}$$

where
$$\overline{\mathbf{P}}_n^{LP} = \begin{bmatrix} \cos n\phi & 0 \\ 0 & \sin n\phi \end{bmatrix} \quad \text{and} \quad \overline{\mathbf{P}}_n^{CP} = \begin{bmatrix} e^{in\phi} & 0 \\ 0 & e^{in\phi} \end{bmatrix} \tag{11a}$$

are the matrices for the angular variation in linear polarization (LP) and circular polarization (CP) problems. The far-field radiation pattern is given by Eqn. (11). For example, Fig. 4 shows a typical radiation pattern in three dimensions as well as projections on E- and H-planes and the contour levels with half-wavelength dipole excitation. One can detect a smaller beam and the presence of small sidelobes in the H-plane, as expected.

3. COMPUTER IMPLEMENTATION

So far, all of the matrices and vectors described have had infinite dimensions. But in practice, a computer implementation need only consider a finite number of modes. For the mode matching method, one chooses N_{coax}, the total number of TM and TE modes in the coaxial basis function. Then, the total number of modes needed in the circular waveguide, N_{cylin}, is chosen to satisfy[16]

$$\frac{N_{cylin}}{w} \gg \frac{N_{coax}}{w - h} \tag{12}$$

Empirical results show that $N_{coax} \sim 40$ yields an error of less than 1% in the radiation pattern.

7

Now, the solution can be rapidly computed from the model described. However, the cylindrical-coaxial mode cross-coupling matrix, $\overline{C}_n[N_{coax} \times N_{coax}]$, involves an infinite integral along the real axis for each term. Moreover, for a lossless problem, there will be singularities and branch points on the real axis. Fortunately, Cauchy's theorem and Jordan's lemma allow the deformation of this integral below the real axis in the complex k_ρ-plane. A detour below the real axis smoothes the integrand and actually increases the computation speed[13]. Empirical results indicate that a detour below the branch point along $k_\rho = k'_\rho - 0.1\ ik_2$ achieves good results. In addition, the integrand falls off as k_ρ^{-4} after the branch point, so the integral converges rapidly. Finally, the number of integrations can be cut in half by utilizing the block anti-symmetric nature of the matrix.

Also, one might expect that the computation becomes excessive as the solution must be summed over the harmonics $e^{in\phi}$. However, a thin wire dipole SBA does not excite the harmonics with even values of n. Furthermore, the $n = 3, 5, 7, \ldots$ harmonics do not contribute significantly to the radiation pattern. In support of this claim, we have plotted the magnitude of the excited TE mode amplitudes for a half-wavelength dipole in an infinitely long circular waveguide, shown in Fig. 5. The waveguide has radius $w = 1.114\ \lambda$. Calculations indicate that only two $n = 1$ TE modes are propagating; along with one $n = 3$ mode and one $n = 5$ mode. It is clear that the $n \geq 5$ modes do not have any significant contribution. Also, comparisons between measured and calculated radiation patterns using only the $n = 1$ modes shows excellent agreement. Thus, the authors claim that the $n = 1$ modes ($e^{i\phi}$ harmonics) result in a good approximation for a thin wire dipole excited SBA. On the other hand, a circular waveguide fed SBA is exactly separable with respect to n.

8

Next, the computer model is used to determine the gain as a function of the parameters of the dipole excited backfire structure (w, h, and d with $d_o = \frac{1}{2}d$). Note that only the $n = 1$ modes were used in all of the computations described hereafter. Computations revealed that the main lobe beamwidth decreases with increasing w, but the number of sidelobes also increases, as expected. The maximum directivity obtained with a rim radius $w = 1.1$ λ is the optimal theoretical size given by Leong et al.[6] where a parallel plate waveguide model is used. Similarly, the radiation patterns are critically dependent on the subreflector radius h. Our model yields the largest directivity with $h = 0.286$ λ. This value is significantly larger than the two-dimensional predictions[6]. Finally, the least sensitive parameter is the cavity length d. Our optimal value of $d = 0.52$ λ is less than the prediction by Leong et al.[6].

Furthermore, the radiation patterns as a function of frequency exhibit the same characteristics already described. Some computed E- and H-plane radiation patterns are plotted in Fig. 6 versus θ for fixed SBA parameters and varying frequencies. The associated directivities are within 3 dB of the peak value over a frequency bandwidth of 35%.

4. EXPERIMENTAL RESULTS

A prototype optimal SBA was constructed with a half-wavelength thin wire dipole excitation and a split-coax balun to suppress the monopole radiation from the outside surface current on the coaxial feed line. The dimensions of the optimal backfire structure chosen with the aid of the computer model were $w = 1.114$ λ, $h = 0.286$ λ, and $d = 0.56$ λ at 3 GHz. The finite flange is practical and previous work has shown that it does not have to be very large[18]. The prototype used a flange of width 0.5 λ and was constructed

9

from 20 oz. copper sheet metal. The directivity measured 19.6 dB with linear polarization, which is in good agreement with the computed value of 19.5 dB (considering $n = 1$ modes only), especially since the antenna does not have an infinite flange. This gain is slightly larger than that obtained by other authors[1-8] excluding those with corrugated rims[9,10]. Fig. 7 shows good agreement between the measured and computed gain pattern in both the E- and H-plane. The sidelobe levels in the H-plane were at -14 dB which is 2 dB more than the computer model predicts. The most probable cause for this difference is the inexact placement of the subreflector at a distance d from the backplate. In support of this claim, computations show that an error in d of 0.04 λ results in a sidelobe level error of 2.5 dB. However, this error could also be attributed to the finite flange effects and the neglected higher harmonics $e^{in\phi}$ in the computed pattern. The cross-polarization measured -17 dB arises from the residual monopole radiation of the coaxial feed line.

5. CONCLUSIONS

The approximation in our model relies on the assumption of the current on the dipole antenna or the incident mode amplitudes in the feed waveguide. Also, computations were simplified by using only the first order harmonic ($e^{i\phi}$). However, the agreement of the measured and computed field patterns indicates the validity of the model. This model was developed for thin wire dipole and circular waveguide excitation, but could be extended to approximate rectangular waveguide excitation. Also, a simple modification in the open region allows modeling of a SBA in a planarly layered half-space. Furthermore, a three-dimensional SBA with a corrugated rim could be modeled similarly with multiple waveguide discontinuities in the cavity.

REFERENCES

1. Ehrenspeck, H.W. (1960) The backfire antenna, a new type of directional line source, Proc. IRE 48 (1): 109–110.

2. Ehrenspeck, H.W. (1965) The short-backfire antenna, Proc. IEEE 53 (6): 1138–1140.

3. Large, A.C. (1976) Short backfire antennas with waveguide and linear fields, Microwave J. 19 (8): 49–52.

4. Hristov, H.D. and Taylor, D. (1972) Rectangular backfire antenna with dielectric surface-wave structure, Electronic Letters 8 (6): 163–165.

5. Chen, K.M., Nyquist, D.P. and Lin, J.L. (1968) Radiation fields of the short-backfire antenna, IEEE Trans. Antennas Propagat. AP-16: 596-597.

6. Leong, M.S., Kooi, P.S., Chandra, and Teo, T.S. (1989) Theoretical and experimental investigations of two-dimensional waveguide-excited short backfire antenna structure, IEE Proc.-H 136 (3): 263–268.

7. Ohmori, S., Miura, S., Kameyama, K. and Yoshimura, H. (1983) An improvement in electrical characteristics of a short backfire antenna, IEEE Trans. Antennas Propagat. AP-31 (4): 644-646.

8. Leong, M.S. and Kooi, P.S. (1984) Performance of a rectangular-waveguide-excited short backfire antenna employing a conical main reflector, Electronic Letters 20 (18): 749-751.

9. Kooi, P.S., Leong, M.S. and Yeo, T.S. (1979) Dipole-excited short backfire antenna with corrugated rim, Electronic Letters 15 (14): 421–423.

10. Leong, M.S. and Kooi, P.S. (1979) Rectangular-waveguide-excited short backfire antenna with corrugated rim, Electronic Letters 15 (17): 533–535.

11. Chew, W.C. and Habashy, T.M. (1986) The use of vector transforms in solving some electromagnetic scattering problems, IEEE Trans. Antennas Propagat. AP-34 (7): 871–879.

12. Marcuvitz, N. (1951) Waveguide Handbook, MIT Radiation Laboratory and Mc-Graw-Hill, New York, pp. 72-80.

13. Chew, W.C. and Kong, J.A. (1980) Resonace of the axial-symmetric modes in microstrip disk resonators, J. Math. Phys. 21 (3): 582-591.

14. Chew, W.C. (1990) Waves and Fields in Inhomogeneous Media, Van Nostrand Reinhold, New York.

15. Abramowitz, M. and Stegun, I.A. (1972) Handbook of Mathematical Functions. National Bureau of Standards, Washington, D.C., p.485.

16. Chew, W.C., Lin, K.H., Friedrich, J. and Chan, C.H. (1991) Reflection and transmission operators for general discontinuities in waveguides, J. Elect. Waves Appl., to appear.

17. Chew, W.C. (1988) A quick way to approximate a Sommerfeld-Weyl type integral, IEEE Trans. Antennas Propagat. AP-36 (11): 1654-1657.

18. Bahl, I.J. and Stuchly, S.S. (1979) Effect of finite size of ground plane on the impedance of a monopole immersed in a lossy medium, Electronic Letters 15 (22): 728-729.
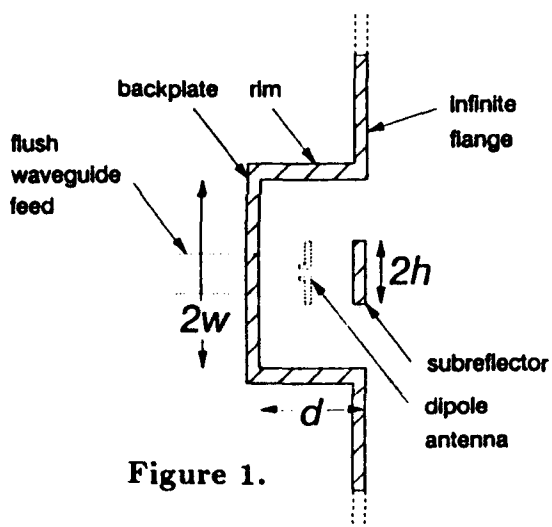
Figure 1.
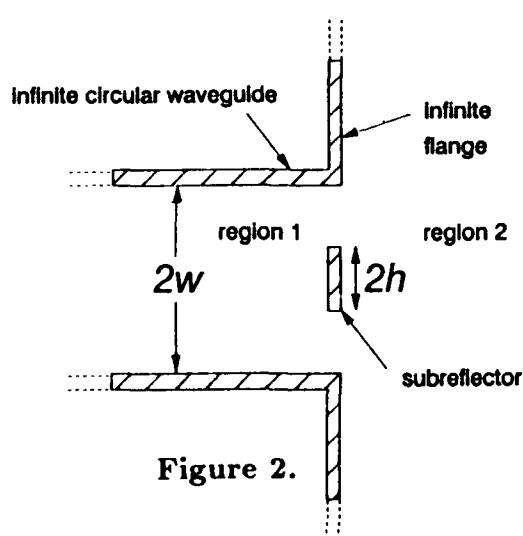
Figure 2.

Figure 1. Model of a three-dimensional short backfire antenna with circular symmetry and an infinite ground plane. The excitations considered are thin wire dipole antennas or flush waveguide feeds.

Figure 2. Geometry of a canonical waveguide discontinuity problem. The incident field emanates from an infinitely long circular waveguide of radius w and impinges on a thin subreflector of radius h.
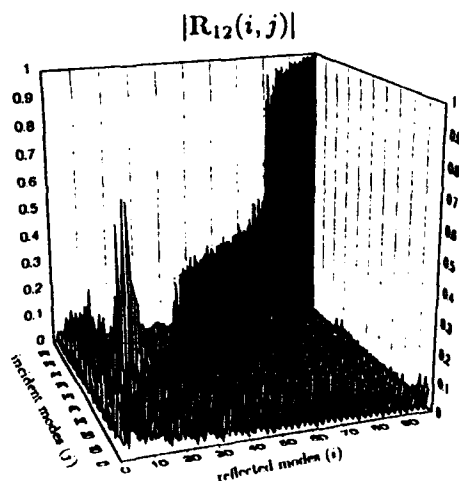
Figure 3.
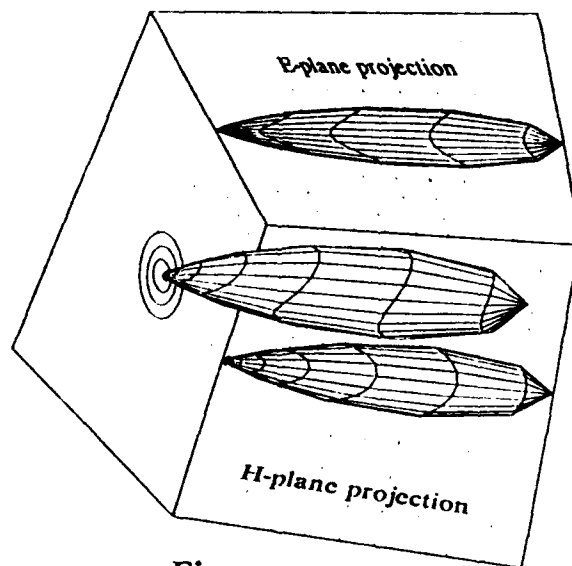
Figure 4.

Figure 3. Magnitude of generalized reflection operator ($\overline{\mathbf{R}}_{12n}$) for the electric field with $n=1$. The rows represent the reflected modes for each incident mode (columns).

Figure 4. Computed radiation pattern in three dimensions, projections on E- and H-plane, and contour levels. The excitation model was a half-wavelength wire dipole.
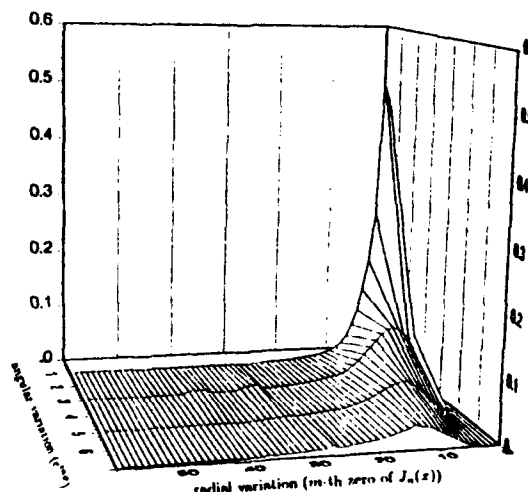
Figure 5. Magnitude of the excited TE mode amplitudes, e_n'. A half-wavelength wire dipole is in an infinitely long circular waveguide of radius $w = 1.114\ \lambda$.

13
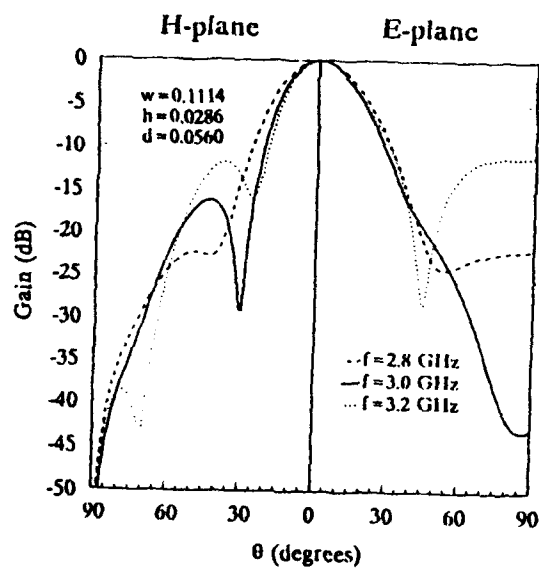
Figure 6. Computed E- and H-plane radiation patterns versus θ for varying frequencies ($w = 0.1114$, $h = 0.0286$, $d = 0.056$, and $d_o = \frac{1}{2}d$).
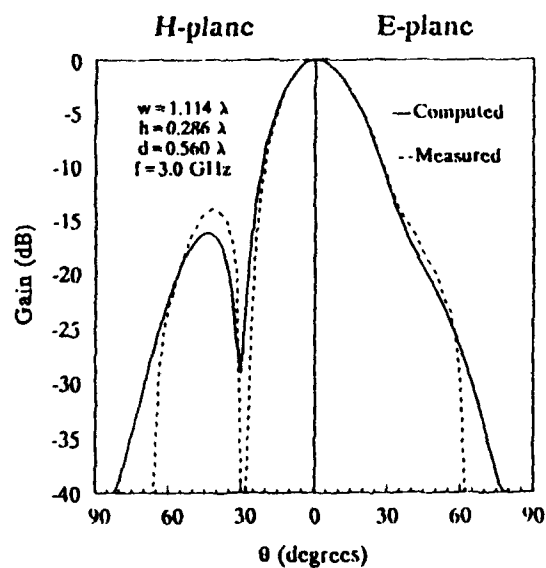
Figure 7. Measured and computed far-field pattern at 3 GHz ($w = 1.114$ λ, $h = 0.286$ λ, $d = 0.56$ λ, and $d_o = \frac{1}{2}d$)

ANTENNA AND RADOME TECHNOLOGY ON MULTIPLE LANDING SYSTEM (MLS) IN THE SOVIET UNION

H. Shnitkin
Norden Systems, Inc.
Norwalk, Connecticut 06856

ABSTRACT

As part of a joint-venture effort between Norden Systems, Inc. and AUSRIRE, a Soviet Electronic Ministry specializing in aircraft landing systems, several Norden engineers visited Leningrad, USSR, for a week in October 1990 to interface with Russian engineering experts to discuss the Soviet Microwave Landing System technology.

As a result, considerable knowledge as to the Russian state-of-the-art in phased arrays and microwave circuitry was gained together with Russian work habits, attitudes, and methods of operation.

This paper reports on this experience. Specifically, Russian engineering capability and performance achieved in the fields of slotted arrays, phased array technology, microstrip phase shifters, solid-state transmitters, radomes, transmission lines, and antenna test ranges are presented. In addition, their technical approach is discussed. Finally, a few words about the Russian language and the city of Leningrad are added.

1. INTRODUCTION

Norden systems decided to enter the competition for a Microwave Landing System (MLS). In an effort to enhance its expertise in microwave landing technology, Norden Systems decided to form a joint venture with AUSRIRE of

Leningrad, USSR. AUSRIRE possesses more than 20 years of design and test experience in the MLS field, placed several systems into operation at major airports (Moskow, Leningrad, et al), has performed flight tests on MLS, and is presently engaged in the fourth redesign of their equipment.

To obtain a first hand look at the equipment, test data and the engineers who produced it, a team of five Norden engineers and one manager visited AUSRIRE in Leningrad. Seven eight-hour joint working sessions were held, at which more than twenty Russian engineers, managers, public relations specialists, and test technicians participated.

Technology was discussed in great detail, test data and test methods were examined, and the AUSRIRE engineering and production facility was toured.

What follows are the high-lights of this meeting. Emphasis is on Russian technology; however, many interesting encounters typifying Russian behavior and Russian thinking will also be discussed. To round out the experience, I took the liberty of including a few comments about the city of Leningrad and the Russian language.

2. SPECIFIC TECHNOLOGY

In the course of the technical discussion a number of antenna and microwave technology subjects were touched, shedding light on Russian technical expertise. These will now be discussed in detail. Because of an agreement between Norden Systems and AUSRIRE design details may not be revealed.

2.1 Slotted Arrays

Standard waveguide for about 5 GHz is 48 mm x 24 mm O.D. Numerous slotted waveguide arrays of unequally spaced inclined slots in the narrow

waveguide wall had been designed, manufactured, and tested. These were shaped beam, travelling wave arrays, whose phase and amplitude distributions had been synthesized by the Woodward method. Slot phase requirement dictated slot position, while slot amplitude dictated slot inclination (See Figure 1). Tests in the presence of neighbors (mutual coupling) showed excellent beam shape correspondence, and achievement of the required 8 dB/deg beam slope at the normal to the aperture. Fabrication tolerances were very close. Interestingly, the Russians always machine the waveguide surface in the vicinity of each radiating slot in order to control aperture flatness and reduce waveguide wall thickness.
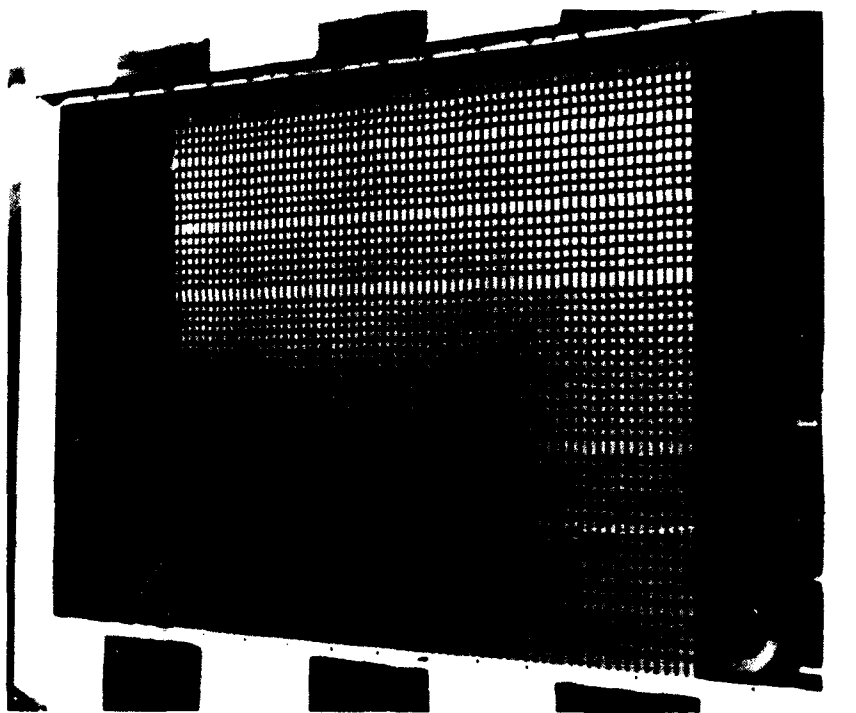
Figure 1. Slotted Array Aperture (ESP-MVL-AZ Antenna)

2.2 Phased Array Technology

The Russian engineers displayed an impressive knowledge of antenna theory, e.g. tapered distributions, phase tolerance, side lobes, scanning phase tapers, grating lobes, and thermal effects upon beam pointing accuracy. Emphasis in design and construction was on simplicity and ruggedness. A linear array of printed dipoles is shown in Figure 2. The corporate feed was simply a 70% efficient travelling wave waveguide with 64 coaxial probes. The latter were individually hand-adjusted to produce the correct illumination function. Phase alignment of aperture was achieved by mechanical adjustment of a coaxial trombone line-stretcher.
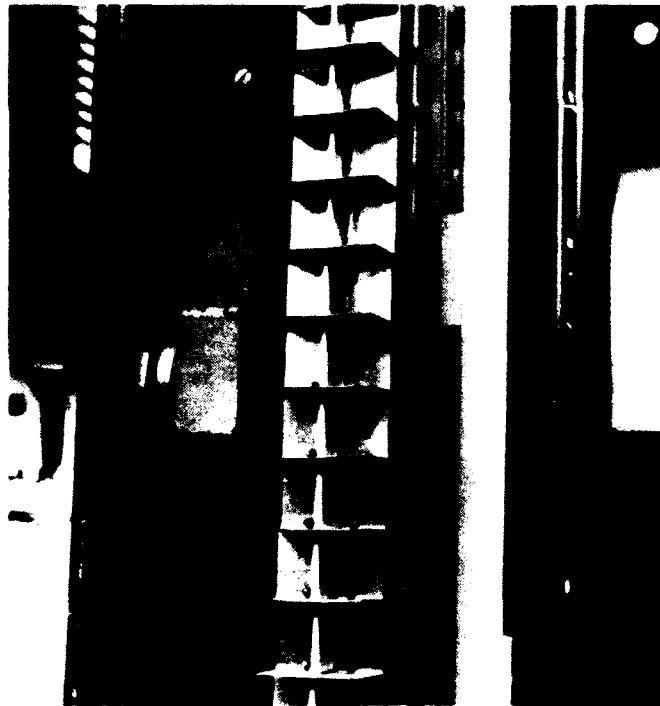
Figure 2. Linear Array of Dipoles

2.3 Microstrip Diode Phase Shifter

The production PIN-diode phase shifters were subcontracted to another electronic ministry about ten years ago. Due to lack of funds the design has not been up-dated since. PIN diodes are used to switch line lengths for 4-bit phase shifting. Strip conductors are welded and gold-plated while the substrate used is "Polycore Ceramic," a mixture of beryllium oxide and polystyrene with an ε of about 4. The standard power supplies are 48 Vdc and all microstrip packages are hermetically sealed.

After phase trimming, i.e. cutting of microstrip stubs, the phase accuracy over a 1.3% frequency band were a disappointing $\pm11°$, $\pm10°$, $\pm8°$, and $\pm7°$, MSB to LSB.

2.4 Medium Power Solid-State Transmitter

A 32-watt 5-GHz MLS transmitter consisted of three hybrid assemblies on polycore ceramic substrate. The output stage paralleled 16 two-watt chips with a set of input and output Wilkenson dividers. A bi-phase modulator, consisting of a 180° bit PIN-diode line switcher, was included.

2.5 Microwave Receiver

The MLS receiver is shown in Figure 3.

2.6 Radome

A 48-mm thick, seven-layer, radome, able to withstand a 50-meter/second wind was constructed out of epoxy/glass, ($\varepsilon = 5$) as shown in Figure 4. It has the unique feature of allowing hot air to be blown through it for deicing. This is accomplished by "waffling" a sheet of epoxy/glass to take the place of the
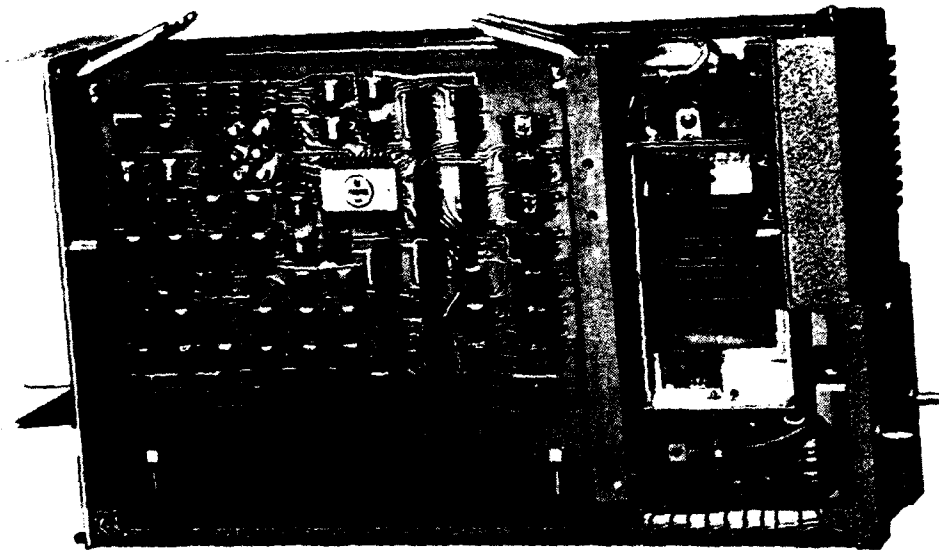
Receiver (as viewed from microprocessor circuit board)
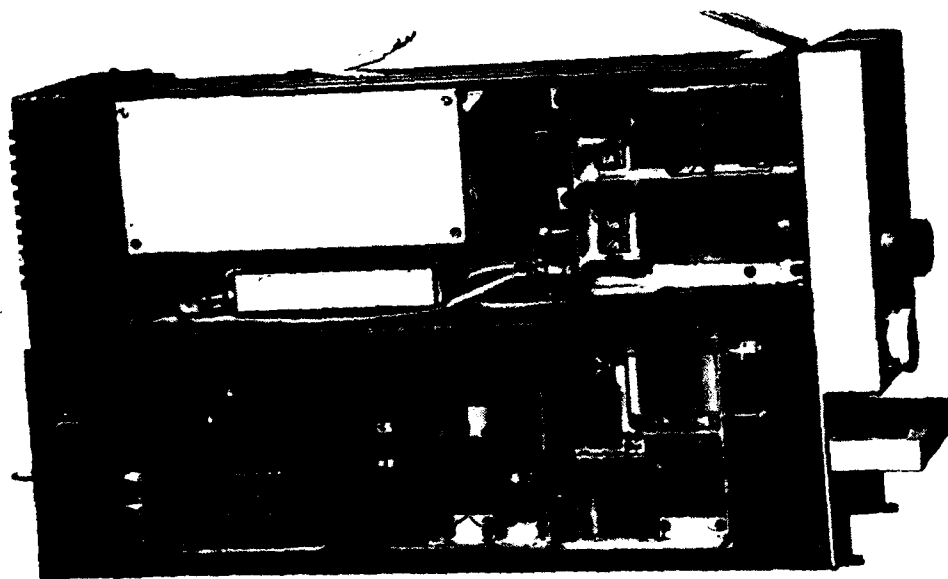
Receiver (as viewed from HF unit)

Figure 3. Microwave Receiver
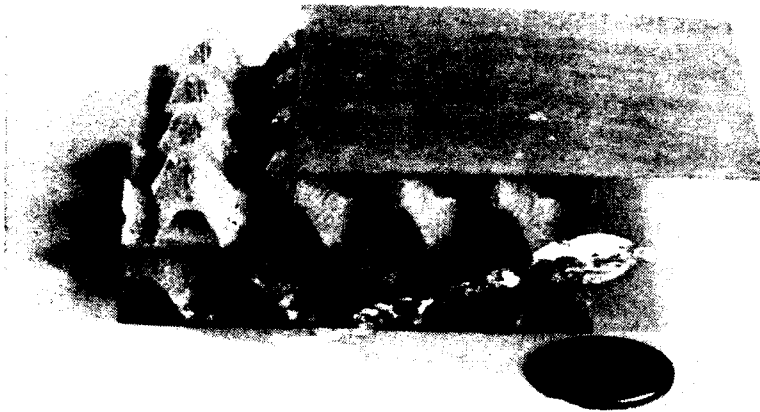
**Figure 4. Five Layer Radome with Provision for Hot Air Deicing**

customary honey-comb, low ε, section. Transmission losses were below 0.4 dB, one-way, up to 60 degrees incidence.

2.7   Waveguide/Coax Transition

A rugged end-on coaxial transition was shown. As all other Russian coaxial connectors, contrary to U.S. convention, the female connector carries the nut.

2.8   Antenna Test Range

Russian pattern ranges are not quite up to U.S. standards. Most patterns are plotted as voltages, giving poor accuracies beyond a 20-dB dynamic range. In
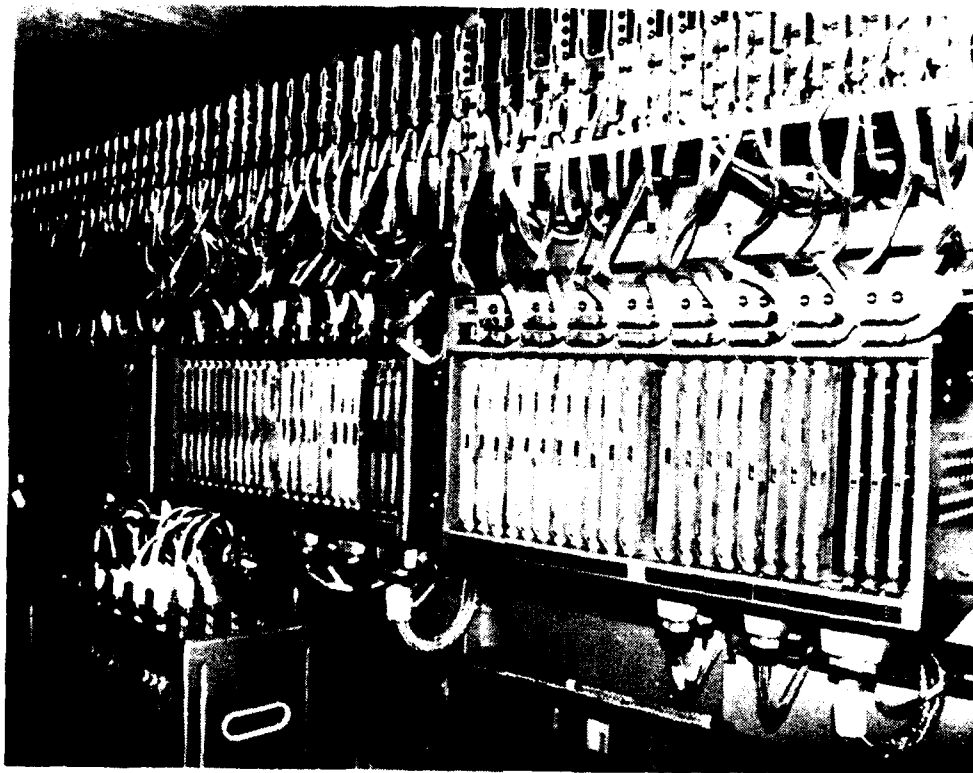
Figure 5. Beam Steering Computer Hardware

addition, pattern range reflections degrade measured sidelobe accuracies at -25 dB below beam peak.

2.9 Beam Steering Computer Hardware

As shown in Figure 5, beam steering was accomplished in a three tier beam steering computer. At the bottom is the main angle/phase computer, across the middle the calibration and beam position memory together with TTL command generators, and across the top the final drivers and self-test monitor circuits for the 4-bit diode phase shifters.
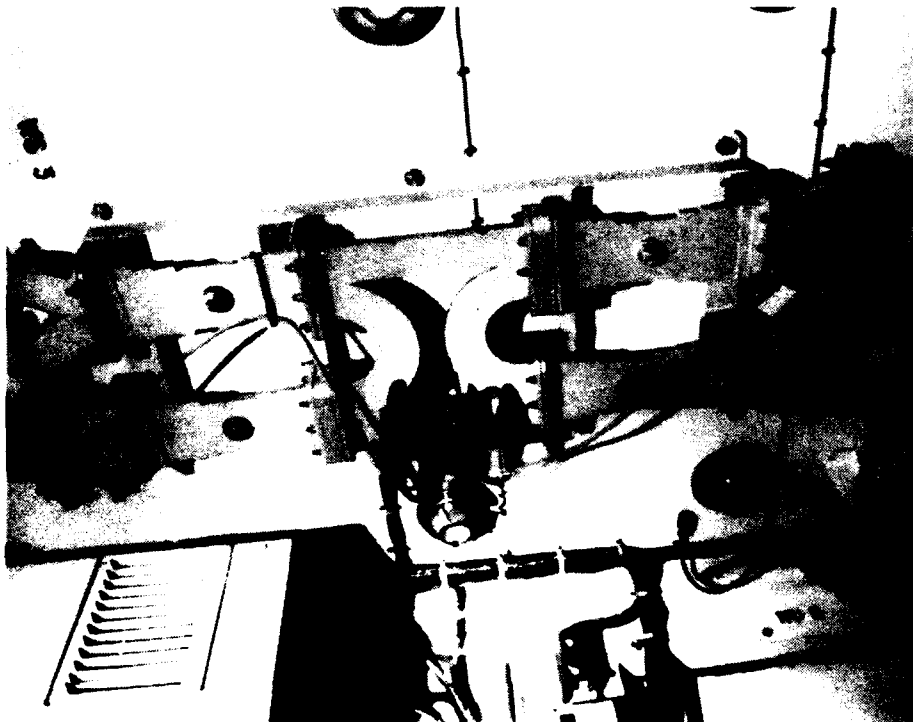
Figure 6. High Power Diode Switch

2.10 High-Power Waveguide Switches

As shown in Figure 6, four waveguide 3-dB couplers together with four diode shorting switches in waveguide, comprise a three-way high power RF switch with under one dB of insertion loss:

3. GENERAL TECHNICAL OBSERVATIONS

In my limited observations I conclude that Russian hardware technology is behind that of the U.S. While Russian scientists have an excellent grasp of the technology, can write good reports, make elaborate computations and prepare clear

fabrication drawings and explanatory diagrams, they are handicapped by the limited availability of hand-held calculators and of computers. The latter must be shared by queueing up for them. They, furthermore, believe in sturdy construction and accurate tolerances.

Since industry is not yet privatized, components must either be designed and manufactured by the ministry charged with producing the electronic system or be procured from another government ministry. This entails requests, approvals, and high (non-competitive) costs. Occasionally, the procurement may fail because of rejection by the subcontract ministry!

We were invited to a tour of their factory where several varieties of MLS antenna systems were in production. Again, the strength and ruggedness of their structural design was impressive.

Time estimating was performed in great detail to an accuracy of less than a minute. But some difficulty was encountered on items such as overhead, fee, profit, and cost of money, which are still foreign to them, and understandibly so.

Finally, don't forget the "fair-well gift." If you spend more than one day with the same person you will be presented with such a gift, small in value but large in sentiment. Obviously, a reciprocal gift is in order!

4. LANGUAGE

To learn to speak Russian is a momentous task, and not necessary. However, learning the Russian alphabet is easy and extremely useful, whether looking at technical data or at street signs. Examples: antenna = AHTEHHA, Leningrad = Λ E H И H Г P A Δ, (Λ E Δ), Pepsi = Π E Π CИ. Note that some

letters are Western, some Greek, and some Hebrew. (P.S., SHNITKIN = Ш H И T K И H)

Many technical terms have been borrowed directly from English, but their pronunciation is phonetic. Examples: dB = "deb-be," phase = "fah-ze." About 20% of Russian engineers speak English, and, of course, we had several interpreters with knowledge of technical terminology.

5. LENINGRAD

It certainly is a great city to visit, this "Venice-of-the-North." Among the various sights are the Hermitage art museum, the KIROV ballet at $45 a seat (INTOURIST controlled), beautiful subway stations at 5 Kopeks a ride (less than a penny), and the former palaces of the Czar and Katherine the Great. It's quite paradoxical that the German army destroyed these magnificent palaces in WWII while Stalin had them restored to their former splendor.

6. CONCLUSION

Three significant conclusions can be drawn from this interface with Russian antenna and electronics engineers:

a. Russian engineers are very talented but are restricted by their lack of sufficient tools.

b. Russian manufacturing quality is very good. Hardware is made to last.

c. Russian technology is several years behind that of the U.S.

FLUSH MOUNTED
FOUR-ARM SPIRAL
WITH
SHALLOW BACKUP CAVITY

JOSEPH KOBUS
and
DAVID MUNGER

Motorola Inc.
Government Electronics Group
Tactical Electronics Division
8220 E. Roosevelt
Scottsdale, Arizona 85252
Mail Drop R1210

MOTOROLA INC.

ABSTRACT

Performance is presented of a four-arm 3.7 inch diameter 2-18 GHz spiral antenna flush mounted on a ground plane containing a shallow recessed backup cavity. The spiral arms are precision etched on a .025 inch fiberglass substrate suspended .150 inch above the bottom of the cavity with a honeycomb spacer, forming a bonded assembly. Both measured and calculated sum and difference patterns, and gain are included. Calculated patterns are obtained, together with currents on the spiral arms, using a wire model Method of Moments simulation.

1 INTRODUCTION

Spiral antennas have considerable bandwidths but, owing to conventional absorbing cavities, are not low-profile or optimally efficient. Several investigators have studied low-profile one- and two-arm spirals placed near conducting ground planes ([4] - [11]). This paper describes a low profile four-arm spiral.

Previous work [4] reveals reduced on-axis circularity from the introduction of a ground plane immediately below a two-arm spiral. Mutual coupling between the arms and their images in the ground plane produces unwanted currents on the spiral arms beyond the first radiation zone. These currents radiate cross-polarized fields, degrading circularity of the principal polarization. The solution was to appropriately truncate the arms, resulting in a high-gain, low-profile, circularly polarized antenna, but with only a 20 percent bandwidth.

Wang and Tripp ([5] - [7]) reduced unwanted currents beyond the first radiation zone by using an outer ring of absorbing material, thereby obtaining usable patterns from 2 to 12 GHz. The outer radius of their spirals is 1.5 inches, with foam absorbing material extending from 1.25 to 1.75 inches, i.e., the overall diameter is 3.5 inches. Loading materials used in their models are always shaped into a half-inch wide annulus, half within and half outside the spiral edge. The thickness is trimmed to fit between the spiral and the ground plane or, in the very close configurations, it is mounted on top of the spiral.

2 MOTOROLA LOW PROFILE DESIGN

Figures 1 and 2 display the low profile hardware and details. The antenna cavity is .15 inch deep and 3.7 inches in diameter, similar to the hardware reported by Wang and Tripp. Copper tape was used to form the outer side wall. An annular ring with effective resistivity of 377 ohms per square is deposited on the inside (facing the cavity bottom) of the fiberglass substrate supporting the spiral. In addition, the spiral arms are terminated

(Figure 3) in a gradual, precise, and producible manner by etching resistors out of a resistor-conductor laminate. The laminate consists of a lossy film on the surface of the substrate and a copper layer over the film. Selective etching of the copper and the resistive film leaves the pattern of series resistors. This technique avoids volumetric absorbers or resistive paint.

A convenient way to terminate the arms with a large number of small printed circuit resistors is to use an Archimedean spiral, because its arms are tightly wound and uniformly wide. As it enters the series resistive termination zone (Figure 3), microwave energy traveling from the center feed along a spiral arm is partially radiated, segment by segment, and gradually dissipated, resistor by resistor, until so little remains that reflections from the end are negligible. Part of the microwave energy is also dissipated in the resistive annular sheet below the spiral. The annulus is electrically coupled through the substrate to the arms. The resistive sheet suppresses surface waves generated by close proximity of the fiberglass substrate to the cavity bottom. These surface waves, not included in the analytical studies, begin to appear just above 12 GHz and become progressively more troublesome as frequency increases.

A four-arm spiral has the characteristic that, regardless of its proximity to a ground plane or resistive termination of the arms, near on-axis circularity can be forced to be close to unity with a suitable broadband beam-forming network. Furthermore, both sum and difference patterns are available for direction finding applications. Useable difference patterns, however, are obtained only above 4 GHz for the present hardware. Approximately twice the diameter would be required to obtain difference patterns down to 2 GHz.

Motorola has combined the high frequency performance advantages of an equiangular spiral with the convenience of resistively terminated Archimedean arms. At a radius of approximately .6 inch, the Figure 3 spiral changes from equiangular in the inner region to

Archimedean in the outer region. At 2 GHz, the one wavelength circumference occurs at a radius of 0.94 inch, which is just inside the 1.18 inch inner radius of the termination. The termination consists of one-hundred 25 ohm resistors. The maximum spacing between any two feed input terminals in .065 inch, corresponding to one-tenth wavelength at 18 GHz.

3 METHOD OF MOMENTS MODEL

A wire model (Figure 4) was selected for calculation of patterns and gain of several spiral/ground plane antennas using MOM (Method of Moments [12]). Special codes were written to obtain the wire model geometries required for inputs to MOM. In addition to generating the spiral arms, the codes develop a square grid approximation to the desired resistive annulus. For the specific parameters pertinent to Figure 4, this results in a square for the small inner contour, while a smoother approximation to a circle occurs for the outer contour.

As used here, MOM computations can yield useful engineering approximations to measured characteristics. However, discrepancies are expected for the following reasons. The spirals tested are printed on a finite thickness dielectric substrate. Surface waves resulting from placement of the spiral/substrate in close proximity to a ground plane are not included in the computed results. The spirals tested are not pure Archimedean, but rather a combination of equiangular and Archimedean, whereas computations are made for a strictly Archimedean geometry. The tested spiral arm widths are self-complementary, whereas the wire model only approximates the arm width by using an equivalent wire diameter. The tested configuration has the spiral in the same plane as a surrounding ground-plane, which is 17 inches in diameter, and has a 3.7 inch diameter cavity ground plane at .15 inch behind the aperture ground plane. The computer model, on the other hand, consists of a spiral placed an equivalent distance in front of an infinite

5

ground plane. Edge diffraction from the finite ground plane is therefore not included in the calculations, nor is the effect of truncating the lower plane with cavity walls.

Finally, the computer model consists of wire segment approximations to the spiral arms. The wire segments subtend constant angles from the center of the aperture, with longest segments near the truncated arm ends and shortest segments close to the feed. This is a desirable arrangement for modeling accuracy, since higher frequency currents radiate closer to the feed. Forcing all segments to be the shortest length determined by the highest frequency would result in an unacceptably large number of segments for data processing. Arm terminations are modeled as series resistors in the wire segments. The computer model employed 50 resistors of 50 ohms each per arm, at an angular spacing of 7.5 degrees, while the tested hardware used 100 resistors of 25 ohms each at an angular spacing of 3.75 degrees. Therefore, the termination on the model is not as smooth as on the hardware, but the total length of termination and resistance per unit length are equivalent.

In spite of the difference between the hardware and computer model, measured patterns and gain are in good agreement with MOM calculations from 2 to 12 GHz. Above 12 GHz, surface waves are caused by the presence of the dielectric substrate in proximity to the ground plane, resulting in significant differences between measured and completed results.

4 RADIATION PATTERNS AND CURRENTS

Figure 5 displays the test instrumentation. Magnitude and phase of patterns for each of the four arms of a given spiral are recorded through 50 ohm .047 inch diameter cables extending in a bundle from the feed to the rear of the mounting fixture, as shown in Figure 1. Unused cables are terminated in 50 ohm loads. For low-profile spirals, the 4-cable bundle passes through a hole in the bottom of the backup cavity and is grounded

6

to it with silver epoxy. The miniature cable connectors are firmly clamped to the test fixture at the rear, where special flexible cables are attached to complete the test paths. Horizontal and vertical polarization links in the anechoic chamber are phase and amplitude calibrated with standard gain horns. Data is recorded separately for each polarization and stored in a DEC MICROVAX II computer. Patterns are recorded for tower head rotations of 0, 45, 90, 180 and 270 degrees, at 1 GHz frequency steps from 2 to 18 GHz. Swept boresight gain is also obtained for sample points at every 80 MHz.

Sum and difference patterns are generated from measured amplitude and phase patterns of the four arms, assuming a perfect combining network, i.e., it is perfectly isolating and introduces no amplitude or phase imbalances. Combiner voltage amplitude weights are all 0.5; phase weights are shown in Figure 6.

Both an absorber backed spiral and two cavity backed versions of the same design were evaluated, one with the resistive annulus and one without. Only patterns for the cavity backed model with the resistive annulus for suppression of surface waves are presented.

Sum patterns are presented in Figures 7-12. Measured pattern agreement with calculated patterns is good in the 2-12 GHz range; gain is typically within 1 to 2 DB of theoretical. Starting at 12 GHz, measured gain falls short of expectations and patterns become excessively flattened. As discussed in Section 5.0, it is believed that this is due to the presence of surface waves. The resistive annulus thus does not entirely remove surface waves. Modification of the annulus parameters could produce better results.

Refer now to the difference patterns shown in Figures 13-17. Agreement with theory is good above 4 GHz; gain levels are again within 1-2 DB of calculations through 18 GHz. In contrast to sum patterns, difference pattern peaks occur at 30 to 60 degrees from broadside and are therefore enhanced by surface waves at higher frequencies, a circumstance consistent with broadening of individual arm element patterns. Difference

7

patterns from 2 to 4 GHz display somewhat lower gain than calculated, probably because the aperture is so small that the active region on the spiral extends farther out than calculated, and into the series resistors terminating the arms.

Calculated current magnitudes on each arm for the sum and difference patterns are presented in Figures 18 and 19. All frequencies are not given, but currents at omitted frequencies are similar. Notice the large reduction of magnitude for the difference mode current at 2 GHz, explaining the substantial loss of gain displayed at 2 GHz in Figure 13. Sum mode currents, on the other hand, are all generally higher for the cavity backed spiral than for the free space spiral, even though the cavity backed spiral has a resistive annulus.

5 PERFORMANCE DISCUSSION AND CONCLUSIONS

Significant gain enhancement (Figure 20) over a conventional absorber-backed antenna is generally produced in the 7-18 GHz band for a four-arm 2-18 GHz quasi-Archimedean spiral with a shallow backup cavity.

Pattern distortions become progressively larger at frequencies above 12 GHz, a phenomenon very likely resulting from surface waves created by close proximity of the conducting cavity bottom to the substrate supporting the spiral. At lower frequencies, the .025 inch substrate is electrically too thin for a noticeable effect. As frequency increases, more power is transferred to these modes. The distortions are similar to those described by Baily and Crosswell [3] for the radiation patterns of a slot. They report substantial pattern distortion from surface waves caused by a finite dielectric slab covering the radiating aperture. The resistive annulus below the spiral yields smoother but nonetheless broad flat patterns between 12 and 18 GHz. A smaller diameter annulus could produce greater low frequency gain while maintaining, or even improving, surface wave mode suppression at higher frequencies.

Another piece of evidence suggesting that surface waves are responsible for these pattern distortions is furnished by return loss measurements (Figure 21). Notice the considerable high frequency increase in mismatch loss extending from approximately 14 to 18 GHz in curve (b), for the case with no resistive annulus. Introduction of the annulus yields curve (c), a considerably better match from 14 to 18 GHz. Although evidence is admittedly indirect, it appears the resistive annulus absorbs a substantial part of the surface wave power.

REFERENCES

1   Rumsey, V.H. (1957) Frequency Independent Antennas, IRE National Convention Record, pt.1, pp. 114-118.

2   Balanis, C.A. (1982) Antenna Theory Analysis and Design, Harper & Row, New York, pp. 414-416.

3   Baily, M.C., and Crosswell, W.F. (1967) Pattern Measurements of Slot Radiators in Dielectric Coated Metal Plates, IEEE Trans. Ants. Prop., pp. 824-826.

4   Nakano, H., Nogami, K., Arai, S., Mimaki, H. and Yamauchi, J. (1986) IEEE Trans. Ants. Prop., Vol. 34, pp. 791-796.

5   Tripp, V.K. and Wang, J.J.H. (1990) Multi-Octave Microstrip Antennas, Antenna Applications Symposium, Robert Allerton Park, Univ. of IL, Urbana, IL.

6   Wang, J.J.H., and Tripp, V.K. (1991) Design of Multioctave Spiral-Mode Microstrip Antennas, IEEE Trans. Ants. Prop., Vol. 39, pp. 332-335.

7   Nordwall, B.D. (1991) Georgia Tech Researchers Develop Thin Conformal Aircraft Antenna, Aviation Week and Space Technology, April, pp. 66-67.

8   Waller, R.W., and Mayes, P.E. (1985) Development of a Flush-Mounted Equangular Spiral Antenna, Electromagnetics Lab Report No. 85-3, Univ. of IL, Urbana, Il.

9   Drewniak, J., Mayes, P., Tanner, D., and Waller, R. (1986) A Log Spiral, Radiating Line Antenna, IEEE AP-S International Symposium Digest, Philadelphia, p. 773.

10   Drewniak, J.L., and Mayes, P.E. (1989) ANSERLIN: A Broad-Band, Low-Profile, Circularly Polarized Antenna, IEEE Trans. Ant. Prop., Vol. 37, pp. 281-288.

11   Wood, C. (1979) Curved Microstrip Lines as Compact Wideband Circularly Polarized Antennas, IEEE Microwaves, Optics and Acoustics, Vol. 3, pp. 5-13.

12   Burke, G.J., and Pogio, A.J. (1981) Numerical Electromagnetics Code (NEC)-Method of Moments, Lawrence Livermore Laboratory Report UCID 18834, Navel Electronic Systems Command (NAVELEX 3041), Navel Ocean Systems Center, San Diego, Calif. 92152.

INCHES
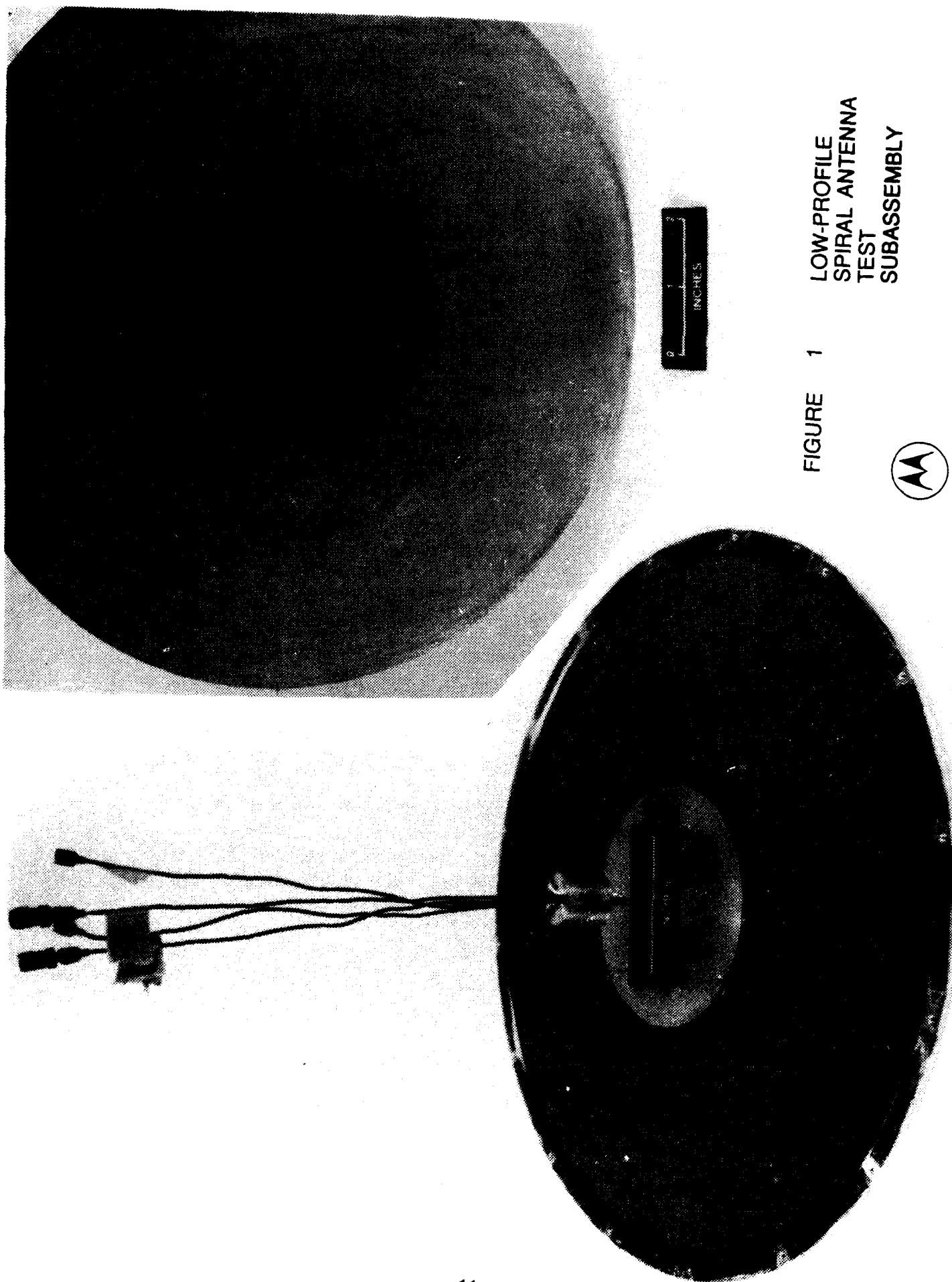
FIGURE 1

LOW-PROFILE
SPIRAL ANTENNA
TEST
SUBASSEMBLY

MOTOROLA INC.

11

HEXCEL
HRH-10-1/8-3.0
HONEYCOMB SPACER

.025 INCH

FOUR-ARM
SPIRAL ETCHED ON
RESISTOR CONDUCTOR LAMINATE

.150 INCH

3.70 INCH DIAMETER GROUNDPLANE

.125 INCH

377 OHMS PER SQUARE
TREATMENT
.716 I.D. X 3.58 O.D.

HEXCEL
HRH - 10 - 1/8 - 3.0
HONEY COMB SPACER

FOUR-ARM
SPIRAL AND COPPER GROUNDPLANE

3.70 INCH DIAMETER
GROUNDPLANE

TEST FIXTURE GROUNDPLANE
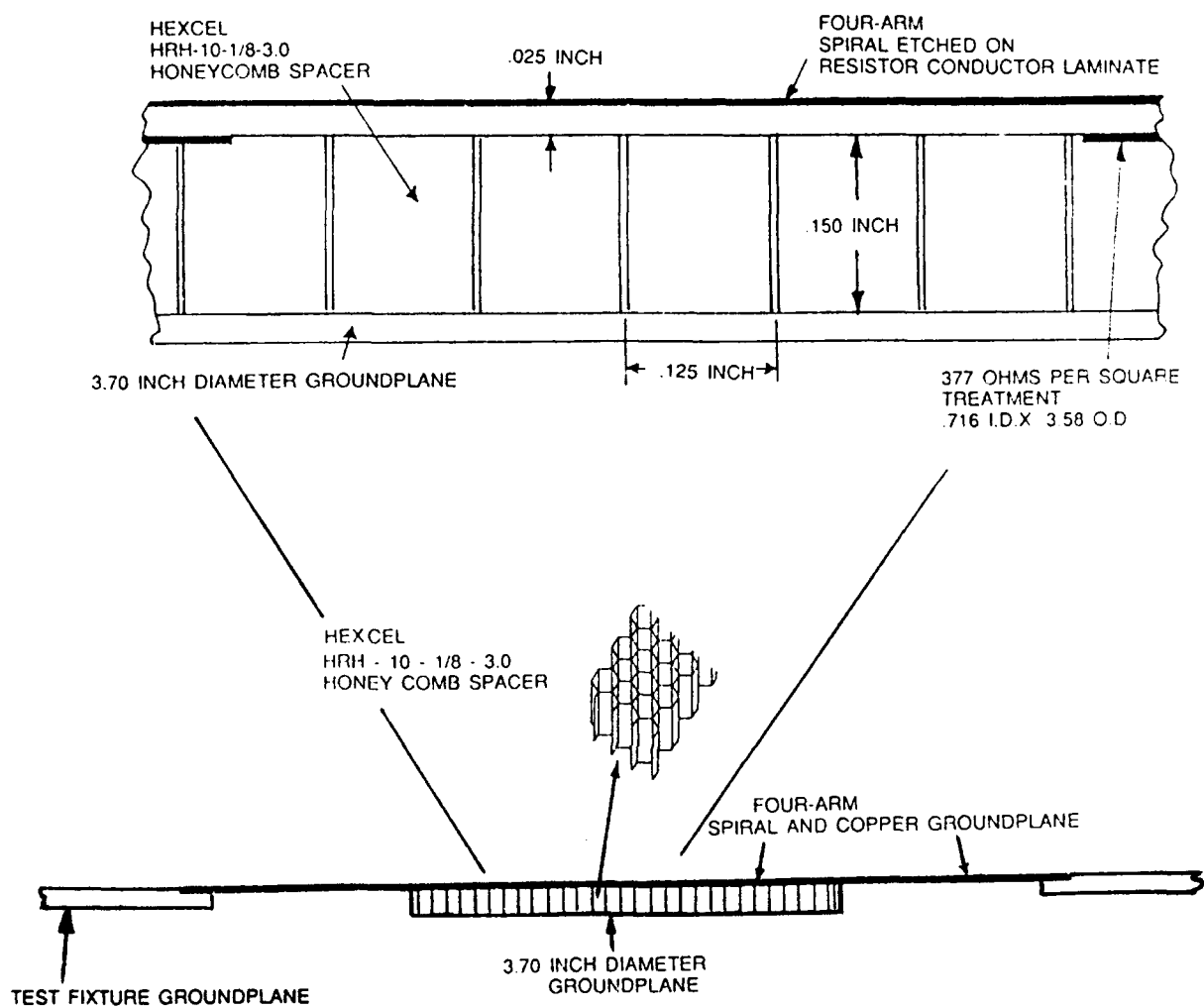
FIGURE   2   LOW PROFILE SPIRAL ANTENNA ELEVATION VIEW

12

Labels in figure:
SPIRAL COPPER ARM
100 OHMS PER SQUARE
W
DELPHI
DEL
RESISTOR CONDUCTOR LAMINATE
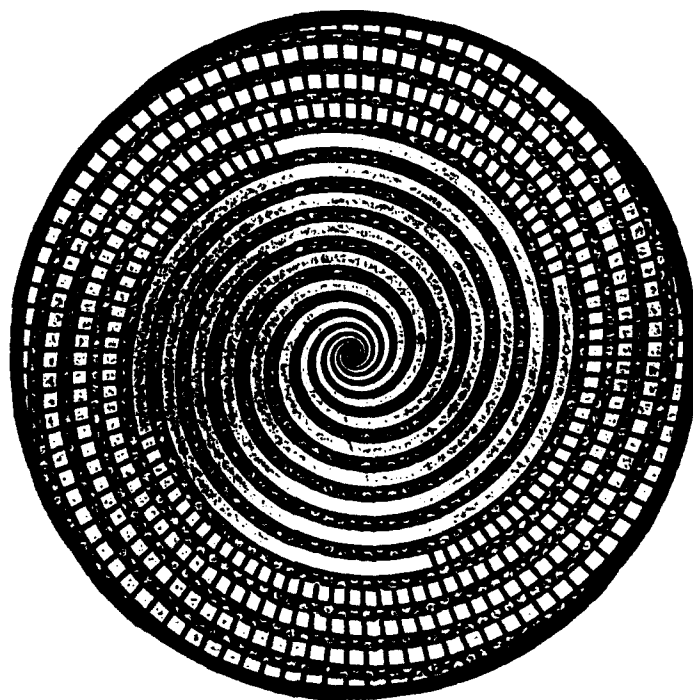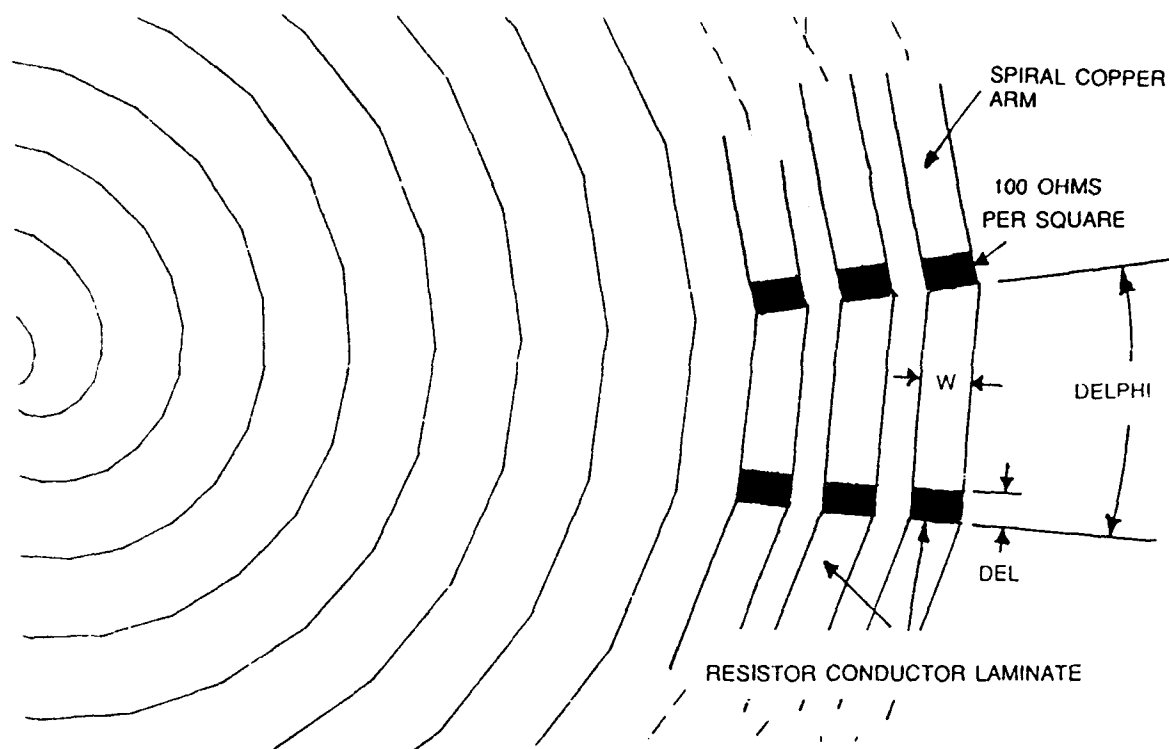
FIGURE 3   RESISTIVE TERMINATION OF SPIRAL ARMS

Y

X

SPIRAL LOCATED
ABOVE INFINITE
GROUND PLANE

RESISTIVELY
TERMINATED ARMS

Z

θ

Y

φ

X

377 OHMS PER SQUARE
.716 I.D. X 3.58 O.D.
SHEET LOCATED
    BELOW SPIRAL

Z=0 ON INFINITE GROUND PLANE
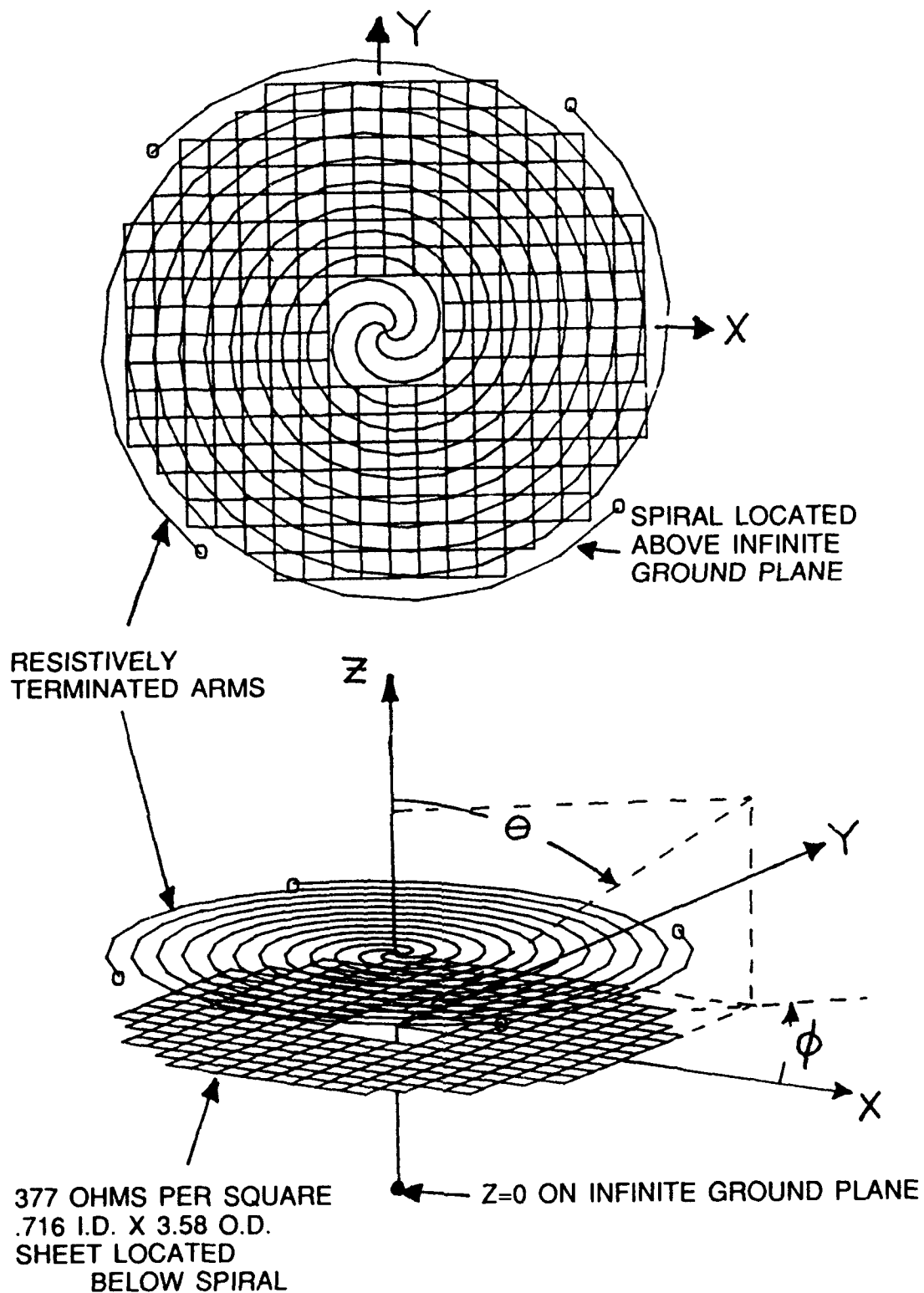
FIGURE   4   WIRE MODEL REPRESENTATION OF FOUR-ARM ARCHIMEDEAN
SPIRAL AND RESISTIVE SHEET FOR METHOD OF MOMENTS
CALCULATION OF CURRENTS AND RADIATION PATTERNS

14
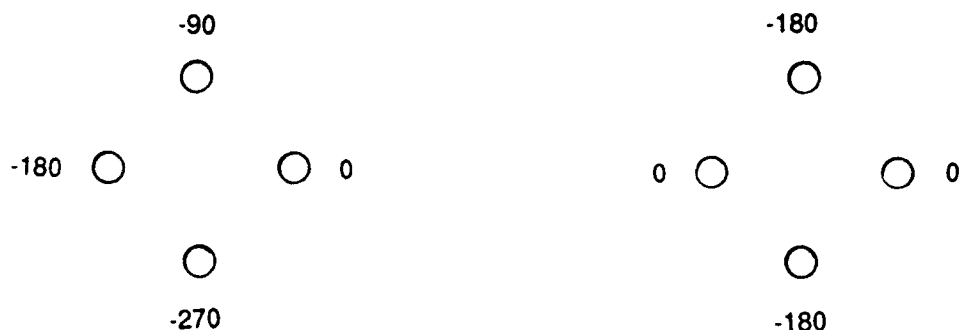
SUM PATTERN
PHASE WEIGHTS

DIFFERENCE PATTERN
PHASE WEIGHTS

FIGURE 6   COMBINER PHASE WEIGHTS USED TO DETERMINE
EXPECTED PATTERNS FROM FIELD PATTERNS OF
INDIVIDUAL SPIRAL ARMS
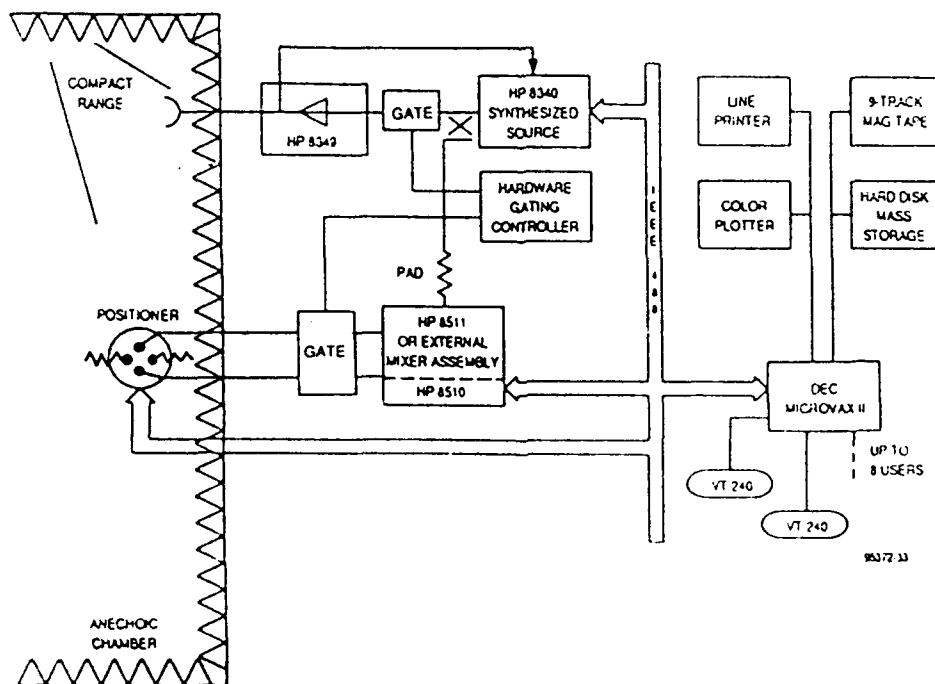
FIGURE 5   BLOCK DIAGRAM OF INSTRUMENTATION FOR RECORDING
AMPLITUDE AND PHASE OF FIELD PATTERNS OF EACH OF
FOUR SPIRAL ARMS

15
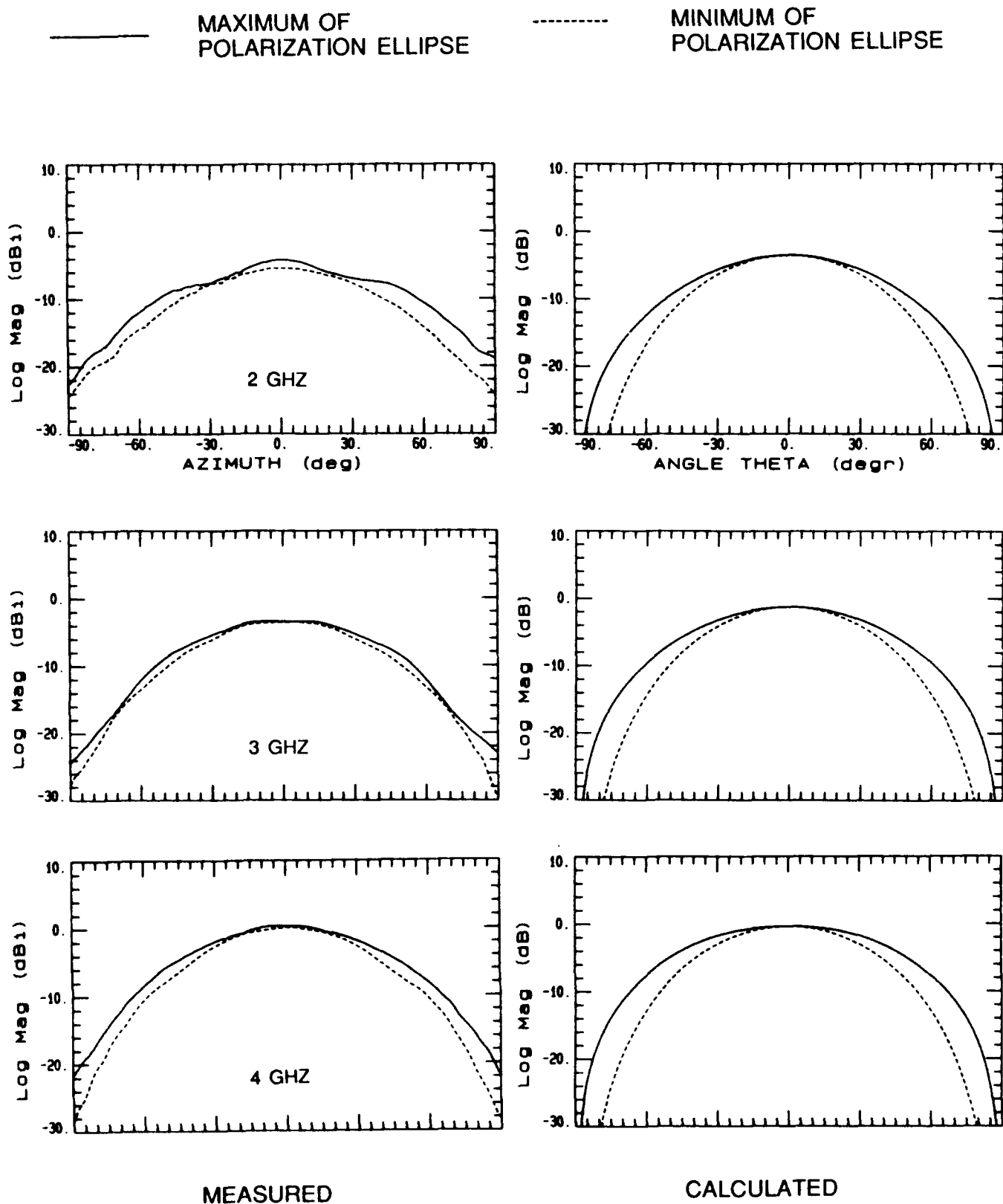
FIGURE 7   RADIATION SUM (DBLI) PATTERNS OF FOUR-ARM SPIRAL
AT 2, 3, AND 4 GHz FOR PHI = 0 DEGREES

MAXIMUM OF POLARIZATION ELLIPSE · · · · · · · · MINIMUM OF POLARIZATION ELLIPSE
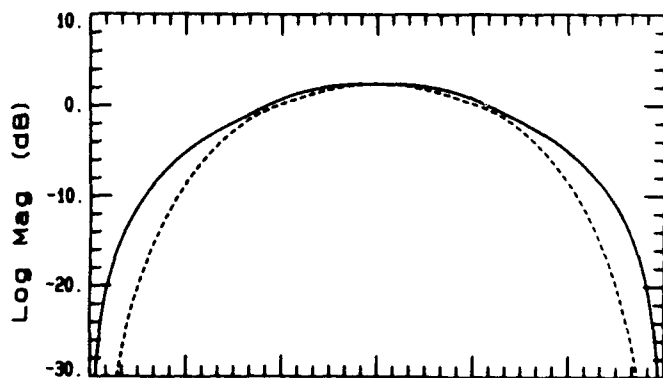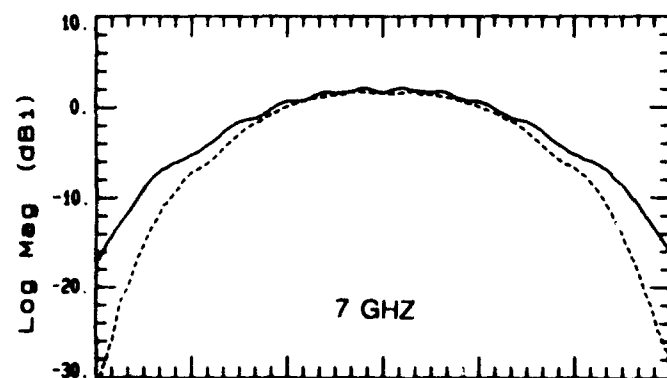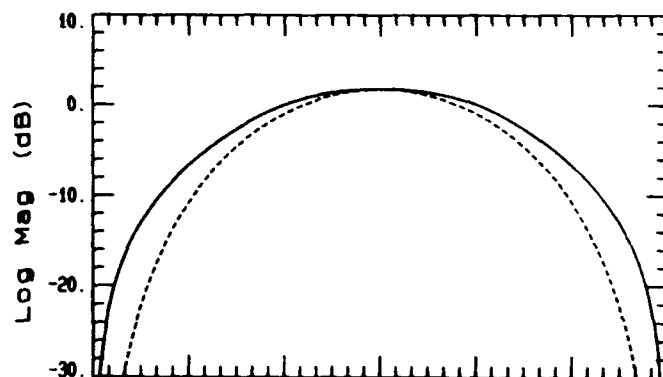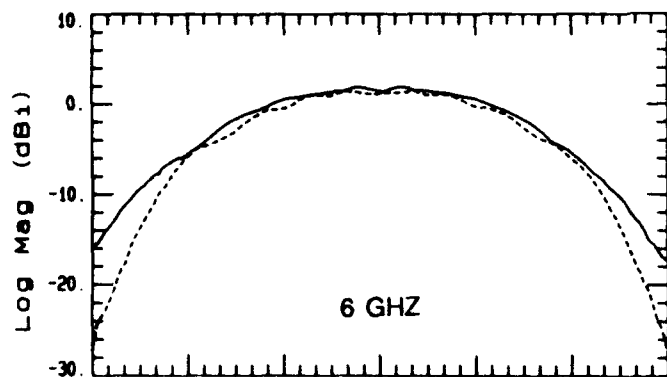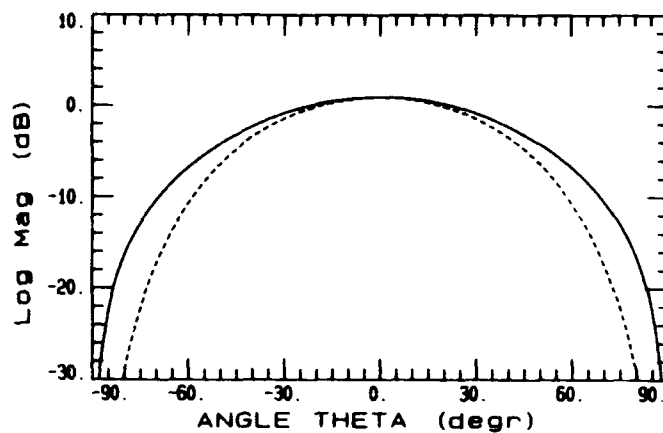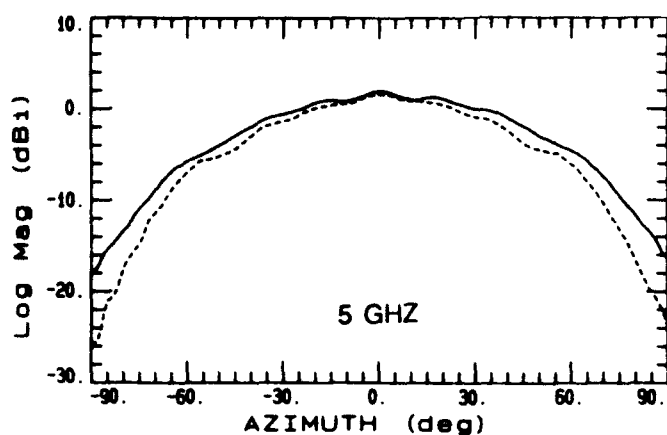
MEASURED   CALCULATED

FIGURE   8   RADIATION SUM (DBLI) PATTERNS OF FOUR-ARM SPIRAL
                    AT 5, 6, AND 7 GHz   FOR PHI = 0 DEGREES

17
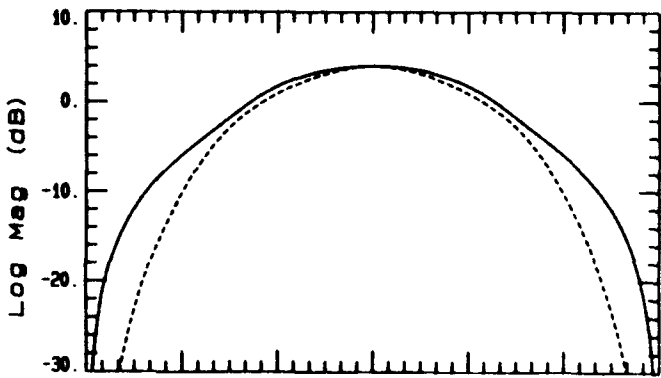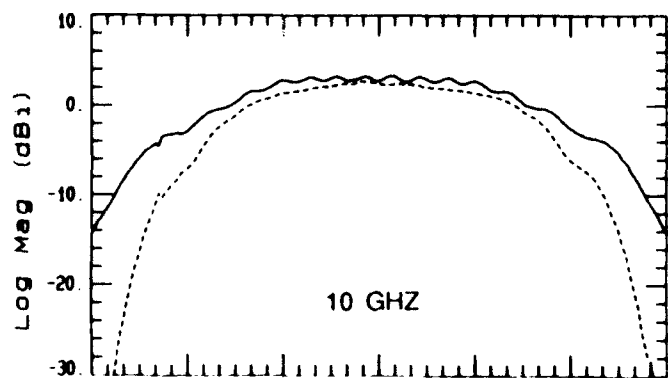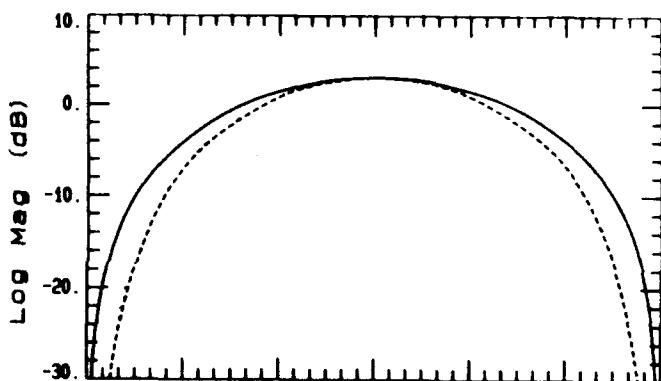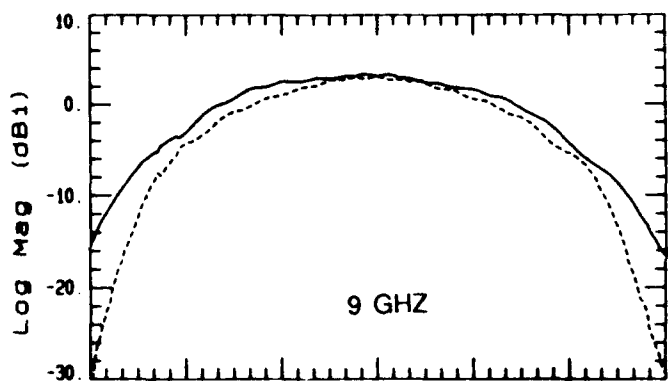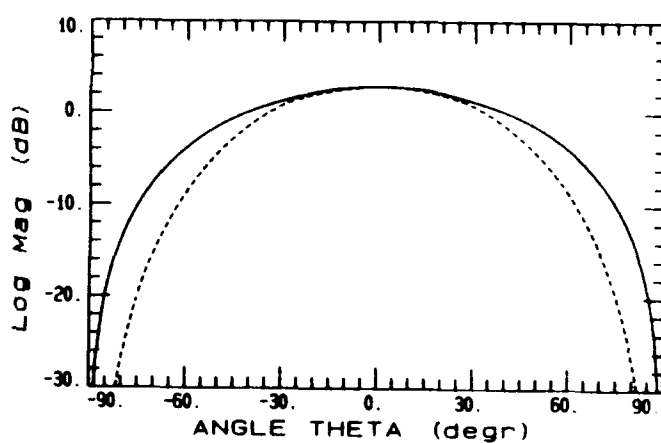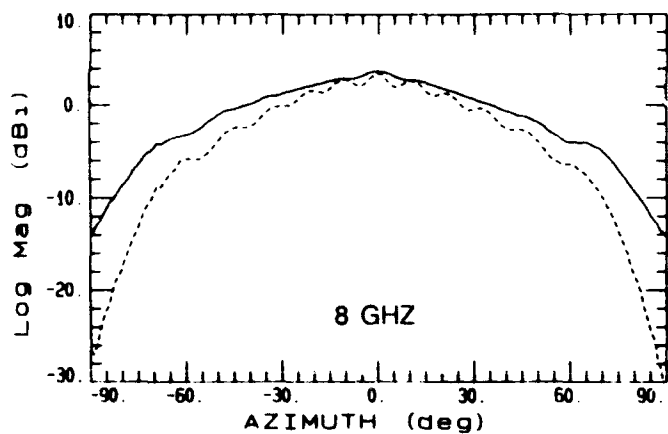
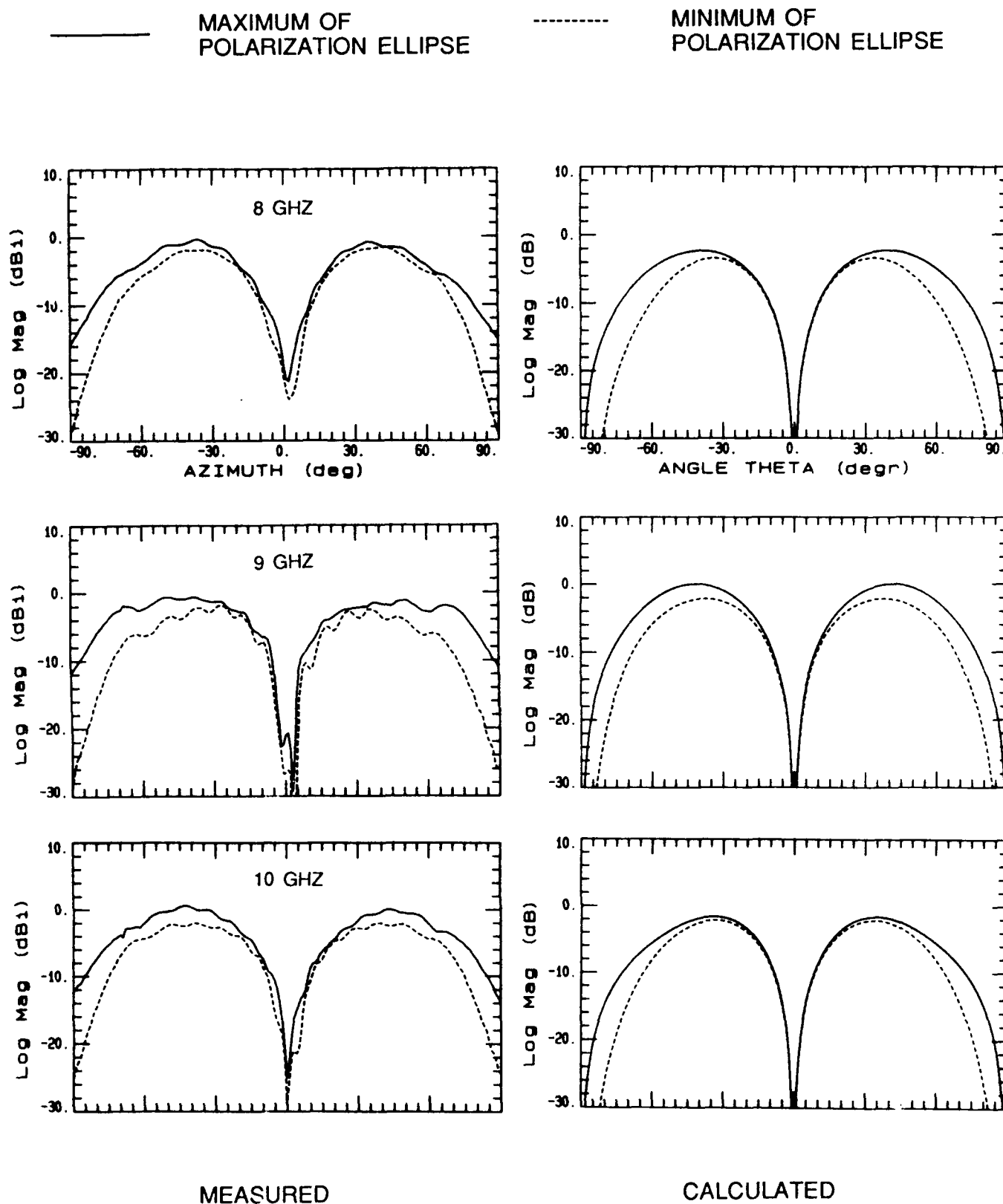FIGURE 9 RADIATION SUM (DBLI) PATTERNS OF FOUR-ARM SPIRAL AT 8, 9, AND 10 GHz FOR PHI = 0 DEGREES
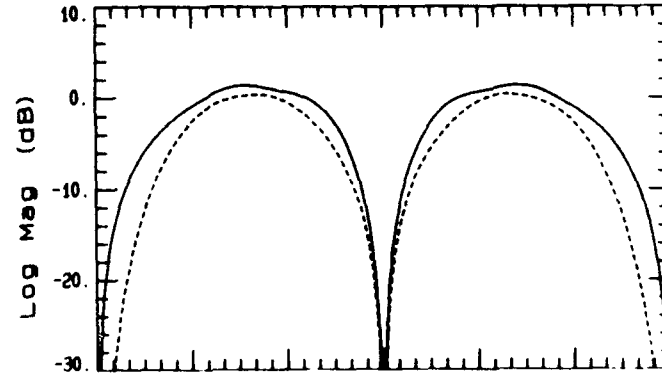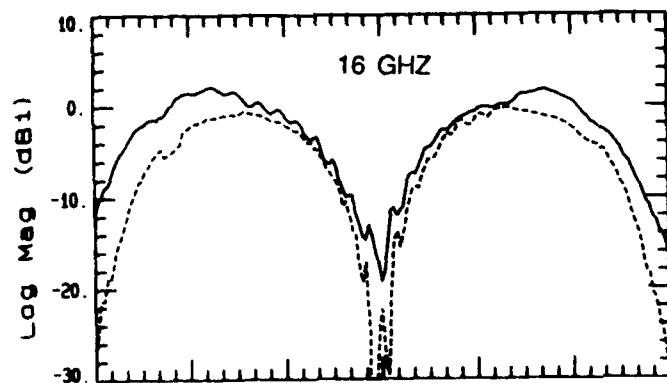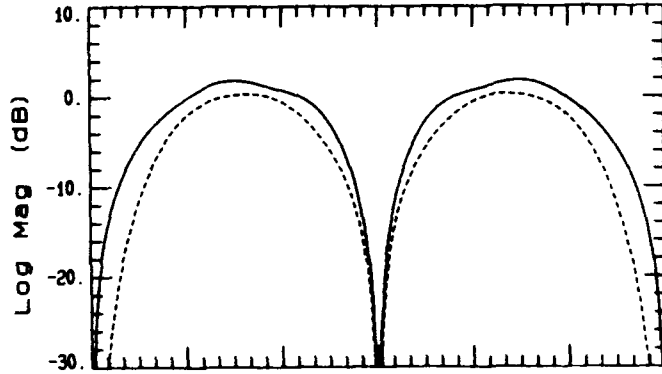
MEASURED   CALCULATED
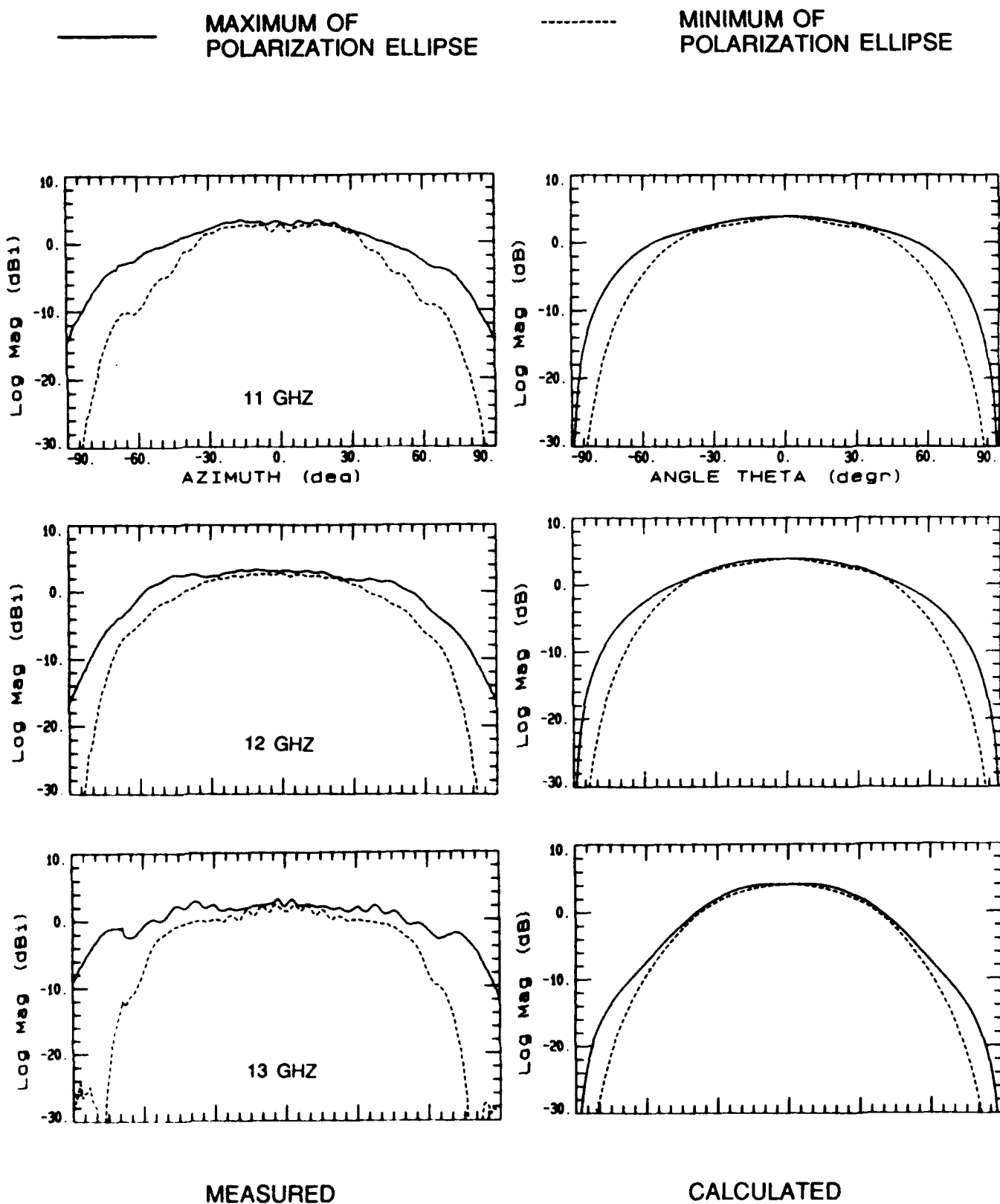
FIGURE   10   RADIATION SUM (DBLI) PATTERNS OF FOUR-ARM SPIRAL
                  AT 11, 12, AND 13 GHz FOR PHI = 0 DEGREES

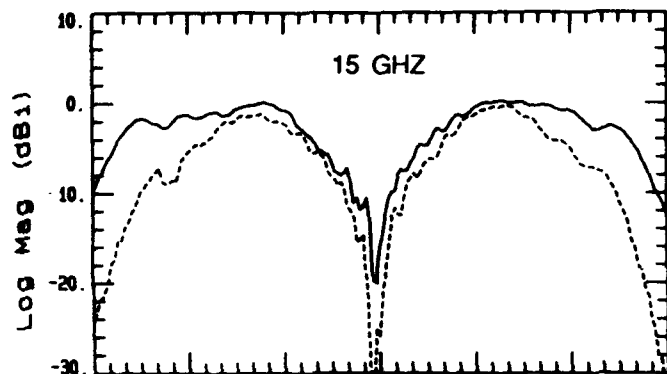MEASURED   CALCULATED
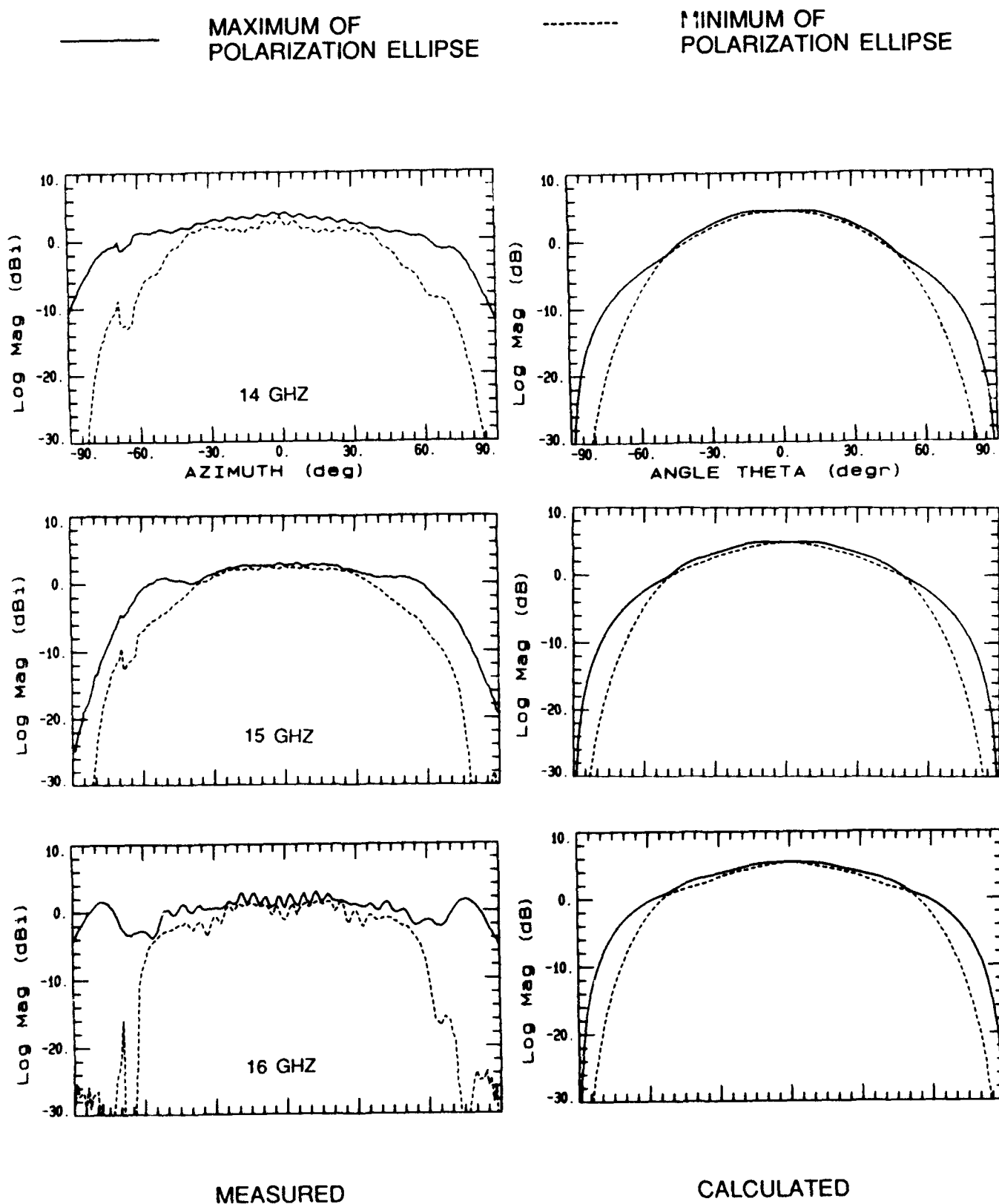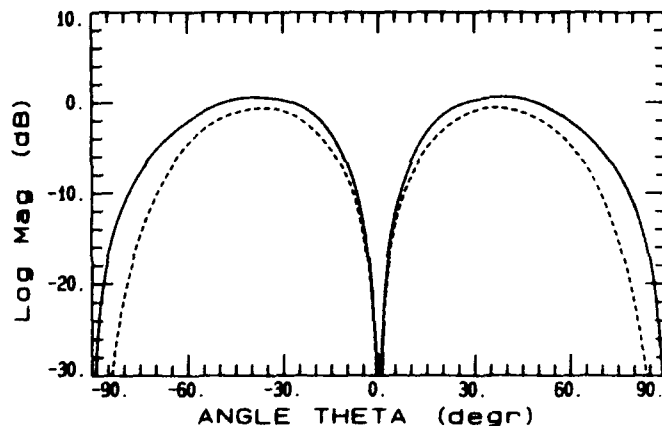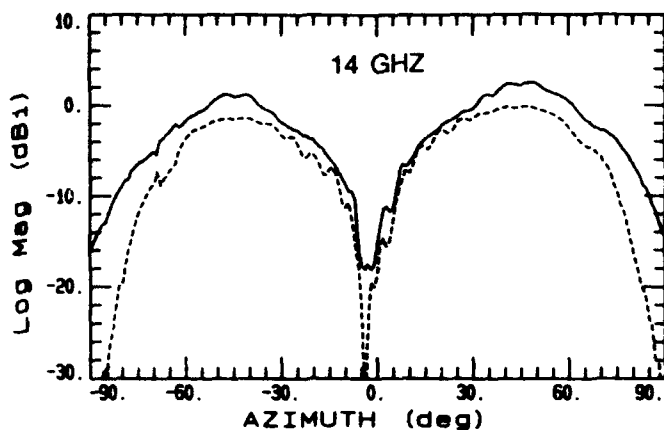
FIGURE   11   RADIATION SUM (DBLI) PATTERNS OF FOUR-ARM SPIRAL
                  AT 14, 15, AND 16   GHz FOR PHI = 0 DEGREES

MAXIMUM OF
POLARIZATION ELLIPSE

MINIMUM OF
POLARIZATION ELLIPSE

17 GHZ

18 GHZ

MEASURED

CALCULATED
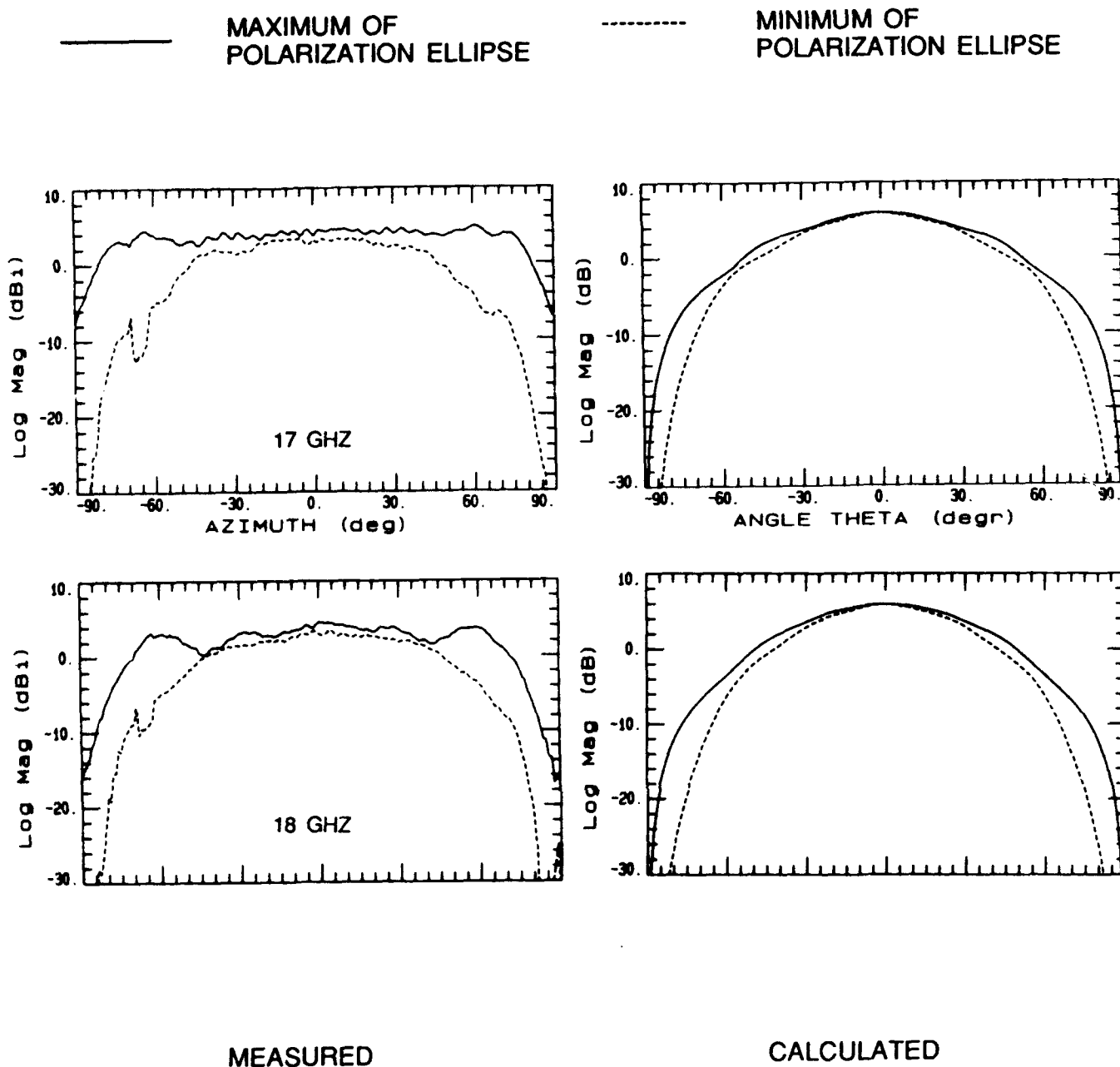
FIGURE   12   RADIATION SUM (DBLI) PATTERNS OF FOUR-ARM SPIRAL
AT 17 AND 18 GHz   FOR PHI = 0 DEGREES

21
394

MAXIMUM OF
POLARIZATION ELLIPSE   MINIMUM OF
                              POLARIZATION ELLIPSE

MEASURED   CALCULATED
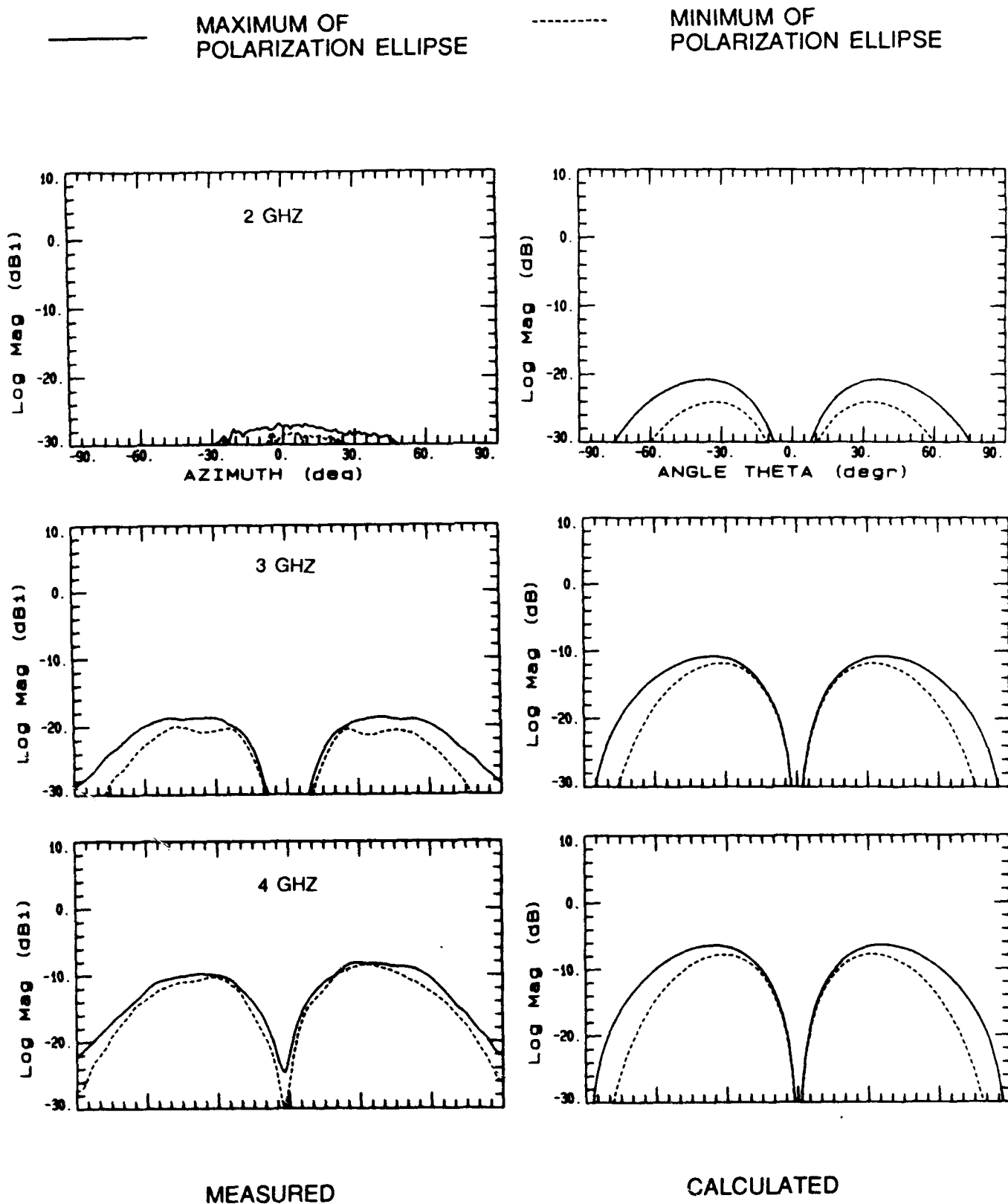
FIGURE   13   RADIATION DIFFERENCE (DBLI) PATTERNS OF FOUR-
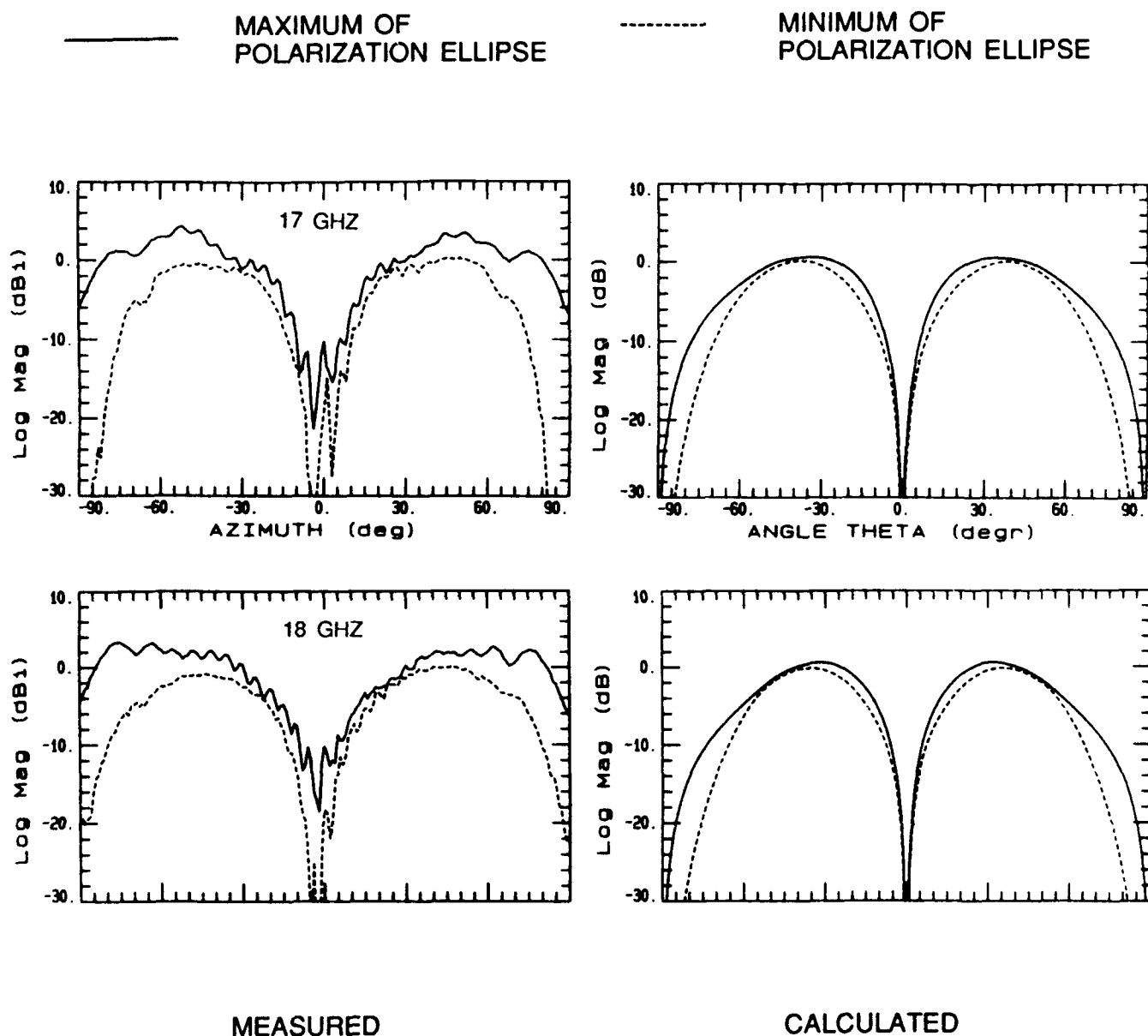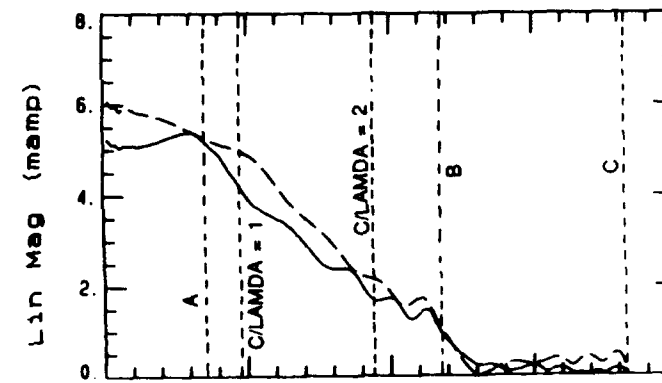   ARM SPIRAL AT 2, 3, AND 4 GHz FOR PHI = 0 DEGREES

22

MEASURED

CALCULATED
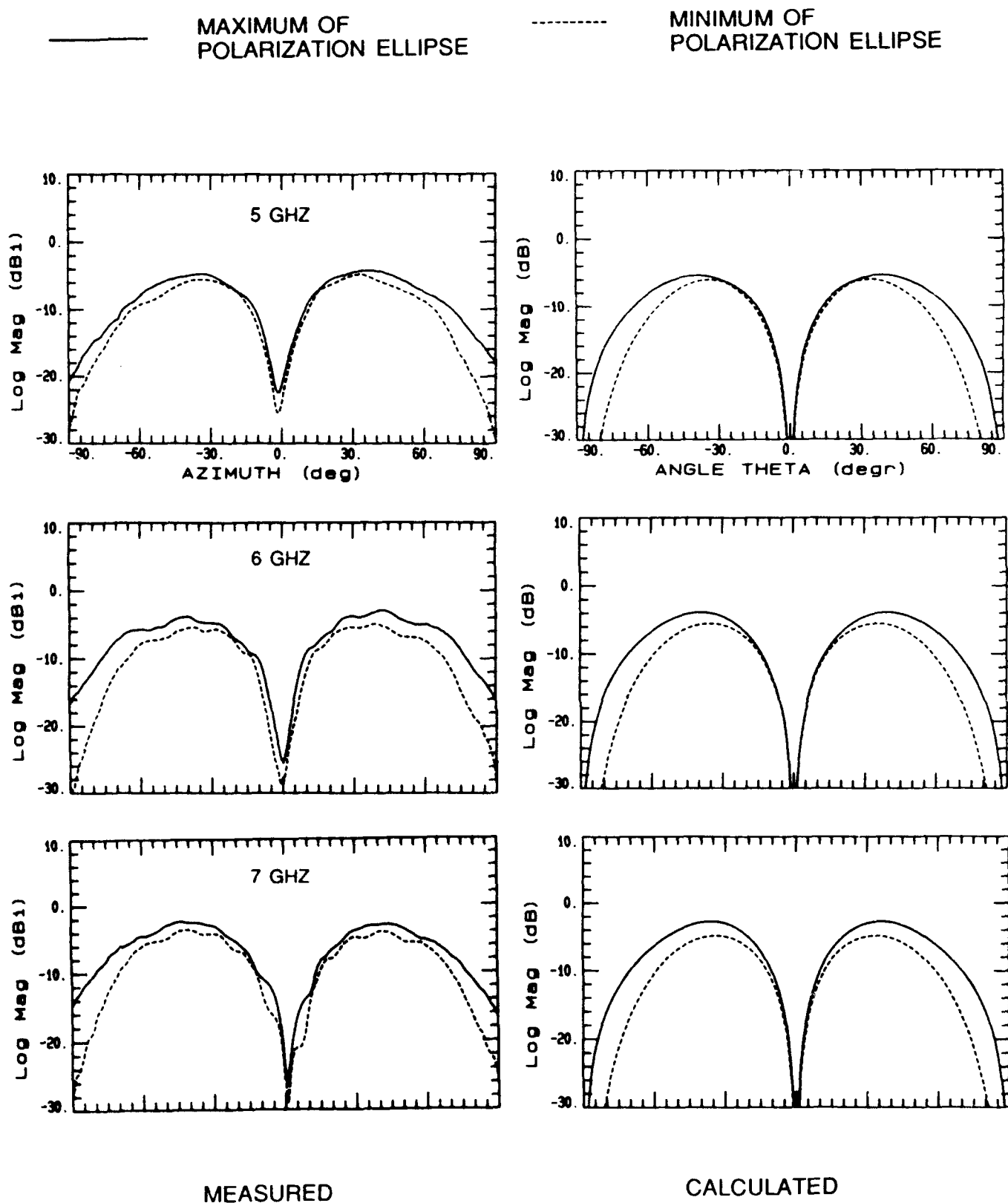
FIGURE   14   RADIATION DIFFERENCE (DBLI) PATTERNS OF FOUR-
ARM SPIRAL AT 5, 6, AND 7 GHz FOR PHI = 0 DEGREES

MEASURED

CALCULATED

FIGURE 15 RADIATION DIFFERENCE (DBLI) PATTERNS OF FOUR-ARM SPIRAL AT 8, 9, AND 10 GHz FOR PHI = 0 DEGREES

MEASURED   CALCULATED

FIGURE 16   RADIATION DIFFERENCE (DBLI) PATTERNS OF FOUR-
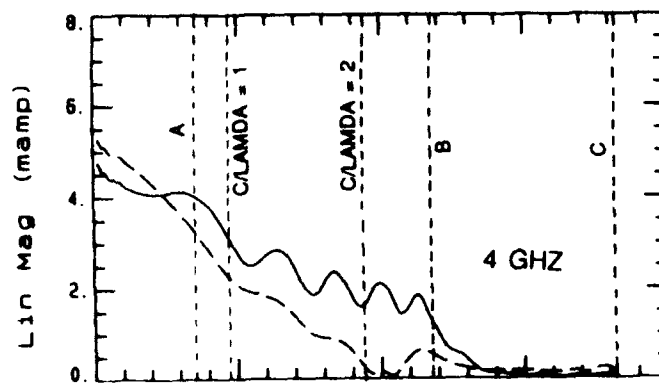   ARM SPIRAL AT 14, 15, AND 16 GHz FOR PHI = 0 DEGREES

MAXIMUM OF ········· MINIMUM OF
POLARIZATION ELLIPSE POLARIZATION ELLIPSE

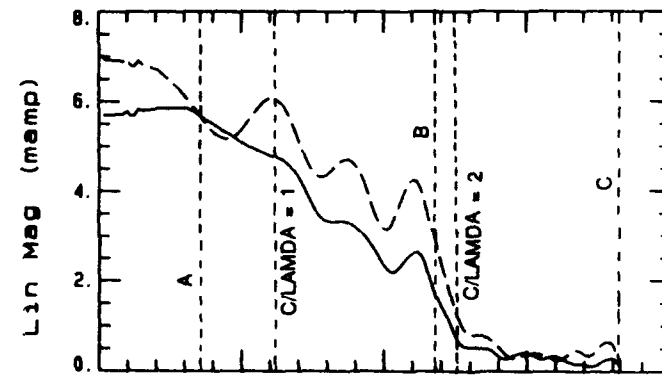MEASURED   CALCULATED
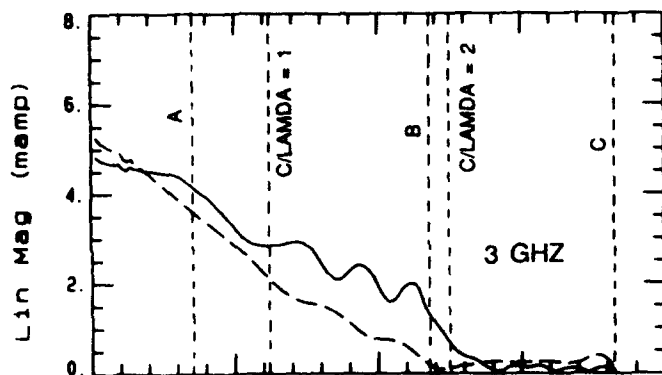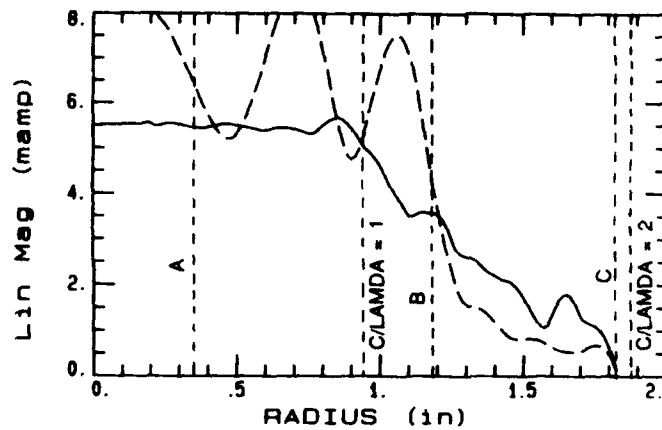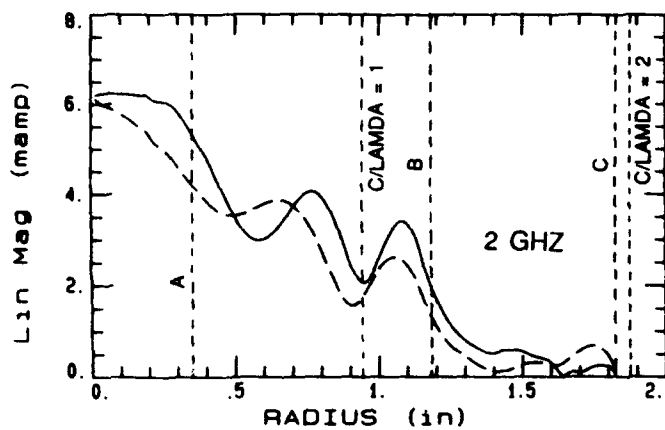
FIGURE   17   RADIATION DIFFERENCE (DBLI) PATTERNS OF FOUR-
                     ARM SPIRAL AT   17 AND 18 GHz FOR PHI = 0 DEGREES

- - - FREE SPACE SPIRAL WITH
ARM LOADING ONLY

SUM

DIFFERENCE

A = START OF   B =   START OF SERIES RESISTOR LOADING ON
RESISTIVE SHEET   SPIRAL ARMS
     C =   END OF ARM LOADING AND RESISTIVE SHEET
FIGURE   18   CALCULATED SUM AND DIFFERENCE PATTERN
                      MODE CURRENT MAGNITUDES ON EACH ARM OF
                      FOUR-ARM ARCHIMEDEAN SPIRAL AT 2, 3, AND 4 GHZ

27
400

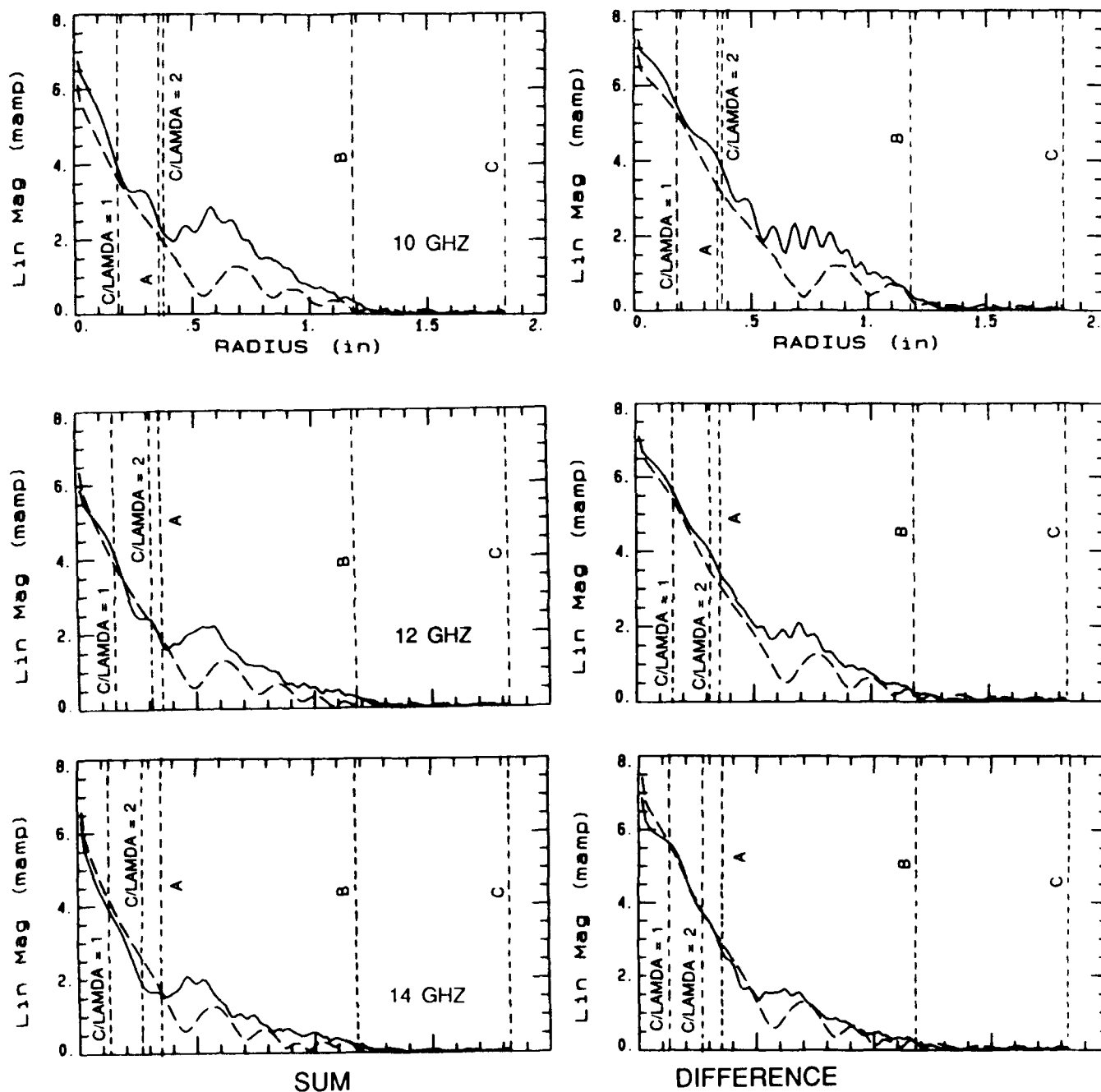--- FREE SPACE SPIRAL WITH ARM LOADING ONLY

SUM

DIFFERENCE

A = START OF RESISTIVE SHEET

B = START OF SERIES RESISTOR LOADING ON SPIRAL ARMS

C = END OF ARM LOADING AND RESISTIVE SHEET

FIGURE 19

CALCULATED SUM AND DIFFERENCE PATTERN MODE CURRENT MAGNITUDES ON EACH ARM OF FOUR-ARM ARCHIMEDEAN SPIRAL AT 10, 12, AND 14 GHz
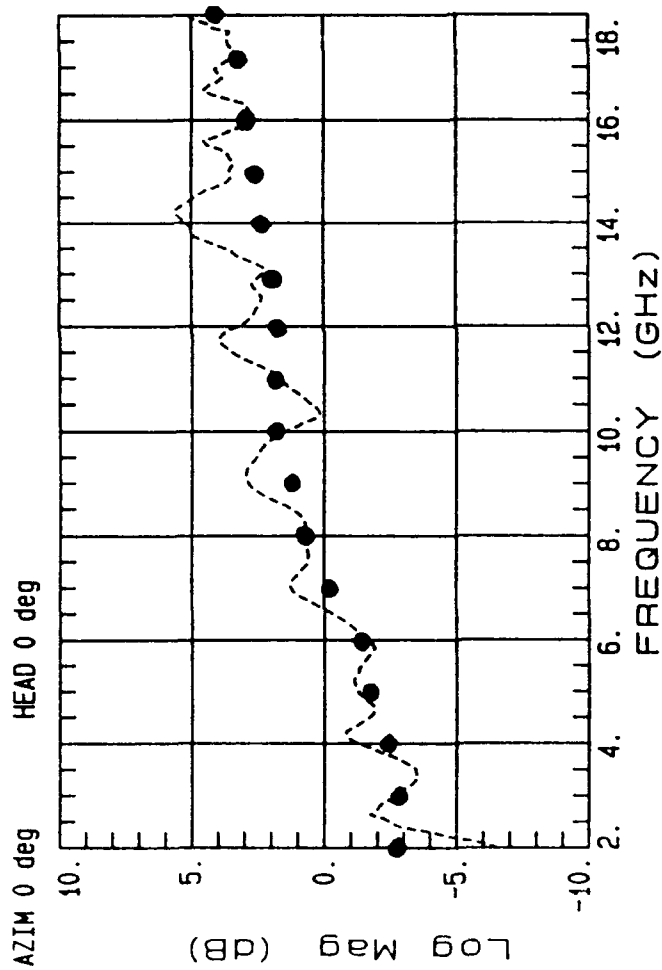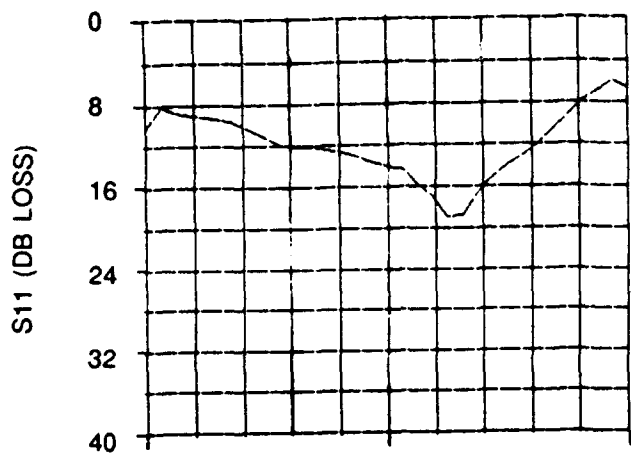
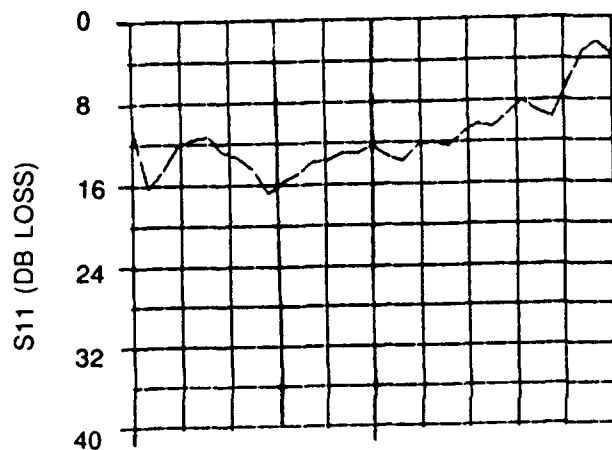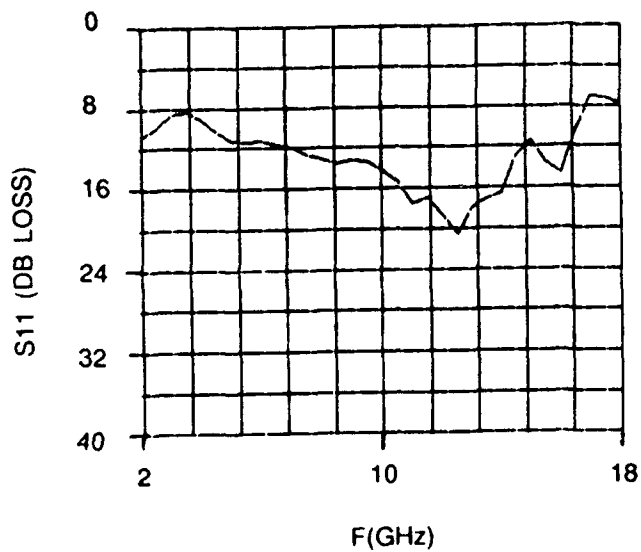CALCULATED FROM METHOD
OF MOMENTS CODE

FIGURE 20   GAIN OF CAVITY-BACKED LOW-PROFILE SPIRAL RELATIVE TO
SPIRAL OVER ABSORBER

(a) SPIRAL OVER ABSORBER

(b) SPIRAL ABOVE BOTTOM OF CONDUCTING CAVITY

(c) SPIRAL AND SURFACE WAVE MODE SUPPRESSOR ABOVE BOTTOM OF CONDUCTING CAVITY

FIGURE   21   RETURN LOSS AT INPUT CABLE TO EACH SPIRAL ARM UNCORRECTED FOR CABLE LOSS

30

SPIRAL ANTENNAS OVER CLOSELY SPACED GROUND

D. W. Smith and P. E. Mayes
Electromagnetics Laboratory
University of Illinois
Urbana, Illinois

Abstract - This paper describes recent progress in the development of low-profile radiating-line antennas for producing circularly polarized (CP) radiation. Numerical studies of annular sector and log-spiral radiating lines have been done using a numerical electromagnetics code based upon patch basis functions. The relative merits and performance limitations of annular sector (ANSERLIN), one-arm spirals, and two-arm spirals are discussed. The results of the computer simulations were used to choose parameters for some physical models. Measured performance is close to that predicted by computer. A limiting factor in achieving large bandwidths has been traced to the rather slow rate of attenuation of the current along the antenna arm. Much greater bandwidth has been obtained by placing an absorbing film between the radiating arm and the ground plane.

1. Introduction: radiating-line antennas

Dyson[1] showed that essentially frequency-independent behavior could be achieved with the equiangular spiral antenna. The primary result of this work was a broadband CP antenna with radiation into

both hemispheres. In an attempt to obtain unidirectional radiation, Carrel[2] examined one- and two-arm conical spirals operated over a ground plane; however, for the cases tried, the radiation patterns were poor. Dyson later demonstrated that broadband, unidirectional radiation could be obtained with a spiral developed on the surface of a cone.[3] However, this method does not address the need for a low-profile CP antenna that can be mounted on a host vehicle. The practice has been to use a planar spiral backed by an absorber-loaded cavity, a solution that is acceptable only if the loss inherent in such a system can be tolerated.

More recently, Waller and Mayes[4] investigated one- and two-arm equiangular spirals operated as radiating transmission lines over a ground plane. Since the ground plane is an integral part of these low-profile radiators, no absorber-loaded cavity is required. This study led directly to the work by Drewniak and Mayes,[5] who investigated the radiation characteristics of various curved transmission lines. They showed that CP radiation perpendicular to the ground plane (broadside) could be obtained if the ratio of electrical phase shift to physical angle of rotation, called m', is equal to unity. They concluded that one of the primary difficulties in obtaining broadside CP radiation from the log-spiral radiating lines was the relatively slow decay of the wave propagating along the structure. As a result, radiation took place not only into the desired m'=1 mode but also into higher-order modes.

Because of the relatively low attenuation, it was not possible to truncate log-spiral radiating-line antennas near the end of the $m'=1$ modal annulus without introducing a lossy termination. Although such a termination could possibly prevent a reflected wave from radiating into the opposite sense of polarization, thereby degrading the axial ratio of the antenna, it would also significantly reduce the efficiency of the antenna. Wang and Tripp[6] have reported increased gain relative to a log-spiral over an absorbing cavity when using absorber only at the outer edge of a planar, balanced, two-arm log-spiral over ground. However, the band of enhanced gain is significantly less than the pattern and impedance bandwidths.

The Annular Sector Radiating Line (*ANSERLIN*) antenna consists primarily of an $m'=1$ modal annulus and a *second* port from which the power remaining in the attenuated wave would be available. Increasing the height above the ground plane increases the rate of attenuation of the current on an ANSERLIN. Another way to increase the attenuation of the current, while introducing a controlled amount of loss, is to place a localized lossy medium, not in all the space beneath the radiating line, but just between each arm and the ground. This paper reports results on these techniques for achieving broadside CP radiation from spiral antennas over a closely spaced ground.

2. Geometries of the antennas

Figure 1 shows the construction of an ANSERLIN element having the center conductors of coaxial cables attached to small tabs at the end of each fin to provide for connection to external circuitry. It was customary in this type of construction to use 50-ohm cables and to maintain, as nearly as possible, the 50-ohm impedance between the coax connectors. With the impedance fixed at 50 ohms, wider strips are associated with increased height, more rapid decay of the current, and a smaller part of the power delivered to the output port. If it is desired to operate an ANSERLIN as an individual element, then the second port should be terminated in a matched load, and the leftover power is lost. On the other hand, as the height is increased, the current wave traveling around the strip is more rapidly attenuated and the resulting asymmetry in the current produces asymmetry in the radiation patterns. For these reasons, ANSERLIN elements are more suitable for use in series-fed arrays than as individual antennas or as elements in corporate-fed arrays.

A one-arm conical spiral with only one or two turns placed relativly high above the ground plane addresses some of the above problems. The limited number of turns reduces the amount of structure that is present in the near field of the radiating region. Although this also reduces the potential bandwidth of the antenna, such a design might be useful where only moderate

bandwidth (less than an octave) is required. Placing the turns

relatively high above the ground plane (roughly one-quarter

wavelength) should increase the attenuation of the wave propagating

around the structure, thus decreasing the contributions to the

radiation fields from a wide range of modal annuli. Finally, the

self-scaling nature of the conical spiral geometry provides the

gradual transition and broadband structure that aid in achieving

wide bandwidths.

The edges of a one-arm conical spiral as shown in Figure 2 are

described by

$$\rho_{\pm}(\phi) = k \; e^{a(\phi \pm \delta)}$$

where k is a scale factor for the spiral, a is the expansion rate,

and δ is related to the amount of rotation between the curves for

the inner and outer edges. The choice of expansion rate a and the

size of the active region dictate the number of turns required for

a given bandwidth. The parameters must be chosen such that the

bandwidth, rate of attenuation, and the radiation patterns are all

satisfactory.

More nearly symmetric patterns can be achieved using a two-arm

spiral. However, this type of spiral is more difficult to feed

because of the need for a balun or other hybrid network. One

technique for achieving a balanced feed is the so-called infinite

balun used by Dyson[1] A coaxial cable is placed along one arm of

the spiral and the center conductor of the cable is connected to

the other arm at the feed point. This structure is somewhat

difficult to make. A more easily made implementation of the infinite balun is described in a brochure of the Ball Corporation.[7] A microstrip feed line connected to one arm of the spiral at the feed point is etched on one side of a thin substrate. The other arm of the spiral is etched on the other side of the substrate and serves as the ground plane for the microstrip line. The microstrip line can be tapered to provide an impedance transformation, if desired.

3. Numerical evaluations

The programs that were used to implement the moment method solution for the various antennas described above are modifications of the Finite Element Radiation Model (FERM) software package developed at MIT Radiation Laboratory.[8] Figure 3 shows a patch model of an ANSERLIN element with microstrip feed. The patch model includes lengths of feed line on the input and output to provide a means for analyzing the input and output currents. Figure 4 shows the currents along one strip of patches on the input and output feeds. The difference between the magnitudes of the currents is due to the radiation loss. Efficiency with Port 2 terminated in a matched load can be evaluated approximately in terms of the fraction of available power (relative power absorbed (RPA)) that is neither reflected at the input port nor delivered to the output port, RPA = $(1-|S_{11}|^2-|S_{12}|^2)$. Table 1 compares computed and

measured values of the beam scan that occurs with frequency
changes, and computed and measured values for the relative power
absorbed.

Table 1

Beam scan and efficiency

Frequency (GHz)	Beam Scan		RPA	
	Computed	Measured	Computed	Measured
2.1	0°	0°	0.41	0.38
2.6	13°	15°	0.64	0.62
3.0	23°	25°	0.80	0.78

One approach to increasing efficiency is to relax the
requirement of 50 ohms (which was chosen largely as a matter of
convenience for construction and measurement). Any impedance
transformation that may be needed can be achieved relatively
easily, at least over moderate bandwidths. FERM was used to
examine the effect of increased height on element performance. Top
and side views of the mesh for an elevated ANSERLIN element and its
image are shown in Figure 5. The width-to-height ratio for the
feed lines and the fins is 1.3, giving a characteristic impedance
of 112 ohms. The feed line on the output side is terminated with
basis functions on which a resistive boundary condition is enforced
to match the line. Figures 6 and 7 show the computed current
distribution (magnitude of current density at the centroid) for
this element at 1.9 and 2.3 GHz. The currents are comparable to
those computed for other ANSERLIN elements except that the rate of

decay is much higher. The efficiency of this element is approximately 89 percent at 1.9 GHz. At 2.1 and 2.3 GHz, the efficiencies are 96 and 98 percent, respectively.

Although the pattern characteristics of the high-efficiency ANSERLIN are similar to those of other ANSERLIN elements, the quality of the circular polarization is not as good and the shape of the beam, particularly at 2.3 GHz, is somewhat more asymmetric. The upper frequency of operation is limited by the pattern degradation that is observed at 2.3 GHz. If the lower edge of the band is determined to be 1.9 GHz based on high efficiency, then the bandwidth is approximately 19 percent.

The bandwidth limitation imposed by the varying rate of decay of the currents along ANSERLIN elements, as well as the inherent scanning of the element pattern, can be at least partially overcome by using spiral geometry to replace the annulus. A one-arm conical spiral with only one or two turns placed relatively high above a ground plane should be expected, therefore, to yield more bandwidth at higher efficiency than an ANSERLIN element with comparable parameters. Numerous geometries were examined using FERM in order to evaluate various choices of parameters. Of these, the performance obtained from the design denoted CS14 is typical of the potentially useful designs. The mesh for CS14 is shown in Figure 8. The conical spiral and its image, and the triangular fins that provide the transition from the conical spiral and its image to a voltage generator can be seen. The active region of this one-turn

spiral is assumed to be from $\phi_1=\pi$ to $\phi_2=2\pi$ at the lowest frequency of operation. The heights of the outer edges at this frequency are $h_1=\lambda/6$ and $h_2=\lambda/3$, and the length along the centerline is $L_c=0.55\lambda$. The parameters are $k=0.0503\lambda$, $a=0.221$, and $\delta=2.66$.

From computed current distributions for CS14 the increasing attenuation at the higher frequencies is evident. Computed radiation patterns show that the axial ratio on boresight is around 3 dB, asymmetries are present in the pattern, and a 10- to 15-degree beam tilt exists.

The inherent asymmetry of the one-arm spiral is responsible for the asymmetry in the patterns. The effects of this asymmetry can be minimized by building spirals which have longer (and more nearly annular) active region. To achieve moderate bandwidths, however, more turns are required. Several multiturn designs were modeled using FERM, among them a two-turn design denoted CS23. The active region of this spiral is assumed to be from $\phi_1=2\pi$ to $\phi_2=4\pi$ at the lowest frequency of operation. The heights of the outer edges at this frequency are $h_1=0.15\lambda$ and $h_2=0.3\lambda$, and the length along the centerline is $L_c=1\lambda$. The spiral parameters are $k=0.054\lambda$, $a=0.11$, and $\delta=\pi/2$.

At lower frequencies the currents decay uniformly along the structure; however, at higher frequencies, a standing wave pattern can be seen along the line. Energy from the inner turn appears to be coupling to the transmission line on the outer turn. The differences in the fields produced by these currents can be seen in

the radiation patterns. The uniformly decaying currents at the lower frequency produce less asymmetric patterns having less beam tilt and better axial ratio than those of the one-turn spirals. However, the coupling that occurs at the higher frequencies produces patterns which show significant degradation. Numerous one-arm, multiturn spirals were modeled; however, each of them exhibited this type of behavior at the higher frequencies. Since the height of the spiral arm is large in order to achieve adequate radiation and the arm-to-arm spacing is relatively small in order to achieve better symmetry, coupling between the arms in this type of spiral probably cannot be eliminated.

Symmetric patterns can be achieved by using two-arm spirals. FERM was used to model a planar, two-arm, one-turn spiral operated over a ground plane. To simplify the model, the balun was replaced by a voltage generator at the feed point. Figure 9 shows top and side views of the mesh used for this spiral. The active region is assumed to be from $\phi_1 = \pi$ to $\phi_2 = 2\pi$ at the lowest frequency of operation. The height of the spiral above the ground plane at the lowest frequency of operation is 0.2λ, and the length along the centerline $L_c = 1.2\lambda$. The spiral parameters for one arm are $k=0.127\lambda$, $a=0.221$, and $\delta=\pi/4$. The second arm is the same as the first, but rotated 180 degree. The two arms are connected with two 180-degree annuli which begin on each arm and extend to the center of the element. Figures 10 and 11 show computed current distributions for this two-arm spiral at $f=1.2$ and $f=1.9$.

Using image theory, a spiral over ground can be considered a two-element array excited 180 degrees out of phase and separated by a distance equal to twice the height of the spiral above the ground plane. The extent to which the radiation patterns of the spiral over a ground plane can be approximated by pattern multiplication of a free-space element pattern and the two-element array factor gives a qualitative estimate of the effects of mutual coupling, i.e., how much the current in the spiral over ground differs from that of the same spiral in free space.

Figure 12 compares the radiation patterns (f=1.8) computed by FERM (for the two-arm spiral and its image) to the radiation patterns resulting from product of the pattern of a single spiral times the array factor. Although the shapes of the beams are similar, coupling does introduce some differences off boresight. The dip in the pattern on boresight is due, in part, to the dip in the two-element array factor since the separation between the element and its image at this frequency is 0.72λ and the elements are 180 degrees out of phase.

4. Some evaluations by measurement

Since the two-arm spiral of the previous section has a diameter at midband of approximately 1.8λ, it is too large to use in an array. Further simulations showed that a self-complementary two-arm spiral having the same shape, but scaled for a diameter of 0.76λ at midband, also produced circularly polarized radiation.

11

Figure 13 shows the geometry for a microstrip-fed implementation of this smaller two-arm spiral. This spiral is designed for operation from 2 to 3 GHz, and the parameters are k=0.38 in (0.08λ at 2.5 GHz), a=0.221, δ=π/4, and φ ranges from 0 to 2π.

The spiral of Figure 13 has both arms etched on the same side of the substrate and the microstrip line etched on the other. A pin connects the end of the feed line to one of the arms. The element was mounted 1.25 in (0.26λ at 2.5 GHz) above a ground plane using Rohacell foam. The feed line was placed toward and the spiral arms were placed away from the ground plane. Radiation patterns that were measured from 2 to 3 GHz showed some asymmetry in the beam and poor axial ratio. Several differences between the element that was built and the one modeled using FERM could account for these effects. First, dielectric was present in the actual element, where FERM assumed free space. Also, the microstrip balun was not modeled in FERM, where an ideal voltage generator was placed between the two arms. Finally, the spiral arms on the element modeled using FERM were truncated abruptly, as in Figure 9. However, the arms were truncated at a constant radius on the element shown in Figure 13. The constant-radius truncation is common for equiangular spirals, and it was assumed that such a truncation would provide an element with improved performance, particularly at the low end of the operating band, compared to the element having the abrupt truncation.

To determine the cause of the poor axial ratio, four elements were constructed without the microstrip balun. Instead, these elements were designed to be fed with the difference ports of a hybrid. One element having an abrupt truncation of the arms was etched on 60-mil substrate, and another was etched on 12.5-mil. Two elements having the constant-radius truncations were similarly etched on thick and thin substrates. Beam symmetry improved significantly for all of the elements fed with the hybrid, indicating that the microstrip balun was probably responsible for much of the asymmetry. However, the axial ratio for the elements with constant-radius truncation remained poor for both the thick and thin substrates, although the patterns were relatively unaffected by the thickness of the dielectric. Patterns for the elements with the abrupt truncation, on the other hand, showed a significantly improved axial ratio and had a useable operating band from about 1.65 to 2.35 GHz. A midband pattern for the element on the 60-mil substrate is given in Figure 14. All patterns were measured with the antenna mounted on a 3-foot diameter circular ground plane.

A linear, four-element, corporate-fed array was designed with the spiral described above as the element. The array elements were designed to have uniform, in-phase excitations in order to produce broadside radiation. The center frequency of the array was designed to be 4 GHz, and except for the width of the microstrip feed line at the center of the spiral, the elements in the array

were half-scale versions of the abruptly truncated spiral etched on a 60-mil substrate.

The power dividers in the corporate feed consist of 50-ohm lines feeding pairs of 100-ohm lines. The 50-ohm connection at each of the two-element subarrays is transformed to 100 ohms using tapered microstrip lines. These two 100-ohm lines are then combined to provide a 50-ohm feed point, to which an SMA launcher is connected. The element spacing for this array was 2 in (0.68λ at 4 GHz). A radiation pattern in the line of the array at 4.0 GHz is shown in Figure 15. The axial ratio is 6 dB or better from 3.0 to 5.5 GHz; however, the onset of the grating lobes above 5.0 GHz effectively limits the upper limit of the operating band. The pattern bandwidth for 3 GHz to 5 GHz operation is 50 percent if a 6 dB axial ratio is used to determine the pattern bandwidth.

In view of the conclusion that multiturn spirals over closely spaced ground have currents that do not decay as rapidly as needed to produce well-formed radiation patterns, some experiments were conducted with resistive thin film placed between a spiral and the ground. A one-arm log-spiral was etched from a thin copper-clad microwave substrate. The substrate was cut along a spiral curve between adjacent arms so that the arm could be supported in a conical shape with the longer turns being a greater distance above the ground plane. The center conductor of a coaxial cable was soldered to the small end of the spiral and the outer conductor was soldered to the ground plane. Figure 16 is a top view of the

14

spiral pattern and Figure 17 shows side views of a cut through the coaxial feed.

Adjustable attenuation of the current wave was provided by means of a thin sheet of resistive material (metal film resistance card). The film was cut into triangular strips with the small angle equal to the angle between the cone of the spiral and the ground plane. The absorber was supported in a vertical position, perpendicular to the ground plane. It was formed to coincide with the same spiral curve that was used to define the radiating arms so that the relative position between the radiative spiral and the absorptive spiral was maintained. By rotating the radiating spiral relative to the absorptive one, placement of the absorptive spiral was made to correspond to positions at either edge or in the center of the radiating spiral arm. Radiation patterns were measured for each of the above positions and with two different resistive films, 100 ohm and 50 ohm. The antennas were identified by consecutive numbers as given in Table 2.

Table 2

Antenna Configurations

Antenna	Film Location	Resistance
1	none	---
2	outside	100
3	middle	100
4	inside	100
5	outside	50
6	middle	50
7	inside	50

The patterns were measured in the elevation plane for several

azimuth angles. A spinning source antenna was used to obtain data on polarization. The pattern outlines, maximum and minimum loci for the spinning source, were digitized and all cuts for a given antenna at a given frequency were plotted on the same grid. Judging the quality of the response to circular polarization over an extended range of angles around zenith is simplified using this data format. The axial ratio over the entire pattern of Antenna 3 has the least variation of these four antennas, although there is slightly more variation in the axial ratio at zenith. At 2 GHz and above, Antennas 3 and 4 both have better pattern shapes than Antennas 1 and 2.

To further facilitate comparison as a function of frequency, plots were made of beam tilt and axial ratio at zenith. Antennas 3, 4, and 5 have comparable variations in beam -pointing direction, about 45 to 50 degrees total. The variation for the others ranges between 80 and 100 degrees. Antenras 2, 3, 4, and 5 all have axial ratios less than 6 dB across the band from 1 to 6 GHz.

5. Conclusions

Several types of spiral, radiating-line antennas have been discussed in this paper. Each of them relies on a traveling wave to obtain moderately broadband performance. The elevated ANSERLIN element is useful for demonstrating the effect that height has on efficiency; such elements are useful over bandwidths of around 20 percent if some degradation in the patterns can be tolerated.

However, the scanning of the element pattern that is inherent in the ANSERLIN design requires the consideration of elements that possess more structural bandwidth, among which are log-spiral geometries.

The one-arm spiral over a ground plane has a more nearly self-scaling structure than that of the ANSERLIN element, and stable behavior was observed over roughly a 40-percent band. Although the computed and measured radiation patterns showed beam asymmetries, beam scans, and only fair axial ratios, the element would be useful in broadside, corporate-fed arrays where beam shape off boresight is not critical. Attempts to improve the symmetry of the patterns by increasing the size of the active region and the number of turns revealed coupling between the turns of the spiral.

The planar two-arm spiral over a ground plane is suitable for bandwidths similar to those of the one-arm spiral, with significantly improved beam symmetry and axial ratio. The difficulty in achieving a balanced feed can be overcome in a two-arm spiral having only one or two turns by using the microstrip implementation of the balun. Of the elements examined, it is the most suitable candidate for the element in a moderate bandwidth, broadside radiating, low-profile, circularly polarized, corporate-fed array.

Preliminary measurements indicate that the pattern shape of a given log-spiral over closely spaced ground can be improved by inserting a lossy strip beneath the spiral. The optimum

configuration has not been determined, but a 100-ohm film between the middle and inside of the spiral, or a 50-ohm film near the outside, all perform better than the same spiral with no film.

REFERENCES

1. Dyson, J. D. (1959) The equiangular spiral antenna, IRE Trans. Antennas Propagat. AP-7:181-187.

2. Carrel, R. L. (1957) Experimental Investigation of the conical spiral antenna, Tech. Rep. 22, Univ. of Illinois Antenna Lab.

3. Dyson, J. D. (1959) A unidirectional equiangular spiral antenna, IRE Trans. Antennas Propagat. AP-7:329-334.

4. Waller, R. W. and P. E. Mayes (1985) Development of a flush-mounted equiangular spiral antenna, Tech. Rep. 22, Univ. of Illinois Antenna Lab, Urbana, IL.

5. Drewniak, J. L., and P. E. Mayes (1989) ANSERLIN: a broad-band, low-profile, circularly polarized antenna, IEEE Trans. Antennas Propagat. AP-37:281-288.

6. Wang, J. J. H., and V. K. Tripp (1991) Design of multioctave spiral-mode microstrip antennas, IEEE Trans. Antennas Propagat. AP-39:332-335.

7. .... (1983) Printed circuit spiral antenna, Product Note AN0275A, Ball Aerospace, Broomfield, Colorado.

8. Stiglitz, I. G., et al (1987) Numerical modeling of RCS and antenna problems, Tech. Rep. 785, Lincoln Laboratory - Mass. Inst. of Tech., Lexington, MA.

Figure 2. One-arm spiral geometry and coordinates.

Figure 1. Probe-fed ANSERLIN element.[5]
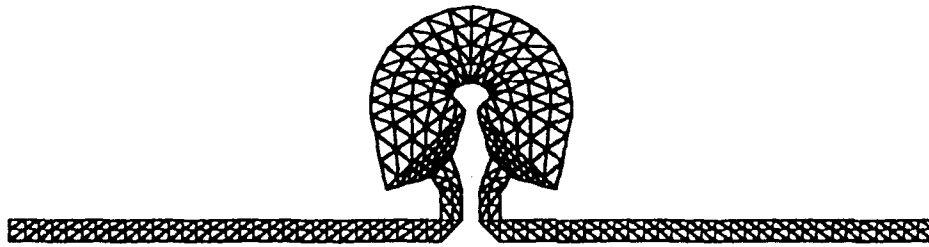
Figure 3. Surface patch model of an ANSERLIN element.

Standing Waves on Input and Output Feed for D01 (2.1 GHz)
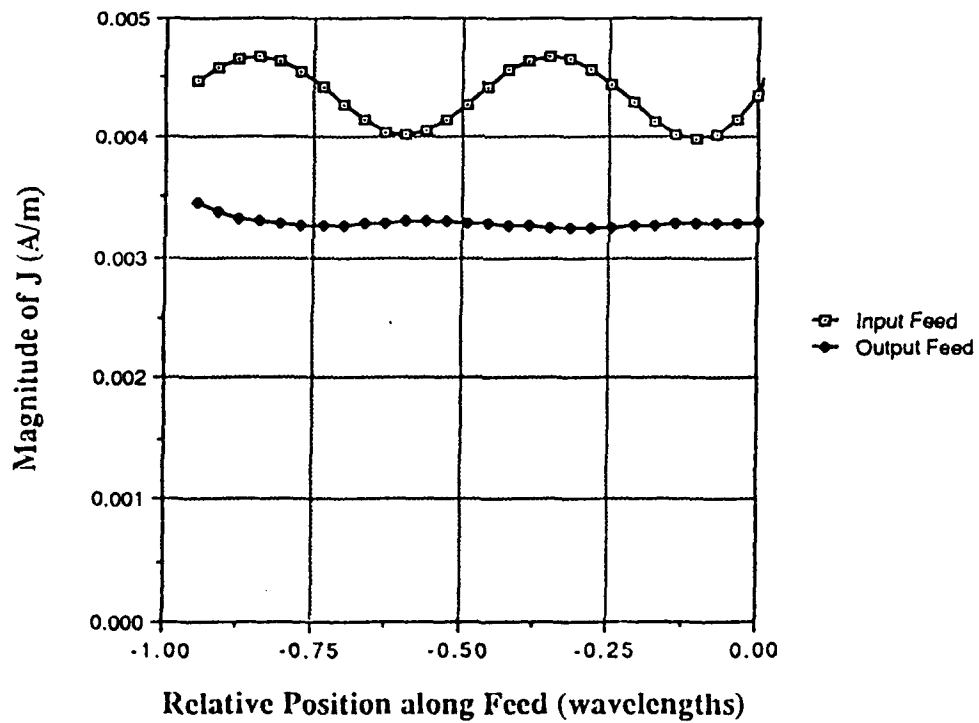
Figure 4. Currents along input and output lines of ANSERLIN.
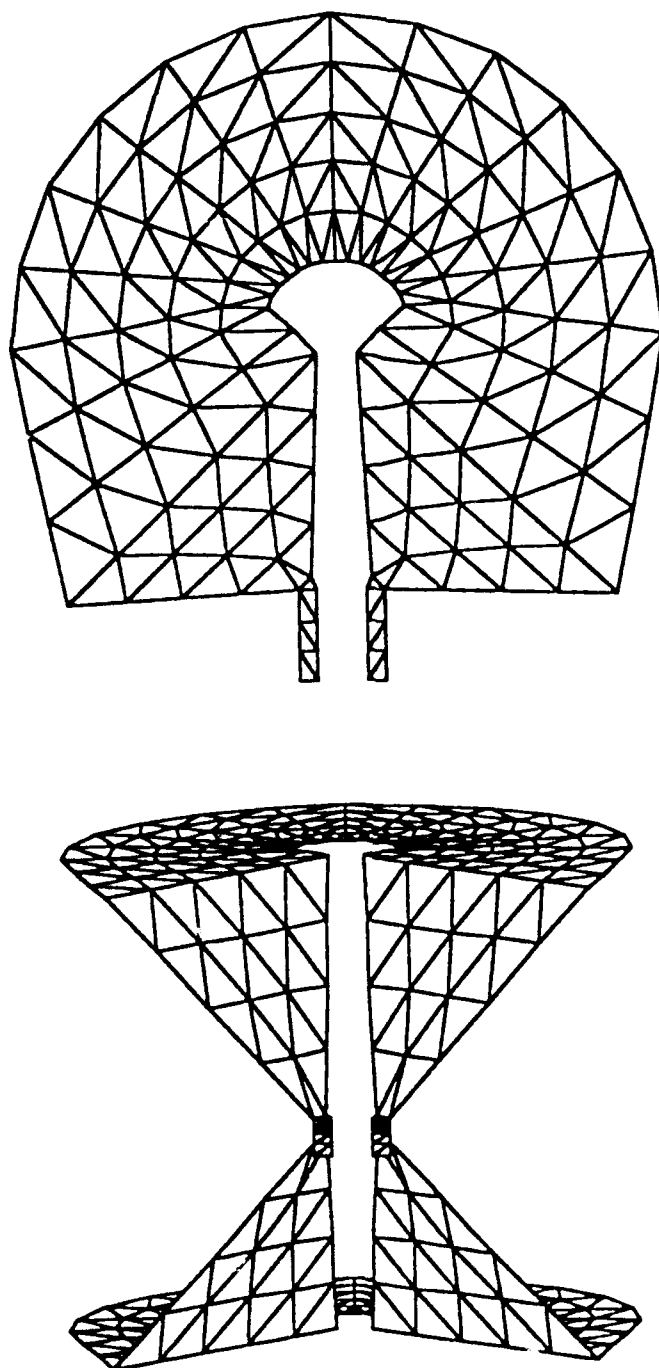
Figure 5.   Top and side views of an elevated ANSERLIN and image.

-40   -30   -20 (dB)
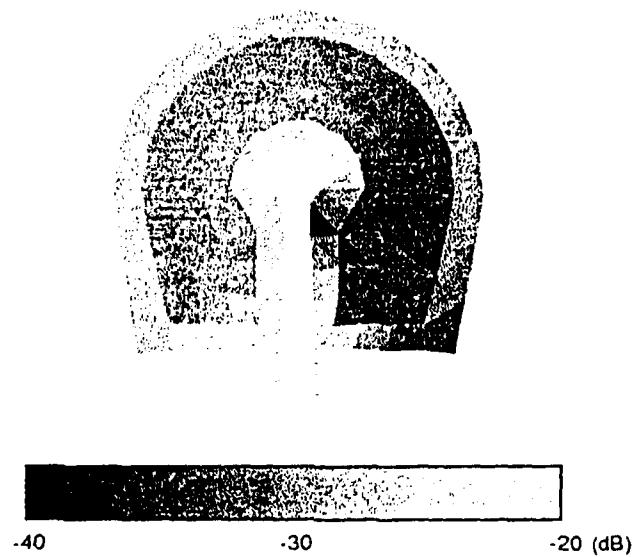
Figure 6.   Current density at patch centroids for elevated ANSERLIN
(1.9 GHz).

-40   -30   -20 (dB)
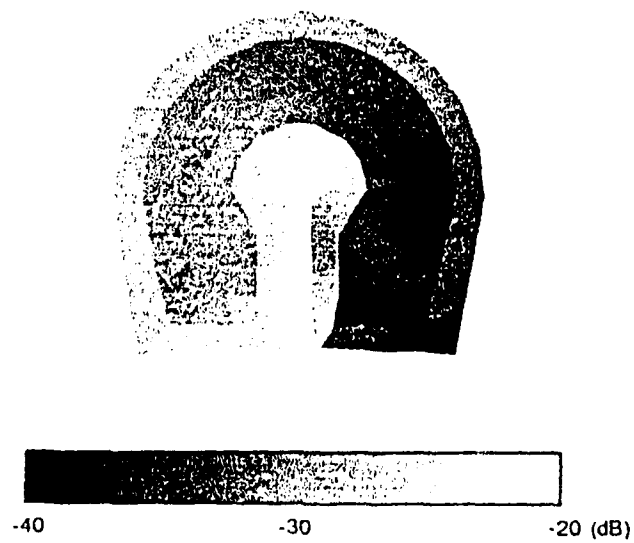
Figure 7.   Current density at patch centroids for elevated ANSERLIN
(2.3 GHz).

Figure 9. Top and side views of a two-arm spiral and image.

Figure 8. Top and side views of a one-arm spiral and image.

-30   -15   0   (dB)

0   90   180 (degrees)
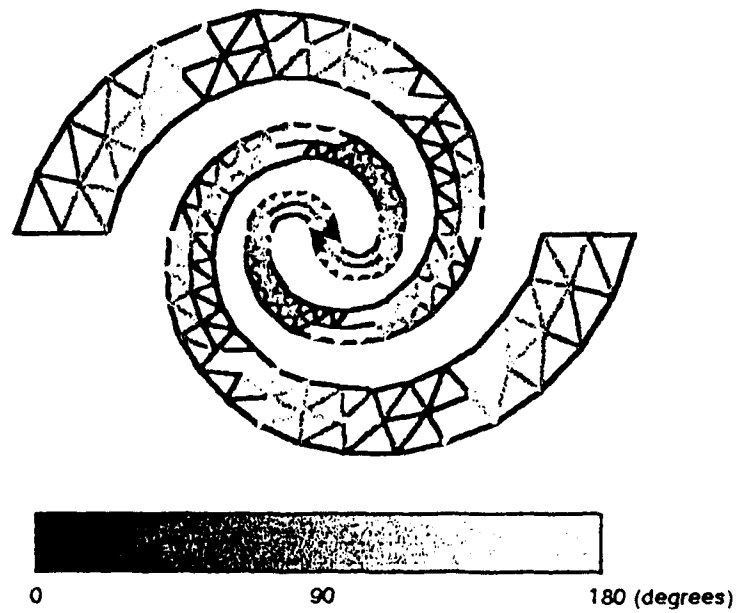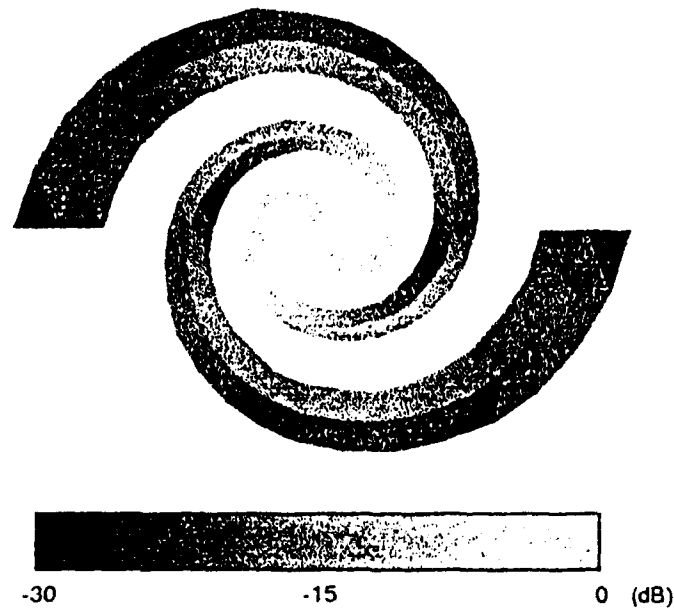
Figure 10. Current density at centroids and phase across the patch edges for a two-arm spiral over ground (f=1.2).

-30   -15   0 (dB)

0   90   180 (degrees)
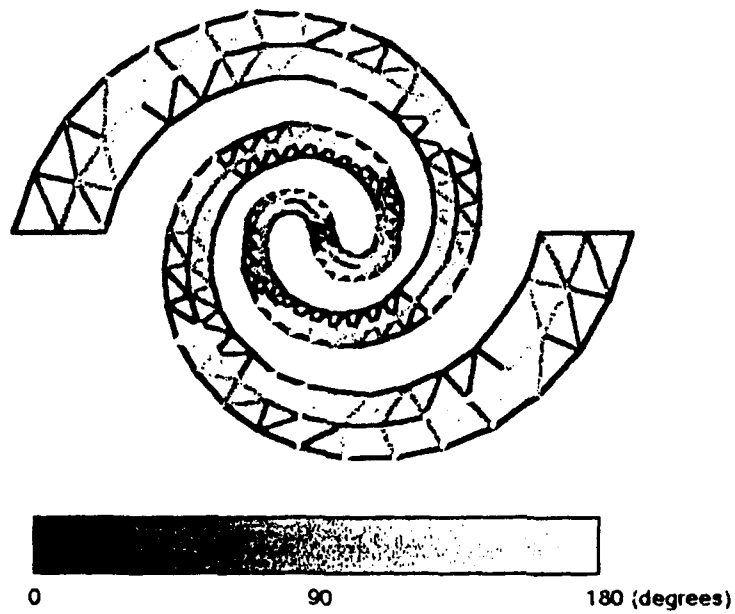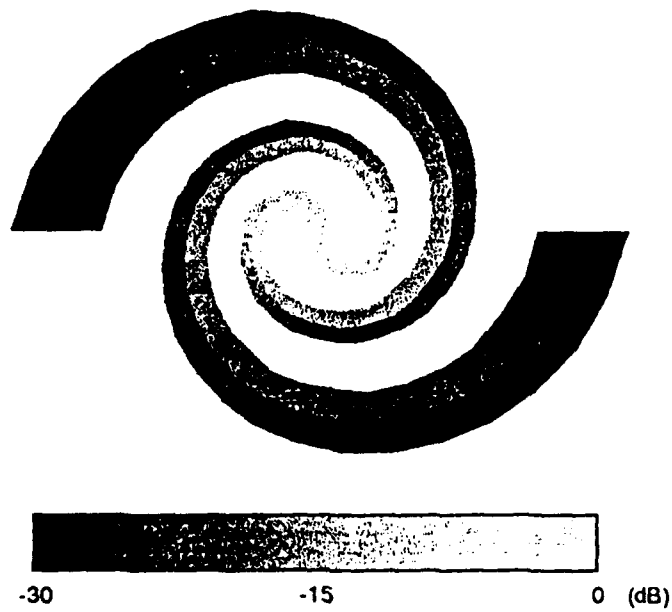
Figure 11. Current density at centroids and phase across the patch edges for a two-arm spiral over ground (f=1.8).
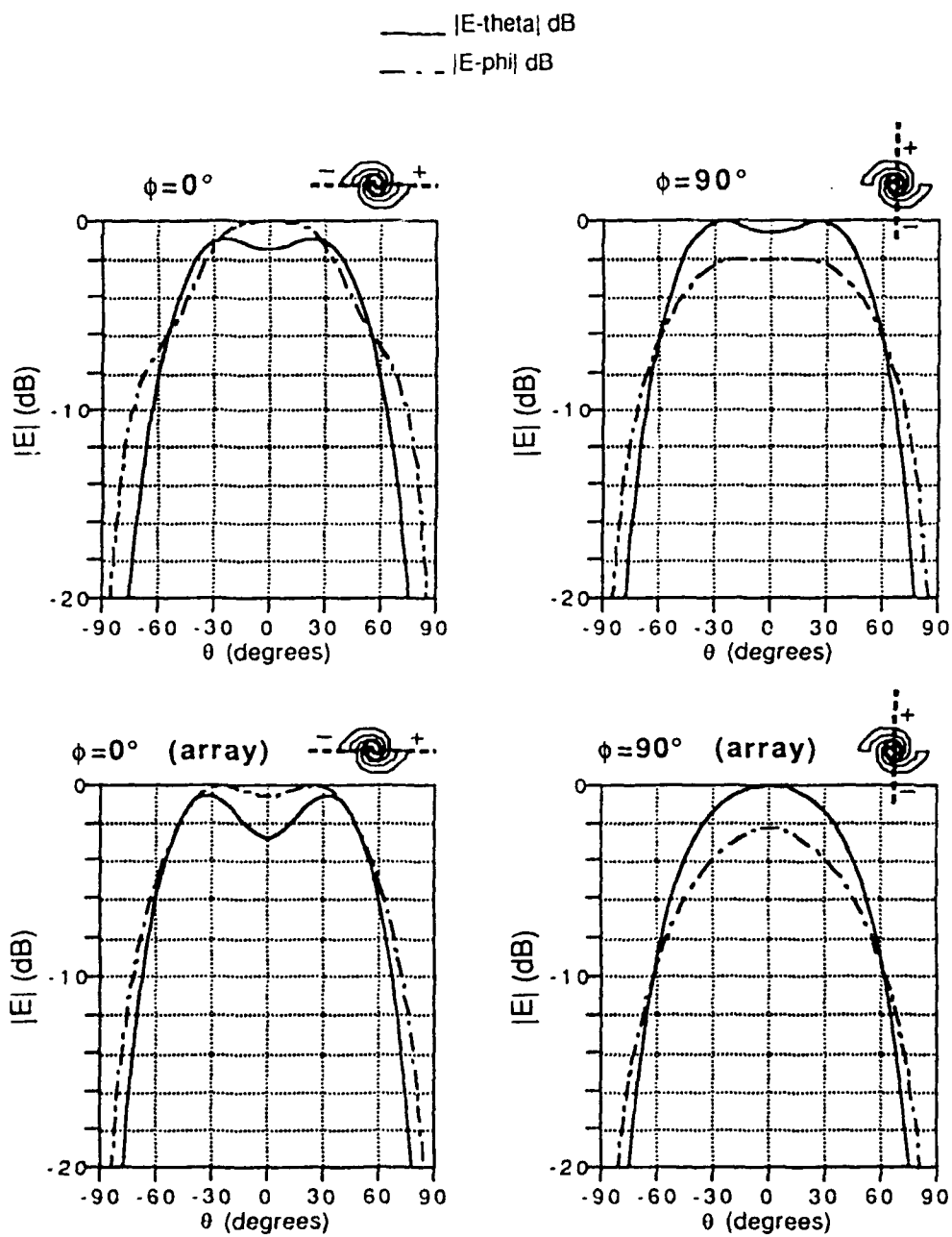
Figure 12. Computed (top) and approximated (bottom) patterns for
the two-arm spiral (f=1.8).
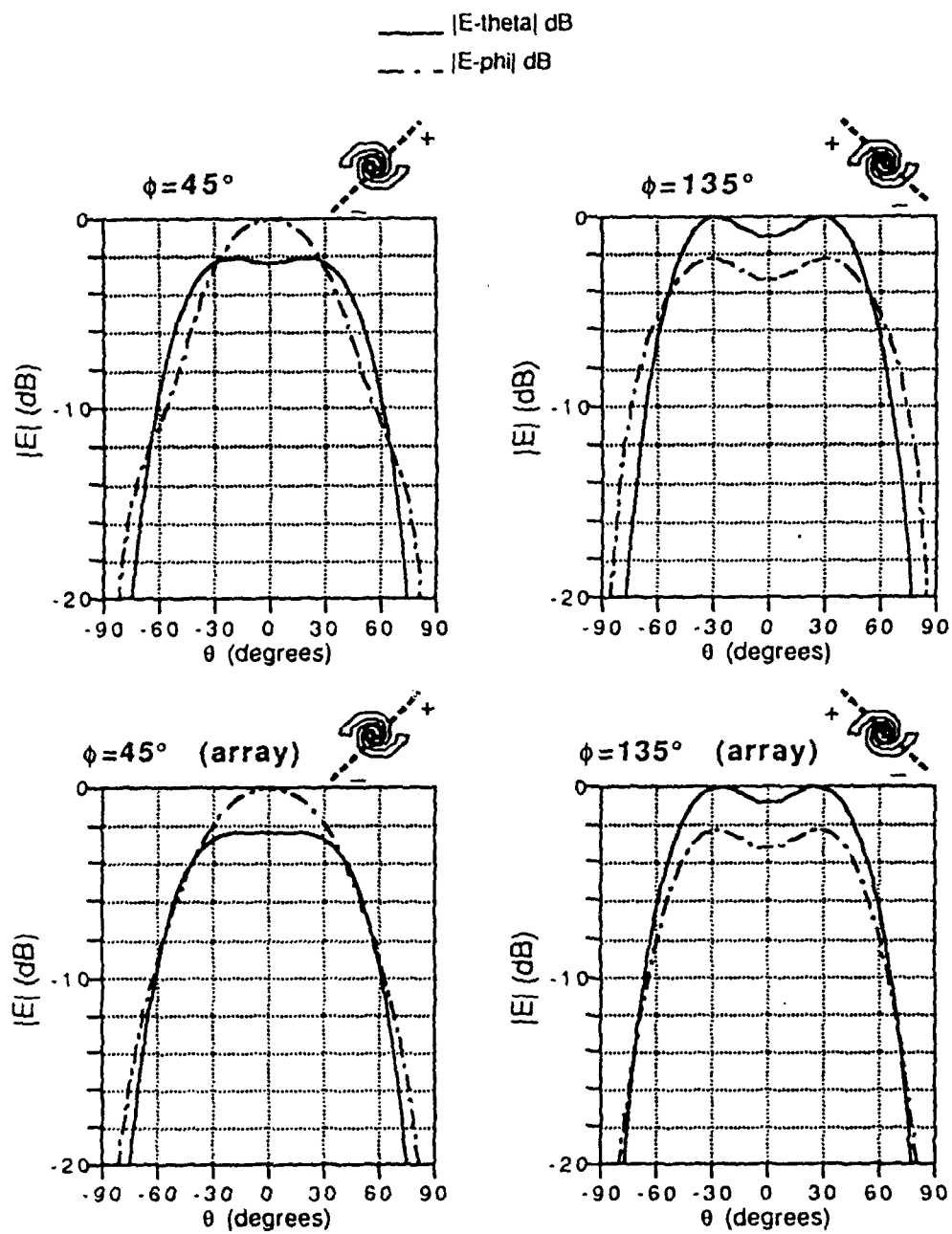
Figure 12 (continued). Computed (top) and approximated (bottom) patterns for the two-arm spiral (f=1.8).

430

fs24-175
November 1990

3300 MILS

4700 MILS
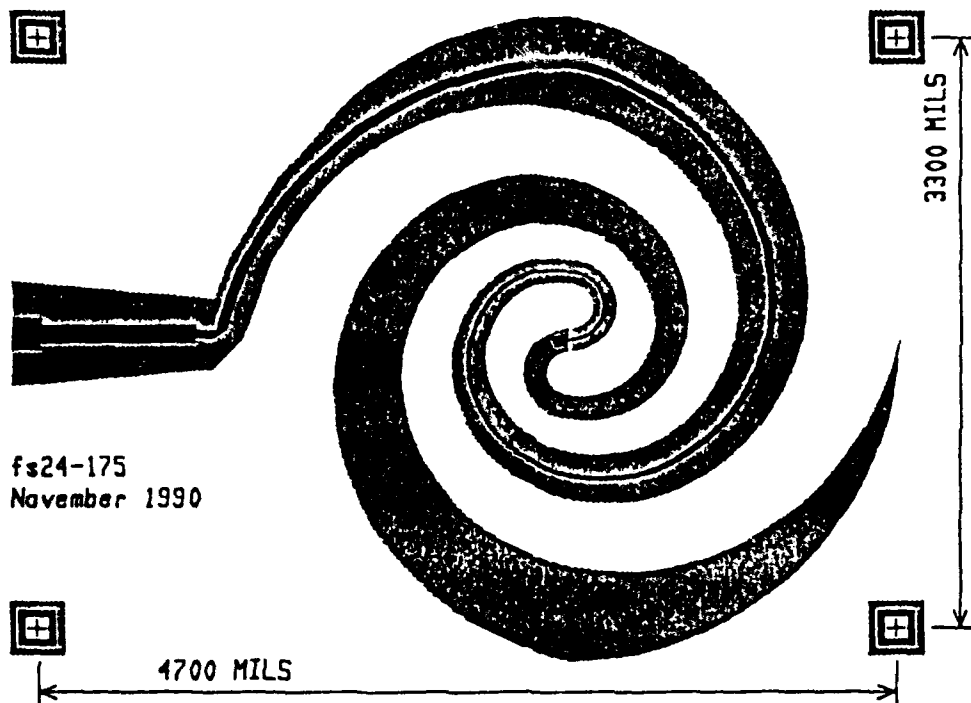
Figure 13. Two-arm log-spiral with microstrip balun.

431

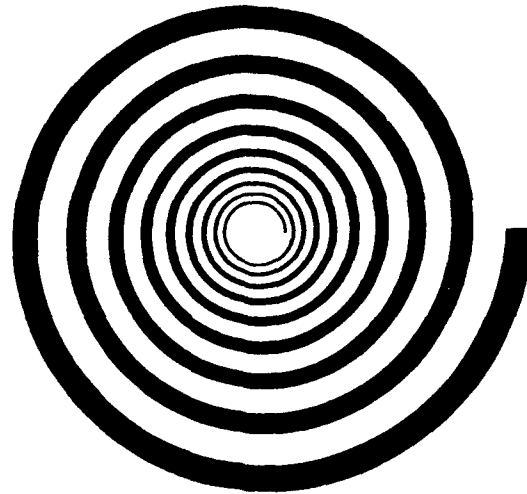Figure 15. Radiation pattern (4.0 GHz) for a four-element array of planar log-spirals over ground.
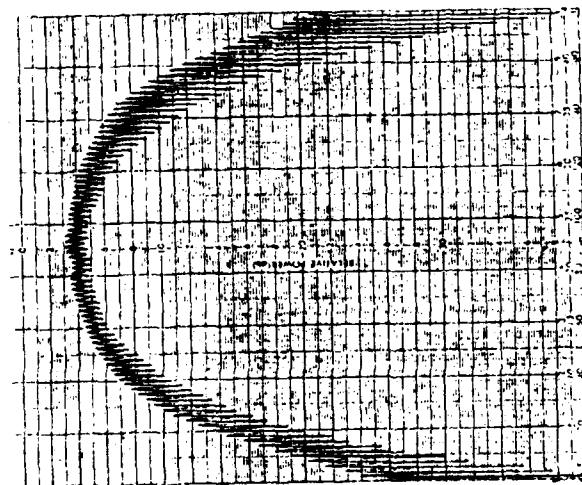
Figure 14. Radiation pattern at 2.0 GHz for an abruptly truncated two-arm log-spiral fed with a hybrid.

432

Figure 16. Top view of one-arm log-spiral used over spiral resistive film.
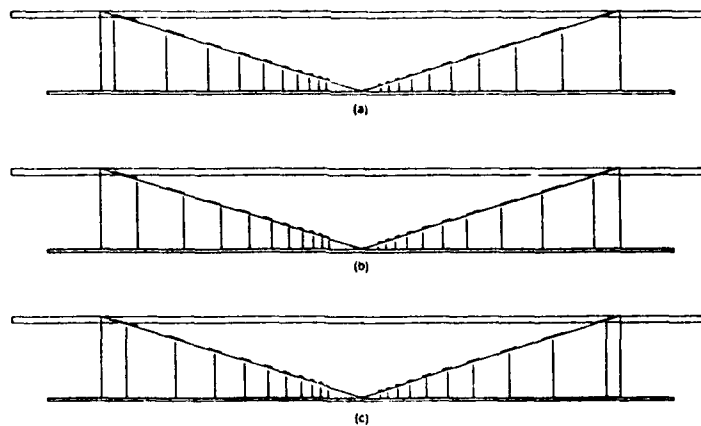
Figure 17. Side view of one-arm radiating spiral over ground showing placement of resistive film underneath (a) outer edge, (b) inner edge, and (c) center of radiating spiral.

Comparison of Sinuous and MAW Spiral Antennas for Wideband, Dual Polarized Multi-Arm Applications

P. G. Ingerson, P. M. Ingerson and D. C. Senior
Antenna Systems Laboratory
TRW Space and Defense
Redondo Beach, CA 90278

Abstract

Recent requirements for wideband dual polarized antennas with good pattern circular symmetry have centered on two feed candidates: cavity backed Modulated Arm Width (MAW) spiral and Sinuous antennas.

Both of these antennas are capable of arbitrarily wide bandwidth operation; practical bandwidths are limited by photo-etching and feedpoint considerations.

The properties of these antennas appear not to be widely known and to date the useful range of design parameters have not been published. This paper will show and compare the properties of two corresponding models of the multi-arm MAW spiral and Sinuous antennas.

The feeds will be compared for the four-arm case which yields dual circular polarization or orthogonal linear operation as well as six-arm versions which can provide both sum and difference mode operation.

Introduction

In this paper we will compare the characteristic performance of the Modulated Arm Width (MAW) spiral antenna and the Sinuous antenna (or as we will show, a "folded" spiral) with those of the corresponding parent spiral. Both the MAW spiral and Sinuous antennas can provide arbitrarily wideband performance with excellent pattern characteristics in planar cavity backed configurations. The two antennas achieve dual polarization operation using completely different mechanisms ,yet both are capable of essentially identical pattern performance and impedance. Both antennas can also provide wideband orthogonal linear polarization operation. In the linear polarization mode, the polarization angle properties as a function of frequency of both antennas are fundamentally different. Neither antenna provides a fixed polarization angle with frequency. The MAW spiral antenna provides an orthogonal linear response whose polarization angle (τ) changes linearly with frequency (with respect to the log of the spiral wrap angle), while the τ angle of the Sinuous antenna demonstrates an oscillating behavior with frequency. In six arm versions, both antennas can provide dual polarized sum and difference mode of operation for tracking and angle of arrival (AoA) applications.

Modulated Arm Width Spiral Antenna

The modulated arm width spiral was first introduced in 1971 [1,2] The performance capability of this antenna was a significant improvement over other Log Periodic (LP) planar configurations, in that it could provide the radiation patterns and input impedance characteristics of logarithmic spirals but with dual senses of polarization over an arbitrarily wide bandwidth.

The swept pattern characterizatics reveal none of the central feed line resonances that the planar LP trapezoidal tooth or circular tooth structures exhibited. (See for example Reference 3, Figure 17, for the "Interlog Antenna")

The four arm MAW spiral antenna concept was extended to six arms, where dual polarized sum and difference modes of operation were demonstrated, but not published, a few years later.

Spiral antennas normally provide radiation characteristics dependent on the direction of the wrap of the arms. That is, placing the thumb in the direction of radiation, Right Hand Circular Polarization (RHCP) would be a counter clockwise wrap direction and left hand would be clockwise. When the N arms of a normal spiral are progressively fed with an integer multiple M of $(2\pi/N)$ phase, all the radiation patterns are polarized in the sense of wrap of the spiral. For a counter clockwise wrapped spiral, only the M = +1 mode with a $+2\pi/N$ clockwise phase progression from arm-to-arm produces radiation normal to the aperture plane. All other modes produce patterns with nulls, if the structure is of a large enough diameter to support the mode's active region.

For M greater than 1, essentially no radiation takes place along the arms until the currents are properly phased in the appropriate active region. If the diameter of the antenna is smaller than that required for a given mode, the energy is reflected at the end of the arms and on traveling back along the arms is phased to radiate efficiently. Since the energy is traveling inward the

sense of polarization is reversed. The bandwidth of this mode of operation is typically much less than 2:1.

The modulated arm width spiral in effect just provides a structural stopband, by means of the arm impedance modulation, to block the energy before the appropriate active region and reflect it inward to provide the opposite polarization sense. If the modulation scales in a log periodic fashion with the appropriate scale factor, the relative stopband location with respect to the active regions will remain fixed and frequency independent bandwidth performance is obtained.

Since the maximum reflection occurs when the length of a wide and narrow section is approximately 1/2 wavelength, the number of modulations around a circumference are chosen to place the stopband before the selected active region. For example to place the stopband after the M = 1 mode active region and before the M = 3 mode for a four arm spiral requires four modulation bands at the two wavelength circumference. To obtain two modes, from a six arm MAW spiral antenna, the stopband is placed after the M = 2 mode and ahead of the M = 4 mode. This results in six modulation bands.

Sinuous Antenna

The Sinuous antenna is a new antenna concept patented by R. H. DuHamel in 1987. As described in his patent [4] the Sinuous antenna comprises an N arm antenna with angular coordinates of each arm having an oscillatory function of radius between two angular limits. Each arm has a rotational symmetry

4

such that a rotation of 360/N degrees about its axis leaves the structure unchanged.

One important embodiment of this antenna is most easily understood as a folded log spiral. That is, a near optimum performance sinuous antenna can be designed by using the parameters of a conventional spiral for the sinuous generatrix. Using the parametric equation form of a log spiral.

$$X = r_0 e^{a\phi} \cos\phi \qquad \text{where} \qquad \phi_{initial} \leq \phi \leq \phi_{final}$$
$$Y = r_0 e^{a\phi} \sin\phi \qquad \text{and} \qquad r_0 = \text{initial radius} \qquad (1)$$

The corresponding sinuous antenna becomes

$$X = r_0 e^{a\phi} |\cos\phi|$$
$$Y = r_0 e^{a\phi} \sin\phi \qquad\qquad (2)$$

This generatrix line spiral is then rotated $\pm \delta/2$ to provide the edge lines of the sinuous antenna. For a self complimentary geometry of an N arm antenna δ is given by:

$$\delta = \frac{360}{2N} \text{ degrees} \qquad\qquad (3)$$

The arms are then progressively rotated by 360/N degrees from each other.

This method of sinuous antenna generation gives near optimum parameters for 4, 6, 8 or higher numbers of arms.

If one views the spiral arm operation in the transmitting case as having an outward traveling wave, it is clear that the phasing along each segment is essentially the same as that of a regular spiral since the total path length along the arms is identical. It then is plausible to understand the sinuous antenna as a combination of segments from RH and LH spirals.

When the wrap angle is tight enough to provide several segments in the active region, the result is the sum of RH and LH radiation which is linear. In the case of a four arm antenna, one can also consider obtaining linear by exciting the sum and difference of RH and LH arm excitations. This is identical to just feeding one pair of opposite arms 180 degrees out of phase.

Pattern Comparisons

Typical patterns of the parent RHCP spiral, Sinuous, and MAW spiral antennas are shown in Figures 1, 2 and 3. These were all measured over a midband frequency segment using the same absorber filled cavity with a cavity and spiral diameter of 7.5 inches. The corresponding antennas are shown in Figure 4.

Figures 5, 6 and 7 show the corresponding swept pattern (averaged) beamwidth. All the antennas showed highly circularaly symmetrical patterns. The beamwidths plotted in Figures 5 thru 7 are averages from several pattern cuts.

Linear Mode Polarization Properties

The polarization angles, τ, for both the Sinuous and MAW spiral antennas are not constant with frequency. The τ angle of the Sinuous antenna oscillates back and forth with a period directly related to the spiral wrap angle parameter a.

$$f_N = f_0\, e^{2Na\pi} \qquad\qquad N = \pm 1, \pm 2, \dots \qquad\qquad (4)$$

This is shown in Figure 8 along with the axial ratio for a four arm sinuous with a scale factor of 0.63 or 1.5 turns per octave (T/O), measured over a midband segment. Figure 9 shows similar performance of a 6 arm Sinuous antenna.

The corresponding polarization angle of a MAW spiral changes linearly with frequency when plotted with respect to the log period of the antenna as shown for the corresponding 6 arm MAW spiral in Figure 10.

Tracking and Angle of Arrival (AoA)

Both the Sinuous and the MAW spiral can be extended to 6 or 8 arm versions shown in Figure 11 giving dual polarization sum (Σ) and difference (Δ) performance. To use these feeds for tracking or AoA applications, the key parameters of interest are the relative phase of the sum to difference patterns and the amplitude ratio of the difference to sum signals. As with conventional spirals, the relative phase angle between the Σ and Δ patterns gives signal direction (clock angle) relative to the difference pattern null while the ratio of the Σ to Δ signals are proportional to the angular separation of the signal from the pattern null. The proportionality factor is

called the scale factor. While actual achievable performance requires inclusion of changes with respect to incident polarization and beamformer errors, Figures 12 and 13 illustrate that both antennas can provide well behaved clock angle phase and scale factor performance for both senses of polarization.

References

1. Ingerson, P.G., "The Modulated Arm Width (MAW) Spiral Antenna ," *Abstracts of the 20th Annual Symposium USAF Antenna Research and Development Program* , Oct 13, 14, 15, 1970.

2. Ingerson, P. G. Inventor "Modulated Arm Width Spiral Antenna," U.S. Patent 3,681,772, August 1, 1972.

3. Hoffer, D. A., Kesler, O. B., Loyet, L. L., "Compact Multi-Polarization Broadband Antenna," *Antenna Applications Symposium,* Sept. 20, 21, 22, 1989.

4. DuHammel, R. H., Inventor, "Dual Polarized Sinuous Antennas," U. S. Patent 4,658,262, April 14, 1987

5. Chu, T. T. and Oltman, H. G. Jr.,"The Sinuous Antenna," *M.S.N. Communications and Technology*, Vol. 18 No. 6, June 1988.

4 Arm RHCP Planar Spiral Antenna (1.5 Turns/Octave) Mounted over a Lossy Cavity with an Ideal BFN

RHCP Response to Eθ and Eφ Incident Signals
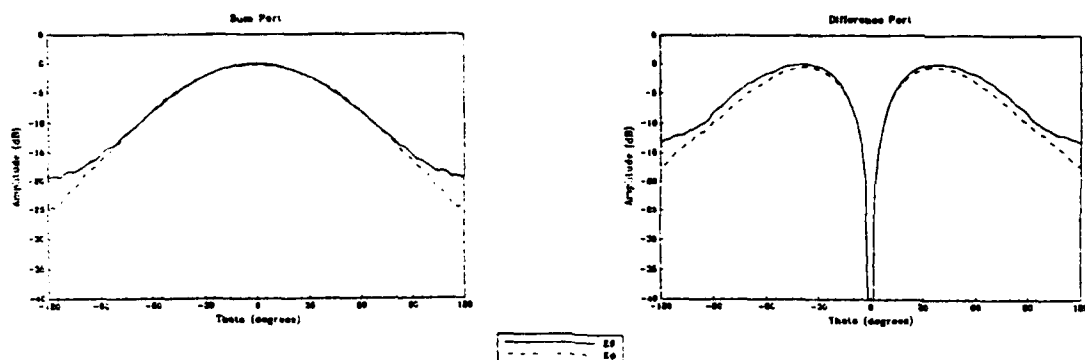
Frequency = 2.0 GHz
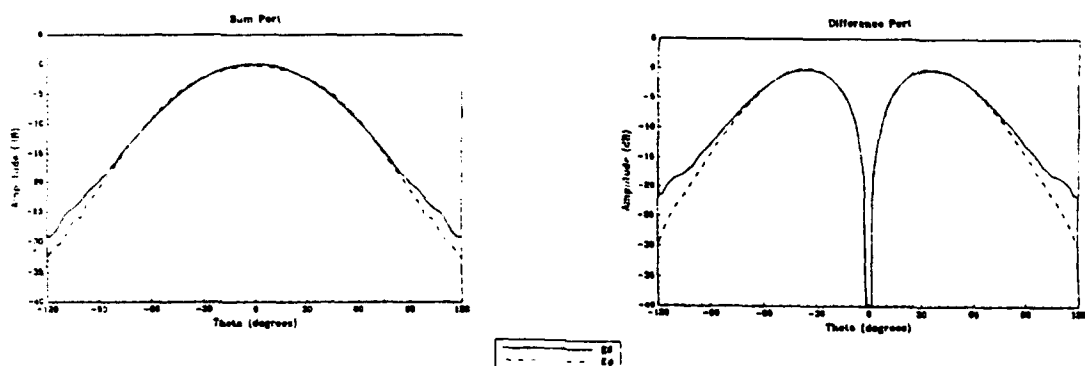
Frequency = 4.0 GHz

Frequency = 6.0 GHz
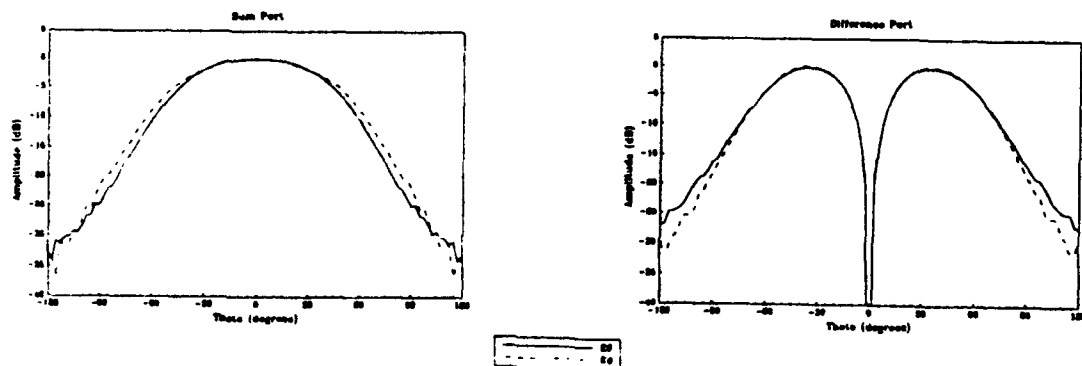
Figure 1

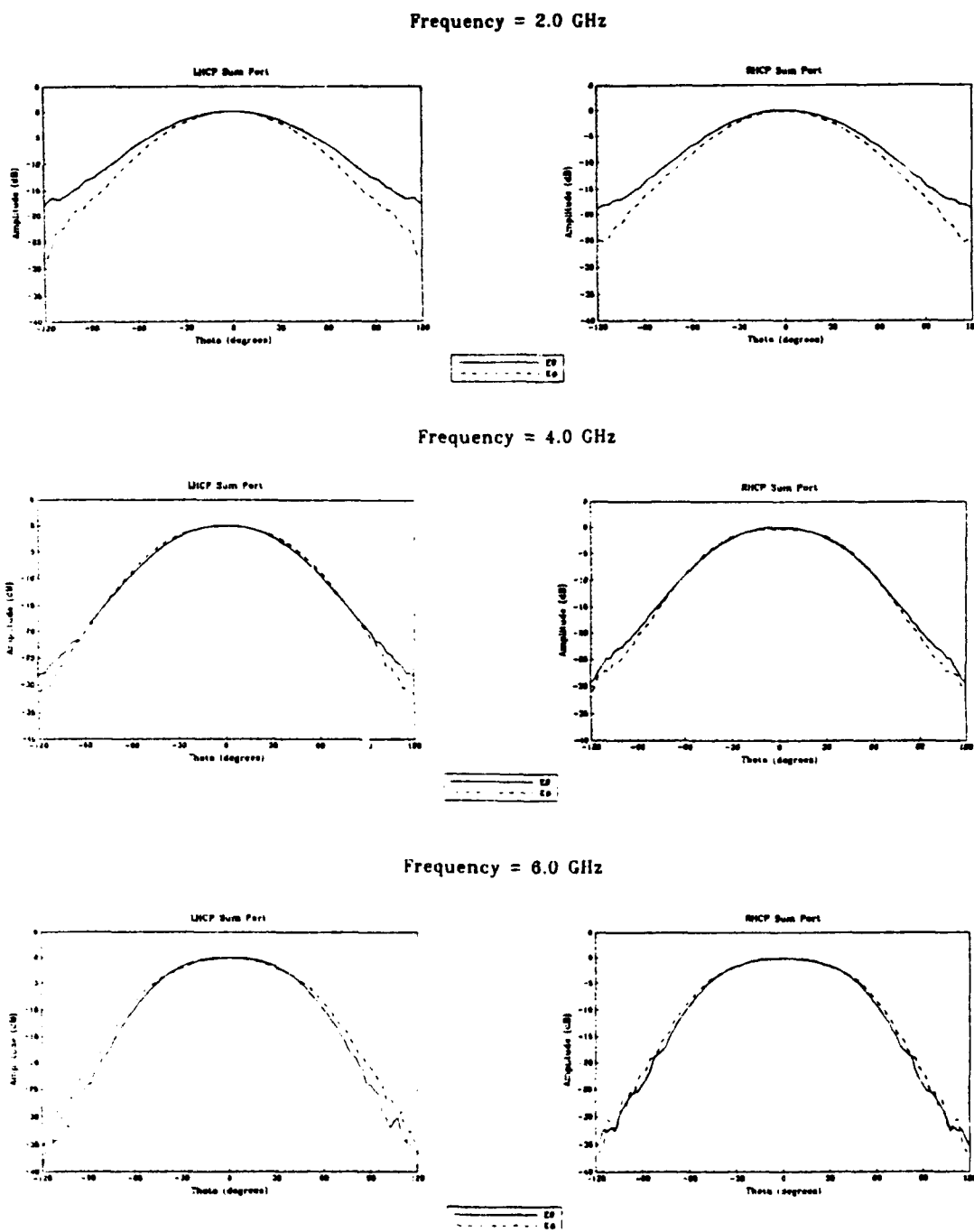# 4 Arm Planar Sinuous Antenna (1.5 Turns/Octave) Mounted over a Lossy Cavity with an Ideal BFN

LHCP & RHCP Responses to Eθ and Eφ Incident Signals

Frequency = 2.0 GHz

Frequency = 4.0 GHz

Frequency = 6.0 GHz
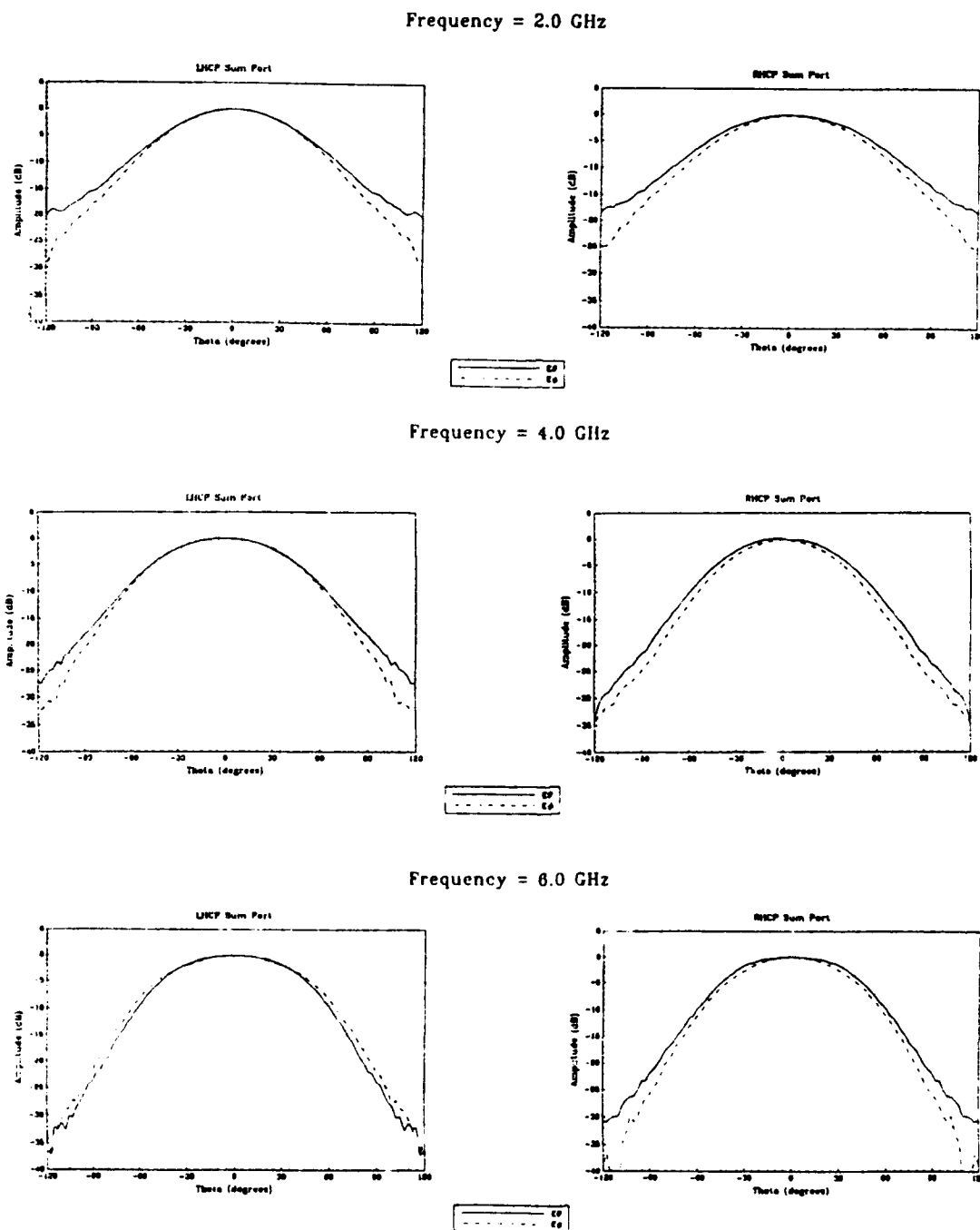
Figure 2

4 Arm Planar MAW Spiral Antenna (1.5 Turns/Octave) Mounted over a Lossy Cavity with an Ideal BFN

LHCP & RHCP Responses to Eθ and Eφ Incident Signals

Frequency = 2.0 GHz

Frequency = 4.0 GHz

Frequency = 6.0 GHz

Figure 3

Four Arm Antenna Geometries

Parent Log Spiral
1.5 Turns/Octave
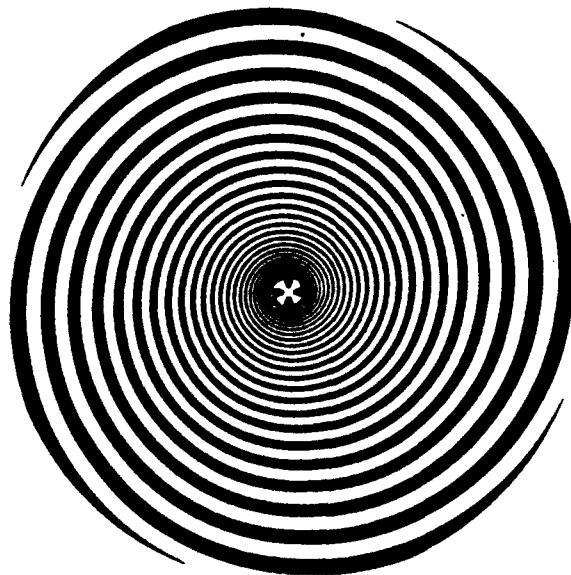
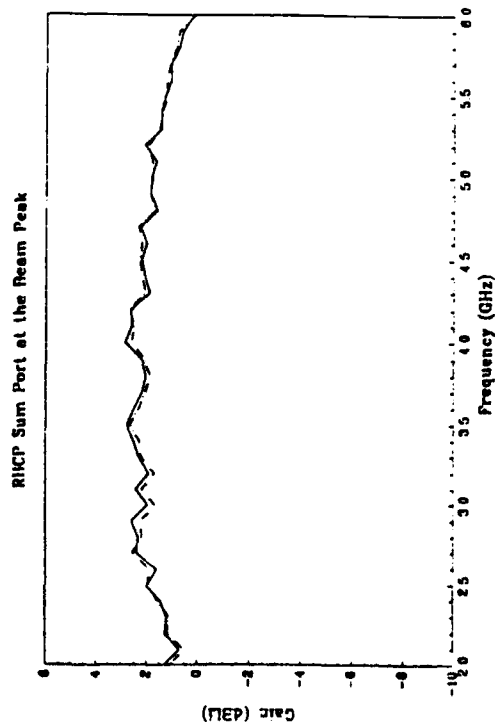**Sinuous (Folded Spiral)**
1.5 Turns/Octave
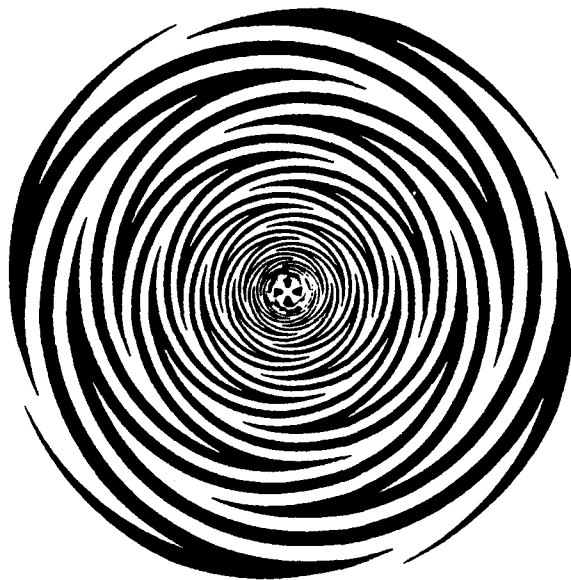
MAW Spiral
1.5 Turns/Octave
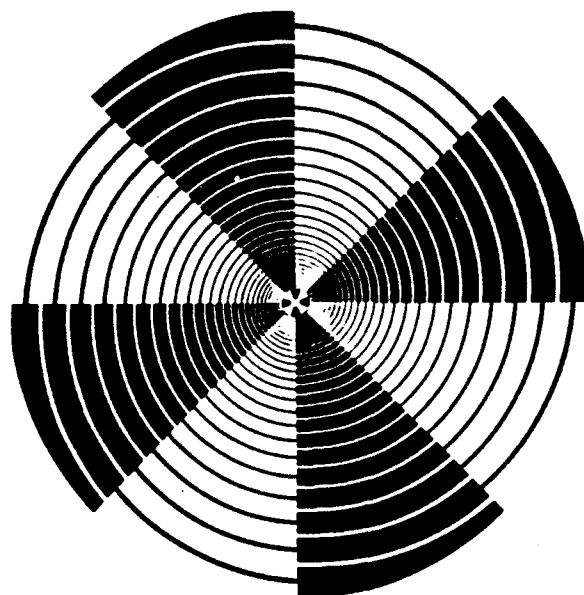
Figure 4

4 Arm RHCP Planar Spiral Antenna (1.5 Turns/Octave) Mounted over a Lossy Cavity with an Ideal BFN
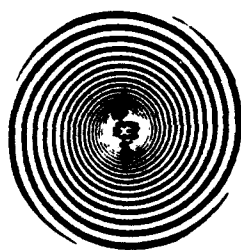
Half-Power Beamwidth vs. Frequency
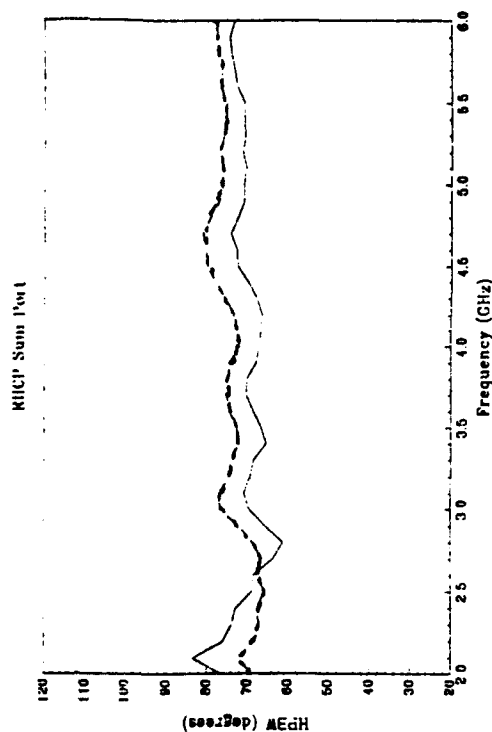
Gain vs. Frequency

Figure 5

4 Arm Planar Sinuous Antenna (1.5 Turns/Octave) Mounted over a Lossy Cavity with an Ideal BFN
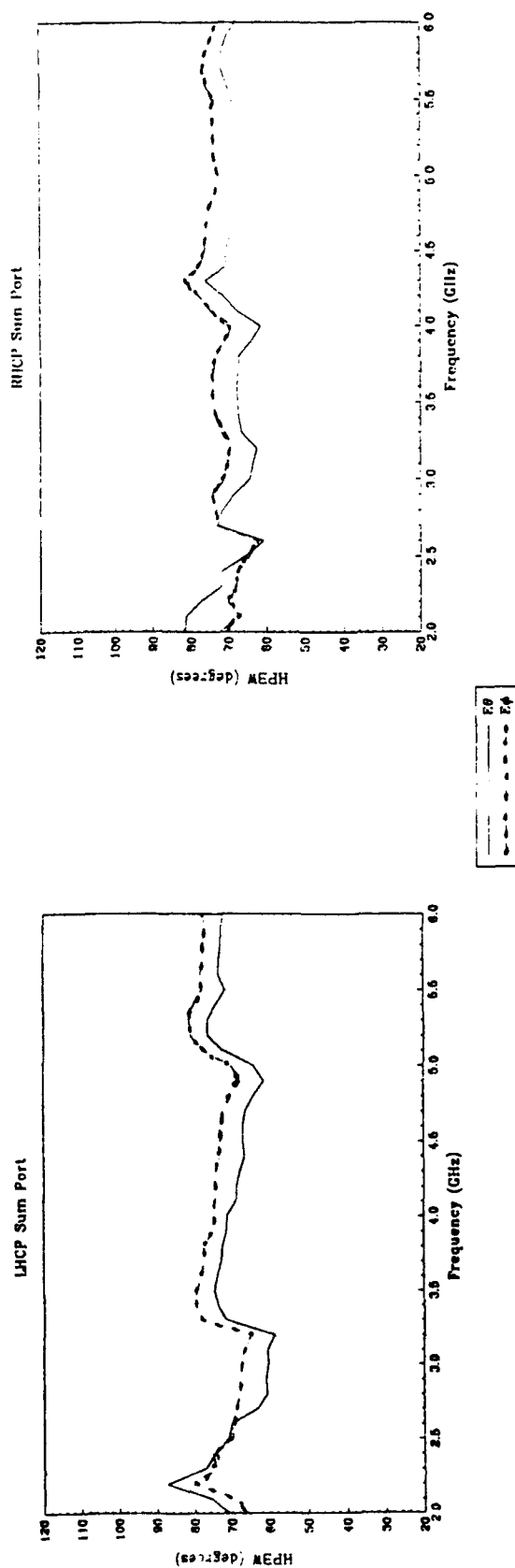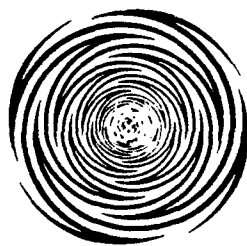
Half-Power Beamwidth vs. Frequency

Figure 6

4 Arm Planar MAW Spiral Antenna (1.5 Turns/Octave) Mounted over a Lossy Cavity with an Ideal BFN
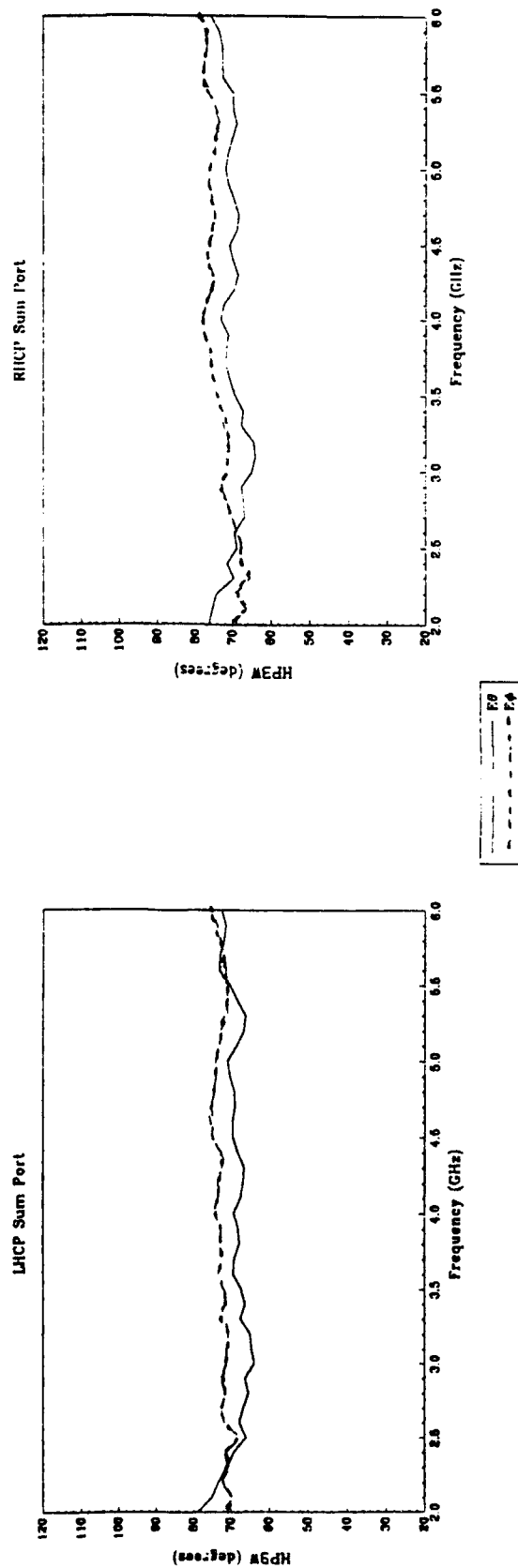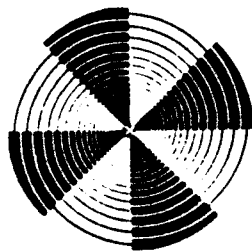
Half-Power Beamwidth vs. Frequency
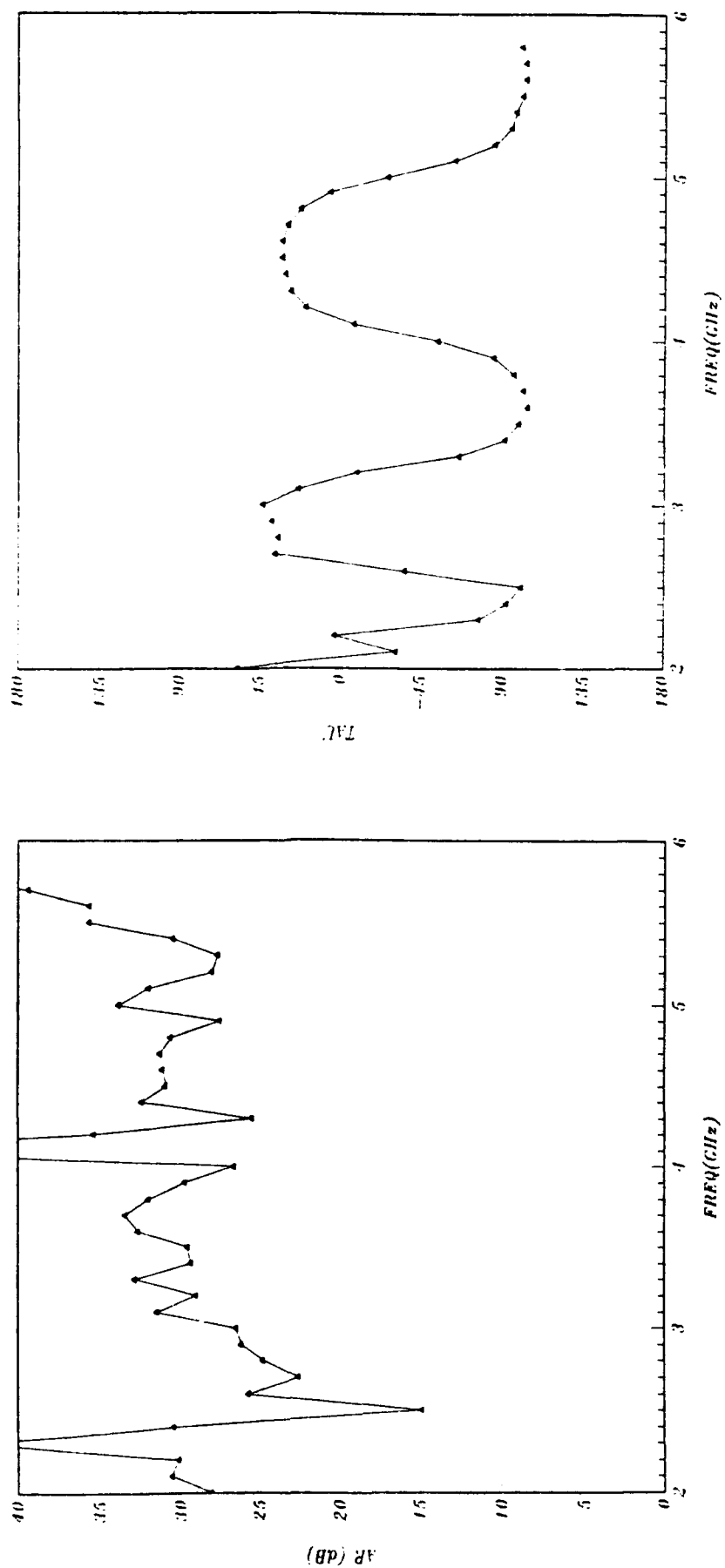

Figure 7

Polarization Properties of a 4 Arm Sinuous Antenna in Orthogonal Linear Mode Operation

Figure 8

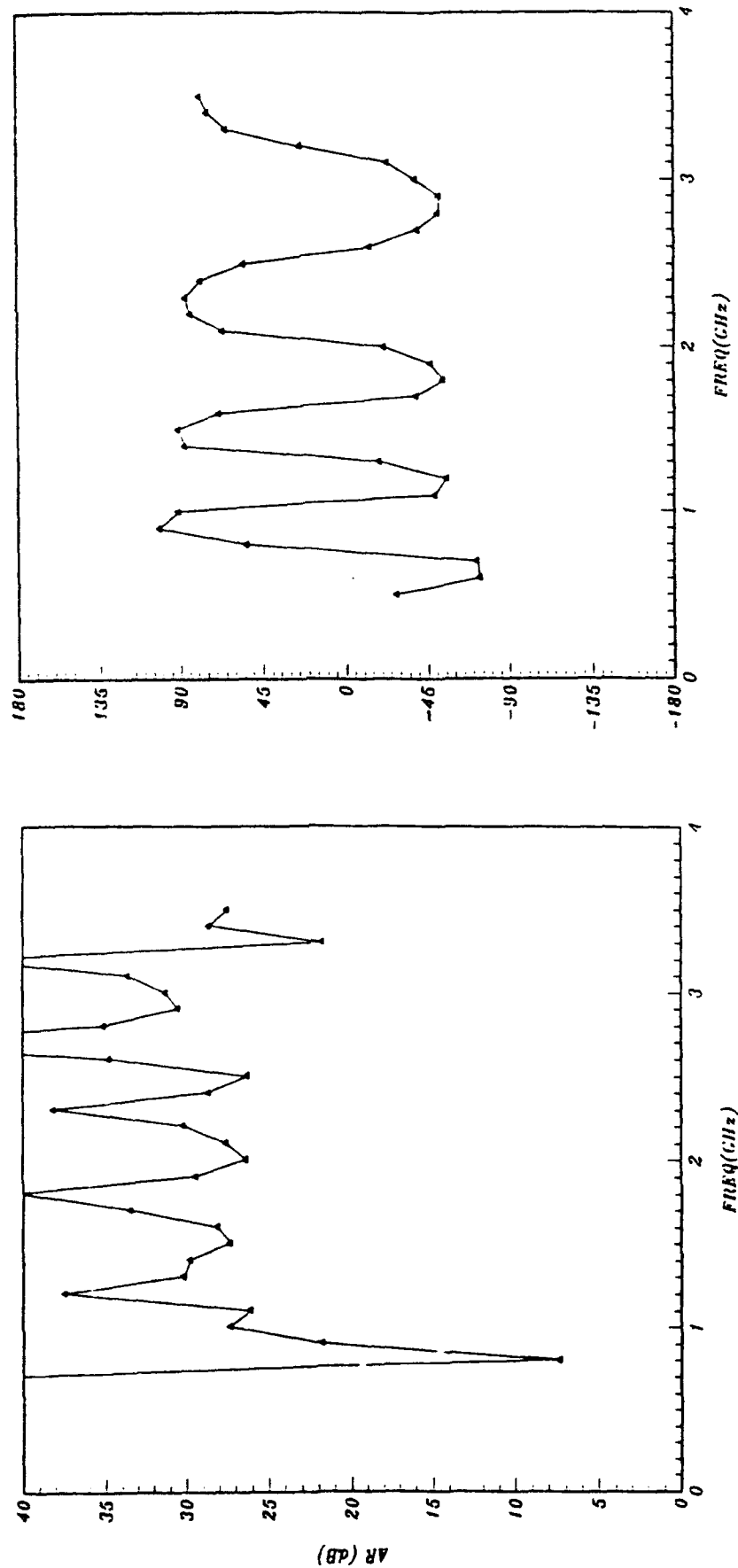# Polarization Properties of a 6 Arm Sinuous Antenna in Orthogonal Linear Mode Operation

Figure 9

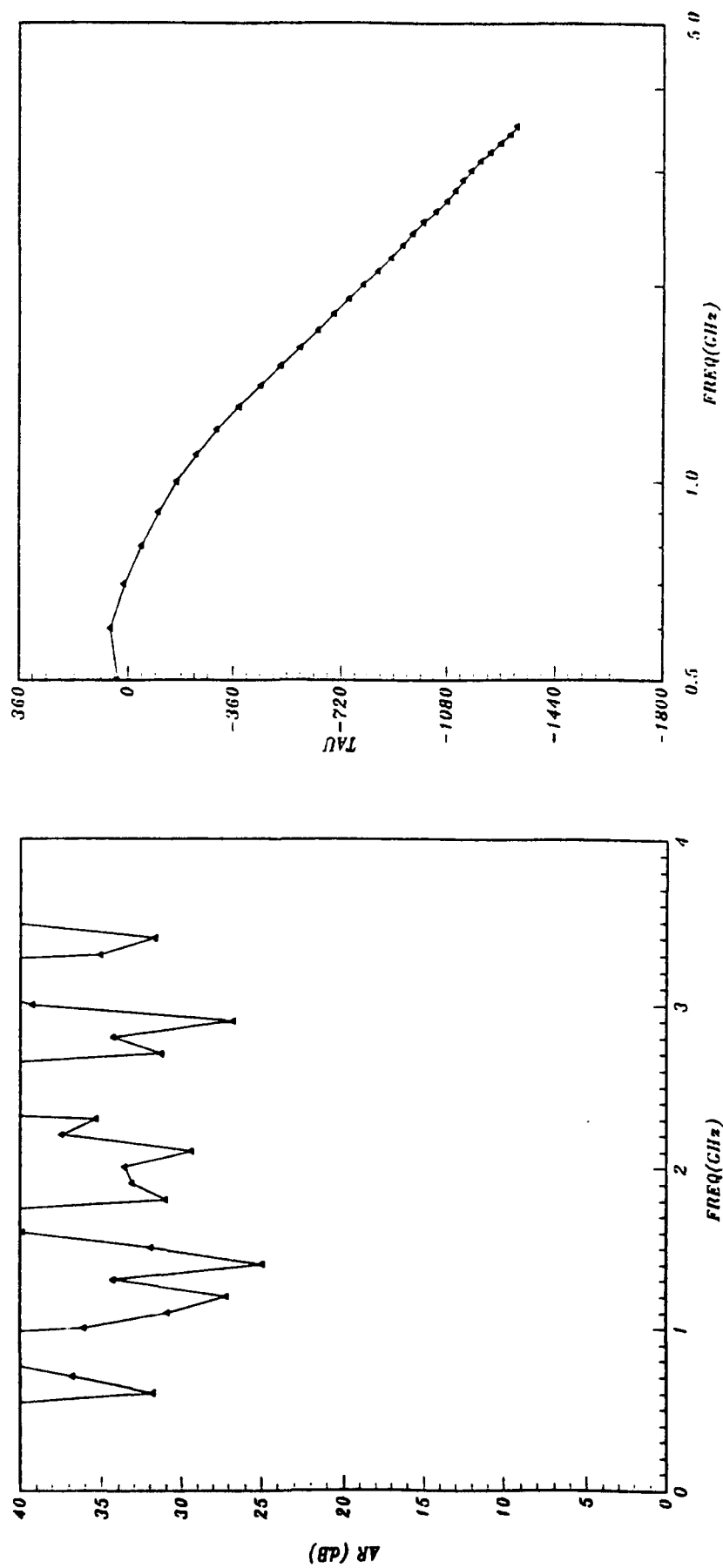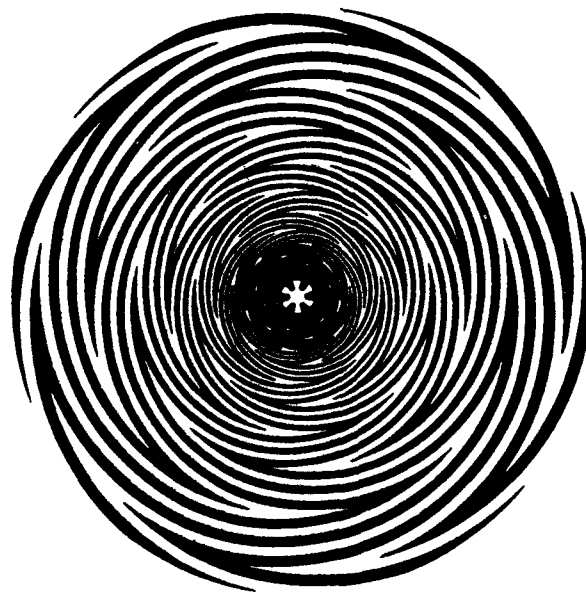# Polarization Properties of a 6 Arm MAW Spiral Antenna in Orthogonal Linear Mode Operation

Figure 10

Six Arm Antenna Geometries

MAW Spiral Antenna
1.5 Turns/Octave

Sinuous Antenna
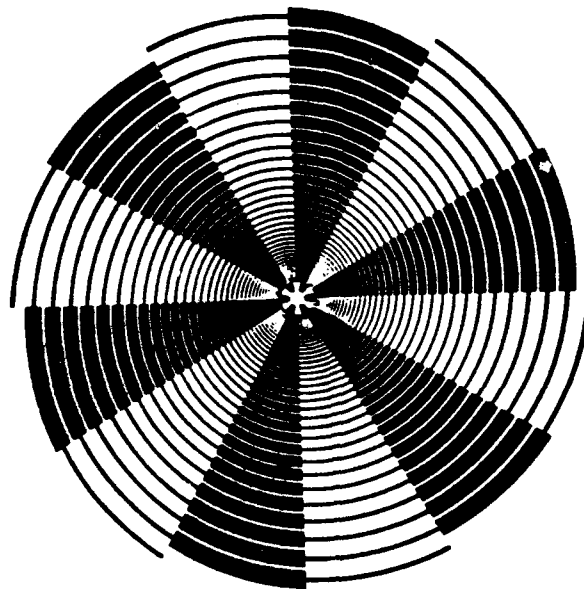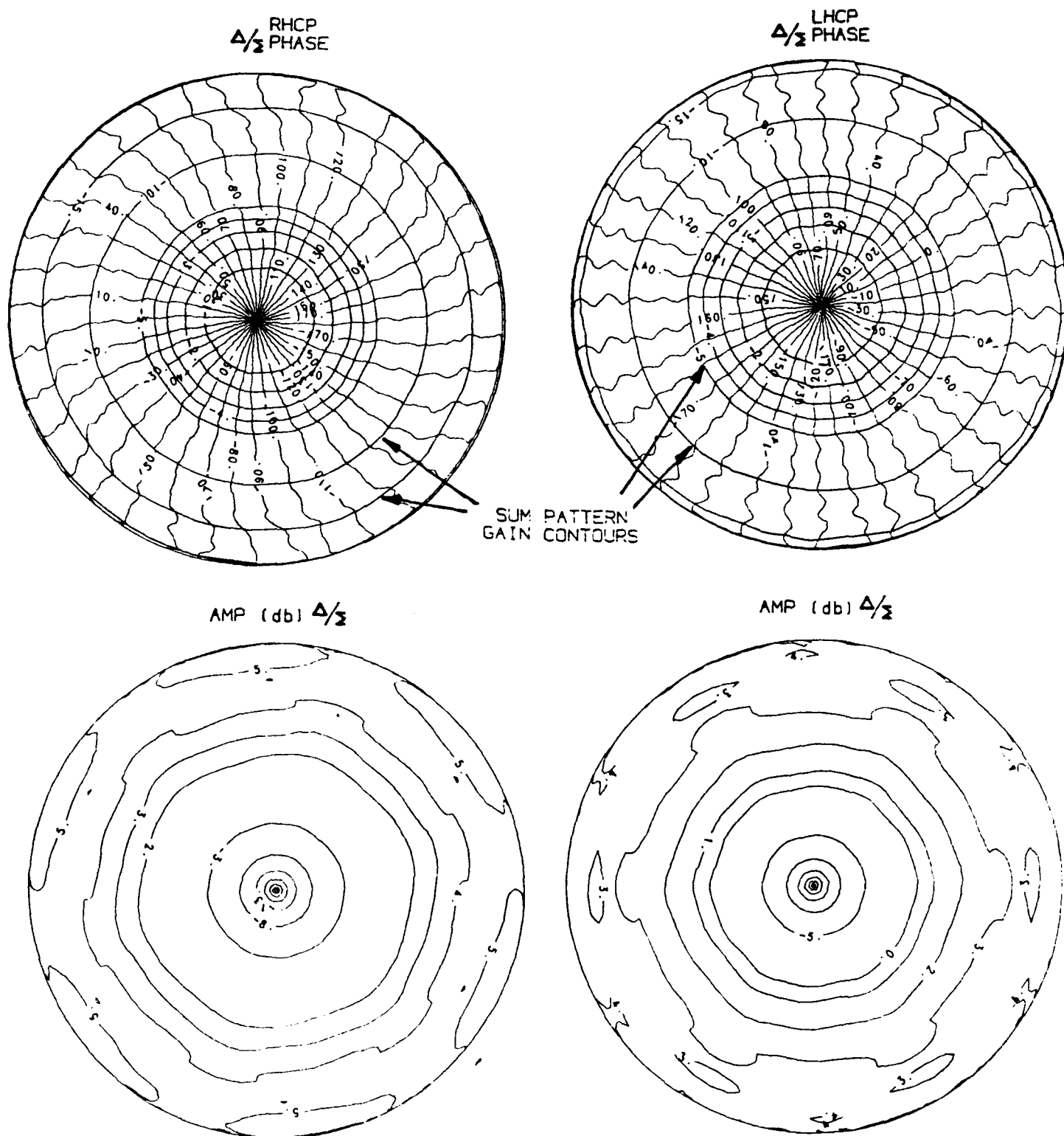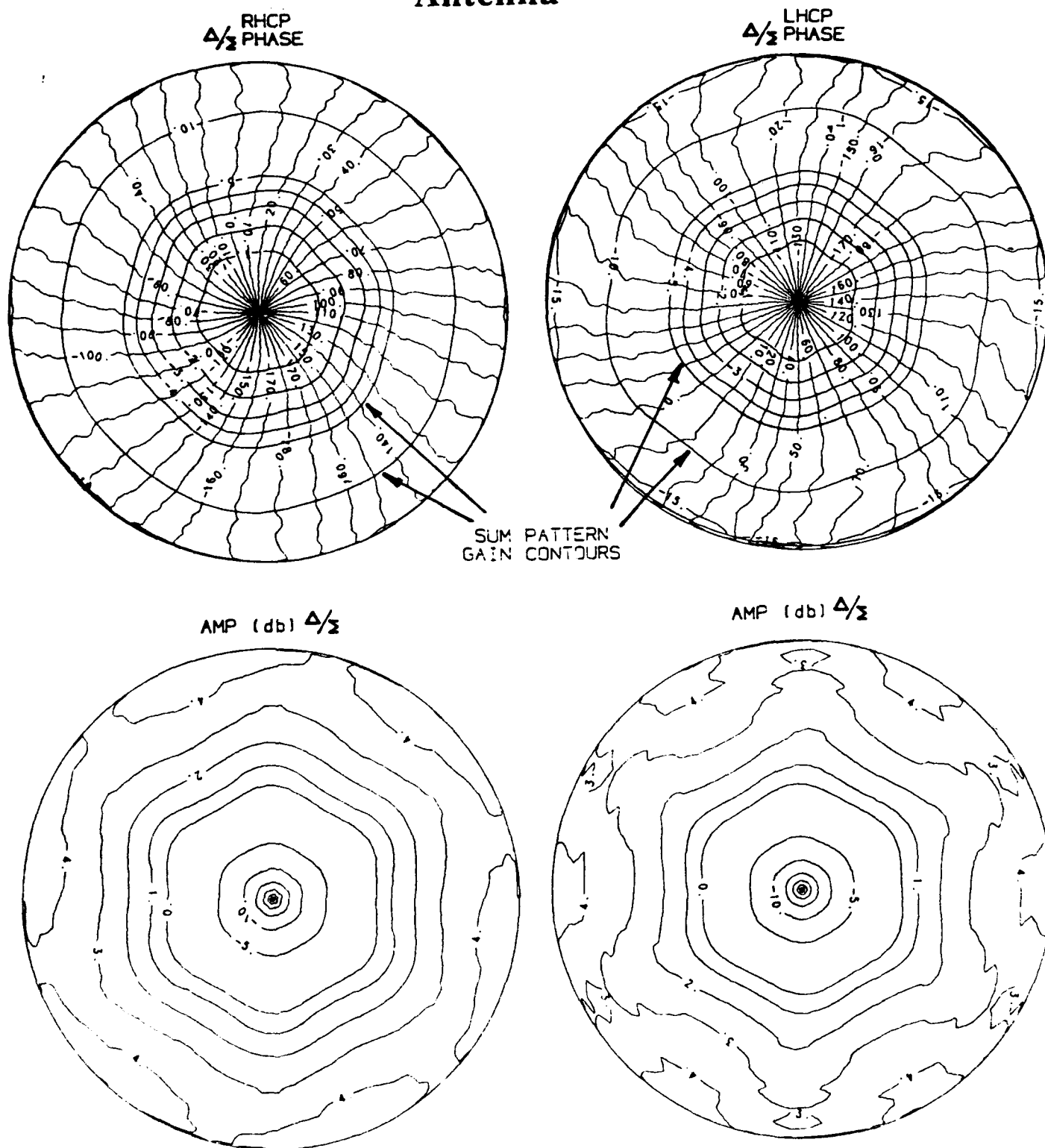1.5 Turns/Octave

Figure 11

Δ/Σ Pattern Behavior of a 6 Arm Sinuous Antenna

Figure 12

Δ/Σ Pattern Behavior of a 6 Arm MAW Spiral Antenna

RHCP
Δ/Σ PHASE

LHCP
Δ/Σ PHASE

SUM PATTERN
GAIN CONTOURS

AMP (db) Δ/Σ

AMP (db) Δ/Σ

Figure 13

LAND MOBILE RADIO PROPAGATION TO SATELLITES

by ALLEN DAVIDSON

MOTOROLA, INC.
SCHAUMBURG, IL.

ABSTRACT

The excess path loss statistics averaged through a 50 Hz bandwidth filter from a satellite to a land mobile platform are shown to be described by two modes, the signal shadowed mode and the two path summation mode. The latter is characterized by a mean near 0 dB and a standard deviation near 2 dB, and the former by a mean that is near 15 dB in the steel canyons of the city, 12 dB in an urban environment, 6.5 dB in a suburban environment and a standard deviation near 5 dB. The characteristics of the signal shadowed mode are very much like traditional terrestrial multipath land mobile propagation. The percent of time spent in each mode is a function of elevation, and varies from 0 percent two path summation when the elevation is near 0 degrees, approaching 100 percent when the elevation is near 90 degrees.

INTRODUCTION

Measurements of path loss to a mobile radio from a satellite platform have often concentrated on areas where the excess path loss above free space is relatively small. This has resulted in many measurements in relatively open areas and where the only blockage is produced by trees [1] [2] [3].   In this study, measurements were made in suburban residential, urban midrise and urban steel canyon areas to quantify the data to all kinds of populated areas where people normally reside.

The Global Positioning System (GPS) presently consists of several satellites orbiting the earth at an altitude of 20,000 km [4]. These satellites radiate circularly polarized signals at L band which are precisely timed so that a receiver which can detect signals from 4 or more of the satellites can determine its precise location in three dimensions.

The system was designed to operate in a free space environment, however, there is sufficient signal strength to permit operation of the system where there is some shadowing of the signal. The signals from the satellites have therefore been used to measure the excess path loss to a terrestrial land mobile receiver in several environments.

The environments will be described in detail, the measured data will be presented, and a model of the mechanism of propagation will be proposed which fits the experimental data. This model is also consistent with a geometrical description of the propagation path.

MEASUREMENT SYSTEM

The block diagram of the prototype receiver used in the measurements is shown in Figure 1. The receiver front end consisted of analog discrete components through the mixer down converter. An Analog to Digital (A/D) converter then digitized the signal for processing by a high speed Digital Signal Processor (DSP).
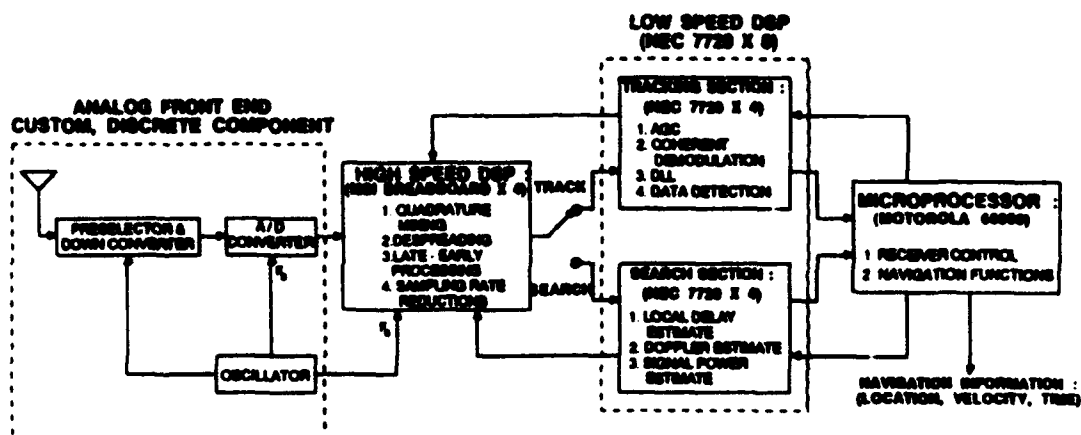

Figure 1. Block diagram of the prototype 4 channel GPS receiver used to make the received signal measurements.

The signal was split into quadrature components at this point, and the sampling rate was reduced. The resulting signal was fed to a slow speed DSP where coherent demodulation and data detection took place.

An AGC circuit was implemented here with a dynamic loop bandwidth which averaged 50 Hz. This AGC voltage was calibrated and used as a measure of the received signal strength. The minimum signal strength which was detectable was -150 dBm at a signal to noise ratio near 0 dB, and the maximum signal received throughout the measurement program was -115 dBm. The resulting dynamic range of the AGC used throughout this program was therefore 35 dB.

The signal level as well as the position information was fed to a M68000 microprocessor which computed the location information of the vehicle as well as the elevation of the satellite. All of the resulting information was recorded on magnetic media for analysis at a later time. The equipment was installed in a 1986 Ford Econovan with a quadrifilar helix antenna with a maximum of 3 dB of gain mounted near the center of the roof of the van to receive the 1575 MHz signals.

MEASUREMENT ENVIRONMENT

Measurements were made in 3 geographical locations shown in Table 1. 175 test miles were driven accumulating 56,500 measurements of received power. All geographical environmental types except European Midrise were encountered in the Chicago area; the Boston area was the only location tested where this European type of environment was encountered. The definitions of the environments quantified for this test program are included in Table 2. By careful definition, it is hoped that it will be possible to predict the propagation based on the measurements reported herein.

TABLE 1
Field Test Location Summary

LOCATION	NUMBER OF DATA POINTS	ROUTE LENGTH IN MILES	ENVIRONMENT
Chicago, IL	27,900	85	Sub. Residential Urban Midrise Urban Highrise Steel Canyons
New York, NY	11,600	45	Urban Midrise Steel Canyons
Boston, MA	17,000	45	Urban Midrise Urban Highrise Urban European

TABLE 2
Definitions of the Environmental Areas Where Data Was Taken

ENVIRONMENT	SUBURBAN RESIDENTIAL	URBAN MIDRISE	URBAN EUROPEAN	URBAN HIGHRISE	STEEL CANYON
PARAMETER					
BUILDING HT. (max, min, avg : ft)	30, 15, 25	100, 30, 50	70, 30, 50	1000, 50, 120	1500, 100, 350
BUILDING TYPE	SINGLE FAMILY HOMES	COMMERCIAL, APARTMENT, TOWN HOUSE	COMMERCIAL, APARTMENT, TOWN HOUSE	COMMERCIAL	COMMERCIAL
BLDG. MATERIAL	WOOD, BRICK, ALUMINUM	BRICK, STONE, STEEL	BRICK, STONE, WOOD	STEEL, GLASS, STONE	STEEL, GLASS STONE
BUILDING SEPARATION (cross-street, adjacent : ft)	100 - 150, 15 - 40	40 - 80, 0 - 10	25 - 40, 0 - 5	50 - 100, 0 - 40	50 - 80, 0 - 20
TREE COVER	MODERATE / HEAVY	LIGHT / MODERATE	NONE / LIGHT	NONE / LIGHT	NONE

The number of measurements made in each environment are graphed in Figure 2. The elevation of the satellite was recorded for each measurement, and this permits the data to be grouped in convenient ranges. The elevation angle is defined as the angle from the horizontal up to the satellite. There was insignificant data below the elevation of 10 degrees for several environments because the large excess path loss which exists at these low elevations frequently reduces the signal below the sensitivity of the receiver. At higher elevation angles, above 65 degrees, the calibration described in the next section was unavailable, and therefore, that data was not processed. Analysis has been completed on the Suburban Residential, Urban Midrise, and Steel Canyon data, and the results of the analysis on that data will be reported herein.
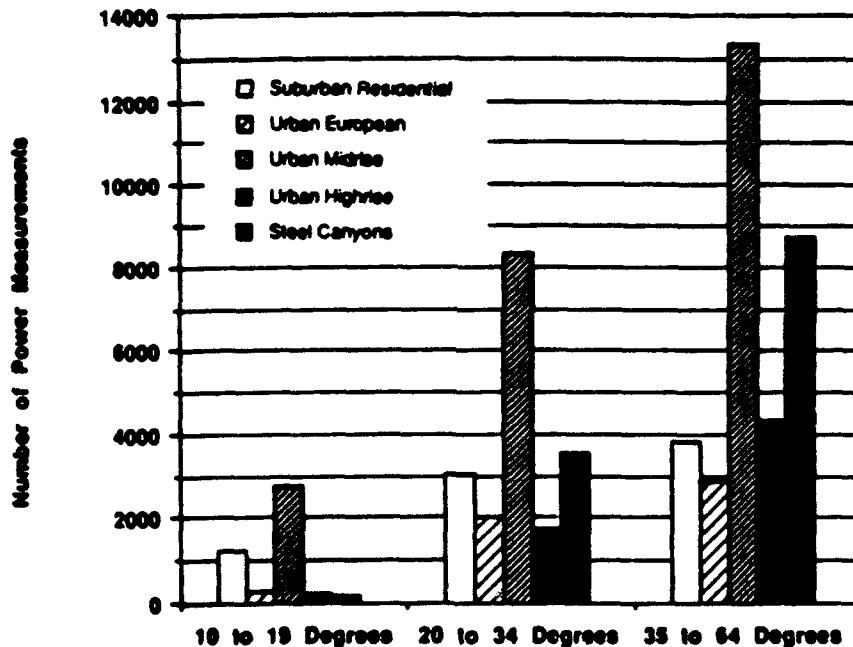

Figure 2. The quantity of data taken in each environment is indicated as well as the elevation at which it was taken.

MEASURED DATA

The van was driven within the test areas at an average speed of 20 MPH. The maximum speed was about 40 MPH and the minimum was 0 as the van came to a stop at stop signs and stop lights. Data was taken approximately every 2 seconds, though at long stops data collection was suspended until the vehicle started to proceed again. At the average speed of 20 MPH, the 50 Hz loop bandwidth of the AGC was adequate to average the signal over about one wavelength.

A simulation of the AGC circuit was run with a Rayleigh distributed signal with zero
mean at a speed of 20 MPH to determine the characteristics of the AGC response.
Figure 3 shows the zero mean signal and the AGC response to that signal. The deep
nulls of the Rayleigh signal are all averaged out, however, the peaks are not always
removed. A stistical analysis of this data shows a slight positive bias with some of the
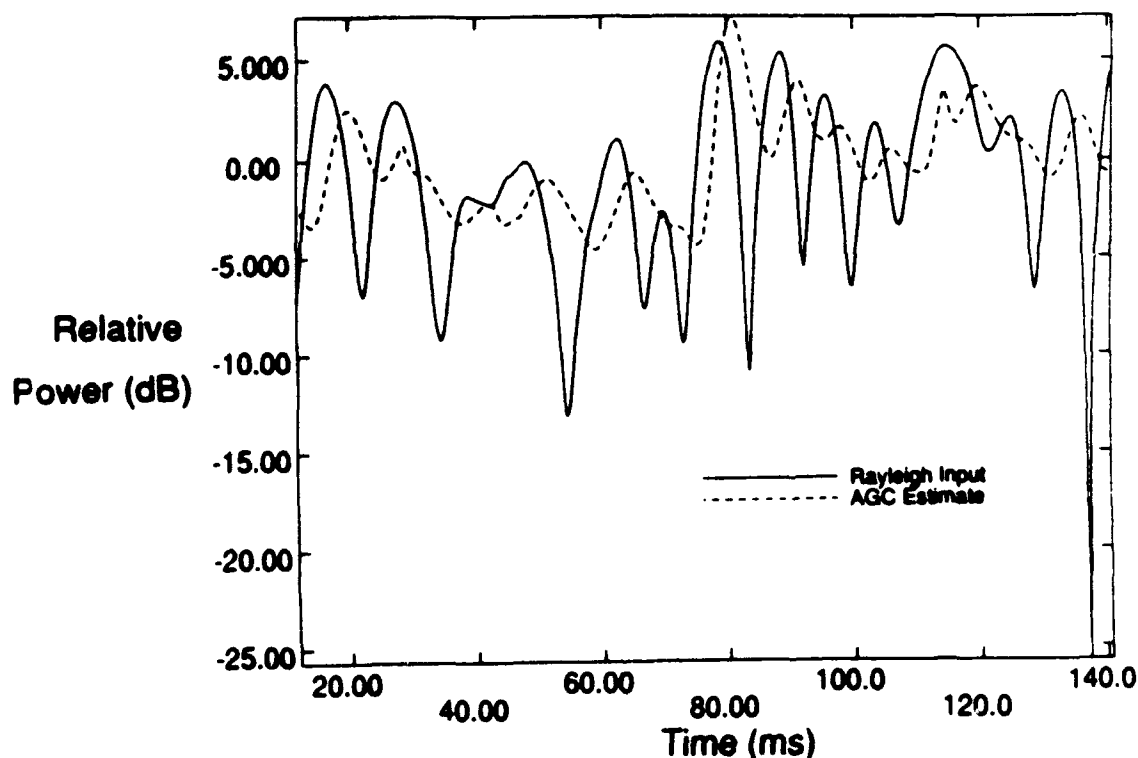short term variation left in the data.

Figure 3. Simulated AGC response of the receiver to a zero mean Rayleigh
distributed signal is superimposed on the received signal. The
vehicle is traveling at 20 MPH.

Examples of the measured received signal as a function of time are shown in Figures
4 and 5. In the suburban residential environment, shown in Figure 4, two
characteristics are readily apparent. First, when the elevation to the satellite is high,
for instance in channel 1 at 70 degrees, the signal does not fade very deeply. And
second, at the lower elevations as in channel 4 at 20 degrees, when the signal does
fade it does not stay low very long.

In Figure 5 where the urban midrise data is presented, the first characteristic is still
evident as seen in channel 1, but the second is no longer present. There are times
when the vehicle passes a large obstruction, for instance in channel 3 at about 22
minutes, and the signal stays in a 20 dB fade for periods of minutes with only brief
excursions above the fade floor. The data for the Steel Canyons exhibits similar
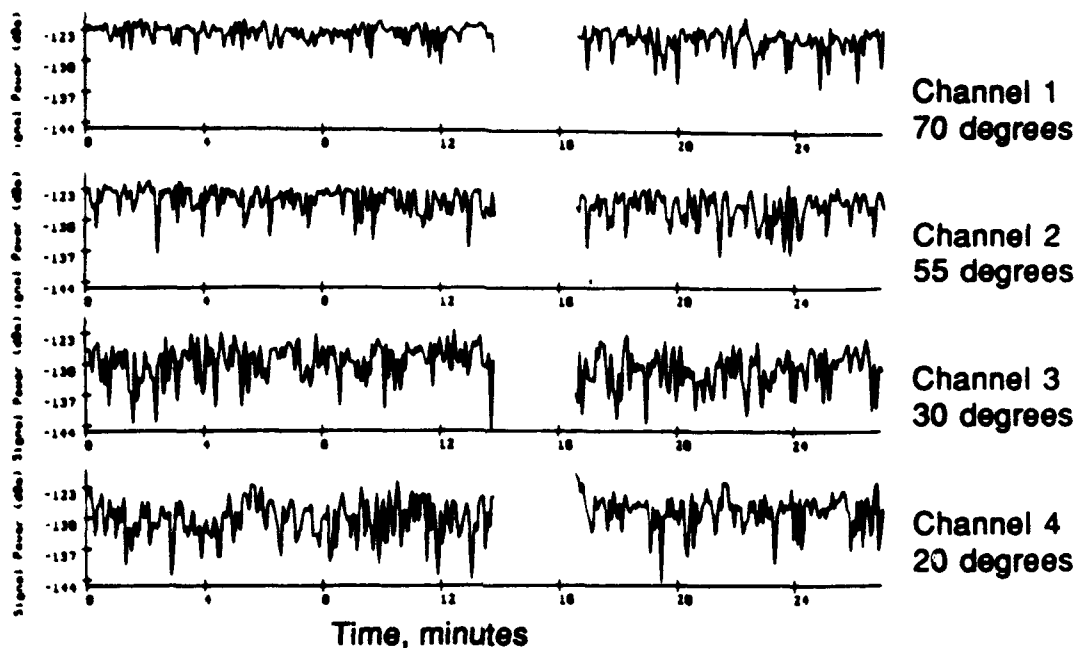characteristics to this latter case.

Figure 4. Received signal on the four channel receiver as a function of time in the suburban residential environment.
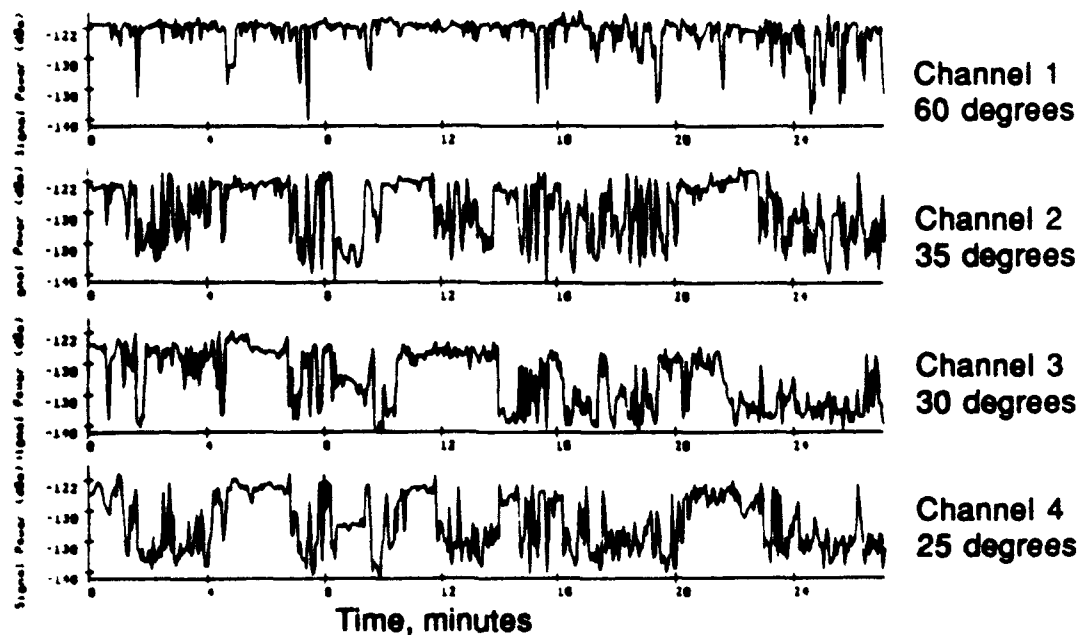
Figure 5. Received signal on the four channel receiver as a function of time in the urban midrise environment.

In order to convert the received signal strength to excess path loss, a means had to be determined which would remove the effect of many variables. The power from the satellite remained a constant, however, the distance to the satellite was a variable, so the free space path loss varied. The angle to the satellite varied so the pattern of the satellite antenna as well as the mobile antenna changed.

It was hypothesized that these effects could be removed by making a measurement in a clear area, free of all obstructions. That measurement as a function of elevation could serve as a calibration for the system. In order to get excess path loss at a particular elevation angle, the calibration value could be subtracted from the measured signal strength at that elevation.

Figure 6 shows the resulting signal strength comprising 13,300 measured data points with a best fit average for use as the calibration. At lower elevation angles the effect of the reflection of the earth is evident in producing a diffraction pattern.
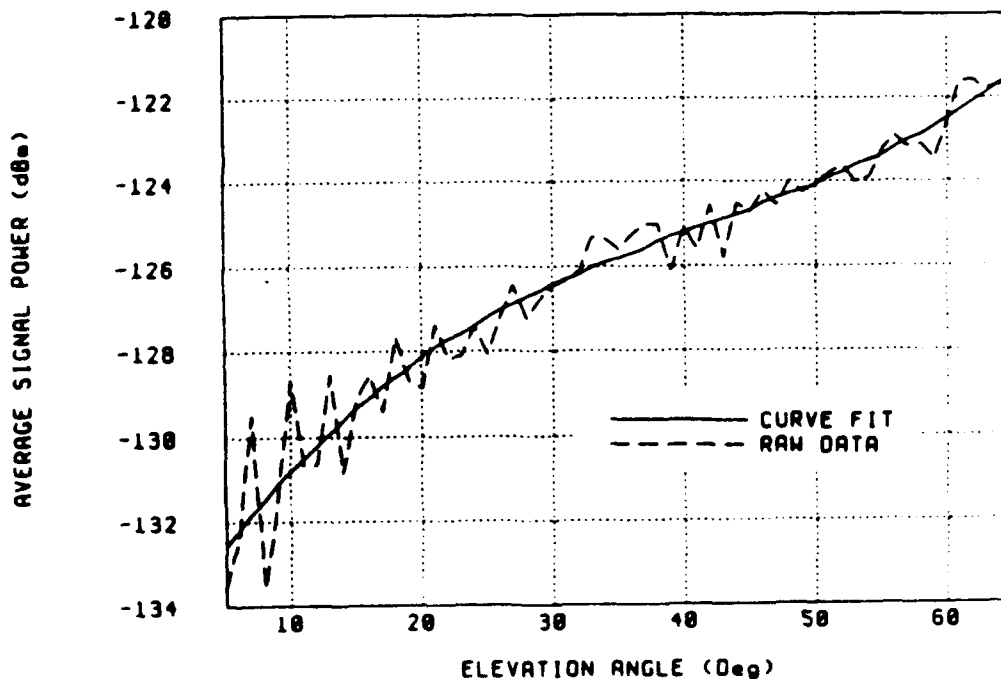

Figure 6. Received signal measurements in the open environment of the Thunderbird Country Club in Rolling Meadows IL. used for calibration of the excess path loss.

The inflection point at an elevation angle of about 50 degrees was of concern, because it appears that the signal is going to continue upward without limit at the higher elevation angles. However, the pattern of the quadrifilar helical antenna does have a point of inflection at that angle. A crude computation of the received signal

461

was made based on the ERP of the satellite, the free space path loss, and the receiving antenna pattern. This computation was within 2 dB of the measured values, and the computed signal does indeed arrive at a maximum at 90 degrees. So it was concluded that this calibration method is valid.

Figures 7, 8, and 9 show the measured Cumulative Distribution Function (CDF) for the elevation ranges previously identified. Several features can be pointed out. First, the left side of all of the curves are grouped and show very near the same mean and standard deviation lognormal characteristics. Second, there appears to be two distinct processes involved one on the right and the second on the left of the curves with a large transition in the center between the two. These trends have been reported previously in data reported by Hess [5]. Finally, there is data compression on the right because of the finite dynamic range of the receiver. These will be discussed in reverse order in the data analysis section.
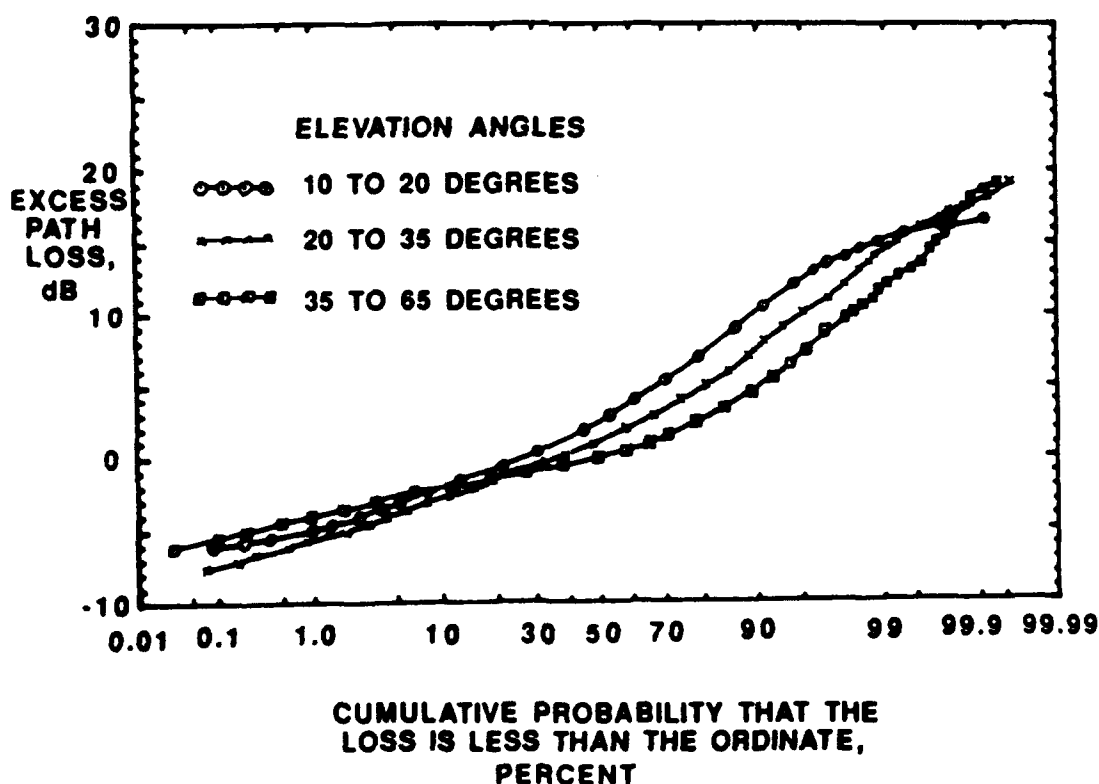

Figure 7. Measured CDF of the excess path loss as a function of elevation angle in the Suburban Residential environment.
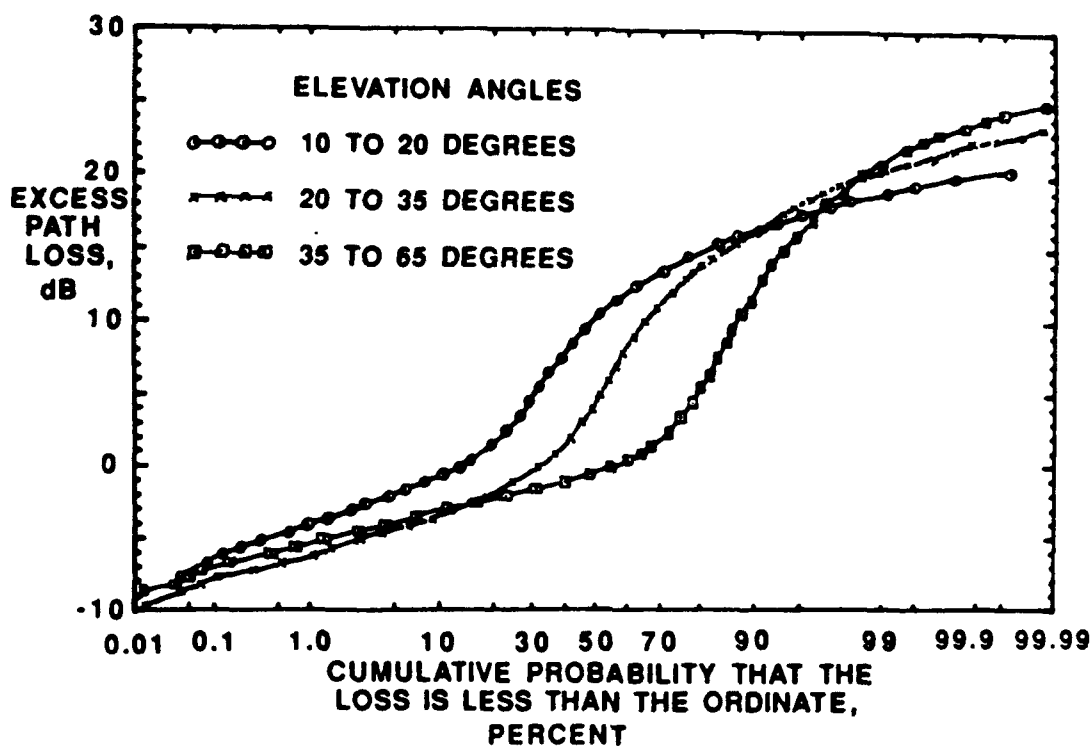
Figure 8. Measured CDF of the excess path loss as a function of elevation angle in the Urban Midrise environment.
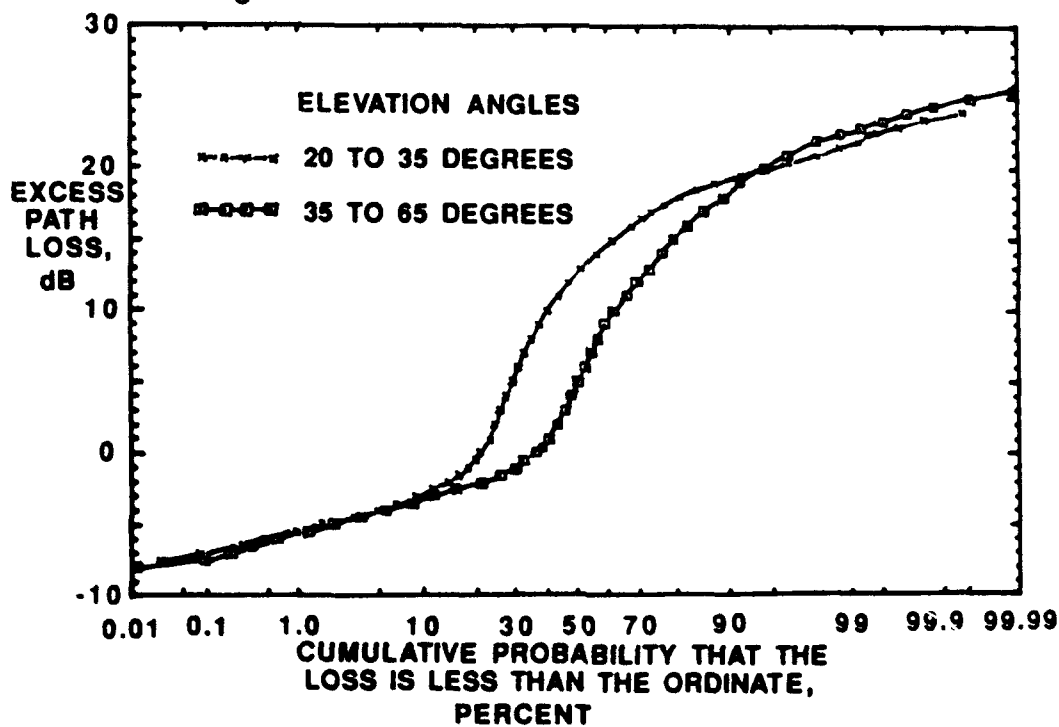

Figure 9. Measured CDF of the excess path loss as a function of elevation angle in the Steel Canyon environment.

Figures 10 and 11 show the measured time variation of the Suburban Residential and Urban Midrise data. Figure 10 shows the fade rate and figure 11 shows the CDF of the fade duration at a 6 dB level. This data is only applicable for satellites which operate at an elevation near 20,000 kM, such as the GPS satellites, since the motion of the satellite influences the result.
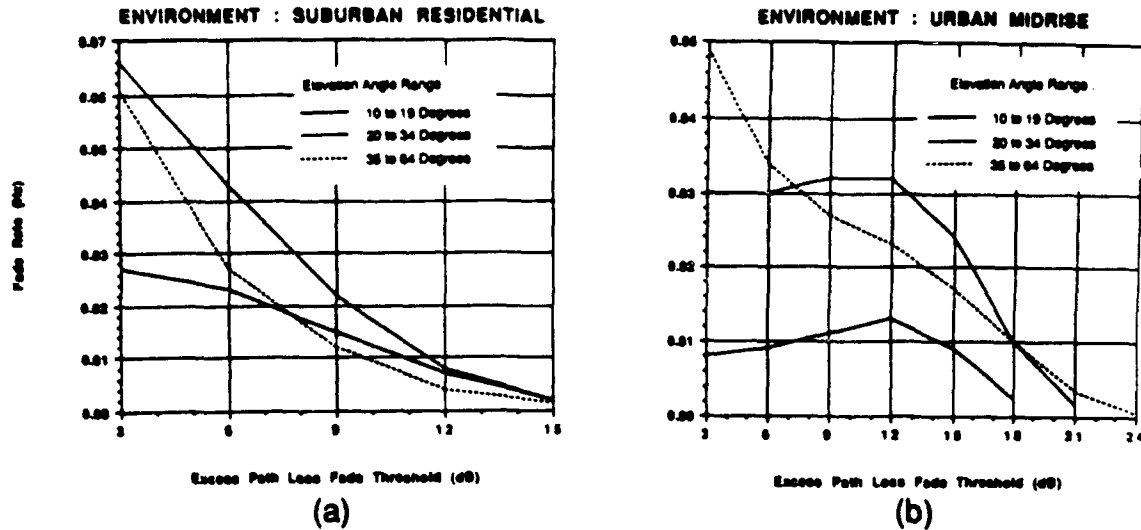

(a)   (b)

Figure 10. Rate of fade of the signals in the (a) suburban residential environment, and (b) urban midrise environment.
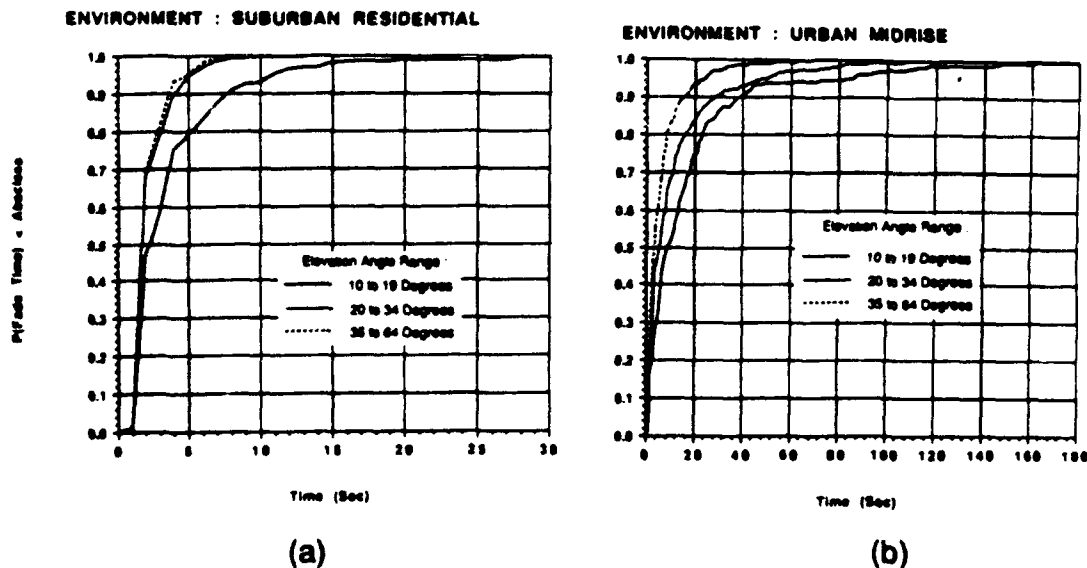

(a)   (b)

Figure 11. CDF of fade duration for a fade of 6 dB in the (a) suburban residential environment, and (b) urban midrise environment.

DATA ANALYSIS

Data Compression
The graphs in Figures 8 and 9 most clearly show data compression. On the right portion of the curves, the highest curve is for the elevation range from 35 to 65 degrees, next is 20 to 35 and the lowest is 10 to 20 degrees. Recall that the excess path loss is produced by subtracting the received calibration from the field test data. Reference to Figure 6 shows that the absolute value of the signal subtracted from the received test signal is greater at lower elevation angles than at higher angles. Thus, the dynamic range should be greater at higher elevation angles, and this is exactly what is seen.

Propagation Modes
There appear to be two processes or modes producing the data of Figures 7 - 9. Upon reflection, these can be explained by two mechanisms. First, there is what will be called the two path summation mode which is illustrated in Figure 12. At low elevation angles, the two paths can be the direct path from the satellite and one reflected from the earth as illustrated in Figure 12 (a). At higher elevation angles where the mobile or portable antenna suppresses the earth reflection, the second path may come from reflection from buildings at the side of the path of travel as illustrated in Figure 12 (b).

It is expected that two path summation will produce signal levels near free space with the vector sum producing addition and subtraction from the free space value. This is the process producing the data on the left side of Figures 7 - 9.
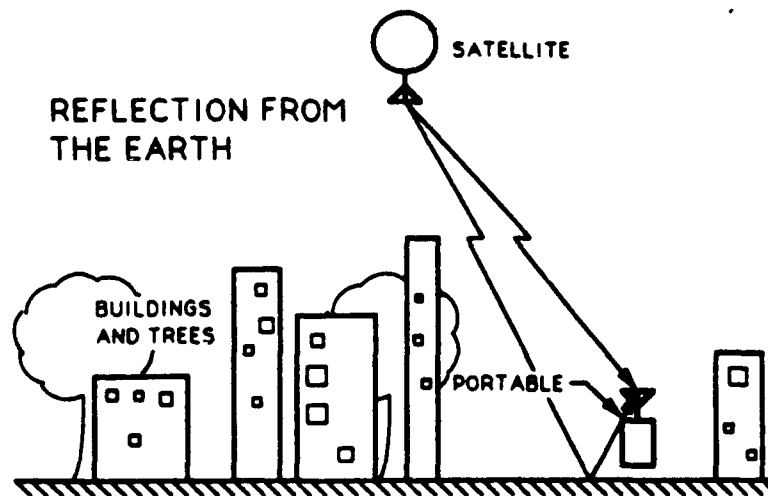

Figure 12 (a). The "two path summation" model is illustrated as the vector sum of two dominant waves arriving at the subscriber unit. The first is

REFLECTION FROM A BUILDING
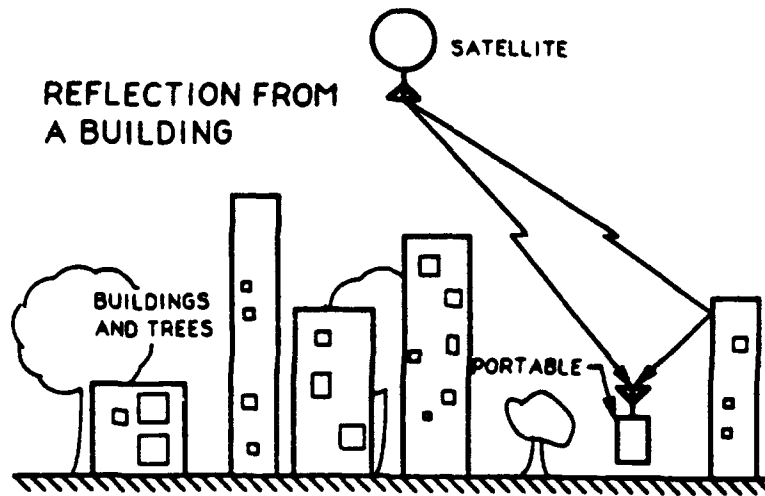
Figure 12 (b). The "two path summation" model is illustrated as the vector sum of two dominant waves arriving at the subscriber unit. The first is the direct wave, and the second is a reflection from a building.

The second process is what will be called the signal shadowed mode which is illustrated in Figure 13. Here the direct wave is kept from view of the satellite by intervening buildings and trees. Thus, the signal arrives from many directions via reflections and diffraction around the obstructions. This process produces the data on the right side of Figures 7 - 9.

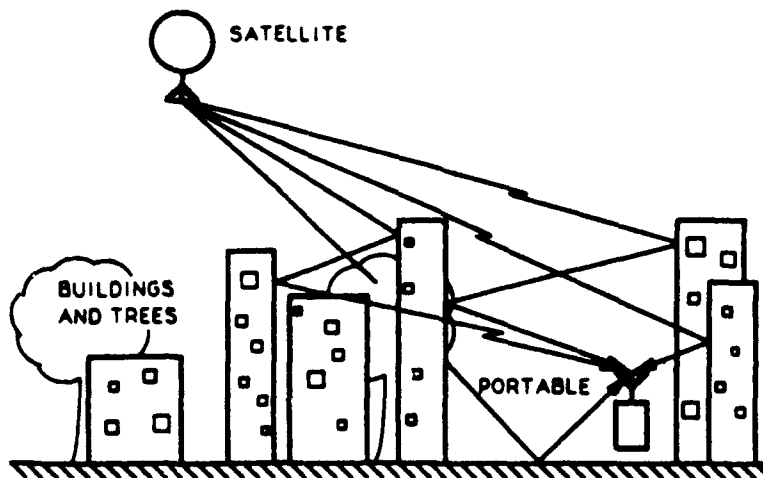Figure 13. The "signal shadowed" model is illustrated as the vector sum of many waves arriving at the subscriber unit from many directions while the direct wave is blocked from direct view.

The transition region in the curves of Figures 9 - 11 progresses from left to right as the elevation angle increases. It is implied that the portion of the time spent in the two path mode is increasing as the elevation increases. This also fits the intuitive view because the satellite should be visible more of the time when the elevation angle is higher.

Simulation Model

In order to quantify the time spent in each mode, and the value of the lognormal parameters assumed for each mode, a simulation was written to fit the data in Figures 9 - 11. The simulation consisted of two lognormal random variables with independent mean and standard deviation. The one with lower mean was limited to a minimum random draw of 7 dB below free space propagation loss. The one with the higher mean was limited to a maximum random draw which was a variable of the simulation to set the receiver noise floor. The other variable in the simulation was the percent of time spent in each mode.

The simulation was run for 10,000 draws each time, and the variables adjusted to fit the measured data. Figure 14 shows the fit obtained for the data obtained over the range of 20-35 degrees in the urban midrise environment. In general the fit is within 0.5 dB.
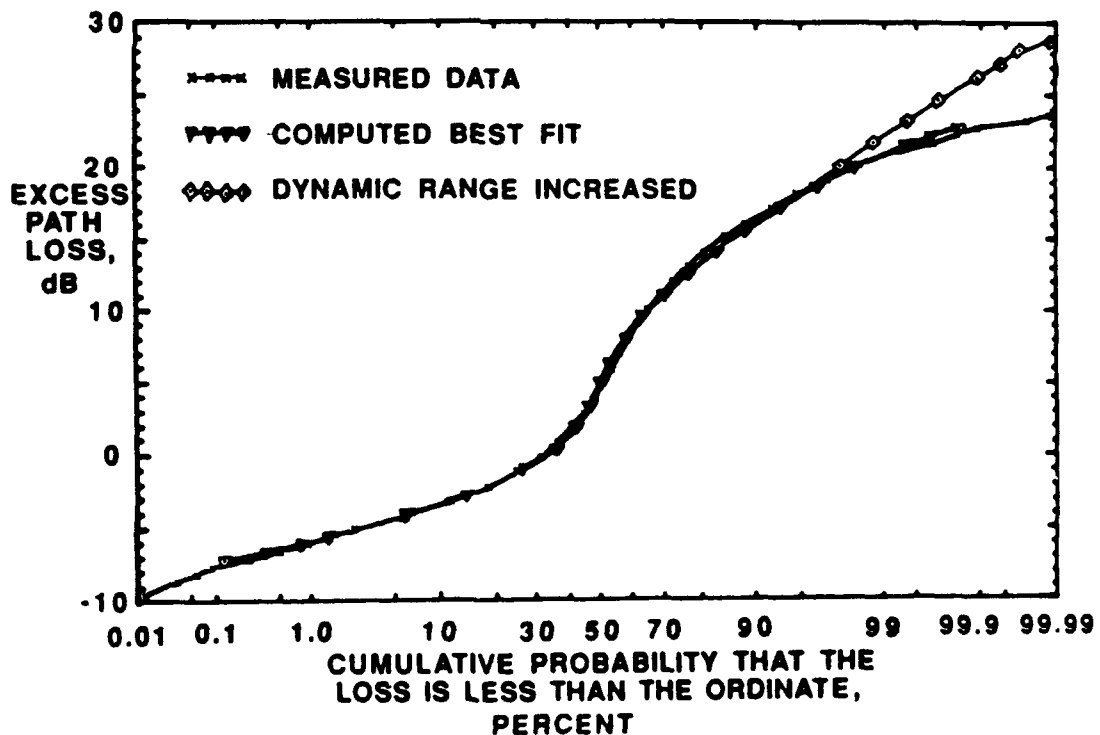
Figure 14. Comparison of measured data and the data fit using the simulation. In addition, the effect of the noise floor of the receiver is illustrated through the simulation.

In addition, by eliminating the receiver noise floor limitation in the simulation, we can see what the actual data should look like. This was done on the third curve in Figure 16, and significant deviation from the measured values take place at the 99 percentile and above. When higher loss was measured, for instance in the Steel Canyons, the deviation takes place at lower percentiles.

Simulation Results

Table 3 shows the results of the simulation for each environment and over each range of elevation angles. In general, the mean and standard deviation for the two path summation portion of the model are the same independent of elevation and environment. Similarly, the standard deviation in the signal shadowed mode is the same for the elevations and environment variables.

TABLE 3
Simulation Model Results

ELEVATION, DEGREES	TWO PATH SUMMATION			SIGNAL SHADOWED		
	MEAN, dB	STANDARD DEVIATION, dB	%	MEAN, dB	STANDARD DEVIATION, dB	MAX., dB
SUBURBAN RESIDENTIAL						
10-20	1.0	2.0	50	6.5	5.0	18.0
20-35	0.5	2.5	70	6.5	4.5	19.0
35-65	1.0	2.0	90	6.5	4.5	22.0
URBAN MIDRISE						
10-20	1.0	2.5	30	13.0	4.0	20.5
20-35	-1.0	2.25	45	12.0	5.0	23.5
35-65	-0.5	2.0	75	11.0	6.0	25.0
STEEL CANYON						
20-35	-2.0	2.0	28	16	5.5	23.0
35-65	-1.0	2.0	45	13.5	6.5	25.5

Figure 15 shows the percent of time spent in each mode as a function of elevation angle. As the elevation angle approaches zero, it is expected that the signal shadowed mode will be encountered virtually 100 percent of the time. As the elevation angle approaches 90 degrees, however, that mode will not go to zero because there are always overpasses and trees that go over the roadway which block the direct path. The trends indicated by the previous qualitative analysis of Figures 9 - 11 are verified by these results.
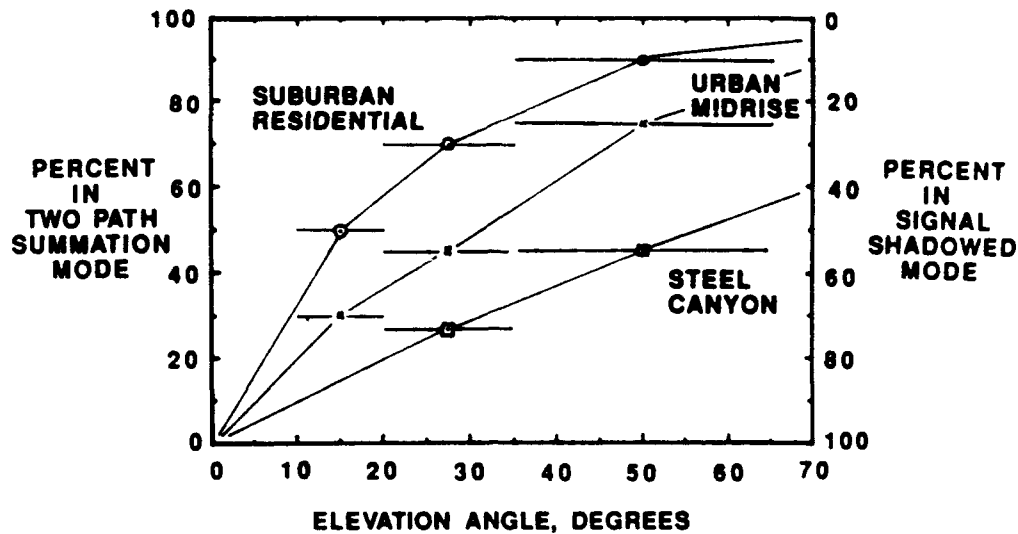
Figure 15. The computed time spent in each mode as a function of elevation angle and environment as obtained from the simulation is shown.

Comparison To Other Data

Similar results to those shown in Figure 15 have been obtained in Scandinavia and Germany over a reduced elevation angle range [6]. There, measurements made in the "city" and on the "highway" have been reported. The city data, over the range of measurement of 13 to 43 degrees, is within a few percent of the Steel Canyon results described herein. The "highway" data is well above the Suburban Residential data of Figure 15 as would be expected of an area clear of obstructions.

The signal shadowed mode is normally encountered in terrestrial land mobile propagation. Okumura et. al. [7] has made extensive measurements of land mobile propagation, and the received field strength as a function of range and base transmitter height were presented at 1.5 GHz. From this, the median excess path loss has been determined as a function of elevation, and that urban data is presented in Figure 16. The mean determined from the simulation for the signal shadowed mode for urban midrise and steel canyons is also shown in the figure, and it is evident that the trend is consistent. A similar analysis by Reudink [8] also shows a similar result.

Okumura reports that the median path loss in a suburban environment is about 11 dB less than when in an urban environment, independent of the tower height or range. Hence it will be independent of the elevation. The results reported herein show the elevation independence for the signal shadowed mode, however, the magnitude is 5 1/2 dB reduced from that in an urban midrise environment and 8 1/2 dB in the steel canyons. The description of suburban environment of Okumura supports the conclusion that there was less blockage in his case, consistent with the results above.
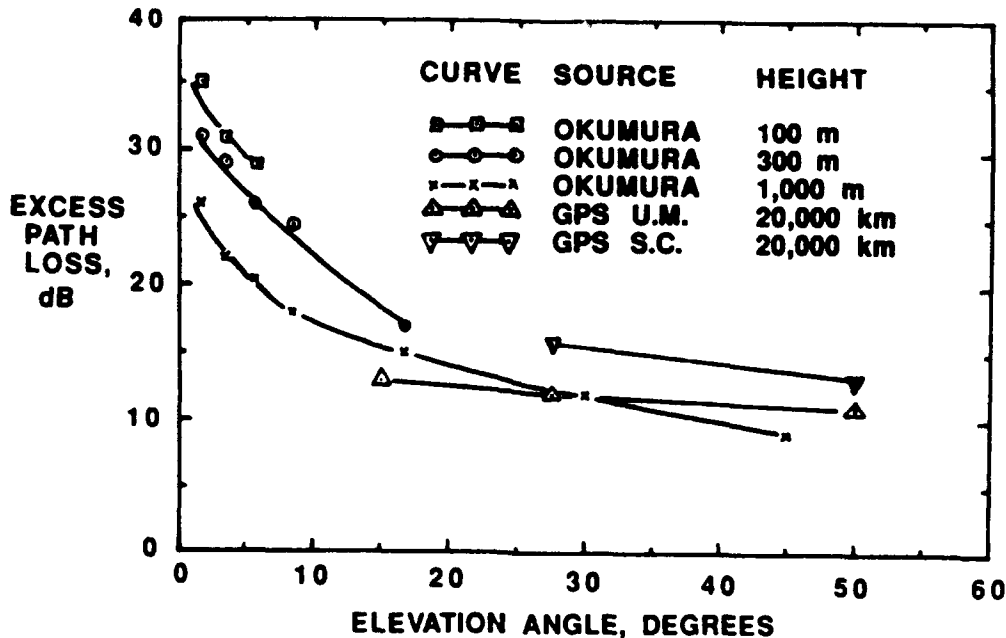
Figure 16. Median excess path loss in a urban environment as a function of
elevation from Okumura and from the measurements in the signal
shadowed mode reported herein.

The measured standard deviation for land mobile propagation as a function of
frequency was presented by Okumura, and those curves are abstracted into Figure 17.
Rubinstein [9] made a careful measurement study of the standard deviation at 800
MHz in the Los Angeles area. Those measurements are also shown in Figure 17
along with the standard deviation in the signal shadowed mode reported herein.

These measurements were taken over different areas so some differences would be
expected. The range of reported values by Rubinstein though very large is less than
reported by Okumura for rolling hilly suburban terrain. It is concluded, as a result of
the large range of Rubinstein, that the standard deviation reported herein is consistent
with terrestrial land mobile propagation even though it is less than Okumura.

PROPOSED PROPAGATION MODEL

It has been shown that a two mode lognormal model fits the measured excess path
loss data taken through a 50 Hz bandwidth averaging filter. One mode has a mean
near 0 dB, and a standard deviation of about 2 dB. The second mode was shown to
be consistent with terrestrial land mobile propagation, and has a mean, presented
herein, determined by the environment, and a standard deviation of about 5 dB. the
percent of time spent in each mode was also presented herein, and is also a function
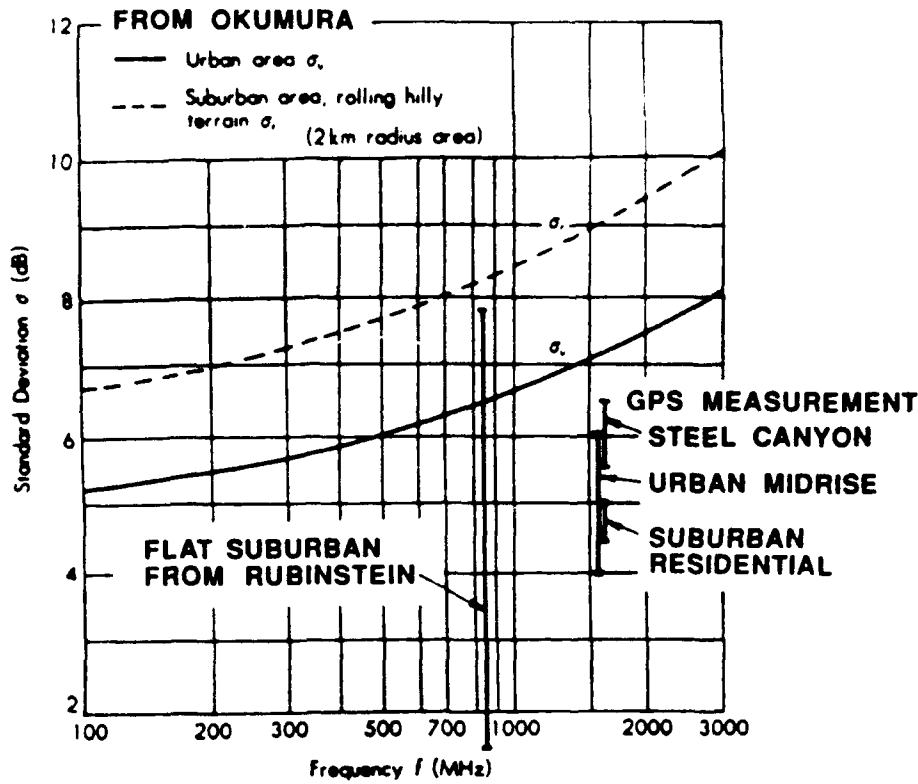
Figure 17. Standard deviation of land mobile signals. Curves abstracted from
Okumura, data from Rubinstein, and data from signal shadowed
mode reported herein are shown.

Over short distances the received power of a terrestrial land mobile signal is Rayleigh
distributed [10]. Therefore, that characteristic should be considered for the signal
shadowed mode reported herein. The two path summation mode has no mechanism
to produce such a distribution, and so it will be assumed that over a short distance the
distribution is nearly constant.

It has been commonly reported that much satellite to land mobile propagation is Rician
distributed [6] [8]. Many of the the measurements reported, have concentrated on
propagation in the presence of and through trees as discussed previously. In that
case, the direct path signal is not completely blocked, and it can provide a dominant
received wave to form the Rician distribution.

When there are many obstructions present, however, the direct wave cannot penetrate
them and a Rayleigh distribution results over short distances. It is therefore
hypothesized that the urban signal shadowed mode has associated with it a Rayleigh
distribution. But in the suburban environment where the blockage is provided by trees
and wood frame buildings, the short distance distribution is more nearly Rician.

CONCLUSION

A two mode model of the averaged excess path loss has been shown to describe the data measured from GPS satellites at a frequency of 1.6 GHz to a land mobile terminal. One mode was shown to have a relatively large excess path loss like terrestrial multipath propagation with similar statistics while the second is near free space. The percent of time spent in each mode is a function of the environment in which the land mobile terminal is located and the elevation angle to the satellite, and this too was presented. The measured fade rate and fade duration which is applicable to satellites near the 20,000 km elevation of the GPS constellation were also presented. Finally, a total propagation model of the land mobile link was described which is consistent with a geometrical description of the propagation path and the measurements reported herein as well as those in the literature.

ACKNOWLEDGEMENTS

REFERENCES

[1] Julius Goldhirsh and Wolfhard J. Vogel, Mobile Satellite System Fade Statistics for Shadowing and Multipath from Roadside Trees at UHF and L-Band, IEEE Trans. on Veh. Tech. vol. 37, no. 4, April 1989, pp. 489-498.

[2] A. J. Bundrock and R. A. Harvey, Propagation Measurements for an Australian Land Mobile-Satellite System, Australian Telecommunications Research, vol. 23, no. 1, 1989, pp. 19-26.

[3] Richard L. Campbell, Attenuated Direct and scattered Wave Propagation on Simulated Land Mobile Satellite Service Paths in the Presence of Trees, Proceedings of the Mobile Satellite Conference, May 3-5, 1988, pp. 101-106.

[4] P. M. Janiczek editor, Global Positioning System, Papers Published in Navigation, Reprinted by The Institute of Navigation, vol. 1, 1980.

[5] Garry C. Hess Land-Mobile Satellite Excess Path Loss Measurements, IEEE Trans. on Veh. Tech. vol. VT-29, no. 2, May 1980, pp. 290-297.

[6] Elrich Lutz, Daniel Cygan, Michael Dippold, Frank Dolainsky, and Wolfgang Papke,The Land Mobile Satellite Communication Channel-Recording, Statistics, and Channel Model, IEEE Trans. on Veh. Tech., Vol. 40, no. 2, May, 1991 pp., 375-386.

[7] Yoshihisa Okumura, Eiji Ohmori, Tomihiko Kawano, and Kaneharu Fukuda, Field Strength in VHF and UHF Land-Mobile Radio Service, Reprinted from the Review of the Electrical Communication Laboratory, vol. 16, no. 9-10, September-October 1968, pp. 825-873.

[8] D. O. Reudink, Estimates of Path Loss and Radiated Power for UHF Mobile-Satellite Systems, The Bell System Technical Journal, vol. 62, no. 8, October 1983, pp. 2493-2512.

[9] Thomas N. Rubinstein, The Standard Deviation of the Local Means of Land Mobile Radio Signals in Flat Suburban Terrain, 1986 IEEE Veh. Tech. Society Conference Record, pp. 52-56.

[10] William C. Jakes, Jr., Microwave Mobile Communications, John Wiley & Sons, 1974, pp. 13.

MISSION

OF

ROME LABORATORY

Rome Laboratory plans and executes an interdisciplinary program in research, development, test, and technology transition in support of Air Force Command, Control, Communications and Intelligence (C^3I) activities for all Air Force platforms. It also executes selected acquisition programs in several areas of expertise. Technical and engineering support within areas of competence is provided to ESD Program Offices (POs) and other ESD elements to perform effective acquisition of C^3I systems. In addition, Rome Laboratory's technology supports other AFSC Product Divisions, the Air Force user community, and other DOD and non-DOD agencies. Rome Laboratory maintains technical competence and research programs in areas including, but not limited to, communications, command and control, battle management, intelligence information processing, computational sciences and software producibility, wide area surveillance/sensors, signal processing, solid state sciences, photonics, electromagnetic technology, superconductivity, and electronic reliability/maintainability and testability.